Theoretical Investigations of Mie Scattering and Virtual Excitations in Nanophotonics

Lepeshov, Sergei

Publication date:
2023

Document Version
Publisher's PDF, also known as Version of record

Citation (APA):
Lepeshov, S. (2023). *Theoretical Investigations of Mie Scattering and Virtual Excitations in Nanophotonics*. Technical University of Denmark.

Doctor of Philosophy
Doctoral thesis in Photonics Engineering

DTU Electro
Department of Electrical and Photonics Engineering

Theoretical Investigations of Mie Scattering and Virtual Excitations in Nanophotonics

Author: Sergei Lepeshov

Supervisor: Prof. Søren Stobbe
Co-supervisors: Dr. Guillermo Arregui Bravo

DTU Electro
Department of Electrical and Photonics Engineering
Technical University of Denmark
Ørsteds Plads
Building 343
2800 Kongens Lyngby, Denmark

Abstract

Nanophotonics represents a dynamic and rapidly expanding area of research focused on investigating fundamentals of light-matter interactions and developing cutting-edge nanoscale devices for high-speed computation, medicine, different kinds of sensors, and renewable energy. To effectively address these technological and social challenges, nanophotonics necessitates a robust and efficient platform. Historically, plasmonics, a branch of nanophotonics harnessing the tightly confined optical resonances in metallic nanoparticles, emerged as a compelling option for both applications and fundamental investigations, but plasmonics suffers from unwanted energy dissipation. In recent years, a novel approach rooted in Mie resonances in dielectric nanostructures has gained attention, offering the prospect of high quality factors and tunable resonances accompanied by negligible losses, in contrast to plasmonics. This paradigm shift, termed ”Mie-tronics,” has brought significant advancements, including photonic bound states in the continuum, supercavity modes, optical anapoles, superscattering, and perfect absorption, giving rise to groundbreaking technologies like nanolasers, Huygens metasurfaces, and metalenses, among others. Thus, further investigations of Mie resonances in connection to other research topics, such as optical levitodynamics and extreme electromagnetic field confinement, are significantly relevant. Moreover, combining Mie resonances with complex frequency excitation, namely, virtual absorption and gain, presents a promising avenue for theoretical studies that can potentially result in new energy-efficient nanophotonic devices.

This thesis investigates approaches provided by Mie resonances and virtual excitations to boost optical trapping, low-loss electromagnetic field confinement, Purcell effect, and tunability of optical properties. The thesis is a collection of the research papers produced during the PhD studies, and, therefore, it consists of a broad introduction including the most central theoretical background and the papers. First, a comparative study of the emission rate enhancement in plasmonic and dielectric nanostructures is carried out. Second, the tunability of nanophotonic structures composed of phase-change materials and photochromatic materials coupled to Mie resonances is explored. Based on these explorations, a tunable phase-change core-shell nanoparticle capable of reversibly switching between nanolaser and cloaking regimes is designed. In addition, a reconfigurable Fano resonance in a hydrogen-rich silicon Mie nanoparticle coupled to a photochromatic material that can change the refractive index when exposed to intense ultra-violet and visible light is proposed. Third, capabilities of dielectric metasurfaces, such as quality factor and spatial localization of light, are extended through the photonic bound states in the continuum and antiferromagnetic order of magnetic Mie resonances. Fourth, Mie-resonant nanoparticles are shown to master optical levitodynamics by enhancing the gradient optical forces induced by counterpropagating gaussian beams. Finally, the impact of virtual excitations on light scattering and optical forces in Mie-resonant nanoparticles is investigated. It is revealed that signals with complex frequencies, i.e., exponentially growing or decaying temporal profiles, can induce pulling optical force or increase pushing force in Mie-resonant nanoparticles. This observation challenges the conventional understanding of the optomechanical interaction of plane wave signals with photonic structures. Also, a significant improvement of optical Kerker, anti-Kerker, and transverse Kerker effect under the complex frequency excitation is uncovered, revisiting the optical theorem in the complex frequency plane. These groundbreaking fundamental results can pave the way for nanophotonic devices beyond the existing constraints, improve their tunability and sensitivity.

Resume

Nanofotonik repræsenterer et dynamisk og hurtigt voksende forskningsområde, hvis fokus er at undersøge de grundlæggende principper for lys-stof-vekselvirkning samt at udvikle banebrydende nanoskala-enheder til højtydende computere, medicin, forskellige former for sensorer og vedvarende energi. For effektivt at adressere disse teknologiske og sociale udfordringer kræver nanofotonik en robust og effektiv platform. Historisk set er plasmonik, som en gren af nanofotonik, der udnytter de tæt indesluttede optiske resonanser i metalnanopartikler, som en interessant mulighed til både anvendelser og grundlæggende undersøgelser, men plasmonik lider af uønskede energitab. I de seneste år er der opstået interesse for en ny tilgang baseret på Mie-resonanser i dielektriske nanostrukturer, hvilket giver udsigt til høje godheder og justerbare resonanser ledsaget af negligerbare tab, hvilket står i kontrast til plasmonik. Dette paradigmeskifte, kaldet "Mie-tronics", har ført til betydelige fremskridt, herunder fotoniske bundne kontinuum-tilstande, superkavitets-egentilstande, optiske anapoler, super-spredning og perfekt absorption, hvilket videre har ført til banebrydende teknologier heriblandt nanolasere, Huygens-metaoverflader og metalinser. Derfor er yderligere undersøgelser af Mie-resonanser i forbindelse med andre forskningsemner, såsom optisk levitodynamik og ekstrem elektromagnetisk feltindeslutning, ganske relevante. Derudover udgører kombinationen af Mie-resonanser og excitationer med kompleks frekvens, navnligt virtuel absorption og forstærkning, en lovende retning for teoretiske studier, der potentielt kan føre til nye energieffektive nanofotoniske enheder.

Denne afhandling undersøger brugen af Mie-resonanser og virtuelle excitationer til forstærkning af optiske fælder, elektromagnetisk feltindeslutning med lave tab, Purcell-effekten og justerbarheden af optiske egenskaber. Thesisset er en samling af de forskningsartikler, der er produceret under ph.d.-studierne, og den består derfor af en bred introduktion, der inkluderer den mest centrale teoretiske baggrund og artiklerne. Først laves en sammenlignende undersøgelse af emissionsrateforstærkning i plasmoniske og dielektriske nanostrukturer. Dernæst udforskes justerbarheden af nanofotoniske strukturer som er sammensat af faseændrende materialer og fotochromatiske materialer der er koblet til Mie-resonanser. Baseret på disse undersøgelser designes en justerbar kerne-skal faseændrings-nanopartikel som reversibelt kan skifte mellem nanolaser- og cloaking-regimet. Derudover foreslås en rekonfigurerbar Fano-resonans i en Mie-nanopartikel af hydrogenrig silicium som er koblet til et fotochromatisk materiale, der kan justere brydningsindekset, når det udsættes for intens ultraviolet og synligt lys. For det tredje udvides dielektriske overfladers egenskaber, såsom godhed og rumlig lokalisering af lys, ved brug af fotoniske bundne kontinuum-tilstande og antiferromagnetisk orden af magnetiske Mie-resonanser. For det fjerde vises det, at Mie-resonante nanopartikler mestrer optisk levitodynamik ved at forstærke de optiske gradientkræfter induceret af modsatrettede gaussiske stråler. Endelig undersøges effekten af virtuelle excitationer på lysdispersion og optiske kræfter i Mie-resonante nanopartikler. Det findes at signaler med komplekse frekvenser, altså eksponentielt voksende eller aftagende tidsprofiler, kan inducere en trækkende optiske kraft eller øge den skubbende kraft i Mie-resonante nanopartikler. Denne observation udfordrer den konventionelle forståelse af optomekanisk interaktion mellem planbølgesignaler og fotoniske strukturer. Desuden afdækkes en betydelig forbedring af de optiske Kerker-, anti-Kerker- og transverse Kerker-effekter ved excitation med en kompleks frekvens, hvilket giver anledning til at genbesøge det optiske teorem. Disse banebrydende resultater kan vise vejen mod nanofotoniske enheder som omgår eksisterende begrænsninger og derved forbedrer deres justerbarhed og følsomhed.

Kongens Lyngby, 18th October 2023

Sergei Lepeshov

Acknowledgements

I begin this section with a profound sense of gratitude for the journey that led me to this point in my research path. My PhD studies have been unique, marked by unexpected turns and resilience. It began at ITMO University in Russia, but due to the unfortunate circumstances of the war between Russia and Ukraine, I was forced to relocate and continue my research elsewhere. I am deeply grateful to everyone who supported and guided me through this transformative experience.

First of all, I express my heartfelt gratitude to my supervisor, Prof. Søren Stobbe, for providing me the opportunity to continue my studies at DTU. Søren not only provided me with this opportunity but also offered unwavering support at every step of my relocation to Denmark. His belief in my capabilities, the exceptional research project he entrusted me with, and his mentorship in expanding my expertise beyond theory toward experiments and fabrication have been instrumental in shaping my research path. I am thankful for the access to world-class facilities and the knowledge he imparted to me, enhancing my research vision. I am also grateful to the Department of Electric and Photonic Engineering, Nanophoton Research Center, and DTU PhD school for welcoming me into their academic community and allowing me to complete my PhD.

Furthermore, I express my gratitude to Prof. Alex Krasnok, my former scientific advisor, colleague, and friend, who introduced me to scientific research during my undergraduate years. He nurtured my foundational skills in theoretical and numerical calculations. Alex's mentorship extended beyond the theoretical skills, teaching me how to write impactful research papers, manage my work, and effectively collaborate. I firmly believe his guidance was crucial in shaping my research path, and I am proud to be his student.

Next, I would like to thank my former PhD supervisor, colleague, and friend, Prof. Andrey Bogdanov, who guided me during the initial steps of my PhD studies. Andrey is a brilliant theoretician who enhanced my proficiency in theoretical physics and provided invaluable insights into theoretical photonics. Moreover, he taught me the significance of soft skills in scientific communication and generously shared his expertise in preparing successful research proposals. His mentorship has been a defining influence on my research path, and I am genuinely grateful for his support and friendship.

I wish to pay tribute to the memory of Prof. Yuri Baloshin, who passed away in 2022, whose advice and unwavering enthusiasm inspire me to persevere in the face of research challenges.

My time at ITMO University was marked by fruitful scientific discussions, invaluable classes in theoretical physics, and a friendly atmosphere. I express my sincere gratitude to my former colleagues who contributed to this memorable phase of my research path, including Prof. Mihail Petrov, Prof. Dmitry Zuev, Prof. Ivan Iorsh, Prof. Maxim Gorlach, Dr. Kirill Koshelev, Dr. Oleg Yermakov, Dr. Zarina Sadrieva, Dr. Dmitry Pidgaiko, and Ekaterina Tiguntseva. I would also like to thank my former students, Maxim Esmantovich, Alexander Shchekochihin, and Vladimir Pirogov, for their enthusiasm, patience, and the exciting experience I had while supervising them.

I am grateful for the invaluable guidance and scientific discussions provided by Prof. Yuri Kivshar and Prof. Andrea Alu at different steps of my research path. I sincerely thank Prof. Romain Quidant and Dr. Nadine Meyer for expanding my research horizons into optomechanics. Their support during my external stay at ETH Zurich and their immeasurable help in my relocation during the onset of the war are greatly appreciated.

I also express my deep appreciation to my present colleagues from the Photonic Nanotechnology research group at DTU. I want to thank my co-supervisor, Dr. Guillermo Arregui Bravo, and Prof. Babak Vosoughi Lahijani for their pivotal role in introducing me to the world of experimental nanophotonics and Dr. Bingrui Lu for teaching me essential skills in fabricating nanophotonic devices. My heartfelt thanks go to the entire team, including Anastasia Vladimirova, Daniel Alec Farbowitz, Thor August Schimmell Weis, Christian Anker Rosiek, Søren Engelberth Hansen, Ali Nawaz Babar, Konstantinos Tsoukalas, and Dr. Alireza Shabani, for the invaluable scientific discussions and welcoming atmosphere that makes our research efforts both productive and enjoyable.

Finally, my deepest appreciation goes to my family for their unwavering support throughout my journey. Their love and encouragement have been my constant motivation.

List of publications

- **S. Lepeshov**, M. Yesmantovich, and A. Bogdanov. Topological enhancement of evanescent field localization in all-dielectric metasurfaces. *Optica* 10, 797-800 (2023). Doi: 10.1364/OPTICA.488420

- **S. Lepeshov** and A. Krasnok. Virtual optical pulling force. *Optica* 7, 1024-1030 (2020). Doi: 10.1364/OPTICA.391569

- **S. Lepeshov** and A. Krasnok. Tunable phase-change metasurfaces. *Nature Nanotechnology* 16, 615–616 (2021). Doi: 10.1038/s41565-021-00892-6

- **S. Lepeshov**, N. Meyer, P. Maurer, O. Romero-Isart, and R. Quidant. Levitated Optomechanics with Meta-Atoms. *Physical Review Letters* 130, 233601 (2023). Doi: 10.1103/PhysRevLett.130.233601

- **S. Lepeshov**, A. Vyshnevyy, and A. Krasnok. Switchable dual-mode nanolaser: mastering emission and invisibility through phase transition materials. *Nanophotonics* 12, 3729-3736 (2023). Doi: 10.1515/nanoph-2023-0249

- S. Kim, **S. Lepeshov**, A. Krasnok, and A. Alù. Beyond Bounds on Light Scattering with Complex Frequency Excitations. *Physical Review Letters* 129, 203601 (2022). Doi: 10.1103/PhysRevLett.129.203601

- M. Wang, A. Krasnok, **S. Lepeshov**, G. Hu, T. Jiang, J. Fang, B. Korgel, A. Alù, and Y. Zheng. Suppressing material loss in the visible and near-infrared range for functional nanophotonics using bandgap engineering. *Nature Communications* 11, 5055 (2020). Doi: 10.1038/s41467-020-18793-y

- B. Borodin, F. Benimetskiy, V. Davydov, I. Eliseyev, A. Smirnov, D. Pidgayko, **S. Lepeshov**, A. Bogdanov, and P. Alekseev. Indirect bandgap $MoSe_2$ resonators for light-emitting nanophotonics. *Nanoscale Horizons* 8, 396-403 (2023). Doi: 10.1039/D2NH00465H

- A. Rahimzadegan, **S. Lepeshov**, W. Zhou, D.-Y. Choi, J. Sautter, D. Arslan, C. Zou, S. Fasold, C. Rockstuhl, T. Pertsch, Y. Kivshar, and I. Staude. Optically induced antiferromagnetic order in dielectric metasurfaces with complex supercells. *Journal of the Optical Society of America B* 40, 994-998 (2023). Doi: 10.1364/JOSAB.478307

- D. Yakimchuk, E. Kaniukov, **S. Lepeshov**,V. Bundyukova, S. Demyanov, G. Arzumanyanm, N. Doroshkevich, K. Mamatkulov, A. Bochmann, M. Presselt, O. Stranik, S. Khubezhov, A. Krasnok, A. Alù, and V. Sivakov. Self-organized spatially separated silver 3D dendrites as efficient plasmonic nanostructures for surface-enhanced Raman spectroscopy applications. *Journal of Applied Physics* 126, 233105 (2019). Doi: 10.1063/1.5129207

Abbreviations

CMT	Coupled mode theory
QNM	Quazi-normal mode
PT	Parity-time
BIC	Bound state in the continuum
CPA	Coherent perfect absorption
CVA	Coherent virtual absorption

Contents

Introduction

In the last century, extensive technological growth, fueled by prodigious scientific discoveries, has led humankind to tremendous advances in manufacturing, education, and health care. The agricultural industry has reached a new level, providing food for the majority of countries in the world and postponing global hunger for at least decades. Modern transportation and navigation methods have significantly shortened travel times, enabling people with different social backgrounds to journey between cities and continents easily. Thanks to sustainable progress in medicine and pharmacology, human lifespan upraises steadily; humanity courageously confronts global challenges such as pandemics and improves medical treatment of cancer and hereditary and chronic diseases. The World Wide Web allows people from different corners of the Earth to keep in touch with each other, exchange information, and even learn new professions remotely. All of the aforementioned technological and social breakthroughs are a part of our reality owing to the ubiquitous implementation of electronics.

Electronic gadgets have become deeply ingrained in human life, seamlessly integrating into daily routines, taking the form of household appliances and computational devices. The last ones, well-known as computers, are versatile tools for information processing and data analysis, various calculations, communication, and even recreation. The improvement of computers has boosted progress in computationally consuming research fields, from cosmology and spacecraft to molecular biology and bioinformatics. Hence, the significance of electronics and its impact on modern society cannot be overestimated, yet the persistent challenges, such as acceleration of information processing, early disease detection, and environmental crisis, to name a few, demand further intensive development of new energy-efficient, high-performance instruments.

Another crucial branch of science and technology that has brought metrology, sensing, and construction to a new level of accuracy is optics. Optics, on its own, has given birth to high-precision telescopes for near- and far-space observation and microscopes for detecting low-dimensional objects. More than that, when combined with electronics, it has triggered a revolution in renewable energy with solar cells, enabled advanced imaging with digital cameras, and facilitated high-speed signal transmission over long distances using optical fibers and lasers.

The shift of optics from merely observing objects and phenomena to its application in mission-critical technologies has marked the inception of photonics. This new science explores the fundamentals of light-matter interactions and develops new principles and devices for light generation, manipulation, and detection. To this day, the greatest achievement of photonics is the invention of the laser, a source of spatially and temporally coherent light, and the optical fiber, a transparent medium that can guide light over long distances. Optical fibers have emerged as an efficient replacement for their electrical counterparts, metal wires, for high-speed information transfer. Since then, opposing photonics as an effective substitution for electronics in many technical fields has become a trend [1–5]. While electronics is based on the transformation and routing of electrical currents in metals and semiconductors, i.e., moving electrons and holes, photonics is meant to bend and convert light, that is the flow of photons. At low frequencies, electrical signals are indispensable information carriers; however, as the frequency rises up to 50 GHz, significant losses occur in electrical circuits, resulting in signal distortion and heating [6]. Contrarily, high-frequency optical signals encounter minimal losses and can propagate over distances exceeding 10 km in highly transparent silica fibers without amplification and heating [1]. Moreover, electrical signals are highly susceptible to external electrical fields, which can result in interference [7]. On the other hand, photons carrying the optical signals exhibit weak interactions with other electromagnetic fields and with each other, making optical signals highly resistant to interference. Thus, replacing electronics with photonics can substantially improve ultra-fast computational devices that require high-frequency signal processing and energy efficiency [2].

Nowadays, photonics is not only a rapidly developing fundamental science about light-matter interactions [8] but a burgeoning industry of optical sensors [9], telecommunication equipment [1] and lasers of various kinds and purposes [10]. Attempts to reproduce electronic computing on a photonic platform have laid the foundation for nanophotonics, light manipulation at the nanoscale, and photonic integrated circuitry [11]. Modern photonics aims to find solutions for unaddressed challenges of all-optical quantum computing based on the quantum superposition principle [12], quantum cryptography [13], and secured optical networks based on quantum entanglement [14]. To produce an adequate replacement of electronics, the interaction between light and quantum emitters should be sufficiently strong [15]. For that reason, new materials, including graphene and monolayer semiconductors, are proposed as a platform for optical counterparts of electronic transistors, offering enhanced quantum efficiency [16–18]. Another approach is compressing the light down to the scale of electronics using the interaction between photons and plasmons, which are collective oscillations of electron gas in metals [19]. The coupling strength between emitters and photons can be substantially increased in various kinds of artificial media known as photonic crystals [20], metamaterials [21], and metasurfaces [22], composed of identical nanoparticles or nanoparticle assembles, meta-atoms, extending the concept of a crystal from solid-state physics to optics.

Carefully designed photonic nanostructures can establish a new generation of nanosized sensors, empowering single molecule detection [23–25], intracellular microscopy [26, 27], and targeted drug delivery [28]. A nanophotonic device with a specially engineered shape can squeeze photons to the size of a biological molecule, thereby significantly enhancing molecule visibility in an optical microscope [23]. Plasmonic nanoparticles [29], nanolasers [30], and quantum dots [31] are developed for fluorescent imaging of biological cells for real-time monitoring of underinvestigated intracellular molecular processes; the new findings have the potential to advance human understanding of biology and medicine, offering new avenues for the treatment of various pathologies. Nanocarriers can deliver drugs directly to tumors and blood clots, enabling more effective and precise cancer treatment and stroke prevention [32, 33]. On the other hand, nanoparticles themselves can be harnessed for therapeutic purposes by utilizing their ability to generate heat when exposed to light (thermo-optical heating) [34].

Although, as discussed above, nanophotonics promises to establish a sustainable platform for future innovations in high-speed data processing and to address the global issues in sensing technologies and life sciences, the current solutions have serious problems that prevent the practical realization of fundamental findings in industry [35–37]. Firstly, nanophotonics suffers from low precision of nanostructure manufacturing and respectively arising fabrication imperfections [38]. Divergencies in geometrical parameters of the fabricated structures from the design result in an undesired shift of spectral position of optical resonances, and the impurities decrease the overall performance by inducing scattering and dissipation losses [39]. The problem can be overcome by utilizing silicon, the most prominent material for nanophotonics due to its well-developed and mature fabrication techniques resulting from its extensive use in electronic integrated circuits [40]. However, photonic circuits require a versatile material platform that combines light sources, guides, and receivers on the same chip [41]. Despite silicon-based devices supporting good transmissivity [42] and silicon photodetectors being widely used [43,44], silicon suffers from insufficient quantum efficiency of photon radiation following from its indirect bandgap [45]. Thus, research into new materials that combine excellent light emission properties with high-precision manufacturing is still ongoing.

Secondly, weak interactions between photons and the guiding medium, as well as among photons themselves, resulting in small losses and insignificant interference, is rather a disadvantage in applications where light is controlled by light, such as all-optical computing [46]. Recent trends in the miniaturization of bulky optical devices, including non-linear crystals for high harmonic generation, down to nanosized flat structures, bring forward the challenge of dealing with poor non-linear material properties [47,48]. To overcome these limitations, one could capture photons in time and space to strengthen the interaction using specially designed nanocavities possessing both high quality factors (Q-factors) and local field enhancement [49]. However, sufficiently high Q-factors usually require a large-scale photonic structure [50, 51], while spatial localization of photons in small volumes comes at the cost of scattering and dissipation losses [52–54]. To compete with electronics, the scale of a photonic structure unit should be less than 100 nm, but as the structure's size reduces, the resonances' Q-factors drop drastically, providing weak light-matter interactions [55].

Thirdly, nanoscale optical memory, ultra-fast photonic switches, and post-fabrication adjustment demand not only sustainable and highly efficient nanophotonic structures but also tunability of their properties [56]. Nevertheless, most existing solutions for tunable nanostructures possess at least one disadvantage: they either reconfigure at long time scales, lack reversibility and repeatability, cause superior damage to the structure after several switching cycles, or combine hardly compatible fabrication techniques [57–59].

Thus, it is essential to develop new approaches to break the barriers limiting the penetration of nanophotonics into applications.

Recently, a new field in nanophotonics has emerged based on high-refractive index dielectric nanoparticles supporting optical resonances of electric and magnetic nature [60, 61]. These resonances were first discovered in 1908 by Gustav Mie and appear when the optical size of the particles is compared to the wavelength of light [62]. A few years ago, it was recognized that the Mie-resonant nanoparticles might serve as an efficient replacement for metal nanoparticles, exhibiting surface plasmon resonances due to low material losses and internal field localization, and replacement of bulky photonic crystal cavities due to nanoscale sizes and more straightforward design and fabrication procedures [61]. Besides, the multipolar nature of the Mie resonances enables the engineering of optical beam shape [63], scattering response in the frequency domain [64], thermo-optical properties [65], and non-linear harmonic generation [66]. The research field focusing on the investigation and application of Mie-resonant nanoparticles is called Mie-tronics [67, 68]. It has been observed that the Mie resonances can turn to a supercavity mode [69], providing high Q-factors, enable anti-reflection coatings [70], and improve light coupling to quantum emitters [71], empowering single-photon sources, LED, and nanolasers. Utilizing Mie nanoparticles as building blocks for artificial 2D and 3D media, metasurfaces, and metamaterials opens the door for tunable flat lenses [72], vortex beam generation [73], and on-chip sensing [74].

Conversely, a new family of optical phenomena has been discovered when a photonic structure is pumped by electromagnetic waves with a complex frequency - monochromatic waves with exponentially growing or decaying amplitude in the time domain. The unique phenomena occurring under the complex frequency excitation are called virtual effects in the literature [75–77]. In 2017, coherent virtual absorption has been demonstrated, which can store energy with significant efficiency in a lossless material and then release it on demand [75]. Exponential modulation of the temporal profile of the incoming field can suppress scattering and transmission through the resonant structure due to destructive interference between input and output fields. Thus, the light captured inside the resonator remains unreleased as long as the excitation by an exponentially modulated field continues. Virtual absorption is analogous to coherent perfect absorption, appearing in photonic structures with balanced radiative and non-radiative losses under monochromatic excitation [77]. The concept of complex excitations has been extended to coherent virtual gain, facilitating the realization of systems requiring material gain, such as lasers, and parity-time symmetry [76].

The purpose of this thesis is to investigate new approaches, enabled by Mie resonances, along with the phenomena of virtual excitation, to enhance light-matter interactions in nanophotonic devices, such as nanoantennas and metasurfaces, thereby increasing their performance. First, I explore the spontaneous radiation rate and near-field localization intensity enhancement in the presence of plasmonic (metal) and dielectric nanostructures. I study the performance of unconventional self-organized dendrite nanostructures for surface-enhanced Raman spectroscopy. Then, I focus on a dielectric disk resonator made of bulk transition metal dichalcogenides exhibiting excitonic transitions. I investigate the dependence of the emissivity of the excitonic disk on the order of the modes and disk radius and observe a 100-fold improvement in photoluminescence intensity compared to an unpatterned flake. Second, I examine the tunability of nanophotonic structures composed of phase-change materials, which can significantly change their optical properties upon transition between amorphous and crystalline phases. I design a tunable phase-change core-shell nanoparticle capable of switching between nanolaser and cloaking regimes reversibly. I estimate laser threshold, betta- and confinement factors, and nanolaser parameters crucial to enter coherent light emission. I demonstrate that the tunable nanoparticles can be arranged into a metasurface switching between coherent light emission and transparency, suitable for large-scale applications, such as optical transceivers in LIDAR. Also, I demonstrate a reconfigurable Fano resonance in a hydrogen-rich silicon Mie nanoparticle coupled to a photochromatic material that can change the refractive index when radiated by intense ultraviolet and visible light. Third, I reveal new mechanisms to extend the capabilities of dielectric metasurface made of multipolar Mie-resonant particles. I engineer an artificial photonic analog of antiferromagnetic material and numerically study its optical characteristics, comparing it with experimental measurements. I observe that antiferromagnetic properties in these materials can be associated with photonic bound states in the continuum. Further, I explore the phenomenon of bound states in the continuum to improve spatial localization of light in dielectric periodic nanostructures approaching the limit of plasmonics. Fourth, I demonstrate that Mie resonances can master optical levitodynamics, increasing the gradient optical force in counterpropagating Gaussian beams. I calculate the trap depth of optical potential and nanoparticle oscillation frequency inside the trap of a high-index Mie nanoparticle, showing its supremacy over an ordinary non-resonant particle conventionally used in optical levitodynamics. I discover that multipolar resonance configuration in Mie nanoparticles creates alternating bright and dark trapping regimes depending on the nanoparticle size. Finally, I explore the light scattering and optical forces under virtual excitation of Mie-nanoparticles. I show that under complex frequency signals with a negative imaginary part, a nanoparticle with constant permittivity exhibits negative absorption, i.e., virtual gain. Conversely, signals with a positive imaginary part of the frequency result in virtual absorption in the same nanoparticle. I find regimes in the lower complex frequency half-plane, where the pushing optical force generated by a plane wave, typically occurring in optomechanics, changes to the pulling force. This observation challenges the conventional understanding of the optomechanical interaction of plane wave signals with photonic structures. I uncover a significant improvement in optical Kerker, anti-Kerker, and transverse Kerker effect under the complex frequency excitation, revisiting the optical theorem in the complex frequency plane. These groundbreaking fundamental results can pave the way to extend the limitation of standard nanophotonic devices and improve their tunability and sensitivity.

The thesis is a collection of the research papers produced during my PhD studies, and it is split into four chapters. In Chapter 1, I present the basic theory of light-matter interactions in various nanophotonic structures. Using coupled mode theory and scattering matrix formalism, I explain general light scattering phenomena in resonant nanophotonic structures. I present the basic theory of a cavity interacting with a dipole in weak and strong coupling regimes. Additionally, I discuss the Purcell effect of an emitter near a resonant particle using coupled mode theory and classical electrodynamics. Furthermore, I provide an introduction to the theory of Fano resonances in optics and the phenomenon of photonic bound states in the continuum. I present a standard Mie theory of light scattering by a spherical non-magnetic nanoparticle, viewing it in a new light by extending it into the complex frequency plane. I give theoretical background on optical forces induced by plane waves, and Gaussian beams acting on arbitrary structures, particularly planar resonators and spherical nanoparticles. In Chapter 2, I overview the current state of the research field of Mie-tronics. I discuss the recent advances in the design and manufacturing of Mie-resonance-based nanostructures for wavefront engineering, sensing, tunable photonics, non-linear optics, and nanolasers. In Chapter 3, I explain the fundamentals of coherent virtual phenomena and comprehensively review the pioneering works in this emerging research field. In Chapter 4, I summarize and conclude the thesis and provide an outlook on the future development of Mie-tronics and phenomena induced by virtual excitations. The peer-reviewed journal papers are included in the Appendices A-J.

CHAPTER 1

Fundamentals of light-matter interactions in nanophotonic structures

This Chapter presents the theoretical background for investigating optical phenomena in nanophotonic structures. Starting with the Lippmann-Schwinger equation in Section 1.1, I introduce the derivation of coupled mode theory (CMT) and scattering matrix formalism, versatile tools to describe various systems of coupled resonators or emitters. I discuss the properties of CMT equations and scattering matrix, focusing on poles and zeros of scattering matrix eigenvalues emphasizing their significance for light-matter interactions. Further, in Section 1.2, I attribute the poles of the scattering matrix to Hamiltonian and explore different regimes of interaction between subsystems of photonic structures. I reveal a condition for the strong and weak coupling regime as well as for exceptional points. In Section 1.3, I present a derivation of a standard formula for spontaneous emission rate modification factor, namely, the Purcell factor, from CMT and make a connection between the Purcell effect and antenna effect in classical electrodynamics. I explain the physical significance of Fano resonances for optical systems and derive the famous Fano formula for a single-mode system in Section 1.4. I introduce bound states in the continuum (BIC), unique states in nanophotonic systems without radiative losses, and derive conditions for BICs in two-mode systems. The presence of BICs in periodic structures, their impact on Q-factors, and the role of topological charges are discussed in Section 1.5, alongside the non-existing theorem in compact 3D structures. In the next section, I give a classical derivation of the Mie theory for a scattering of electromagnetic field on non-magnetic spherical nanoparticles and generalize it to complex frequencies, attributing the Mie resonances in scattering spectra to the poles in the lower complex frequency half-plane. Beyond the effects of light bending by nanostructures, I consider the optomechanical effects of nanostructures manipulated light in Section 1.7. I obtain the average optical force acting on a plate and a nanoparticle in dipole approximation. Finally, I summarize the Chapter in Section 1.8.

1.1 Scattering matrix formalism and coupled mode theory

Interacting with photonic structures, light, as an electromagnetic wave, experiences absorption or amplification, reducing or gaining its intensity (I) respectively, elastic scattering, resulting in a change of the wave vector ($\mathbf{k}$) direction, or non-elastic scattering, accompanied with photon frequency (ω) conversion [78]. Considering the scattering phenomena in photonic structures, different scattering regimes can be distinguished depending on the structure size and optical density [79]. Rayleigh scattering regime occurs when the object size is significantly less than the wavelength of light λ, which is typically valid for dielectric particles smaller than 100 nm. The intensity of Rayleigh scattering increases as $I \sim 1/\lambda^4$. Onwards, when the particle size rises to values comparable with the wavelength ($\lambda = nD$, n is the refractive index), it enters the Mie scattering regime. Mie scattering is enabled by the excitation of Mie modes and characterized by resonant behavior of the scattering intensity; in other words, peaks of scattering intensity appear when the frequency of the modes coincides with the frequency of the incident wave. One should mention that plasmonic nanoparticles in the Rayleigh regime also demonstrate resonant behavior, diverging from $1/\lambda^4$ relationship, owing to the excitation of localized surface plasmons. In macroscopic ($\lambda << D$) or planar objects such as mirrors, lenses, waveguides, and metasurfaces, the light scattering phenomena is referred to as reflection whose spectral behavior is mainly defined by the material constants and geometrical resonances.

Absorption of light exhibits due to the excitation of higher energy states of electrons, atoms, and molecules inside the material and the transformation of the energy of these states to other forms, primarily heat or spontaneous light emission that is, photoluminescence. On the contrary, a material, initially in the excited state, serves as a gain medium for incoming photons; each generates a new identical photon in the stimulated emission process, thus contributing to the intensity amplification of the incoming optical signal. Propagating through more exotic active (gyrotropic) and non-linear media, light experiences conversion of polarization and frequency. In non-linear materials, the light with sufficiently high intensity can induce other electromagnetic fields at lower or higher frequencies, giving rise to high-harmonic generation, parametric down-conversion, frequency comb generation, Raman scattering, and supercontinuum generation. In gyrotropic materials, different circular polarization components of light couple differently to atomic transitions within the material, resulting in rotation of the electric field polarization vector. Piezoelectric crystals support the acoustic-optical effect, enabling modulation of amplitude, frequency, and phase of light by mechanical waves or, conversely, inducing acoustical waves through light propagation.

Generally, most of the phenomena mentioned above are effectively described by Maxwell's equations. However, certain phenomena, such as spontaneous light emission, can only be explained via quantum mechanics approaches [12]. Nevertheless,

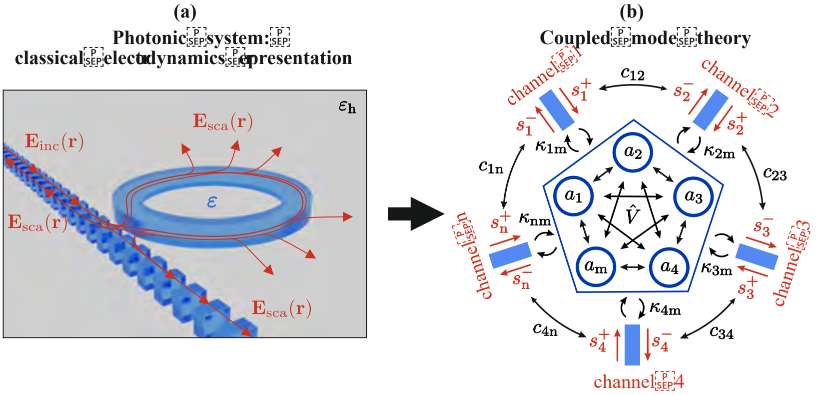
(a) Photonic system: classical electrodynamics representation

(b) Coupled mode theory

Figure 1.1. (a) An illustration of a typical photonic system and electromagnetic wave scattering process. (b) Representation of light scattering problem in coupled mode theory with the interplay between quasinormal modes and scattering channels.

associated effects, namely, the Purcell effect and electromagnetically induced transparency (EIT), do not require quantum mechanical formalism and can be addressed by classical electrodynamics, as shown further. Figure 1.1(a) illustrates a typical electromagnetic wave scattering problem, appearing in nanophotonics: light propagates inside a waveguide made of a periodic structure, penetrating to a microring cavity and exciting cavity resonances that scatter the light back to the waveguide and surrounding medium. The material of the waveguide, microring, and the material of the host medium are described by complex value dielectric permittivities ϵ and $\epsilon_{\rm h}$. Here, the consideration is restricted to linear isotropic non-magnetic optical materials without temporal or spatial dispersion. The incoming optical signal is described by $\mathbf{E}_{\rm inc}(\omega, \mathbf{r})$ while the scattered signal is $\mathbf{E}_{\rm sca}(\omega, \mathbf{r})$. For solution of the problem of light propagation in such systems, Maxwell's equations can be derived as follows:

$$\nabla \cdot \mathbf{D} = \rho_{\rm f}, \tag{1.1}$$

$$\nabla \times \mathbf{E} = -\partial \mathbf{B}/\partial t, \tag{1.2}$$

$$\nabla \cdot \mathbf{B} = 0, \tag{1.3}$$

$$\nabla \times \mathbf{H} = \mathbf{j}_{\rm f} + \partial \mathbf{D}/\partial t, \tag{1.4}$$

where $\rho_{\rm f}$ and $\mathbf{j}_{\rm f}$ are the free charge density and free current density. In the absence of free charges and external currents in frequency domain, Maxwell's equations can be rewritten as follows:

$$\nabla \cdot \mathbf{D} = 0, \tag{1.5}$$

$$\nabla \times \mathbf{E} = i\omega \mathbf{B}, \tag{1.6}$$

$$\nabla \cdot \mathbf{B} = 0, \tag{1.7}$$

$$\nabla \times \mathbf{H} = -i\omega \mathbf{D}. \tag{1.8}$$

Dielectric displacement $\mathbf{D}$ and magnetic field $\mathbf{B}$ are related to the electric $\mathbf{E}$ and magnetizing $\mathbf{H}$ fields through constitutive relations, that, in the frequency domain, are:

$$\begin{aligned} \mathbf{D} &= \varepsilon\varepsilon_0 \mathbf{E} = \varepsilon_0 \mathbf{E} + P, \\ \mathbf{B} &= \mu\mu_0 \mathbf{H} = \mu_0 \mathbf{H} + \mu_0 \mathbf{M}. \end{aligned} \tag{1.9}$$

Here, $\mathbf{P}$ is the electric polarization expressed through bound currents as $\mathbf{P} = -i\omega \mathbf{j}_\mathrm{b}$, $\mathbf{M}$ is the magnetization, identical to zero in non-magnetic media, ε_0 and μ_0 are dielectric and magnetic constants, ε and μ are material dielectric permittivity and magnetic permeability. Substituting Maxwell's equations one into another, one can get a Helmholtz equation for the electric field with the electric polarization as a source of the field:

$$\nabla \times \nabla \times \mathbf{E} - \omega^2/c^2 \mathbf{E} = \omega^2 \mu_0 \mathbf{P}. \tag{1.10}$$

Using the electromagnetic boundary conditions in the absence of free charges and currents:

$$\begin{aligned} \mathbf{n} \times (\mathbf{E}_1 - \mathbf{E}_2) &= 0, \\ \mathbf{n} \times (\mathbf{H}_1 - \mathbf{H}_2) &= 0, \\ \mathbf{n} \cdot (\mathbf{D}_1 - \mathbf{D}_2) &= 0, \\ \mathbf{n} \cdot (\mathbf{B}_1 - \mathbf{B}_2) &= 0 \end{aligned} \tag{1.11}$$

together with the Helmholtz equation, one can find analytical solutions for certain 1D, 2D, or 3D photonic structures possessing different kinds of symmetry, such as a multilayer sphere, infinitely long cylinder, or alternating layers of metals or dielectrics [79, 80]. For more complicated geometries, the solution can be found using Green's function approach:

$$\nabla \times \nabla \times \overset{\leftrightarrow}{\mathbf{G}} - \omega^2/c^2 \overset{\leftrightarrow}{\mathbf{G}} = \omega^2 \mu_0 \delta(\mathbf{r}), \tag{1.12}$$

where $\overset{\leftrightarrow}{\mathbf{G}}$ is the dyadic Green's function, δ is the Dirac delta function. Then, the scattered field can be derived from the Lippmann-Schwinger equation:

$$\mathbf{E}_\mathrm{sca}(\omega, \mathbf{r}) = \int d\mathbf{r}'^3 [\varepsilon(\omega, \mathbf{r}') - \varepsilon_\mathrm{h}] \overset{\leftrightarrow}{\mathbf{G}} (\omega, \mathbf{r}, \mathbf{r}') [\mathbf{E}_\mathrm{inc}(\omega, \mathbf{r}') + \mathbf{E}_\mathrm{sca}(\omega, \mathbf{r}')]. \tag{1.13}$$

One can notice that Equation 1.13 is an integral equation. Formally, one can simplify the task by introducing an integral operator $\hat{L}$ [81]: $\mathbf{E}_\mathrm{sca} = \hat{L}(\mathbf{E}_\mathrm{inc} + \mathbf{E}_\mathrm{sca})$. Then, the solution of the integral equation can be written as $\mathbf{E}_\mathrm{sca} = \hat{S}\mathbf{E}_\mathrm{inc}$, where $\hat{S}$ is the scattering operator. $\mathbf{E}_{\mathrm{inc}}$ and $\mathbf{E}_{\mathrm{sca}}$ can be expressed in the basis of incoming and outgoing waves, that propagate in scattering channels $\mathbf{E}_{\mathrm{inc}} = \sum_{\mathrm{n}=1}^{\mathrm{N}} s_{\mathrm{n}}^{+}\mathbf{e}_{\mathrm{in,n}}$, $\mathbf{E}_{\mathrm{sca}} = \sum_{\mathrm{n}=1}^{\mathrm{N}} s_{\mathrm{n}}^{-}\mathbf{e}_{\mathrm{out,n}}$. Here, s^{+} and s^{-} are the amplitudes of the ingoing and outgoing fields $\mathbf{e}_{\mathrm{in,n}}$ and $\mathbf{e}_{\mathrm{in,n}}$ respectively. Scattering channels are the solutions of Helmholtz equations in the absence of scatterers and may be represented as spherical, cylindrical, or plane waves existing in the host environment (vacuum modes) or as waveguide modes.

In tasks involving optical interactions between multiple photonic subsystems, it is often more convenient to transit from a strict solution of Maxwell's equation to a solution for scattering channels and amplitudes of system modes. This solution can be found utilizing coupled mode theory (CMT) [82]. Figure 1.1(b) demonstrates a transition from classical electrodynamics representation to CMT that describes coupling between amplitudes of the modes a_{m} and scattering channels $s_{\mathrm{n}}^{+}, s_{\mathrm{n}}^{-}$. CMT is a phenomenological approach that was initially developed for coupled optical waveguides [83] and microwave transmission lines [84]. Although there are different ways to derive CMT, including Schrodinger equation [81, 85], one can show a derivation of CMT equations from the Lippmann-Schwinger equation. The scattered field outside and inside the photonic structure can be expanded into the basis of open system modes, quasinormal modes (QNMs) [86]:

$$\mathbf{E}_{\mathrm{sca}}(\omega, \mathbf{r}) = \sum_{\mathrm{m}=1}^{\mathrm{M}} a(\omega)_{\mathrm{m}} \mathbf{E}_{\mathrm{m}}(\mathbf{r}), \tag{1.14}$$

where $\mathbf{E}_{\mathrm{m}}$ is normalized electric field of a m-th QNM. QNMs are solutions of the Helmholtz equation in the absence of incoming fields:

$$\nabla \times \nabla \times \mathbf{E}_{\mathrm{m}} - \varepsilon \omega_{\mathrm{m}}^{2}/c^{2} \mathbf{E}_{m} = 0, \tag{1.15}$$

where ω_{m} is the eigenfrequency of a m-th QNM. The Green's function of the photonic system can be rewritten using the QNM expansion approach [87]:

$$\overset{\leftrightarrow}{\mathbf{G}}(\omega, \mathbf{r}, \mathbf{r}') = \sum_{\mathrm{m}=1}^{\mathrm{M}} \frac{\omega}{2(\omega - \omega_{\mathrm{m}})} \mathbf{E}_{\mathrm{m}}(\mathbf{r}) \otimes \mathbf{E}_{\mathrm{m}}(\mathbf{r}'). \tag{1.16}$$

Substituting Equation 1.14 into the left and right sides of the Lippmann-Schwinger equation, using Equation 1.16 for the Green's function, and expanding the incident field into the basis of modes of the scattering channels, one can derive the following system of M linear equations:

$$\begin{aligned}
(\omega-\omega_{\mathrm{m}})a_{\mathrm{m}}\mathbf{E}_{\mathrm{m}} &= \\
&=\mathbf{E}_{\mathrm{m}}(\mathbf{r})\otimes\left(\frac{\omega}{2}\int d\mathbf{r}'^3[\varepsilon(\mathbf{r}')-\varepsilon_{\mathrm{h}}]\mathbf{E}_{\mathrm{m}}(\mathbf{r}')\cdot\sum_{\mathrm{n=1}}^{\mathrm{N}}\frac{s_{\mathrm{n}}^{+}\mathbf{e}_{\mathrm{in,n}}(\mathbf{r}')}{\sqrt{v_{\mathrm{g,n}}}}\right)+ \\
&+\mathbf{E}_{\mathrm{m}}(\mathbf{r})\otimes\left(\frac{\omega}{2}\int d\mathbf{r}'^3[\varepsilon(\mathbf{r}')-\varepsilon_{\mathrm{h}}]\mathbf{E}_{\mathrm{m}}(\mathbf{r}')\cdot\mathbf{E}_{\mathrm{m}}(\mathbf{r}')\right)+ \qquad (1.17)\\
&+\mathbf{E}_{\mathrm{m}}(\mathbf{r})\otimes\left(\frac{\omega}{2}\int d\mathbf{r}'^3[\varepsilon(\mathbf{r}')-\varepsilon_{\mathrm{h}}]\mathbf{E}_{\mathrm{m}}(\mathbf{r}')\cdot\sum_{\mathrm{q\neq m}}^{\mathrm{M}}\mathbf{E}_{\mathrm{q}}(\mathbf{r}')\right).
\end{aligned}$$

The first term of the right-hand side of Equation 1.17 represents the interaction between the m-th QNM and N scattering channels. The temporal dispersion of the scattering channel modes is implicitly included in the group velocity $v_textrmg,n = |\partial\omega/\partial\mathbf{k}|$ [81]. The second term denotes the interaction of the QNM with itself, i.e., the internal losses. The third term depicts the coupling of the m-th QNM to other modes. Multiplying Equation 1.17 by $-i$ and integrating over the volume of the system, one can come up with the following system of equations for the QNM amplitudes in the frequency domain:

$$-i(\omega-\omega_{\mathrm{m}})a_{\mathrm{m}}=\sum_{\mathrm{n=1}}^{\mathrm{N}}\kappa_{\mathrm{mn}}s_{\mathrm{n}}^{+}-\gamma_{\mathrm{m}}a_{\mathrm{m}}-\sum_{\mathrm{q\neq m}}^{\mathrm{M}}g_{\mathrm{mq}}a_{\mathrm{q}}. \qquad (1.18)$$

Here, κ_{mn} is the coupling strength between the m-th QNM and n-th scattering channel, γ_{m} is the sum of mode losses, g_{mq} is the interaction energy between m-th and q-th modes. Similarly, an equation for the scattering channel amplitudes can be obtained by substitution of the Green's function for a waveguide [88] $\overset{\leftrightarrow}{\mathbf{G}}(\omega,\mathbf{r},\mathbf{r}')=\sum_{\mathrm{n=1}}^{\mathrm{N}}\frac{ia\omega}{2v_{\mathrm{g,n}}}\mathbf{e}_{\mathrm{out,n}}(\mathbf{r})\otimes\mathbf{e}_{\mathrm{out,n}}(\mathbf{r}')$ into Equation 1.13 and expanding the scattered field $\mathbf{E}_{\mathrm{sca}}$ into the series $\mathbf{E}_{\mathrm{sca}}=\sum_{\mathrm{n=1}}^{\mathrm{N}}s_{\mathrm{n}}^{-}\mathbf{e}_{\mathrm{out,n}}$:

$$s_{\mathrm{n}}^{-}=\sum_{\mathrm{k=1}}^{\mathrm{N}}c_{\mathrm{nk}}s_{\mathrm{k}}^{+}+\sum_{\mathrm{m=1}}^{\mathrm{M}}\eta_{\mathrm{nm}}a_{\mathrm{m}}, \qquad (1.19)$$

where c_{nk} is the element of the matrix of direct scattering from n-th to k-th scattering channel, η_{nm} is the coupling constant between n-th channel and m-th mode. It can be shown that $\kappa_{\mathrm{mn}}=\eta_{\mathrm{nm}}*$ are complex conjugates of each other, indicating reciprocity in the interaction between the QNMs and scattering channels [89]. Finally, one can obtain CMT for mode and scattering channel amplitudes in a general form in the frequency domain:

$$\frac{d}{dt}|a\rangle=-i\hat{H}_0|a\rangle/\hbar-i\hat{V}|a\rangle/\hbar+\hat{K}^T|s^+\rangle, \qquad (1.20)$$

$$|s^-\rangle = \hat{C}|s^+\rangle + \hat{K}|a\rangle, \tag{1.21}$$

where $|a\rangle = a_1, a_2, a_3, a_\mathrm{M}$, $|s^+\rangle = s_1^+, s_2^+, s_3^+, s_\mathrm{N}^+$, $|s^-\rangle = s_1^-, s_2^-, s_3^-, s_\mathrm{N}^-$, $|s^-\rangle$ and $|s^+\rangle$ are related through the scattering matrix $|s^-\rangle = \hat{S}|s^+\rangle$, $\hat{H}_0$ is the interactionless Hamiltonian, i.e., a diagonal matrix of QNM eigenfrequencies, $\hat{V}$ is the perturbation to Hamiltonian representing QNM coupling to each other, $\hat{K}$ is the operator of coupling between QNMs and channels, $\hat{C}$ is the direct scattering matrix. Substitution of Equation 1.20 to 1.21 gives a general expression for the scattering matrix:

$$\hat{S} = \hat{C} + \hat{K}\frac{i}{\omega - \hat{H}_0 - \hat{V}}\hat{K}^T, \tag{1.22}$$

revealing a close connection between scattering matrix properties and the Hamiltonian. Further, it can be shown that the Hamiltonian eigenvalues result in poles of the scattering matrix, which is an important conclusion that benefits the analysis of the optical properties of the system.

To unfold the connection between scattering matrix properties and the Hamiltonian of the system, one can diagonalize the scattering matrix by solving the eigenproblem [81]:

$$\hat{S}|\psi_\mathrm{k}^+\rangle = \sigma_\mathrm{k}(\omega)|\psi_\mathrm{k}^+\rangle, \tag{1.23}$$

where σ_k form a set of N scattering matrix eigenvalues, $|\psi_\mathrm{k}^+\rangle$ is a corresponding eigenvector composed of scattering amplitudes $s_1^+, s_2^+, s_3^+, s_\mathrm{N}^+$. According to Equation 1.23, excitation of the system through scattering channels with the wave amplitudes conforming to the k-th eigenvector reflects to the same set of channels with an amplitude

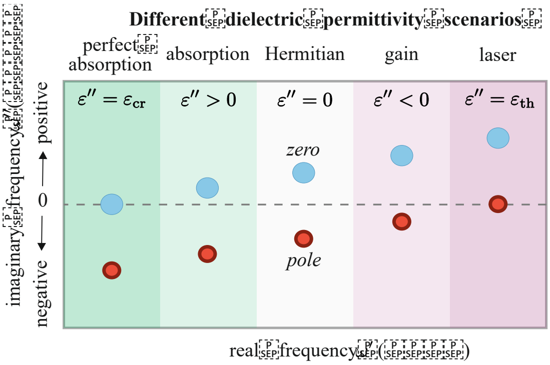

Figure 1.2. Scattering matrix eigenvalue poles and zeros in the complex frequency plane and their configuration illustrating different phenomena in the photonic system concerning the imaginary part of dielectric permittivity: perfect absorption when the permittivity reaches critical value $\varepsilon'' = \varepsilon_\mathrm{cr}$, absorption at positive values $\varepsilon'' > 0$), lack of dissipative losses when the permittivity is Hermitian $\varepsilon'' = 0$, amplification or gain at $\varepsilon'' < 0$, and laser generation when the system reaches a threshold $\varepsilon''_\mathrm{th}$).

multiplier σ_k. In the case of the system described by Hermitian dielectric permittivity ε, the scattering matrix is a unitary operator $\hat{S}\hat{S}^\dagger = \hat{1}$. The absolute value of the unitary matrix eigenvalue is equal to one ($|\sigma_\mathrm{k}(\omega)| = 1$), signifying that the incident field, given by $|\psi_\mathrm{k}^+\rangle$, merely experiences a phase shift of $\arg \sigma_\mathrm{k}$. Injection of losses into the system by supposing a positive imaginary part of permittivity ($\varepsilon'' > 0$) reduces $|\sigma_\mathrm{k}(\omega)|$ such that $0 < |\sigma_\mathrm{k}(\omega)| < 1$. Oppositely, systems with gain, i.e., negative imaginary permittivity ($\varepsilon'' < 0$), increase $|\sigma_\mathrm{k}(\omega)|$. Furthermore, one can analytically continue $\sigma_\mathrm{k}(\omega)$ in the plane of complex frequencies $\omega = \omega' + i\omega''$. In the complex frequency plane, $|\sigma_\mathrm{k}(\omega)|$ can reach any values between 0 and inf, matching zeros and poles of the scattering matrix, that have direct physical meaning. The poles of the scattering matrix originate from the zeros of the denominator of Equation 1.22, when ω coincides with the Hamiltonian eigenfrequencies and are associated with excitation of QNMs. The causality principle dictates that these poles can only be located in the lower complex frequency half-plane unless the system is unstable, which can be the case for amplifying media ($\varepsilon'' < 0$) [90]. On the other hand, zeros of the scattering matrix correspond to the vanishing of outgoing field amplitudes. The eigenvalues of the scattering matrix can be expanded into a special product using the Weierstrass factorization theorem [91]:

$$\sigma_\mathrm{k}(\omega) = A \exp(iB_\mathrm{k}\omega) \prod_\mathrm{m}^\mathrm{M} \frac{\omega - \omega_\mathrm{z,m}}{\omega - \omega_\mathrm{p,m}}, \tag{1.24}$$

where $\omega_\mathrm{z,m}$ and $\omega_\mathrm{p,m}$ are the complex frequencies of zeros and poles of the m-th QNM, indicating that the response of the system is fully determined by their position in the complex frequency plane. Under time-reversal transformation of $\hat{S}$-matrix of the system with Hermitian permittivity, the poles and zeros exchange the position in the complex plane, implying that for $\varepsilon'' = 0$, pole and zero frequencies are complex conjugated, i.e., $\omega_\mathrm{z,m} = \omega_\mathrm{p,m}^*$, as depicted in Figure 1.2. In the systems with $\varepsilon'' = 0$, the distance between pole/zero and the real frequency axis determines radiative losses provided by leakage of energy to scattering channels $\gamma_\mathrm{r,m} = \mathrm{Im}\,[\omega_\mathrm{z,m}] = -\mathrm{Im}\,[\omega_\mathrm{p,m}]$. In the case of absorptive media $\varepsilon'' > 0$, the permittivity becomes non-Hermitian, and $\omega_\mathrm{z,m}$ and $\omega_\mathrm{p,m}$ are no longer conjugated. Instead, upon increasing ε'', the pole and zero drift downwards in the complex plane. At $\varepsilon'' = \varepsilon_\mathrm{cr}$, the zero reaches the real axis, and the system turns into a perfect absorber. The regime of perfect absorption, referred to as critical coupling in the literature [92], occurs when the non-radiative losses $\gamma_\mathrm{nr,m}$, induced by the imaginary part of permittivity, balance radiative losses $\gamma_\mathrm{r,m}$. When $\varepsilon'' > \varepsilon_\mathrm{cr}$, one can say that the system is undercoupled, meaning that the rate of dissipation losses exceeds the excitation rate. Otherwise, if $\varepsilon'' < \varepsilon_\mathrm{cr}$, the system is overcoupled, as a part of the field scatters back to the channels. The opposite zero-pole dynamics is observed in the complex plane when $\varepsilon'' < 0$: pole and zero migrate towards the upper half-plane. As ε'' reaches a threshold value ε_th, the pole reaches the real frequency axis, and the system turns into a laser, a source of coherent emission, whose coherence is insured by the singular spectral response. The farther decrease ε'' results in unstable system behavior characterized by exponentially increasing mode amplitude. Those systems, that are usually tricky to treat mathematically and to physically interpret, find their application in structures with parity-time symmetry [93].

1.2 Light-emitter interaction. Strong and week coupling regimes

Interactions between light and a quantum emitter play a central role in the functionality of nanophotonic devices. However, generally, these interactions are quite weak due to the significant mismatch between the emitter characteristic size and the wavelength of light – the emitter size is much smaller than the wavelength, particularly in the visible and near-infrared spectral ranges [94]. This can be understood from the analysis of the spontaneous emission decay rate of a two-level system with electric transition dipole moment $\mathbf{d}$ and transition energy $\hbar\omega_0$:

$$\gamma = \frac{\omega_0^3|\mathbf{d}|^2}{3\pi\epsilon_0\hbar c^3} \tag{1.25}$$

where $\hbar$ is the Plank's constant. The spontaneous emission decay rate, also known as one of Einstein's coefficients [95], describes the rate with which the emitter undergoes a transition from the excited to the ground state accompanied by photon radiation and characterizes the efficiency of the emitter's coupling to the "bath" of the photonic modes of the surrounding environment [12]. Remarkably, the decay rate scales with ω_0 similar to the Rayleigh scattering, implying that the emission efficiency drops in the long-wavelength limit. Although Equation 1.26 is typically derived in Wigner-Weisskopf theory after the second quantization of electromagnetic field [12], the decay rate can be obtained using classical electrodynamics, considering a point dipole $\mathbf{p}$ oscillating at frequency ω_0 in vacuum. The electric field induced by a point dipole can be found as follows:

$$\mathbf{E}(\omega,\mathbf{r}) = \omega_0^2\mu_0 \overset{\leftrightarrow}{\mathbf{G}}_0 (\omega,\mathbf{r},\mathbf{r}')\mathbf{d}, \tag{1.26}$$

where $\overset{\leftrightarrow}{\mathbf{G}}_0$ is the Green's function of the point dipole located at $\mathbf{r}$, which can be obtained from Equation 1.12. Averaged power, dissipated in the point dipole, is described by the Pointing theorem:

$$P = -\frac{1}{2}\mathrm{Re}\left[i\omega_0\mathbf{p}^*\mathbf{E}(\omega,\mathbf{r}')\right] = \frac{\omega_0^3\mu_0}{2}\mathbf{p}^*\mathrm{Im}\left[\overset{\leftrightarrow}{\mathbf{G}}_0 (\omega,\mathbf{r}',\mathbf{r}')\right]\mathbf{p}. \tag{1.27}$$

Using Green's function for a point dipole, one can get the final expression for the power radiated by the point dipole:

$$P = \frac{\omega_0^4|\mathbf{p}|^2}{12\pi\varepsilon_0 c^3}. \tag{1.28}$$

The time-averaged radiated power and the decay rate can be related through the photon energy $\gamma = P/\hbar\omega_0$. Substituting Equation 1.28, one can derive a formula of a classical decay rate resembling the Wigner-Weisskopf decay rate:

$$\gamma = \frac{\omega_0^3 |\mathbf{p}|^2}{12\pi\varepsilon_0 \hbar c^3}. \tag{1.29}$$

It has to be mentioned that the classical dipole moment differs $\mathbf{p}$ from the quantum mechanical expectation value of the transition dipole moment operator $\hat{\mathbf{d}}$ [96]. While $\mathbf{p}$ is associated with the charge distribution induced by external electromagnetic fields, $\hat{\mathbf{d}}$ provides coupling between the ground and excited states assisted by electromagnetic fields, those amplitudes can be zero $\langle\hat{E}\rangle$=0 as in the case of vacuum fluctuations.

Equation 1.27 reveals the dependence of the emitter decay rate on the Green's function. It signifies that the decay rate depends on the electromagnetic environment and can be substantially modified for quantum emitters placed in a dielectric media or in the vicinity of a photonic structure. Furthermore, one can show that the emitter decay rate is directly proportional to the photonic local density of states $\rho(\omega_0, \mathbf{r}')$ at the position of the emitter $\mathbf{r}'$ [80, 96]:

$$\gamma = \frac{\pi\omega_0}{\hbar\varepsilon_0} |\mathbf{d}|^2 \rho(\omega_0, \mathbf{r}'), \tag{1.30}$$

where $\rho(\omega_0, \mathbf{r}') = \frac{2\omega_0}{\pi c^2 |\mathbf{d}|^2} \mathbf{d}^* \mathrm{Im}\left[\overset{\leftrightarrow}{\mathbf{G}}\right] \mathbf{d}$.

The photonic local density of states (LDOS) reflects the number of photonic states, i.e., electromagnetic modes, per unit volume and frequency. Equations 1.27, 1.30 provide useful insights into manipulating the emitter properties, enabling enhancement of the spontaneous emission rate or, conversely, trapping the emitter in the excited state for a sufficiently long time [97]. Moreover, when the emitter is coupled to a photonic cavity, it opens the door for achieving hybrid states of photons and matter, known as polaritons [15].

The interaction between the cavity and emitter, as well as effects arising from such interaction, can be effectively described within CMT. Here, a single mode cavity with field amplitude a and resonance frequency $\omega_0 + \Delta$ is considered to be coupled to an emitter with oscillation amplitude b and transition frequency $\omega_0 - \Delta$. The oscillations of the cavity and emitter are dumped with dumping rates γ_a and γ_b, respectively. The cavity is coupled to a single scattering channel with a coupling constant $\sqrt{2\gamma_a}$, implying lack of dissipation losses. The emitter is assumed to be weakly coupled to the radiation continuum. Consequently, its interaction with the external fields is fully assisted by the cavity. Then, the CMT equations for two coupled subsystems in the time domain can be derived as follows:

$$\frac{da}{dt} = -i(\omega_0 + \Delta - i\gamma_a)a - igb + \sqrt{(2\gamma_a)}s^+(t), \tag{1.31}$$

$$\frac{db}{dt} = -i(\omega_0 - \Delta - i\gamma_b)b - iga, \tag{1.32}$$

$$s^-(t) = -s^+(t) + \sqrt{(2\gamma_a)}a, \tag{1.33}$$

where g is the interaction energy between the emitter and the cavity, defined as $\mathbf{dE}/\hbar$, and which accounts for polarization of the dipole with respect to the cavity field. The scattering matrix of the single-channel system is represented by a scalar and defined in the frequency domain as:

$$\hat{S}(\omega_0) = -1 + \frac{2i\gamma_a(\Delta + i\gamma_b)}{(-\Delta + i\gamma_a)(\Delta + i\gamma_b) - g^2}. \tag{1.34}$$

The poles of the scattering matrix can be determined from the denominator of the scattering coefficient $\hat{S}$ and coincide with the eigenvalues of the Hamiltonian $\hat{H} = \hbar \begin{bmatrix} \Delta - i\gamma_a & g \\ g & -\Delta - i\gamma_b \end{bmatrix}$. The eigen energies of the Hamiltonian are given by the following expressions:

$$\hbar\Omega_{1,2} = \hbar\omega_0 - i\hbar\frac{\gamma_a + \gamma_b}{2} \pm \hbar\sqrt{\left(\frac{2\Delta - i\gamma_a + i\gamma_b}{2}\right)^2 + g^2}. \tag{1.35}$$

The eigenfrequencies $\Omega_{1,2}$ correspond to the new eigenstates of the system, referred to as “dressed” states in contrast to “bare” initial states of uncoupled emitter and cavity. For $\Delta = 0$, Equation 1.35 can be simplified to $\Omega_{1,2} = \omega_0 - i\frac{\gamma_a+\gamma_b}{2} \pm i\sqrt{\left(\frac{\gamma_a-\gamma_b}{2}\right)^2 - g^2}$. One can notice that the eigenfrequencies of the dressed states are entirely determined by the interplay between the coupling rate and damping, giving rise to different coupling regimes between the cavity and emitter. The interactions can be classified based on the relative value of g with respect to the loss difference of the cavity and emitter $\gamma_a - \gamma_b$.

When the difference between the cavity and emitter losses γ_a and γ_b exceeds the interaction energy g, the cavity and emitter are in the weak coupling regime. In the weak coupling regime, the modes of the cavity and emitter are generally considered nearly unperturbed by each other [82]. Therefore, the cavity and emitter oscillation frequencies remain unchanged (see Figure 1.3(a), panel (i)). However, the dumping rates of the dressed states, i.e., the imaginary part of the eigenfrequencies, can be sufficiently modified. Figure 1.3(a), panel (i) illustrates the situation when the emitter decay rate γ_b is less than the cavity decay rate γ_a, indicated in the literature as a “bad cavity” limit [98]. Approaching $\Delta = 0$, one can observe a significant modification of the decay rates of the oscillators. Specifically, the decay rate of the emitter rises while the cavity decay rate drops. In the “good cavity” limit, the situation is reversed: when the emitter decays faster than the cavity, the radiative decay rate of the emitter is decreased compared to the uncoupled state. Below, a detailed analysis of the eigenfrequencies in the bad cavity limit is presented. Applying the assumptions $g \ll (\gamma_a - \gamma_b)/2$ and $\gamma_a \gg \gamma_b$, Equation 1.35 can be reduced to:

$$\Omega_1 = \omega_0 - i\gamma_b - i\frac{g^2}{\gamma_a}, \tag{1.36}$$

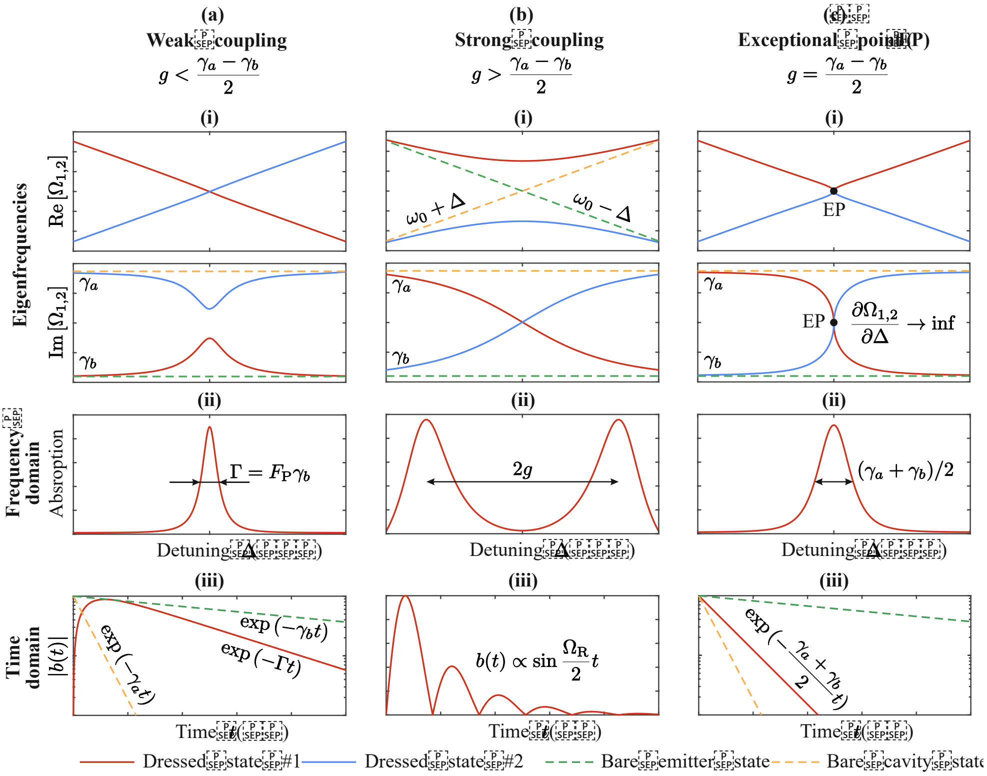

Figure 1.3. Coupling regimes occurring at the interplay between the cavity and emitter. (a) Weak coupling regime is observed at $g < (\gamma_a - \gamma_b)/2$; (b) strong coupling regime is characterized by $g > (\gamma_a - \gamma_b)/2$; (c) exceptional point (EP) in the parametric space appears when $g = (\gamma_a - \gamma_b)/2$. Entering one of the coupling regimes affects real and imaginary parts of eigenfrequencies (panel (i)), spectral properties such as absorption (panel (ii)), and time-domain response (panel (iii)).

$$\Omega_2 = \omega_0 - i\gamma_a + i\frac{g^2}{\gamma_a}. \tag{1.37}$$

Ω_1 describes the eigenfrequency of the emitter perturbed by interaction with the cavity. It can be deduced that the emitter's decay rate is augmented in comparison to its bare state by a factor known as the Purcell factor (F_P) [97]. The Purcell factor is given by the ratio of $\mathrm{Im}\,[\Omega_1]$ to γ_b, which can be expressed as:

$$F_\mathrm{P} = \frac{\mathrm{Im}\,[\Omega_1]}{\gamma_b} = 1 + \frac{g^2}{\gamma_a \gamma_b}. \tag{1.38}$$

The effect of modification of the emitter's decay rate by the cavity is referred to as the Purcell effect [97] and is discussed in detail in the next section. Figure 1.3(a), panels (ii-iii) depict the impact of the Purcell effect on the emitter's spectral and temporal characteristics. The linewidth of the absorption peak in the spectrum, associated with the energy dissipation in the emitter, increases by F_P (Figure 1.3(a), panel (ii)). The oscillation amplitude of the emitter exponentially decays upon time evolution with a rate $\Gamma = F_\mathrm{P}\gamma_b$, clearly showing that the decay rate of the emitter in the presence of the "bad" cavity is sufficiently higher compared to the single emitter embedded in the free space.

When the coupling strength between the cavity and emitter surpasses the difference between cavity and emitter losses ($g > (\gamma_a - \gamma_b)/2$), the system enters the strong coupling regime. The states in the strong coupling regime are commonly addressed as polaritonic states – the hybrid states of photons and other particles such as excitons, phonons, and plasmons, where the emitter and cavity cannot be distinguished [15]. One of the key features of the strong coupling regime is the repulsion of the energy levels resulting in anti-crossing of the real parts of the eigenfrequencies upon detuning in contrast to the imaginary part of $\Omega_{1,2}$ experiencing crossing at $\Delta = 0$ (see Figure 1.3(b), panel (i)). The strong coupling regime is particularly intriguing since it enables electromagnetically induced transparency [99]. In this regime, losses at the resonance can be significantly reduced or even completely eliminated due to the coupling between the oscillators. The absorption spectrum in Figure 1.3(b), panel (ii) demonstrates a pronounced dip between two peaks associated with polaritonic states. In the time domain, the energy exchange between the cavity and emitter gives rise to oscillations known as Rabi oscillations (Figure 1.3(b), panel (iii)). These oscillations were first observed as a periodic variation in the population of the emitter's excited and ground states induced by classical electromagnetic fields [12]. The frequency of these oscillations is referred to as the Rabi frequency Ω_R and related to the interaction constant in CMT formalism as $\Omega_\mathrm{R} = \sqrt{4g^2 - (\gamma_a - \gamma_b)^2}$.

The regime of exceptional point (EP) emerges at the interface between weak and strong coupling regimes when the coupling strength and losses are in balance ($g = (\gamma_a - \gamma_b)/2$). EPs are spectral features in the parameter space of the system, corresponding to full degeneracy of both real and imaginary parts of $\Omega_{1,2}$ and, remarkably, their corresponding eigenvectors (Figure 1.3(c), panel (i)). As shown in a number of recent works [100–102], the optical properties of systems in the vicinity of such spectral features are changed dramatically, which makes them extremely promising, for example, for supersensitive optical detectors and for control of mode composition in multimode lasers. Figure 1.3(c), panel (i), illustrates that the extreme sensitivity in the EP is owing to divergence of $\partial\Omega_{1,2}/\partial\Delta$. That implies a more significant response of the system to a small disturbance. This property of EPs is, at the same time, their main disadvantage and an obstacle to their experimental observation since, in practice, the parameters of the manufactured sample always differ from the nominal ones due to the fabrication imperfection, presence of roughness, and various kinds of fluctuations. Figure 1.3(c), panel (ii), shows that the EP is manifested as a significantly broadened absorption peak, those width approaches the limit of the Purcell decay rate enhancement. Therefore, in the time domain (Figure 1.3(c), panel (iii)), both dressed states of the emitter and cavity evolve indistinguishable as exponentially decaying curves with a decrement equal to the averaged losses of the system

$\Gamma = (\gamma_a + \gamma_b)/2$.

1.3 Purcell effect

The modification of the spontaneous decay rate is a crucial phenomenon that governs the functioning of light sources at the nanoscale [103, 104]. The concept that spontaneous emission can be enhanced by a cavity was first proposed by E. Purcell in his renowned work in 1946 [97]. By following Purcell's approach, one can delve deeper into the modification of the spontaneous emission rate of an emitter by a cavity. Equation 1.38 denotes that the Purcell enhancement factor, dictated by the ratio of the decay rate in the presence of a cavity and in vacuum $F_\mathrm{f} = \Gamma/\gamma_b$, is inversely proportional to the coupling intensity between the emitter and the cavity g, and inversely proportional to the cavity decay rate γ_a. That implies that the decay rate increases with the cavity Q-factor:

$$Q = \frac{\omega_0}{2\gamma_a}, \tag{1.39}$$

which represents the number of oscillations before the mode energy decays by a factor of e. Based on the second quantization of the electromagnetic field, one can rewrite the formula for the coupling constant between the dipole moment $\mathbf{d}$ and the electric field of QNM of the cavity polarized along $\mathbf{e}_a$ in the location of dipole moment $\mathbf{r}'$ [12]:

$$g = \frac{\mathbf{d}\mathbf{E}(\mathbf{r}')}{\hbar} = \sqrt{\frac{\omega_0}{2\hbar\varepsilon\varepsilon_0 V_\mathrm{eff}}}\mathbf{d}\mathbf{e}_a(\mathbf{r}'), \tag{1.40}$$

where V_eff is the effective mode volume obtained from the following equality [105]:

$$\frac{1}{V_\mathrm{eff}} = \mathrm{Re}\left[\frac{1}{\varepsilon(\mathbf{r}')|E(\mathbf{r}')|^2}\left(\int_V \varepsilon(\mathbf{r})|E(\mathbf{r})|^2 d\mathbf{r}^3 + \frac{ic}{\omega_0}\oint_S |E(\mathbf{r})|^2 d\mathbf{r}^2\right)\right]. \tag{1.41}$$

Here, the volume and surface integrals from the right-hand side of Equation 1.41 stand for the normalization of QNMs proposed in Ref. [105]. Noteworthy, the effective mode volume is a local quantity determined by the normalized electric field value in the point of the emitter location. Substitution of Equations 1.40–1.41, as well as Equation 1.25 for the decay rate of the emitter located in a dielectric medium with refractive index $n = \sqrt{varepsilon}$, to Equation 1.38 in the limit of sufficiently high Purcell factors, one can obtain the famous formula proposed in [97]:

$$F_\mathrm{P} = \frac{3}{4\pi^2}\left(\frac{\lambda}{n}\right)^3 \frac{Q}{V}\frac{\mathbf{d}\mathbf{e}_a}{|\mathbf{d}|}. \tag{1.42}$$

It is worth mentioning that Equation 1.42 is applicable only in the absence of detuning between the resonance frequencies of the emitter and cavity; otherwise, it requires a pre-factor $\gamma_a^2/(\gamma_a^2 + 4\Delta^2)$ [106].

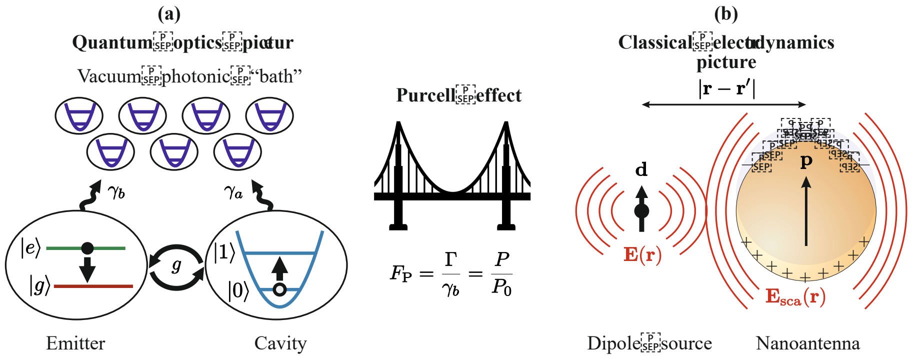

Figure 1.4. Different representations of light emission exhibitting the same Purcell enhancement. (a) Quantum optics model of TLS interaction with a photonic bath of vacuum modes and cavity mode, governing spontaneous emission rate enhancement. (b) Classical point dipole radiation loss enhancement provided by dipolar nanoantenna.

Although spontaneous emission can be fully described only in quantum mechanics, the paradigm of the Purcell effect can be expanded to classical electrodynamics, where it is related to antenna radiation (see Figure 1.4). Then, the Purcell factor can be redefined as $F_{\rm f} = \Gamma/\gamma_b = P/P_0$, where P and P_0 stand for the power radiated by a dipole source in the presence of a photonic structure and vacuum respectively [94]. Merging the concepts of quantum emitter's spontaneous emission modification and antennas has given rise to optical nanoantennas [71]. Figure 1.4(b) shows a sketch of a typical nanoantenna: an optically small plasmonic nanoparticle exhibiting a localized surface plasmon resonance is placed in the vicinity of a dipole source of light polarized along z. Diamond nanoparticles with point defects in the crystalline lattice (NV and CV centers) [107], quantum dots [108], or different types of dyes [109] have been proposed as potential light source candidates for nanoantennas. In the frequency domain, the optical response of the plasmonic nanoparticle of a radius R can be described within quasi-static approximation and effective electric polarizability:

$$\alpha_e = 4\pi R^3 \varepsilon_0 \frac{\omega_0^2}{\omega_0^2 - \omega^2 - i\gamma_a \omega}. \tag{1.43}$$

When placed in the vicinity of the dipole source at $\mathbf{r}$, the dipole moment of the nanoparticle obeys the following relation:

$$\mathbf{p} = \alpha_e(\omega)\mathbf{E}(\omega,\mathbf{r}) = \alpha_e(\omega)\omega^2\mu_0 \overset{\leftrightarrow}{\mathbf{G}}(\omega,\mathbf{r},\mathbf{r}')\mathbf{d}. \tag{1.44}$$

On the other hand, the field scattered by the plasmonic nanoparticle back to the dipole can be found as follows:

$$\mathbf{E}_{\rm sca}(\mathbf{r}') = \omega_0^2\mu_0 \overset{\leftrightarrow}{\mathbf{G}}(\omega,\mathbf{r}',\mathbf{r})\mathbf{p}(\omega). \tag{1.45}$$

Using Equation 1.45 together with Equation 1.44, applying Pointing theorem, and considering resonant scenario ($\omega = \omega_0$), one can come up to the solution for the modified radiated power:

$$P = \frac{\omega_0}{2}\mathrm{Im}\left[\mathbf{d}^*\omega_0^2\mu_0 \overset{\leftrightarrow}{\mathbf{G}}(\omega_0, \mathbf{r}', \mathbf{r})\alpha_e(\omega_0)\,\omega_0^2\mu_0 \overset{\leftrightarrow}{\mathbf{G}}(\omega_0, \mathbf{r}, \mathbf{r}')\mathbf{d}\right] + P_0. \tag{1.46}$$

In the quasi-static limit ($\lambda \gg |\mathbf{r} - \mathbf{r}'|$), the Green's function can be replaced by $\omega_0^2\mu_0 \overset{\leftrightarrow}{\mathbf{G}}(\omega_0, \mathbf{r}', \mathbf{r}) = -\frac{1}{4\pi\varepsilon_0|\mathbf{r}-\mathbf{r}'|^3}$. Normalizing the modified radiated power P by the radiated power in vacuum P_0, one can receive an expression for the Purcell factor of a dipole in the presence of a plasmonic nanoparticle:

$$F_{\mathrm{P}} = 1 + \frac{3}{4\pi^2}\lambda^3 Q \frac{R^3}{2\pi|\mathbf{r} - \mathbf{r}'|^6}, \tag{1.47}$$

which confirms the direct correspondence between classical and quantum Purcell enhancement. $\frac{R^3}{2\pi|\mathbf{r}-\mathbf{r}'|^6}$ performs as the mode volume of plasmonic nanoparticle, indicating that the electric field scattered by the nanoparticle increases with its size.

1.4 Fano resonance

Asymmetric resonance shape of the scattering response is a widespread phenomenon arising in resonant systems under certain circumstances, specifically when a sharp scattering peak interferes with a spectrally broad background reflection. At first, asymmetric peaks were discovered in the absorption spectrum of Rydberg spectral lines of atoms by H. Beutler in 1935 [110] and theoretically explained by U. Fano in the same year [111]. The formula proposed by Fano allows to describe and predict the shape of resonance based on the quantum superposition principle – it was revealed that the asymmetry in the atomic spectra exhibits due to the interference between alternative channels of excitation. The description provided by Fano has made a significant breakthrough in understanding interactions between waves and oscillators not only in quantum optics but also in a broader field of wave physics. The Fano line shapes, which are referred to as Fano resonances in the literature [112, 113], have been observed as optical Wood anomalies in diffraction gratings, where the asymmetric sharp resonances were successfully fitted by the Fano formula with good accuracy [114]. The Fano resonances play one of the key roles in modern photonics as they provide sharper resonant features compared to symmetric Lorentzian resonances, consequently providing higher sensitivity of the amplitude and phase to external perturbations [115]. In its critical limit, Fano resonance is observed as a symmetric dip in the scattering spectrum, which can reach zero, enabling electromagnetically induced transparency [116] and cloaking [117]. The properties of the Fano resonance make it attractive for a variety of applications, including high-sensitive detectors, tunable photonic devices, modulators, low-threshold lasers, perfect absorbers, and non-linear optical components [115].

The Fano line shape in the scattering spectrum of photonic structures can be effectively explained within the CMT approach, incorporating direct wave scattering between two or more channels and indirect scattering assisted by the cavity mode [89]. Here, for the sake of simplicity, the consideration is restricted to a single mode cavity coupled to two scattering channels (see Figure 1.5(a)), yet it provides a response function suitable for fitting more complex systems. CMT equations for such a system in the time domain can be derived as follows:

$$\frac{da}{dt} = -i(\omega_0 - i\gamma_a)a + \hat{K}^\dagger |s^+\rangle, \tag{1.48}$$

$$|s^-\rangle = \hat{C}|s^+\rangle + \hat{K}a, \tag{1.49}$$

where $\hat{K}$ and $\hat{K}^\dagger$ are Hermitian conjugated 2×1 matrices of coupling constants of the cavity to the scattering channels, indicating their reciprocal interaction, $\hat{C} = \begin{pmatrix} r & it \\ textit & r \end{pmatrix}$ is the direct scattering matrix of reflection r and transmission t coefficients with $|r|^2 + |t|^2$. According to Equation 1.22, one can rewrite the scattering matrix of the system under consideration:

$$\hat{S} = \hat{C} + \frac{i\hat{K}\hat{K}^\dagger}{\omega - \omega_0 + i\gamma_a}. \tag{1.50}$$

To obtain the coupling operator $\hat{K}$ in an explicit form, one can examine the case of the absent external incoming waves $|s^+\rangle = 0$. In this case, Equations 1.48– 1.49 turns into an eigenmode problem and can be rewritten for the energy of the mode and outgoing waves:

$$\frac{d|a|^2}{dt} = -2\gamma_a)|a|^2, \tag{1.51}$$

$$\langle s^{-*}|s^-\rangle = \hat{K^\dagger}\hat{K}|a|^2. \tag{1.52}$$

Using the energy conservation law, such that the energy lost by the cavity mode is transformed to the outgoing waves $d|a|^2/dt = -\langle s^{-*}|s^-\rangle$, one can come to the following relationship between coupling coefficients:

$$\hat{K}\hat{K^\dagger} = 2\gamma_a, \tag{1.53}$$

signifying an obvious equivalence between the coupling rates to the scattering channels and the cavity decay rate in a system with Hermitian permittivity. Further, one can perform a time-reversal transformation of Equations 1.48– 1.49, implying that the system is excited at zero of the scattering matrix by a signal with amplitudes $|s^{-*}\rangle$, and no outgoing waves are observed. At the same time, one can make a substitution

$|s^{-*}\rangle = \hat{K}^* a^*$, obtained from Equation 1.52, to the time-reversed Equations 1.48–1.49 resulting into the following equalities:

$$0 = \hat{C}|s^{-*}\rangle + \hat{K}a^* = \hat{C}\hat{K}^* a^* + \hat{K}a^*, \tag{1.54}$$

$$0 = \hat{C}\hat{K}^* + \hat{K}, \tag{1.55}$$

which identifies a connection between cavity excitation and de-excitation processes and direct scattering. Combining Equations 1.54–1.55 and applying the direct scattering matrix definition, one can determine the matrix elements of $\hat{K}$ and get the final expression for the scattering matrix of the considered system:

$$\hat{S} = \begin{pmatrix} r & t \\ t & r \end{pmatrix} - \frac{i\gamma_a}{\omega - \omega_0 + i\gamma_a} \begin{pmatrix} r \mp it & r \mp it \\ r \mp it & r \mp it \end{pmatrix}. \tag{1.56}$$

Here, it is assumed that the system possesses a mirror symmetry as depicted in Figure 1.5(a), such that the coupling rates between the channels and the cavity are identical, and $\mp$ stands for the odd (+) and even (−) field distributions of the mode. The diagonal element of the scattering matrix represents the amplitude reflection coefficient, and the intensity reflection coefficient can be derived as follows:

$$|\hat{S}_{11}|^2 = R = r^2 \frac{\left(\frac{\omega - \omega_0}{\gamma_a} \mp \frac{t}{r}\right)^2}{\left(\frac{\omega - \omega_0}{\gamma_a}\right)^2 + 1}, \tag{1.57}$$

which coincides with the famous Fano formula for the scattering cross section provided elsewhere [113]:

$$C_{\text{sca}} = C_0 \frac{(\epsilon \mp q)^2}{\epsilon^2 + 1}. \tag{1.58}$$

The parameter $q = r/t$ defines the asymmetry of the Fano line shape and measures the scattering ratio to the direct (background) scattering process. In a multimode system, the Fano resonance can appear between a low-Q (bright) mode and a high-Q (dark) mode, interacting through scattering channels [118]. Generally, it implies that the scattering spectrum of the bright mode is substantially perturbed by the dark mode and can give rise to electromagnetically induced transparency in the weak coupling regime depending on detuning between the modes [113]. Figure 1.5(b) demonstrates different cases of the Fano resonance in the reflection spectrum of the cavity depending on the asymmetry parameter. When the reflection coefficient r of the direct scattering matrix $\hat{S}$ is equal to 0, the Fano asymmetry parameter turns to infinity ($q \to \inf$), and the spectral response of the cavity behaves as a symmetric Lorentzian (Figure 1.5(b), blue curve). As the value of r rises up to 0.5, the resonance gets an asymmetric shape and acquires a minimum and a maximum (Figure 1.5(b), red curve). It is worth noticing that the relative position of the minimum and maximum with respect to $\omega - \omega_0 = 0$ experiences a mirror reflection with a change of the

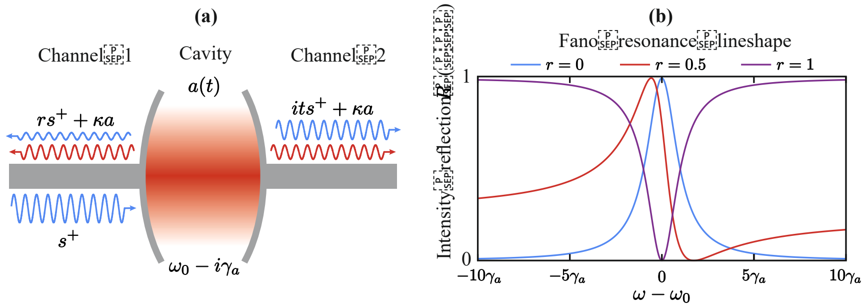

Figure 1.5. (a) A sketch of a single mode cavity coupled to two scattering channels exhibiting an asymmetric Fano resonance due to interference between direct and indirect scattered waves. (b) Intensity reflection spectra of the single mode cavity depending on direct reflection coefficient r. Different values of r correspond to different Fano line shapes: at $r = 0$ the resonance resembles a standard Lorentzian curve (blue line); upon increasing of r, the resonance becomes asymmetric (red curve); finally, it turns into a dip at $r = 1$ (violet curve).

sign of q. Approaching r to 1 and, therefore, q to 0, one can observe a dip rather than a peak in the reflection spectrum, which is a signature of electromagnetically induced transparency (Figure 1.5(b), violet curve).

1.5 Bound states in the continuum

In the previous sections, it has been shown that the imaginary part of an emitter or a cavity can be dramatically changed by coupling to another oscillator. For the cavity, it results in modification of its Q-factor, which is one of the key parameters characterizing the performance of the cavity in nanophotonic devices for sensing, non-linear optics, and lasing [30, 119, 120]. The Q-factor determines the number of oscillations of the wave before its amplitude decays by a factor of e. It means that the Q-factor defines how long the cavity can trap photons. The Q-factor can be substantially increased, theoretically reaching infinity, in so-called bound states in the continuum [121]. Bound states in the continuum (BICs) are unique states of optical, acoustic, or quantum mechanical systems that lack radiative losses, yet they are located in the domain of leaky modes. It has to be mentioned that non-radiative losses associated with the non-Hermitian part of dielectric permittivity, as well as scattering dissipation on fabrication imperfections, can still be present in the system, saturating the Q-factor of the state [122]. Nevertheless, as soon as the radiative part is absent, the BIC is not coupled to any scattering channel, which forbids both light coupling and radiation, making BIC hardly observable [123].

There are multiple ways to achieve BIC in a photonic system. One of the approaches is to completely isolate the cavity mode by utilizing materials with $\varepsilon = 0$,

$\varepsilon = \infty$, $\mu = 0$ or $\mu = \infty$ [124, 125]. However, this approach fails, as no real materials possess inf values of material parameters, and, generally, when the real part of ε is equal to 0, the imaginary part of ε becomes significant, turning the BIC into a leaky mode. Another way, which is also the most common, is coupling between two or more resonances [121]. The BICs appeared upon the interaction between the resonances of two unperturbed sub-systems or two modes of an individual cavity can be effectively described within CMT. One can consider a system of two cavity modes coupled to two scattering channels, as depicted in Figure 1.6(a). The CMT equations in the frequency domain can be derived as follows:

$$-i\omega a_1 = -i\omega_1 a_1 - \gamma_1 a_1 - iga_2 - i\sqrt{\gamma_1}s_1^+ - i\sqrt{\gamma_1}s_i^-, \tag{1.59}$$

$$-i\omega a_2 = -i\omega_2 a_2 - \gamma_2 a_2 - iga_1 - i\sqrt{\gamma_2}s_i^+, \tag{1.60}$$

$$s_i^+ = s_1^+ + i\sqrt{\gamma_1}a_1 e^{i\phi}, \tag{1.61}$$

$$s_i^- = i\sqrt{\gamma_2}a_2 e^{i\phi}. \tag{1.62}$$

Here, the direct reflection from the cavities to the scattering channels are considered to be 0, and $\phi = \mathbf{kr}$ is the phase obtained by the waves propagating from one cavity to another within the scattering channel. Substituting $s^\pm$ to Equations 1.59–1.60, one can receive the full Hamiltonian of the system:

$$\hat{H} = \hbar \begin{pmatrix} \omega_1 & g \\ g & \omega_2 \end{pmatrix} - i\hbar \begin{pmatrix} \gamma_1 & \sqrt{\gamma_1\gamma_2}e^{i\phi+i\pi} \\ \sqrt{\gamma_1\gamma_2}e^{i\phi+i\pi} & \gamma_2 \end{pmatrix} \tag{1.63}$$

The BIC non-leakage condition implies that the imaginary part of one of the Hamiltonian eigenfrequencies turns to 0 at specific parameters of the system. Given that, one can find the conditions for BIC formation in a coupled cavity scenario:

$$g(\gamma_1 - \gamma_2) = \sqrt{\gamma_1\gamma_2}(\omega_1 - \omega_2), \tag{1.64}$$

$$\phi = \pi n, n \in Z, \tag{1.65}$$

where Equation 1.64 represents the condition for two modes of the same cavity, assuming $\phi = -\pi$ (Friedrich-Wintgen BICs) [126], and Equation 1.65 corresponds to two identical cavities separated in space (Fabri-Perot BICs) [127].

Figure 1.6(b) illustrates the dynamics of poles and zeros of the scattering matrix of two identical spatially separated cavities and demonstrates the formation of Fabri-Perot type BIC. It can be seen that the variation of ϕ from $\pi/2$ to 2π brings one of the poles from the lower complex frequency half-plane to the real frequency axis. At the same time, the other pole migrates down to the lower complex half-plane. The state with reduced radiative losses is the dark state, while the other one with increased losses is the bright state. Importantly, the zeros of the scattering matrix manifest the same behavior in the upper complex half-plane, and one of the zeros merges with the pole at the real axis. The phenomenon of merging poles and zeros is an inherent

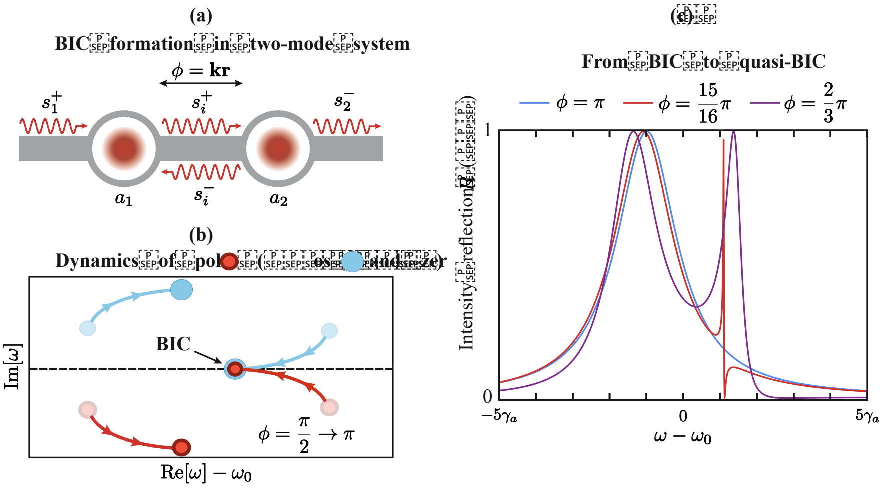

Figure 1.6. (a) Schematic representation of a two-mode system coupled to two scattering channels that can be tuned to BIC. (b) Dynamics of poles and zeros in the complex frequency plane of the two-mode system upon the phase change ϕ from $\pi/2$ to pi. (c) The reflection spectrum of the system experiencing the transition from BIC (blue curve) to quasi-BIC (red curve) and leaky state (violet curve) upon the change of ϕ.

attribute of any BIC, signifying its disappearance from the observer's field of view [81, 123]. The real frequency spectrum of the system with Fabri-Perot BIC is shown in Figure 1.6(c). The spectrum reveals a broad resonant response corresponding to the bright state. Diverging ϕ from the BIC condition, dictated by Equation 1.65, leads to "backlighting" of the BIC appearing as a Fano resonance, revealing a direct connection between them [128, 129]. Such an imperfect and lossy BIC can be called quasi-BIC and is indicated in most experiments with BIC in photonics [130].

BICs are commonly observed in periodic structures such as sub-wavelength and diffraction gratings, photonic crystals, and metasurfaces [121]. The discovery of BICs in periodic structures has attracted a lot of attention due to the singular behavior of BIC's Q-factor [131]. The singularities in the Q-factor appear when the averaged electric field of the unit cell, associated with far-field radiation in the subwavelength regime, is nullified [132]. It was later revealed that the existence of BICs in periodic structures is owing to the conservation of a certain symmetry [133]. Preservation of parity with respect to the plane perpendicular to the reciprocal grating vector leads to the indispensable formation of a BIC in Γ-point of the Brillouin zone, usually called symmetry-protected BIC (see Figure 1.7(a)). Simultaneously, the preservation of in-plane symmetry of the grating sustains an off-Γ BIC located in an accidental point of the Brillouin zone. Importantly, the location of this "accidental" BIC in the reciprocal space is strongly affected by the geometrical and material parameters of the grating [134]. Figures 1.7(b) and (c) demonstrate the direct correspondence between singularities of the Q-factor caused by symmetry-protected and accidental BICs and the cancellation of the averaged electric field. While the averaged electric field, namely, the 0th order Fourier coefficient of the Fourier expansion of the field, is turned to 0, the 1st and -1st Fourier coefficients, responsible for the near-field localization, are boosted, giving rise to the enhanced electric field localization, detailly discussed in Appendix A.

Furthermore, it has been shown that the creation and annihilation of BICs are related to the conservation of topological Chern numbers, sometimes referred to as topological charges, defined as [132]:

$$C_n = \frac{1}{2\pi} \int \nabla_{\mathbf{k}} \Phi d\mathbf{k}, \tag{1.66}$$

where Φ is the Berry phase of polarization vector (E_x, E_y), and the integration is taken in the closed contour in the complex plane around the BIC in the reciprocal space. The non-trivial topology of the polarization vector in the vicinity of BIC causes vortex beam generation in the far-field. Besides, tuning of the grating parameters affects the location of topological charges in the Brillouin zone, leading to the annihilation and creation of positive and negative charges as well as migration of charges below the light line [132].

It must be underlined that the true BIC cannot appear in a compact 3D structure unless the structure is isolated by non-transparent boundaries. This comes from the non-existence theorem of BICs in compact structures [135]. The theorem can be proved by expanding the electric field of eigenmodes into a basis of spherical harmonics and spherical Hankel functions. One can observe that, to ensure the BIC, all far-field components of the field should be canceled out, yet all expansion terms

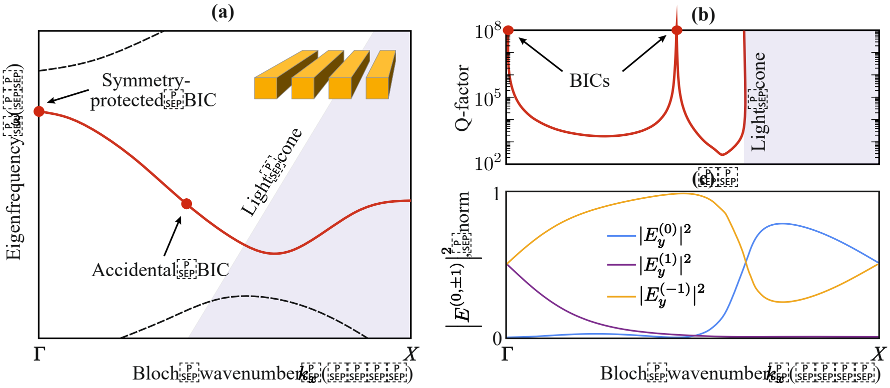

Figure 1.7. Band diagram of a subwavelength dielectric grating with the refractive index of 3. Symmetry-protected and accidental BICs are indicated in Γ point and an off-Γ point of the diagram. (b) Q-factor of a mode with BICs. (c) Averaged electric field (0th Fourier coefficient) of the grating unit cell along with the 1st and -1st Fourier expansion coefficients.

carry the far-field components. Consequently, in order to provide non-leakage, all terms should turn to 0. This situation can be partially realized in anapole states and supercavity modes, which are discussed in the next sections.

1.6 Light scattering by nanoparticles. Generalized Mie theory

First described in spheres by Gustav Mie in 1908 [62] to explain different colors produced by colloidal particles, Mie resonances are associated with the spectral response of individual nanoparticles, whose dimensions are comparable with electromagnetic wavelength in the nanoparticle material ($a \approx \lambda/n$). It has been shown that Mie resonances can facilitate all the above-discussed phenomena, such as inter-resonant strong and weak coupling [136], exceptional points [137], electromagnetically induced transparency [138], Fano resonances [139], and Purcell enhancement of embedded and surrounding emitters [140]. In contrast to localized surface plasmon resonances, Mie resonances concentrate the electric field in the particle volume, enabling thermo-optical and non-linear effects in the particle material. One of the intriguing properties of the Mie resonances is the magnetic response at optical frequencies, even in completely non-magnetic materials. The magnetic response arises due to the circular currents induced in Mie particles by external fields, as indicated in Figure 1.8(a). Besides, when the wavelength of the incoming waves is larger than the particle size, resonances corresponding to high-order multipoles (quadrupole, octupole, etc.) can

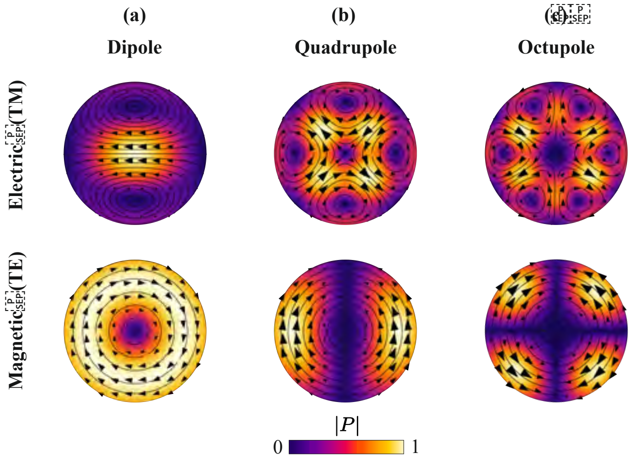

Figure 1.8. Polarization field distributions of different electric and magnetic modes of a spherical Mie particle: (a) dipole, (b) quadrupole, and (c) octupole. Black arrows point in the direction of polarization currents.

be excited. Figure 1.8(a-c) represents a family of Mie resonances in a dielectric spherical particle from dipole to octupole of both electric and magnetic nature. The maps in Figure 1.8 show the normalized polarization field distributions of Mie modes, and the black arrows indicate the direction of polarization currents. It is worth mentioning that at sufficiently large sizes, plasmonic nanoparticles also demonstrate high-order multipolar resonances, but exclusively of the electric type.

Generally speaking, multipolar Mie resonances appear in a scattering problem of nanoparticles, which can be formulated as follows: a nanostructure of a certain shape and size composed of materials with given a permittivity is illuminated by a monochromatic plane wave with a given frequency and polarization [79]. Then, the linear optical response of such a nanostructure can be quantified using scattering (C_{sca}), absorption (C_{abs}), and emission (C_{sca}) cross-sections:

$$C_{\text{sca}} = \frac{P_{\text{sca}}}{I}, \tag{1.67}$$

$$C_{\text{abs}} = \frac{P_{\text{abs}}}{I}, \tag{1.68}$$

$$C_{\text{ext}} = \frac{P_{\text{ext}}}{I}, \tag{1.69}$$

where P_{sca} and P_{abs} define the power scattered/absorbed by the nanostructure, $P_{\text{ext}} = P_{\text{sca}} + P_{\text{abs}}$, and I is the intensity of the incoming plane wave, sometimes called irradiance. The cross sections are a common measure in particle physics, intended to identify the probability of a particle or particle assembly interacting with a beam, irradiating a fixed area. In the physics of Mie resonances, it is common to normalize the cross sections by geometrical cross-section, which is the area of the nanoparticle projected onto a plane. For a spherical nanoparticle, it is defined as $\mathrm{C}_{geo} = \pi R^2$. In order to calculate the power loss upon scattering and overall extinction processes, one can utilize the Pointing theorem, considering incident and scattered fields $\mathbf{E}_{\text{inc}}$, $\mathbf{E}_{\text{sca}}$, $\mathbf{H}_{\text{inc}}$, $\mathbf{H}_{\text{sca}}$ on a spherical surface S inclosing the nanostructure:

$$P_{\text{sca}} = \frac{1}{2} \oint_S \mathrm{Re}\left[\mathbf{E}_{\text{sca}} \times \mathbf{H}^*_{\text{sca}}\right] d\mathbf{S}, \tag{1.70}$$

$$P_{\text{ext}} = \frac{1}{2} \oint_S \mathrm{Re}\left[\mathbf{E}_{\text{inc}} \times \mathbf{H}^*_{\text{sca}} + \mathbf{E}_{\text{sca}} \times \mathbf{H}^*_{\text{inc}}\right] d\mathbf{S}. \tag{1.71}$$

The scattered electromagnetic fields in Equations 1.70– 1.71 can be obtained by solving the Helmholtz equation. Nevertheless, the analytical solution can be found for a limited number of systems, including a spherical nanoparticle and infinitely long cylindrical rod. The consideration is restricted to non-magnetic dielectric spheres to demonstrate theoretical approaches widely used to describe nanostructures in Mie-tronics. The incident and scattered electric and magnetic fields in spherically symmetric problem can be expanded into a basis of vector spherical harmonics $\mathbf{M}^{1,3}_{plm}$ and

$\mathbf{N}^{1,3}_{plm}$, which satisfy the Helmholtz equation, as follows:

$$\mathbf{E}_{\text{inc}} = E_0 \sum_{l=1}^{\infty} i^l \frac{2l+1}{l(l+1)} (\mathbf{M}^{(3)}_{ol1} - i\mathbf{N}^{(3)}_{el1}), \tag{1.72}$$

$$\mathbf{H}_{\text{sca}} = E_0 \sum_{l=1}^{\infty} i^l \frac{2l+1}{l(l+1)} (-b_l\mathbf{M}^{(1,3)}_{el1} + ia_l\mathbf{N}^{(1,3)}_{ol1}), \tag{1.73}$$

$$\mathbf{H}_{\text{inc}} = -\frac{E_0\sqrt{\varepsilon_{\text{h}}}}{c} \sum_{l=1}^{\infty} i^l \frac{2l+1}{l(l+1)} (\mathbf{M}^{(3)}_{el1} + i\mathbf{N}^{(3)}_{ol1}), \tag{1.74}$$

$$\mathbf{H}_{\text{sca}} = \frac{E_0\sqrt{\varepsilon_{\text{h}}}}{c} \sum_{l=1}^{\infty} i^l \frac{2l+1}{l(l+1)} (a_l\mathbf{M}^{(3)}_{el1} + ib_l\mathbf{N}^{(3)}_{ol1}), \tag{1.75}$$

where the lower subscripts indicate the parity of the functions (p), angular momentum or multipole order (l), azimuthal number (m) always identical to 1 for spherically symmetric tasks, and the upper index represents the kind of functions, for which (1) stands for standing waves and (3) corresponds to propagating waves. The vector functions $\mathbf{M}^{1,3}_{plm}$ and $\mathbf{N}^{1,3}_{plm}$ can be derived from a scalar function $\psi(r,\phi,\theta)$ using the relations:

$$\begin{aligned} \mathbf{M} &= \nabla \times (\mathbf{r}\psi), \\ \mathbf{N} &= \frac{c}{\omega}\nabla \times \mathbf{M}, \end{aligned} \tag{1.76}$$

and $\psi(r,\phi,\theta)$ is a solution of the scalar Helmholtz equation in spherical coordinates. The particular form of $\mathbf{M}^{1,3}_{plm}$ and $\mathbf{N}^{1,3}_{plm}$ can be found, for instance, in Ref. [141] and commonly serves for visualizing fields inside and outside nanoparticles, as well as for multipolar decomposition of nanostructure response and complex electric and magnetic fields in various numerical methods [142]. The expansion coefficients a_l and b_l are of greater interest for Mie-tronics because they provide useful insight into the spectral response of the system. a_l and b_l correspond to electric and magnetic multipoles of the order of l, where $l = 1$ stands for a dipole, $l = 2$ for a quadrupole, etc., and can be determined from the boundary conditions (Equation 1.11) of the fields at the interface between the nanoparticle and host media:

$$a_l = \frac{n\psi_l(nx)\psi_l'(x) - \psi_l(x)\psi_l'(nx)}{n\psi_l(nx)\xi_l'(x) - \xi_l(x)\psi_l'(nx)}, \tag{1.77}$$

$$b_l = \frac{\psi_l(nx)\psi_l'(x) - n\psi_l(x)\psi_l'(nx)}{\psi_l(nx)\xi_l'(x) - n\xi_l(x)\psi_l'(nx)} \tag{1.78}$$

where n is the relative refractive index $n = \sqrt{\varepsilon/\varepsilon_{\text{h}}}$, x is the dimensionless size of the sphere $x = 2\pi R/\lambda$, ψ and ξ are the spherical Bessel and Hankel functions, and subscript $'$ refers to the derivative with respect to the argument of the function.

Substitution of Equations 1.72–1.75 to Equations 1.67– 1.71 gives the final answer for the normalized cross sections of a spherical nanoparticle:

$$\frac{C_{\text{sca}}}{C_{\text{geo}}} = \frac{2c^2}{\omega^2 a^2} \sum_{n=1}^{\infty} (2l+1)(|a_l(\omega)|^2 + |b_l(\omega)|^2), \tag{1.79}$$

$$\frac{C_{\text{ext}}}{C_{\text{geo}}} = \frac{2\pi c^2}{\omega^2 a^2} \sum_{n=1}^{\infty} (2l+1)\text{Re}\left[a_l(\omega) + b_l(\omega)\right], \tag{1.80}$$

$$C_{\text{abs}} = C_{\text{ext}} - C_{\text{sca}}. \tag{1.81}$$

Equations 1.79– 1.81 allow to visualize the spectral response of a spherical nanoparticle. In fact, Equation 1.79 can be used to compute the scattering efficiency of any compact system if the expansion coefficients a_l and b_l are properly found. $\mathbf{M}^{1,3}_{plm}$ and $\mathbf{N}^{1,3}_{plm}$ form a basis and satisfy Maxwell's equations, thus, the electric and magnetic field of any structure can be expanded into series of $b_{lm}\mathbf{M}^{1,3}_{plm}$ and $a_{lm}\mathbf{N}^{1,3}_{plm}$ vector harmonics. Such decomposition is called spherical multipole decomposition and can be useful for predicting the near-field properties of the nanostructures based on their far-fields and vice versa [142].

Figure 1.9(a) demonstrates the scattering cross-section of a nanoparticle and its multipole decomposition with respect to the wavelength. The dielectric permittivity of the nanoparticle is taken 16 and real. The scattering spectra demonstrate distinct peaks associated with Mie resonances, such as magnetic dipole (MD), electric dipole (ED), magnetic quadrupole (MQ), electric quadrupole (EQ), magnetic octupole (MO), and electric octupole (EO). One can notice that the higher the multipole order, the higher the Q-factor of the resonances, which is a signature of weaker interaction of the high-order multipole modes with light. It can be easily understood from the expansion of an incident plane wave in Equation 1.72: the impact of the multipole term to the field drops with the multipole order. Consequently, the coupling constant between the multipole excited in the nanoparticle is smaller for the high-order multipoles. Moreover, multipole contributions to the total scattering, such as ED and MD, possess numerous peaks in the spectrum, indicating the excitation of several modes associated with the same multipole. It must be noted while each mode of a spherical nanoparticle is linked to a specific vector spherical harmonic, a single spherical harmonic does not exclusively correspond to a single Mie mode. This is because a single spherical harmonic describes the fields of a series of Mie modes of the same kind. In non-spherical nanostructures, spherical harmonics lose their physical meaning and rather serve as a convenient basis for analyzing the nanostructure modes.

The Mie expansion coefficients a_l and b_l are analytical functions, and, therefore, Equations 1.77– 1.78 can be analytically continued in the plane of complex frequencies. Figure 1.9(b) reveals the scattering cross-section map in the complex frequency plane. While the function in the upper half-plane remains analytical, in the lower half-plane it manifests singularities, which are exactly the QNMs of a spherical nanoparticle. Such a map provides a useful tool for analyzing the response of nanoparticles and

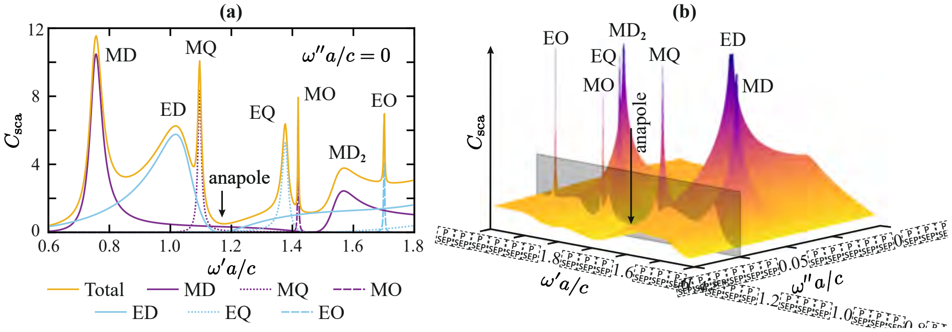

Figure 1.9. (a) Normalized scattering cross section (C_{sca}) of a dielectric nanoparticle with $\varepsilon = 16$ in vacuum depending on dimensionless real frequency. C_{sca} is expanded into a multipole series of magnetic dipole (MD, violet solid), electric dipole (ED, blue solid), magnetic quadrupole (MQ, violet dotted), electric quadrupole (EQ, blue dotted), magnetic quadrupole (MO, violet dashed) and electric quadrupole (EO, blue dashed). (b) A map of C_{sca} in the complex frequency plane. The map reveals poles in the plane of negative imaginary frequencies corresponding to Mie QNMs. Grey shadowed area highlights C_{sca} spectrum at the real frequency axis.

establishes a direct relation between the peaks of the real frequency spectrum and the poles in the lower half-plane.

Another property of Mie nanoparticles, which is worth mentioning, is the non-scattering or anapole regime [143]. In Figure 1.9(a), one can observe pronounced dips in the scattering spectrum originating from complete cancellations of one of the multipole contributions. Such an intriguing behavior of the scattering coefficients, referred to as anapole states or anapole modes, has attached a particular interest due to the nullification of the external nanoparticle fields with the preservation of the internal fields localized in the nanoparticle volume. This situation can lead to various optical phenomena, including perfect absorption and cloaking [144, 145]. It's crucial to emphasize that while the anapole suppresses scattering, it does not necessarily result in complete scattering suppression. The formation of anapoles in compact systems is commonly explained as interference between ED and toroidal modes [146]. Moreover, one can observe the anapole-like features in the scattering response of all other multipoles. Therefore, the nature of anapoles can be explained as the Fano resonance, appearing due to the interaction between the multipole modes of the same kind. Figure 1.9(b) indicates that no additional poles stand behind the anapole in the complex frequency, revealing that the anapole is a feature of the scattering response of Mie QNMs rather than another mode.

1.7 Light action on photonic structures: Optical forces

Beyond just the effects of light controlled by nanostructures, photonics investigates and applies the phenomena of mechanical driving of nanostructures by light [147,148]. Particularly, when the electromagnetic field is exposed to nanostructures, it can induce attractive and repulsive forces or even torque [149, 150]. The area of research which aims to study the mechanical action of light is called optomechanics. Optomechanics has attracted a lot of attention in the last decades because it allows the manipulation of the position and orientation of nanoscale objects, including nanoparticles and molecules [151]. Optical tweezers, namely, focused laser beams invented by Arthur Ashkin in 1970 [152], have not only revolutionized the field of physics but have also provided an invaluable playground for research in molecular biology [153]. Specifically, the attractive force created by optical tweezers can effectively trap and manipulate DNA, proteins, and even living cells in liquids, which has brought numerous discoveries in intrasaccular biology [154]. Besides, the boom in optical tweezers has led to a rise in optical levitodynamics, which explores the dynamics of nanoparticles levitated in gases or vacuum by means of optical forces [155]. Optical levitodynamics of nanoparticles is promised to establish a platform for high-precision measurements, sensors, and fundamental tests in quantum mechanics, as one can draw parallels between a mesoscopic particle and an atom captured by an optical trap [156].

The physics of optomechanical interaction between nanostructures and light can be effectively described within Maxwell stress tensor formalism, which introduces the momentum conservation law in electrodynamics [80]. The equation for momentum conservation can be easily obtained from the Lorentz force density $\mathbf{f}_\mathrm{L}$, derived as follows:

$$\mathbf{f}_\mathrm{L} = \rho\mathbf{E} + \mathbf{j}\times\mathbf{B}, \tag{1.82}$$

Substituting Maxwell's equations to Equation 1.82 and using the vector identities, one can come up with the following relation between the force density and electromagnetic fields:

$$\begin{aligned}\mathbf{f}_\mathrm{L} = {} & \varepsilon_0(\nabla\cdot\mathbf{E})\mathbf{E} + \varepsilon_0(\mathbf{E}\cdot\nabla)\mathbf{E} + \mu_0(\nabla\cdot\mathbf{H})\mathbf{H} + \mu_0(\mathbf{H}\cdot\nabla)\mathbf{H} - \\ & - \frac{1}{2}\nabla(\varepsilon_0|\mathbf{E}|^2 + \mu_0|\mathbf{H}|^2) - \varepsilon_0\mu_0\frac{\partial}{\partial t}(\mathbf{E}\times\mathbf{H}).\end{aligned} \tag{1.83}$$

Further, one can rewrite Equation 1.83 introducing a second rank tensor $\overset{\leftrightarrow}{\mathbf{T}}$, namely, the Maxwell stress tensor:

$$\mathbf{f}_\mathrm{L} = \nabla\cdot\overset{\leftrightarrow}{\mathbf{T}} - \frac{1}{c^2}\frac{\partial}{\partial t}(\mathbf{E}\times\mathbf{H}), \tag{1.84}$$

where $\overset{\leftrightarrow}{\mathbf{T}}$ is given by:

$$\overset{\leftrightarrow}{\mathbf{T}} = \varepsilon_0\left(\mathbf{E}\otimes\mathbf{E} - \frac{1}{2}\overset{\leftrightarrow}{\mathbf{I}}\,|\mathbf{E}|^2\right) + \mu_0\left(\mathbf{H}\otimes\mathbf{H} - \frac{1}{2}\overset{\leftrightarrow}{\mathbf{I}}\,|\mathbf{H}|^2\right). \tag{1.85}$$

In Equation 1.84, the Lorentz force term on the left-hand side represents the mechanical momentum density flux, while the cross-product on the right-hand side is associated with the field contribution to the overall momentum density flux. Averaging over the time period of the field oscillations cancels out the field contribution; therefore, the averaged Lorentz force density is obtained as:

$$\langle \mathbf{f}_{\mathrm{L}} \rangle_t = \nabla \cdot \langle \overset{\leftrightarrow}{\mathbf{T}} \rangle_t, \tag{1.86}$$

and can be rewritten in the integral form:

$$\langle \mathbf{F} \rangle_t = \int_S \langle \overset{\leftrightarrow}{\mathbf{T}} \rangle_t d\mathbf{S}, \tag{1.87}$$

where S is a conveniently chosen surface surrounding the object. Equation 1.87 is typically used for calculations of optomechanical forces acting on different objects. For instance, one can consider monochromatic light passing through an infinitely long and wide dielectric plate with a finite thickness, a simple example of a 1D electromagnetic system exhibiting Fabri-Perot resonances and characterized by Fresnel reflection (r) and transmission (t) coefficients. **E** and **H** fields from the sides of the plate can be written as follows [80]:

$$\mathbf{E}_1 = \mathbf{n}_x E_0 \left(e^{ik_z z} + r e^{-ik_z z} \right) e^{-i\omega t}, \tag{1.88}$$

$$\mathbf{E}_2 = \mathbf{n}_x E_0 t e^{ik_z z} e^{-i\omega t}, \tag{1.89}$$

$$\mathbf{H}_1 = \mathbf{n}_y \sqrt{\frac{\varepsilon_0}{\mu_0}} E_0 \left(e^{ik_z z} + r e^{-ik_z z} \right) e^{-i\omega t}, \tag{1.90}$$

$$\mathbf{H}_2 = \mathbf{n}_y \sqrt{\frac{\varepsilon_0}{\mu_0}} E_0 t e^{ik_z z} e^{-i\omega t}. \tag{1.91}$$

Substitution of the fields from Equations 1.88– 1.91 to Equation 1.85 for the Maxwell stress tensors reveals cancellation of non-diagonal terms and leads to the following expression for the radiation pressure for the dielectric plate:

$$p = \frac{\varepsilon_0 E_0^2}{2} \left(1 + |r|^2 - |t|^2) \right), \tag{1.92}$$

and may also describe the pressure produced by monochromatic fields into planar nanostructures, i.e., metasurfaces. Similarly, one can obtain an optical force for a spherical particle of radius a, illuminated by a monochromatic plane wave with intensity I [79]:

$$\begin{aligned} F = \frac{\pi a^2 I}{c} (C_{\mathrm{ext}} - C_{\mathrm{sca}} \langle \cos\theta \rangle) = \frac{2\pi I}{k^2 c} \sum_l \mathrm{Re}\left[(2l+1)(a_l + b_l) \right] + \\ + \frac{2\pi I}{k^2 c} \sum_l \mathrm{Re}\left[\frac{2l(l+2)}{l+1} (a_l a_{l+1}^* + b_l b_{l+1}^*) + \frac{2l+1}{l(l+1)} a_l b_l^* \right], \end{aligned} \tag{1.93}$$

where θ is the polar angle characterizing the direction of light scattering. Equations 1.92– 1.93 show that plane and monochromatic waves can provide only repulsive action onto nanostructures, which is the direct consequence of the momentum conservation law [80]. However, this statement can be reviewed, considering a nanostructure based on an amplifying medium or complex frequency excitation, detailly discussed in Appendix B, where an attractive action is discovered.

The attractive optical force is a key feature of optical tweezers utilizing non-paraxial Gaussian beams with spatially varied intensity (see Figure 1.10(a)). The fundamentals of the optomechanical response of nanoparticles in Gaussian laser beams are convenient to demonstrate in a dipole approximation. One can rewrite Equation 1.82 for the Lorentz force density using the relations $\rho = -\nabla \cdot \mathbf{P}(\mathbf{r}, t)$, $\mathbf{j}(\mathbf{r}, t) = \partial \mathbf{P}(\mathbf{r}, t)/\partial t$, $\mathbf{P}(\mathbf{r}, t) = \alpha\varepsilon_0 \mathbf{E}(\mathbf{r}_0, t)\delta(\mathbf{r} - \mathbf{r}_0)$:

$$\mathbf{f}_\mathrm{L}(\mathbf{r}, t) = \alpha\varepsilon_0(-\mathbf{E}(\mathbf{r}_0, t)\nabla\delta(\mathbf{r} - \mathbf{r}_0))\mathbf{E}(\mathbf{r}, t) + \alpha\varepsilon_0 \frac{\partial \mathbf{E}(\mathbf{r}_0, t)}{\partial t} \times \mathbf{B}(\mathbf{r}, t)\delta(\mathbf{r} - \mathbf{r}_0), \quad (1.94)$$

where $\mathbf{r}_0$ is the position of the dipole, $\delta(\mathbf{r} - \mathbf{r}_0)$ is the 3D Dirac δ-function, and spatial derivatives are taken with respect to $\mathbf{r}$. Using the properties of δ-function and its derivative, one can perform volume integration and obtain the Lorentz force $\mathbf{F}_L$ acting on a dipole located at $\mathbf{r}_0$:

$$\mathbf{F}_\mathrm{L} = \alpha\varepsilon_0(\mathbf{E}(\mathbf{r}_0, t)\nabla)\mathbf{E}(\mathbf{r}_0, t) + \alpha\varepsilon_0 \frac{\partial \mathbf{E}(\mathbf{r}_0, t)}{\partial t} \times \mathbf{B}(\mathbf{r}_0, t), \quad (1.95)$$

and the spatial derivatives are now taken with respect to $\mathbf{r}_0$. Applying vector identities and Maxwell's equations, one can transform Equation 1.95 to a new form:

$$\mathbf{F}_\mathrm{L} = \alpha\varepsilon_0 \nabla(\mathbf{E}(\mathbf{r}_0, t))^2 + \alpha\varepsilon_0 \frac{\partial}{\partial t}(\mathbf{E}(\mathbf{r}_0, t) \times \mathbf{B}(\mathbf{r}_0, t)). \quad (1.96)$$

Assuming monochromatic field dependencies $\mathbf{E}(\mathbf{r}_0, t) = \mathbf{E}_0(\mathbf{r}_0)e^{-i\omega t}$ and $\mathbf{B}(\mathbf{r}_0, t) = \mathbf{B}_0(\mathbf{r}_0)e^{-i\omega t}$, one can evaluate time-averaged Lorentz force $\langle \mathbf{F} \rangle$:

$$\begin{aligned}\langle \mathbf{F}_\mathrm{L}(\mathbf{r}_0) \rangle &= \frac{1}{2}\mathrm{Re}\left[\alpha\varepsilon_0 \nabla|\mathbf{E}(\mathbf{r}_0)|^2 - i\omega\alpha\varepsilon_0\mu_0 \mathbf{E}(\mathbf{r}_0) \times \mathbf{H}^*(\mathbf{r}_0)\right] = \\ &= \frac{1}{2}\mathrm{Re}\left[\alpha\right]\varepsilon_0 \nabla|\mathbf{E}(\mathbf{r}_0)|^2 + \frac{1}{2}\mathrm{Im}\left[\alpha\right]\omega\varepsilon_0\mu_0 \mathbf{E}(\mathbf{r}_0) \times \mathbf{H}^*(\mathbf{r}_0) = \\ &= \frac{\mathrm{Re}\left[\alpha\right]}{c}\nabla I(\mathbf{r}_0) + \frac{\omega \mathrm{Im}\left[\alpha\right]}{c^2} I(\mathbf{r}_0).\end{aligned} \quad (1.97)$$

One can observe that the final expression for $\langle \mathbf{F}_\mathrm{L} \rangle$ in Equation 1.97 contains two terms. The first term depends on the gradient of the intensity of the Gaussian beam and is proportional to the real part of the dipole polarizability. The gradient contribution to the Lorentz force is referred to as a gradient force and normally gives rise to the attractive force towards the intensity maximum, ensuring the dipole trapped around the maximum [157]. However, if the sign of $\mathrm{Re}\left[\alpha\right]$ is changed to the opposite, the attraction switches to repulsion, and the trapping around the intensity maximum

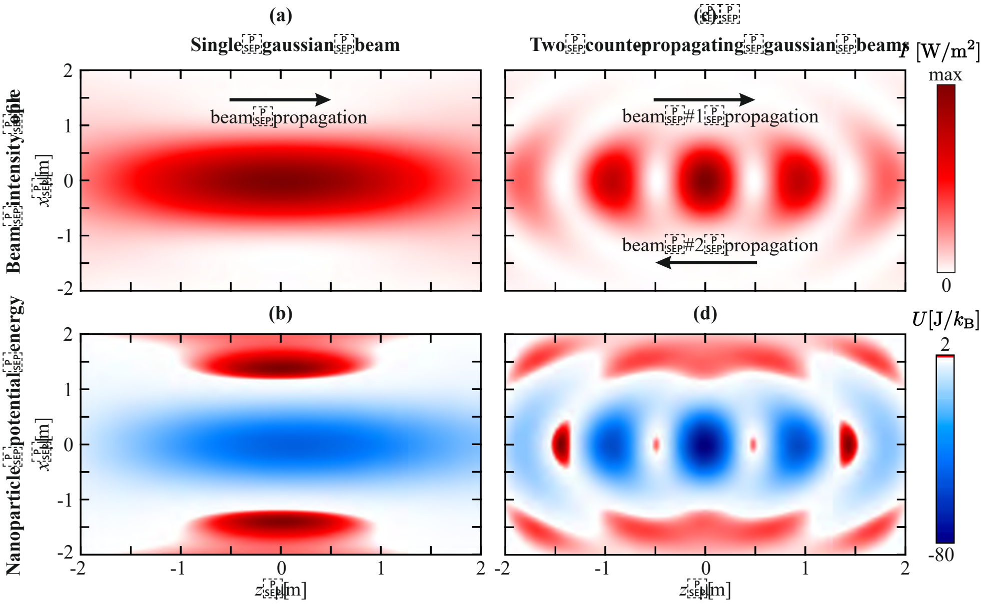

Figure 1.10. (a) Intensity profile of a Gaussian beam with a numerical aperture (NA) of 0.8 and wavelength of 1550 nm. (b) The potential energy of a silicon nanoparticle with a radius of 100 nm illuminated by a single Gaussian beam. (c) Intensity profile of two counter-propagating co-polarized beams with beam NA of 0.8 and at 1550 nm. (d) The potential energy of a silicon nanoparticle of a radius of 200 nm in the counter-propagating beam geometry.

is disabled. Yet, it is still possible to trap the dipole in the intensity minima, e.g., of a Bessel beam [158]. The second term of Equation 1.97 includes the value of the intensity of the beam and the imaginary part of the polarizability and can be called a scattering force. The scattering force is associated with the momentum transfer and typically plays against the trapping gradient force [157]. Therefore, the nanoparticles with strong Mie resonance, exhibiting strong scattering forces, cannot be trapped by means of a standard optical tweezer. But, as for the gradient force, change of $\mathrm{Im}\left[\alpha\right]$ sign can produce a pulling scattering force, theoretically observed in nanoparticles with gain [159]. On the other side, when the nanoparticle size is significantly larger than the wavelength of the laser beam, the scattering force enables trapping around the laser focus due to momentum conservation between the incoming and scattered/refracted photons [160]. Figure 1.10(b) demonstrates the potential energy of a nanoparticle in dipole approximation in a Gaussian beam with a beam numerical aperture (NA) of 0.8 and power of 100 mW. As long as the potential energy is negative, the nanoparticle is trapped around the center of attraction. Because of the repulsive action of the scattering force, the location of energy minimum diverges from the focus of the beam shifted towards the propagation direction.

The mechanical motion of a nanoparticle trapped in a focused laser beam can be described in the non-harmonic oscillator formalism. The non-harmonic behavior is owing to the non-parabolic Gaussian optical potential. Nevertheless, if the nanoparticle oscillation energy is sufficiently small, i.e., the nanoparticle is in its motional ground state, the potential can be approximated as parabolic [161]. Then, the frequency of the nanoparticle motion can be found as $\Omega = \sqrt{\varsigma/m}$, where ς is the stiffness of the parabolic potential and m is the nanoparticle mass. The mechanical frequency is one of the essential parameters for optomechanics-based sensors and quantum optics, and it is normally detected in most levitodynamics experiments as beats of the scattered light intensity, namely, frequency modulation of inelastically scattered light exposed onto an oscillating nanoparticle [162]. Another crucial parameter is the depth of the potential well produced by the optical field, and it characterizes the energy threshold for the nanoparticle to escape the optical trap.

One can violate the scattering force by introducing two counter-propagating Gaussian beams instead of one [162]. If the intensity of the beams is balanced, the scattering force is canceled out, and the optomechanical response is only determined by the gradient contribution. This type of trap can be potentially used to capture resonant particles in the Mie scattering regime. The interference between the beams produces minima and maxima along the axis of beam propagation (see Figure. 10(c)), if the scattering forces are balanced. Intriguingly, the configuration of Mie resonances can significantly affect the gradient optical forces produced by the beams. It has been observed that the sign and the magnitude of the force vary depending on whether the excitation is resonant or not and which multipole resonance is excited. Importantly, some regimes in Mie resonances give rise to attraction to intensity minima rather than maxima. This phenomenon is known as dark trapping and is discussed in detail in Appendix D. The potential energy of the nanoparticle of a radius of 200 nm is illustrated in Figure 1.10(d) and indicates that the trapping may occur around the minima of the interference pattern.

1.8 Summary

In this Chapter, I have reviewed theoretical approaches to describe various optical phenomena exhibited in photonic nanostructures. I have derived the CMT and scattering matrix for an arbitrary multi-mode and multi-scattering channel system from the Lippmann-Schwinger equation. I have explored the properties of scattering matrix eigenvalues, particularly their poles and zeros, in cases of Hermitian and different non-Hermitian states of dielectric permittivity. Then, I applied CMT and Hamiltonian formalism to describe different regimes of light-matter interactions, including strong and weak coupling and exceptional points. I have demonstrated that in a simple two-oscillator system, the coupling regime is determined by the ratio between the interaction constant and loss difference. I have provided a definition for the Purcell effect in quantum optics and classical electrodynamics. I have obtained a standard expression for the Purcell factor from CMT and considered the Purcell enhancement in a system of a dipole source coupled to a resonant nanoparticle. Further, I have presented a derivation of Fano resonance and bound state in the continuum (BIC) phenomena from CMT. I have revealed that the Fano resonance originates from the interference between spectrally broad and narrow (resonant) responses. Moreover, from CMT, I have extracted conditions for BIC existence in a two-mode system, considering two limiting cases of identical spatially separated cavities and different modes of the same cavity. I have discussed BICs in periodic structures, specifically, gratings, their impact on Q-factors, and topological origin. I have presented a classical derivation of the Mie theory for the scattering of an electromagnetic field on non-magnetic spherical nanoparticles and have extended it to complex frequencies. I have attributed the Mie resonances in scattering spectra to the poles in the lower complex frequency half-plane and discussed the physics of anapole states. Additionally, I have examined the optomechanical effects of light manipulation by nanostructures. I have obtained equations for the average optical force that acts on a dielectric plate from the Maxwell stress tensor approach and on a nanoparticle in the dipole approximation.

CHAPTER 2

Applications of Mie-tronics

The rise of Mie-tronics, a branch of photonics exploiting Mie resonances, has shifted the focus from metal-composed nanostructures exhibiting surface plasmon resonances to dielectric and semiconductor nanostructures [67]. Even though plasmonics can potentially engage for compact nanoscale solutions compatible with dimensions of microelectronics [163], due to excitations of extremely localized surface states, it critically suffers from dissipation losses [54]. The dissipation losses limit guided wave propagation in plasmonic nanostructures, saturate the Q-factor, and produce undesirable heating and thermal noise, which cannot be tolerated in quantum information and photonic integrated circuits [164]. Although the losses in plasmonics is the stone that everyone stumbles over when it comes to real-world applications, it can still be used for Purcell enhancement, providing a factor of 1000 [103], comparable with bulky photonic crystal cavities, local nanoscale heating [165], and even sensing [166]. From the other side, Mie-resonant nanostructures made of low-loss, high-refractive index dielectrics and semiconductors enable long-range propagating waves [167] and sufficiently large and tailorable Q-factors thanks to the distribution of Mie-modes in the nanostructure volume [168]. A unique ability of Mie nanostructures and one of the key differences between Mie-tronics and plasmonics is a strong magnetic response in completely non-magnetic materials, facilitating advanced wavefront control [169].

Mie nanostructures can be utilized as building blocks for discrete waveguides, photonic topological insulators, and metalenses [67]. The last ones have laid a foundation for flat optics to replace bulky optical components (lenses and mirrors) with thin photonic nanostructures [170]. When periodically assembled, Mie nanostructures or “meta-atoms” produce collective resonances such as van-Hove singularities and BICs, opening doors for high-Q factors at the nanoscale [131, 171]. In this chapter, I review recent advances in Mie-tronics and its applications for light generation and manipulation as well as for sensing. In Section 2.1, I present the state of the art in wavefront engineering by interplay between Mie resonances in dielectric nanostructures. In Section 2.2, I reveal how Mie-tronic devices can establish a new generation of nanoscale optical sensors. Specifically, I show that BICs have proven themselves as a convenient platform for spectrophotometry, refractometry, and chirality sensing. Section 2.3 introduces different approaches for tunable Mie-tronic devices, considering particular examples of tunable devices based on phase-change materials, liquid crystals, thermo-optical effects, and twistronics. Section 2.4 provides recent achievements in non-linear harmonic generation produced by quasi-BIC supercavity modes and metasurfaces. Section 2.5 demonstrates several approaches for nanolaser based on van Hove singularities, exceptional points, and merging BICs. Finally, I conclude the Chapter in Section 2.6.

2.1 Wavefront engineering

As mentioned above, one of the main advantages of Mie-resonant dielectric and semiconductor structures is supporting multipolar magnetic and electric resonances [79]. Simultaneous excitation of different multipolar resonances can result in exotic scattering scenarios, such as unidirectional or bi-directional scattering, enabling advanced control of quantum emitter radiation patterns [172], anti-reflective coatings [70], and phase gradient metasurfaces [173]. Figure 2.1(a) reveals the mechanism of the formation of unidirectional scattering in Mie-resonant nanostructures: when magnetic dipole (MD) and electric dipole (ED) are excited at the same time and perpendicular to each other, the superposition of their fields produces an asymmetric scattering pattern. The amplitudes of the fields of MD and ED are determined by Mie expansion coefficients a_1 and b_1 given by Equations 1.77– 1.78. If $a_1 = b_1$, which implies that MD and ED are balanced and oscillating in-phase, the fields radiated in one direction are positively summed, and in the opposite direction are canceled, resulting in a unidirectional radiation pattern (see Figure 2.1(a), panel (i)). On the other hand, out-of-phase oscillations of MD and ED ($a_1 = -b_1$) expectedly lead to the reversed situation shown in panel (ii) of Figure 2.1(a). Thus, the conditions of the unidirectional scattering can be formulated as follows:

$$a_1 = b_1 \tag{2.1}$$

or

$$a_1 = -b_1. \tag{2.2}$$

For a Mie nanoparticle with MD and ED resonances induced by a plane wave Equation 2.1 results in an enhanced forward scattering to the direction of the plane wave propagation and, ideally, complete cancellation of back-scattered fields. Nevertheless, Equation 2.2 outcomes in a strong back-scattering with suppression of the forward scattering, the forward scattering cannot be fully canceled, which is dictated by optical theorem, establishing a relationship between the scattering efficiency in the forward direction and total extinction cross-section [79]:

$$C_{\text{ext}} = \frac{4\pi}{k^2} \text{Im} \left[\frac{\mathbf{E}_{\text{sca}}(\theta = \pi/2, \phi = 0) \cdot \mathbf{E}_{\text{inc}}}{|\mathbf{E}_{\text{inc}}|^2} \right], \tag{2.3}$$

where $\mathbf{E}_{\text{inc}}$ is the incident electric field, and $\mathbf{E}_{\text{sca}}(\theta = \pi/2, \phi = 0)$ is the electric field of the wave scattered in the forward direction (direction of the incident field propagation). As a consequence, strong back-scattering response comes with the price of reduced total extinction, which, in non-amplifying systems, implies suppressed total scattering. However, this limitation can be overcome utilizing gain media [90] or coherent virtual excitation of zeros of the forward scattering efficiency, discussed in Appendix F. The effect of unidirectional scattering in spherical magnetic nanoparticles was first discovered by Kerker et al. [174] in 1982. In the modern literature, the effect of unidirectional forward scattering is well-known as the Kerker effect, while predominantly backward scattering is referred to as the anti-Kerker effect, and Equations 2.1 are Kerker conditions [175]. Moreover, the Kerker effect was generalized for multipole moments beyond dipolar, facilitating the engineering of complex scattering patterns [63]. Ref. [176] describe the transverse Kerker effect, enabled by simultaneous excitation of quadrupole resonances, characterized by suppression of forward and backward scattering and magnification of scattering in directions perpendicular to the incident field propagation.

In Ref. [172], the authors utilize Kerker and anti-Kerker effects in silicon nanostrips to boost the photoluminescence signal from a monolayer WS_2. This monolayer is part of a large class of 2D semiconductor transition metal dichalcogenides (TMDCs). When WS_2 is a bulk material, it reveals an indirect bandgap producing a weak photoluminescence signal. However, in a monolayer phase, its bandgap becomes direct, and the monolayer exhibits remarkably bright photoluminescence owing to exciton recombination, which has gained significant attention in quantum optics and material science in recent years. The authors attempt to enhance the photoluminescence of the monolayer WS_2 by coupling it to a silicon nanostrip with a silica spacer between the nanostrip and monolayer (see Figure 2.1(b), panels (i-ii)). Placing the monolayer on top of the nanostrip and varying the thickness of the spacer, the authors achieve the Kerker condition for forward emission in the absence of a spacer and anti-Kerker condition for enhanced backward emission at the spacer thickness of 135 nm. Besides, to further improve the directional photoluminescence signal, the authors change the width of the nanostrip and the overall number of nanostrips coupled to the monolayer WS_2. In addition, they provide the data for a bilayer WS_2, which exhibits sufficiently strong photoluminescence. Their findings are summarized in Figure 2.1(b), panel (iii), indicating that the width and number of nanostrips critically influence the output signal. Both total and backward photoluminescence experience maximum at the nanostrip width of 250 nm, corresponding to resonant excitation of the electric quadrupole. Moreover, assembling the nanostrips into dimers leads to a 6-fold increase of the output signal in numerical calculations and a 3-fold increase in the experiment. Finally, the authors observe a 9-fold enhancement in the measured backward photoluminescence. The proposed mechanism of the photoluminescence enhancement relies on far-field interactions between the excitons in the monolayer WS_2 and modes of the nanostrip in contradiction to a more common near-field interaction, opening intriguing opportunities for distant manipulations of the photoluminescent properties of the emitter.

Using meta-atoms in Kerker condition as building blocks for metasurfaces gives rise to so-called Huygens metasurfaces [179]. These metasurfaces are based on Huygens's principle that every point on a wavefront is a secondary source of outgoing

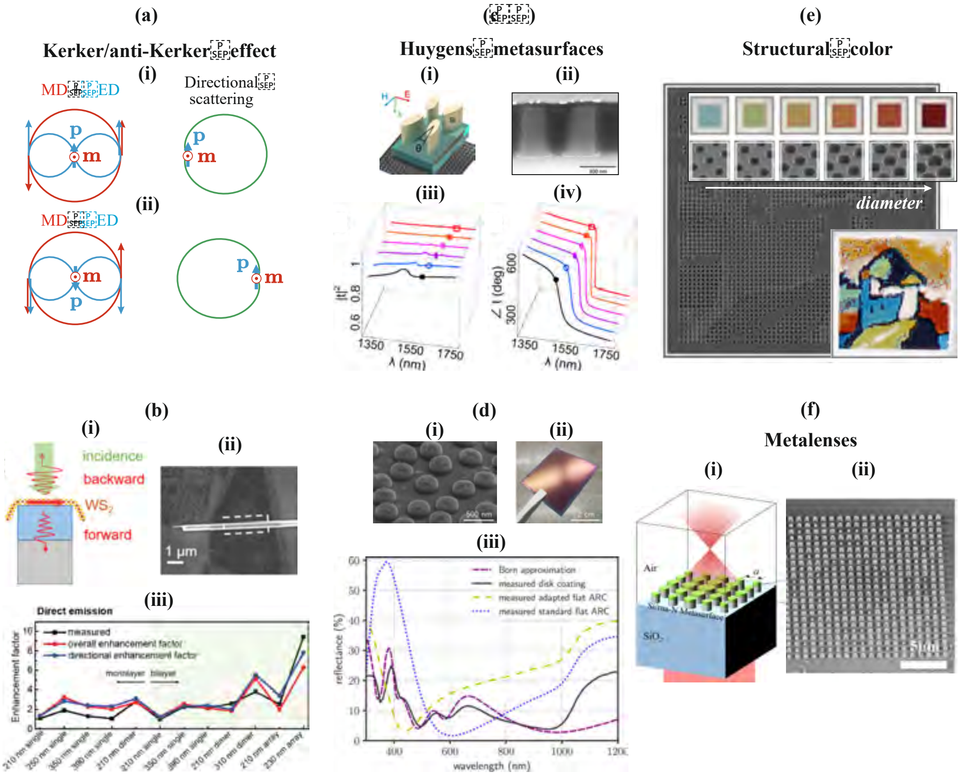

Figure 2.1. (a) Intuitive explanation of unidirectional scattering in Mie-resonant nanostructures: when magnetic and electric dipoles are balanced and oscillating in-phase, superposition of their far-fields gives rise to scattering one direction (panel (i)), while out-of-phase oscillating dipoles produce enhanced scattering in the opposite direction (panel (ii)). (b) Example of backward photoluminescence enhancement induced by anti-Kerker effect between Mie magnetic resonant dielectric nanorod and excitonic electric dipole moments of monolayer WS_2. Panels (i-ii) show a sketch of the system and its SEM image. Panel (iii) is a data collection summarizing the photoluminescence enhancements in different nanostructure configurations [172]. (c) Illustration of principles of Huygens metasurfaces: panels (i-ii) shows a scheme and SEM of the investigated metasurface supporting quasi-BIC; panel (iii) depicts a transmission intensity spectrum, typical for Huygens metasurfaces, for different meta-atom twists; panel (iv) demonstrates transmission phase spectra, representing a characteristic 2π phase shift in the Huygens regime for different meta-atom twists [177]. (d) Anti-reflection coating based on a disordered Huygens metasurface: panels (i-ii) presents SEM and optical images of the metasurface, panel (iii) demonstrates reflectance spectra of the metasurface, measured (black line) and calculated (violet dashed line), as well as the reflectance of a standard (blue dashed line) and adopted (yellow dotted line) anti-reflection coatings [70]. (e) Experimental images of structural colors produced by Mie voids of different sizes [178]. (f) Sketch (panel (i)) and SEM image (panel (ii)) of a metalense composed of silicon nanosized disks [173].

waves. As a consequence of this principle, meta-atoms possessing electric and magnetic resonances at the same frequency, thereby primarily inducing forward scattering, endow the metasurface with an almost perfect transmittance under negligible dissipation losses. The remarkable transmittance of Huygens metasurfaces enables refractive index unlimited anti-reflective coatings [70] and advanced control of directional light emission from nanoscale sources, such as TMDCs and quantum dots [180]. However, the critical feature of Huygens metasurfaces is their intriguing phase response, which undergoes a smooth 2π change near the resonances [177]. Such a distinguishing phase behavior, diverging from an ordinary sharp π-phase transition of a single resonance, comes from the superposition of merging ED and MD resonances. Figure 2.1(c) depicts spectra of the intensity transmission coefficient and phase shift of the transmitted wave of a Huygens metasurface composed of zigzag arrays of dielectric elliptical cylinders. In this case, near-unity transmissivity is achieved by tuning the structure geometrical parameters to merge two quasi-BICs of ED and MD nature [177]. The phase characteristic indicates that the metasurface is within the Huygens regime. Moreover, by adjusting the zigzag arrays' twist angle, the quasi-BICs' Q-factor can be scaled, which allows fine-tuning of phase dispersion. This adjustment facilitates the achievement of a pronounced 2π-phase transition in the cases of high Q-factors or, alternatively, a gradual phase curvature for low Q-factor scenarios.

The authors of Ref. [70] make one step towards implementing Huygens metasurfaces in photovoltaic technologies, engineering and fabricating a disordered metasurface-based anti-reflection coating on top of a standard silicon heterojunction solar cell. The SEM and optical images of the metasurface are presented in Figure 2.1(d), panels (i-ii). The metasurface is composed of TiO_2 sub-micron sized disks in a disordered arrangement, which are fabricated employing colloidal self-assembly that is applicable virtually irrespective of the material or surface morphology of the device. The authors observe a broadband enhancement of transmissivity and, therefore, reduction of reflectivity down to 10% on average of the spectral range relevant for solar cells (see Figure 2.1(d), panel (iii)). To compare with commercially available solutions, the authors provide the reflectivity data for a standard and optimized anti-reflective indium tin oxide (ITO) layer, which indicates a relatively narrow dip in reflectivity reaching 2-3%. The broadband reduction of the reflectivity by TiO_2 Huygens metasurface improves the short-circuit current of the solar cell by 5.1% in comparison to the anti-reflective ITO layers. The authors applied the first Born approximation to describe the transmittance and reflectance of the disordered Huygens metasurface, assuming the interaction between the meta-atoms was neglected. This method expands the far-field properties of the metasurface in a superposition of the contribution of individual meta-atoms multiplied by a structure factor as the metasurface property and form factor as the single meta-atom property. The structure factor can be received from the images (SEM, optical) of the fabricated disordered metasurface, while the form factor is normally obtained from the single meta-atom numerical calculations (e.g., FEM). Figure 2.1(d), panel (iii), reveals a good correspondence between numerically calculated reflectance in the first Born approximation and experimentally obtained curve in the short-wavelength range. The substantial divergence between the experiment and theoretical description in the long-wavelength limit is explained by the intense reflection from the bottom surface of the solar cell, not taken into account. Other minor divergences in the spectrum are attributed to a mismatch between the model parameters of the meta-atoms and fabricated disks.

The scattering of light by individual nanostructures and their assemblies results in distinct colors determined by the resonance configuration of these nanostructures. This phenomenon can be harnessed to generate colors and even sophisticated images on a micron scale [181]. Such structural coloring has significant advantages compared to conventional dye coloring, such as high accuracy of images and robustness to fading over time [182]. Furthermore, through careful optimization of nanostructure resonant properties by geometrical tuning, a wide array of colors can be achieved. Given the contemporary prominence of metasurfaces in photonics, numerous designs have emerged for implementing such structural coloring [183]. One notable approach, detailed in Ref. [178], utilizes Mie resonances in Mie-voids, namely, cavities or holes embedded in a dielectric medium, that provide light confinement in vacuum or air. Due to such the confinement of light, these Mie resonances do not suffer from the dissipation losses or dispersion of dielectric materials. That allows for obtaining the resonant response in a broad wavelength range, including UV, where most dielectrics and semiconductors possess high losses. The authors of Ref. [178] experimentally demonstrate light confinement at the wavelength of 265 nm (middle UV) in Mie-voids inside silicon wafers. Figure 2.1(e) shows an SEM image of a pattern of different Mie-voids produced by focused ion beam technology. The efficiency of nanoscale structural coloring, enabled by resonant nanostructures, is determined by several factors, such as the resonance linewidth, scattering strength, and tunability of the design. Too narrow or broad resonances produce colors that appear either artificial or dull. Thus, it is of extreme necessity to obtain nanostructures with optimal Q-factors. The proposed Mie-voids appear to demonstrate optimal resonance linewidths, creating natural colors. Moreover, due to the large scattering cross section, one Mie void can serve as a single pixel of the picture. To illustrate Mie-voids' capabilities for structural colors, the authors arrange them in a colorful picture presented in the insert of Figure 2.1(e). Varying the radius of the Mie void, the authors obtain colors of the visible spectral range (see inserts in Figure 2.1(e)).

Engineering properties of individual meta-atoms composing a metasurface creates possibilities for wavefront shaping by demand. In particular, one can engineer a specific gradient of the phase of the wave transmitted through the metasurface, focusing or collimating light. Metasurfaces with phase gradients are known as metalenses, ultrathin structures in contrast to traditional bulky convex or concave lenses [184]. Optimization of meta-atom resonant properties and endowing them with tunability has started the era of functional broadband achromatic lenses [185], birefringence lenses [186], and ultra-thin zoom lenses [187]. To realize the phase gradient of the transmitted wave, one can use different methods for building the metalenses. One of the ways is utilizing the natural properties of individual meta-atom resonances, such as phase shifts between incident and transmitted waves [188]. Varying the size of the meta-atoms, one can modulate the phase front of the transmitted and reflected waves.

However, it comes at the cost of modulated transmissivity, which is undesirable for applications requiring high transparency. An advanced concept for metalens construction is based on the Kerker effect and Huygens metasurface, where each meta-atom represents a combination of MD and ED resonances characterized by unidirectional forward scattering and near-unity transmissivity [189]. This approach is preferred not only because it does not suffer so much from transmissivity modulation but also due to a 2π phase transition providing accurate and smooth phase modulation in contrast to a single resonance with drastic π phase change. Figure 2.1(f) demonstrates a sketch of a silicon-on-insulator (SOI) based metalense and an SEM image of the metalense after fabrication taken from Ref. [173]. In this work, the authors aim to optimize and experimentally verify a concept of a metalense compatible with modern photonic integrated circuits and microelectronics. To design the metalens with a particular focal length, the authors utilized a simple relationship for the phase profile of the meta-atoms:

$$\phi(x, y) = \frac{2\pi}{\lambda}\left(f - \sqrt{x^2 + y^2 + f^2}\right), \tag{2.4}$$

where x and y indicate the coordinates of the meta-atom with respect to the metalense center. The general challenge of Huygens metasurfaces is the inequality of MD and ED contributions to the transmittance and difference in their linewidths, resulting in an imperfect and commonly small transmissivity. The authors attempt to address this challenge by depositing a thin polymer (ma-N) layer on top of silicon, such that the metalense remains quasi-symmetric along the vertical direction. The broadband phase modulation is achieved by tuning the radius of the meta-atoms. Compared to silicon metalens without the polymer layer, the authors observed four times higher focusing efficiency of the metalens preserving the polymer layer.

2.2 Sensing

One of the most advanced applications of photonics is a variety of optical sensors, ranging from sensors for controlling the quality and chemical composition of liquids and gases to nanoscale detectors of biological molecules and chemical reactions, which have rapidly developed in the last decades [190]. The first generation of optics-based sensors utilized lasers and interferometers such as Michelson and Mach–Zehnder interferometers and analyzed interference patterns. Since different substances have different refractive indices and absorption coefficients, the interference pattern at the interferometer output is highly sensitive to the optical properties of the analyte inside. The change of interference pattern results in the variation of light intensity. The sensitivity S of the detectors based on intensity change is defined as:

$$S = \frac{\Delta I}{\Delta n}, \tag{2.5}$$

where ΔI is the light intensity change at the photodiode caused by the change in the refractive index of the analyte Δn. Nowadays, the spatial interferometers based on free-space optics are being replaced by more compact and flexible fiber-optics-based components [191]. The sensitivity of these sensors grows linearly with the contact length L of the fiber and the analyte because the intensity contrast ΔI increases with the phase difference $\Delta\phi$ between two interferent waves inside the fiber according to the relation:

$$\Delta\phi = 2\pi \Delta n \frac{L}{\lambda}, \tag{2.6}$$

where λ is the wavelength. Hence, it can be concluded that the smaller the change in the refractive index one needs to detect, the longer the fiber should be. Therefore, this approach is promising only in distributed sensors, where the significant dimensions are not of the greatest importance and are inapplicable for the local measurements at the nanoscale. Such measurements include studies of tiny volumes of substances, biological cells, and single molecules.

Further development of fiber sensors has led to the creation of optical detectors based on Bragg gratings, periodic structures inside a fiber with alternating layers of different refractive index [192]. Bragg gratings can serve as mirrors to engineer cavities within the optical fiber with extremely sharp resonances, highly sensitive to the slightest changes in the optical length of the grating. It implies that stretching the Bragg cavity or modifying its refractive index can be used for motion [193], deformation [194], gas [195], microfluidic [196], and temperature sensors [197]. The sensitivity of Bragg cavities is determined by:

$$S = \frac{\Delta\lambda}{\Delta n}, \tag{2.7}$$

where $\Delta\lambda$ is the change of the Bragg cavity resonant wavelength measured by the spectrometer. Such spectral sensitivity is commonly measured in nm per refractive index unit (nm/RIU). Generally speaking, sensitivity is not a characteristic that fully reflects the efficiency of the measurement process since it is often difficult to measure the change in the resonance frequency or intensity due to the high spectral width of the resonance peak. Therefore, to compare the spectral resolution of various sensors, Figure of Merit (FOM) is used, given by:

$$\mathrm{FOM} = \frac{S}{\mathrm{FWHM}}, \tag{2.8}$$

where FWHMis the spectral width of the resonance at the half-maximum of its peak intensity.

Despite the advantages of fiber-incorporated Bragg cavity sensors, this approach is hardly applicable for nanoscale measurements. It has been shown that nanoparticles and metasurface can establish a versatile platform for sensors at the nanoscale, particularly for single molecule detection [23] and lab-on-chip [198]. Figure 2.2 illustrates different techniques to utilize metasurfaces with quasi-BICs for spectrophotometry [74], i.e., detection of the absorption fingerprint of analytes, refractive index [199], and optical chirality measurements [200]. The majority of BIC-based sensors experimentally achieve the enhanced sensitivity of 90 – 170 nm/RIU and FOM of 800 – 16000 [201–203]. In the work [74], the authors propose a pixelated dielectric metasurface for lab-on-chip applications composed of amorphous silicon resonators (see Figure 2.2(a), panels (i-ii)). Tuning the high-Q quasi-BIC by twisting the elliptically shaped resonators, the authors achieve an extremely narrow resonant response at different wavelengths, encoding every pixel. Covering the pixelated metasurface with a protein marker changes the optical response of each pixel individually due to the dispersion of the absorption coefficient of the protein. Thus, detecting the signal collected from the pixels allows for building a spectral fingerprint of the protein shown in Figure 2.2(a), panel (iii). This approach offers the prospect of chemical identification and compositional analysis of organic substances. In the later work [204], the authors extend the metasurface size by 275x275 pixels for high-precision imaging of biomolecule fingerprints and concentration measurements. The presented approach is one of the best candidates for the lab-on-chip realization.

High-Q resonances produced by quasi-BICs in dielectric metasurfaces composed of meta-atoms with broken-summery are very useful for refractive index measurements, as the resonance conditions of dielectric nanostructures are sensitive to the refractive index of the environment [205]. Besides, extremely narrow lines of quasi-BICs offer large values of FOM in contrast to plasmonic nanostructures, whose broad spectral

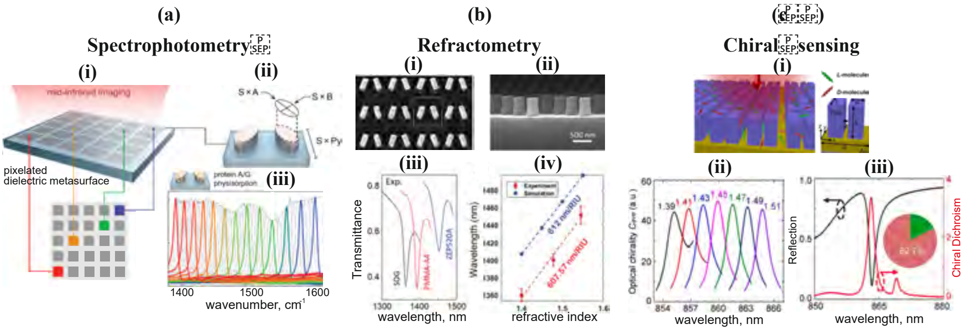

Figure 2.2. Ultra-high sensitivity empowered by BICs. (a) Spectrophotometry of a protein fingerprint based on an array of metasurfaces supporting quasi-BICs. Resonances in each unit cell of the metasurface array are tuned to cover the spectral response of a protein, as depicted in panel (iii) [74]. (b) Refractive index sensor based on a metasurface supporting quasi-BIC. Panels (i-ii) show SEM images of the metasurface. Panel (iii) demonstrates the transmittance spectra of the metasurface coupled to three different analytes. Panel (iv) is a map of simulated and measured sensitivities of the quasi-BIC to the refractive index of the analyte [199]. (c) A metasurface design with quasi-BIC for simultaneous sensing of the refractive index of surrounding media and concentration of molecules with different chirality (panel (i)). Panels (ii-iii) demonstrate chiral dichroism spectra depending on the refractive index change (panel (ii)) and a reflectivity spectrum together with chiral dichroism for 82.7% concentration of right-handed chiral molecules (panel (iii)) [200].

response makes any variations of the resonance wavelength poorly distinguishable, yet the plasmonic nanostructures also exhibit strong interactions with the surrounding medium [206]. These remarkable properties of quasi-BICs in dielectric metasurfaces are effectively utilized to build a refractive index sensor [199]. Figure 2.2(b), panels (i-ii), represents the SEM images of the metasurface composed of amorphous silicon (a-Si) tilted bars. The tilt angle is adjusted to obtain a quasi-BIC with a spectral linewidth of 13.15 nm. Variation of the angle allows the control of the Q-factor of the quasi-BIC, which, in principle, is mainly limited by intrinsic losses. It is worth mentioning that the higher the Q-factor of the quasi-BIC, the stronger the electric field is confined within the structure, implying the weaker interaction with the surrounding medium. Therefore, optimizing the Q-factor of quasi-BICs to obtain critical coupling to the analyte is of great importance for such a sensor. The authors experimentally observed the spectral shift of the quasi-BIC line due to the refractive index change of the environment (see Figure 2.2(b), panel (iii)). The observation is made by covering the top of the metasurface with a 500 nm-thick layer of spin-on glass (SOG), polymethyl methacrylate (PMMA-A4), and ZEP520A with refractive index ranging from 1.4 to 1.545. The experimentally obtained spectral response of the metasurface is numerically verified, and the resulting sensitivities, both theoretical and measured, are shown in Figure 2.2(b), panel (iv), indicating the record sensitivity among the BIC-based metasurfaces (607.5 nm/RIU).

Metasurfaces with BIC are revealed to enhance the chiral dichroism of substances with bi-anisotropic properties [200]. Control of the chiral properties of chemical and biological compounds has significant meaning for pharmacology and medicine production because different enantiomers (stereoisomers without mirror symmetry) demonstrate significantly different biological activity [207]. Figure 2.2(c) illustrates the concept of an optical metasurface-based sensor consisting of pairs of TiO_2 bars on a gold film. The metasurface is optimized to provide molar concentration measurements of right-handed and left-handed enantiomers to determine the enantiomer ratio, as well as their refractive index. The high sensitivity of the metasurface to bi-anisotropy is owing to the simultaneous excitation of two orthogonally polarized quasi-BICs. The analysis of the enantiomer ratio is based on the optical chirality calculation introduced in Ref. [208] and carried out by calculations of metasurface reflectivity and chiral dichroism at the same time (see panel (iii) of Figure 2.2(c)). The sensitivity and FOM of the metasurface extracted from computations are $S =$ 80.6 nm/RIU and 80.6, respectively.

2.3 Tunable nanodevices

Tunable nanostructures are in great demand for photonic applications because they offer capabilities to manipulate the amplitude, frequency, and phase of optical signals, along with controlling photon absorption and emission. Tuning of resonant optical properties of nanostructures can be achieved by dynamic change of resonance conditions, which, for dielectric and semiconductor nanostructures, implies variation of either geometry or optical material properties (refractive index, extinction) [209]. Geometrical tuning of nanostructures can be performed by mechanical stretching or squeezing, changing the relative position of the nanostructure components or gaps between them, commonly obtained via microelectromechanical devices [210], optical forces [211], or thermo-mechanical effects [212]. Despite this approach being simple for optical analysis and providing high tunability, its reconfigurability rate is relatively low [213] and cannot guarantee optical modulation speed above 100 MHz. Besides, microelectromechanical tailoring requires significant efforts for design [214] and engineering to obtain compatibility of photonics and electronics in a single device [215]. Optical manipulations demand high pump intensities inevitably accompanied by strong linear and non-linear material losses [216], and the thermo-mechanical effect is challenging to control [212]. Conversely, strategies based on variation of material parameters, represented by a huge diversity of different phenomena, are well-studied from a material physics perspective and suggest tunability rates scaling from milliseconds to femtoseconds [57]. These phenomena include refractive index modulation via applied voltage (electro-optical effect) [217], temperature change (thermo-optical effect) [218], other intense optical fields (non-linear Kerr effect) [219], magnetic field (Faraday polarization rotation) [220], and more exotic material phase transition between amorphous and crystalline [221]. In this section, a few examples of both recently emerged and mature approaches for nanostructure tuning are considered in application to Mie-tronic devices.

Due to the remarkable property of phase-change materials (PCM) to rapidly and reversibly switch between amorphous and crystalline phases accompanied by pronounced refractive index and extinction coefficient modulation, they are proposed as one of the most prominent platforms for realizing tunable photonic devices [222]. The change of the crystal lattice phase of PCMs from amorphous to crystalline is commonly achieved by laser or electrical heating up to the crystallization temperature of the material below the melting point. Conversely, the amorphization procedure is performed by fast heating the structure above the melting point with subsequent fast cooling. “Freezing” of PCMs in the amorphous phase requires substantial cooling rates of about 10^9 K s^-1 or higher, which can only be achieved when the nanostructure is exposed by ultra-short and intense pulses, and the heat dissipation is well-optimized [222]. Fabrication of PCM devices is a well-developed technology in microelectronics, where these devices have been found applications in phase-change random access memory (PCRAM) and rewritable compact disks [223]. Thus, considering the established technology of PCM manufacturing, the idea of using them for tunable photonics appears promising. Figure 2.3(a), panel (i), illustrates a design of a Mie-resonant metasurface composed of Sb_2S_3 nanodisks on top of a silica substrate and experimental implementation of this design [224]. The reconfigurability of optical characteristics of the metasurface is achieved by tuning the phase of Sb_2S_3, which demonstrates a drastic change of the refractive index in the visible range of the spectrum upon phase change. Notably, the refractive index of Sb_2S_3 undergoes a transition from approximately 3 to 3.5 at the wavelength of 800 nm. Because Q-factor of nanodisk resonators drops significantly in the presence of the silica substrate, the metasurface is covered by a 70 nm-thick Si_3N_4 layer, which allows to mimic symmetry of the structure in the vertical direction and decreases the radiative losses into the substrate. Panel (ii) of Figure 2.3(a) indicates reconfigurable reflectance upon the phase change of the nanodisks. When the structure is in the amorphous phase right after the accomplished fabrication procedure, it exhibits a broad resonance with a resonance wavelength of around 650 nm. As soon as the structure phase is tuned to crystalline, the refractive index of Sb_2S_3 increases along with the losses, and the resonance peak expectedly broadens and shifts towards the longer wavelengths. In this scenario, the normalized reflectance changes by a factor of 10. However, upon a reversed amorphization process by ultra-fast laser melting, the obtained reflectance spectrum appears to mismatch with the initial one. The mismatch is explained by the fact that the bottom part of the nanodisks remains in the crystalline phase due to a weak heat transfer rate during the laser melting.

The most classical way to tune the optical properties by heating or cooling nanostructures is the thermo-optical effect, which implies temperature dependence of the refractive index [225]. Figure 2.3(b), panel (i), depicts the variation of the reflection efficiency of a single InSb nanoparticle induced by temperature tuning [226]. One can observe a significant shift of MD and ED resonances towards the longer wavelengths, originating from refractive index rise due to the heating. Specifically, the reflectance data analysis by Mie theory has revealed a 0.15 linear increase of the refractive index when the temperature is changed from 80 K to 473 K (see insert in Figure 2.3(b), panel (i)). The extracted refractive index change is later used to design a tunable metalense composed of InSb. A sketch of a tunable metalense proposed in Ref. [226] is shown in Figure 2.3(b), panel (ii). Tuning the temperature of the material allows for tuning the chromatic dispersion of the metalens. Figure 2.3(b), panel (ii), demonstrates a variation of the focal wavelength, which is the wavelength of the highest field intensity, depending on the refractive index of InSb, which depends on the temperature of the metalense. The results demonstrate a promising performance of the tunable metalense based on thermo-optical effect in a medium with controllable temperature. However, the thermo-optical effect has a doubtful operation efficiency, particularly stability of operation, when it comes to real-world application in non-controllable environments.

Liquid crystals are another group of materials that can effectively transition between states accompanied by pronounced changes in optical properties [229]. Liquid crystals are a unique state of matter that has characteristics of both liquids and crystals. Notably, they exhibit a liquid ability to flow and take on the shape of their container, and, at the same time, they have ordered molecular structures similar to traditional crystals. Remarkably, under external perturbations, the order of the molecules can be changed. This property of liquid crystals is widely used in modern technologies, first of all, in liquid-crystal displays (LCD). Due to the elongated shape of the liquid crystal molecules, their optical response is similar to anisotropic uniaxial crystals, which results in different refractive indices for different polarizations of light [229]. The applied voltage can manipulate the molecular arrangements

(a)
Phase-change materials

(c)
Liquid crystals

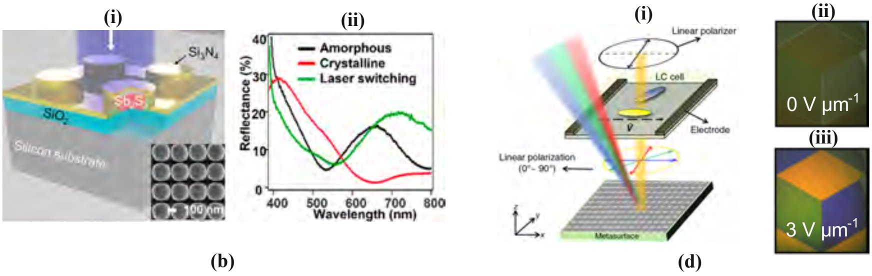

(b)
Thermo-optics

(d)
Twists

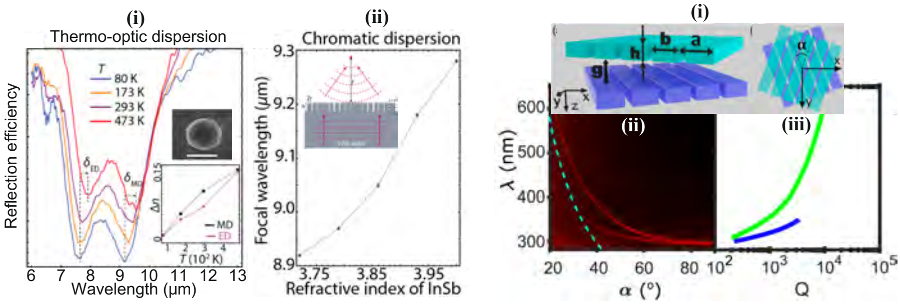

Figure 2.3. Examples of tuning mechanisms for reconfigurable Mie-tronic devices. (a) Tunable metasurface composed of a phase-change material Sb_2S_3 [224]. (b) InSb metalens with thermo-optics tailoring of chromatic dispersion. Panel (i) represents the temperature tuning of an InSb nanoparticle reflection efficiency. Panel (ii) shows the focal wavelength of the metalens versus the temperature-dependent refractive index [226]. (c) Semiconductor anisotropic metasurface combined with a liquid crystal cell for intensity and color control of the reflected light (panel (i)). Panels (ii-iii) depicts the optical image of structural colors generated by the metasurface, controlled by the voltage at the liquid crystal cell [227]. (d) Moire structure based on twisted dielectric gratings (panel (i)). Control of the twist angle allows tuning the position of the resonance (panel (ii)) and Q-factor (panel (iii)) [228].

of liquid crystals, converting the polarization of propagating light [229]. This mechanism, along with polarization filters, is the basic operation principle of pixels of LCD. Besides, liquid crystals exhibit different phases based on their molecular arrangements. The three main types of liquid crystal phases are nematic, smectic, and cholesteric [230]. Nematic crystals have molecules aligned in a particular direction but without specific positional order. Smectic crystals have layers of molecules with significant positional order. Cholesteric crystals have layers similar to smectic phases, but the orientation of the molecules within the layers is rotated. The transition between different phases can be achieved by changing the temperature of crystals or applying pressure, and it significantly affects optical properties, enabling ultra-sensitive temperature detectors [231]. Recently, liquid crystals have been utilized as components of metasurfaces, facilitating electrically and thermally tunable photonic devices for sensing [232], polarization modulation [233], and structural colors [227, 234]. Owing to their liquid nature, these crystals serve as a dielectric environment or a separate layer above/below metasurfaces to manipulate the polarization of the incident light (see Figure 2.3(c), panel (i)) [227]. In that case, the metasurface takes the role of a polarization filter if its meta-atoms are engineered to generate an anisotropic optical response. Metasurfaces with liquid crystals can be applied to reconfigurable structural colors, modulating the intensity of the color produced by the metasurface (Figure 2.3(c), panels (ii-iii)). Furthermore, liquid crystals can be used to adjust MD and ED resonances to enter the regime of Huygens metasurfaces.

Control of the wave function and electronic transport, which occurs through the rotation of overlaid two-dimensional van der Waals heterostructures, has given birth to a new research field at the interface between fundamentals and technology, known as twistronics [235, 236]. During the rotation of one atomic layer relative to another, so-called moiré patterns arise, representing interference patterns with a long-range order [237]. Based on an elegant concept of twistronics, a series of unique phenomena related to the physics of moiré structures have already been demonstrated [238–240]. They include a new type of superconductivity in bilayer graphene [241], moiré excitons in semiconductor bilayer structures [242], and interlayer magnetism in two-dimensional magnetic heterostructures [243]. These effects require complex manipulations with superlattices at the atomic level, such as precise control of the rotation angle between two overlaid atomic lattices. Such a precise control can be achieved by lower cost in optical metasurfaces. The photonic analog of twistronics, based on overlaid and rotated metasurfaces, is an intriguing new direction with numerous exciting applications. However, it has to be mentioned that at the present moment, it largely remains unexplored and not well-studied. In Ref. [228], the authors theoretically investigate the optical resonances and their tunability in a system of two parallel gratings, rotated with respect to each other at the angle α (see Figure 2.3(d), panel (i)). In their study, the gratings are located in a vacuum and separated by a gap of 300 nm. When twisted by a slight angle, two gratings can be considered as a periodic structure with a large supercell, which increases the number of opened diffraction channels and complicates the analysis of moiré patterns. To obtain the numerical solution, the authors adopted a Fourier Modal Method for moiré superlattices. The theoretical analysis of the photonic modes of the twisted gratings indicates strong coupling between the modes of individual gratings, which scales with the distance between them. Varying the twist angle between the gratings, the authors achieve strong tunability of the resonance wavelengths of the moiré superlattice modes, in particular, from 600 nm to 300 nm by changing the angle from 0° to 90° (see Figure 2.3(d), panel (ii)). In addition, the twist of the gratings allows to manipulate the Q-factor of the resonances in a broad range from 10^2 to 10^5 (Figure 2.3(d), panel (iii)).

2.4 Non-linear generation

The generation of optical harmonics in non-linear materials stands as a fundamental principle for generating light at desired frequencies. Given the limited presence of coherent optical sources across all required spectral ranges, especially in the visible and UV, the importance of efficient frequency up- and down-conversion has grown significantly [244]. Non-linear crystals that facilitate second and third-order harmonic generation are extensively employed alongside diode lasers to generate coherent emission at different wavelengths, unavailable for solitary diode lasers [245]. The efficiency of high harmonic generation in bulk non-linear crystals and waveguides is determined by momentum conservation law that dictates that the momentum of initial photons must match the momentum of the generated photons. This condition demands the refractive index of the non-linear material at the fundamental frequency to be identical to the refractive index at the multiplied frequency and is addressed as the phase-matching condition [246]. An emerging trend for miniaturization of optical components, namely, flat optics, targets the replacement of bulky non-linear crystals by nanoscale-thin resonant structures such as individual nanoparticles and metasurface [48]. The demand for compact non-linear photonic devices is also driven by the field of all-optical computing, where strong non-linear response at the nanoscale plays a crucial role [247]. Since translational invariance in individual nanoresonators and metasurfaces is broken in one or more directions, the momentum of photons is no longer conserved, and the overlap integral between the modes at fundamental and multiplied frequencies mainly defines the efficiency of harmonic generation [248]. For second-order non-linear response (second harmonic generation), the non-linear coupling constant between the modes is given by [248]:

$$\alpha_{\mathrm{NL}} = \frac{1}{4}\frac{\int \sum_{ijk} \varepsilon\chi^{(2)}_{ijk}\left(E^*_{1i}E_{2j}E^*_{1k} + E^*_{1i}E^*_{1j}E_{2k}\right)dV}{\int \varepsilon|\mathbf{E}_1|^2 dV\sqrt{\int \varepsilon|\mathbf{E}_2|^2 dV}}, \tag{2.9}$$

where $\mathbf{E}_1$ and $\mathbf{E}_2$ are the electric fields of the modes at fundamental and double frequencies, indices i, j, k span from 1 to 3, and $\chi^{(2)}_{ijk}$ is the non-linear susceptibility tensor.

Figure 2.4(a), panel (i), schematically demonstrates second harmonic generation in a high-index disk nanoresonator on top of a substrate, enabled by multipolar Mie

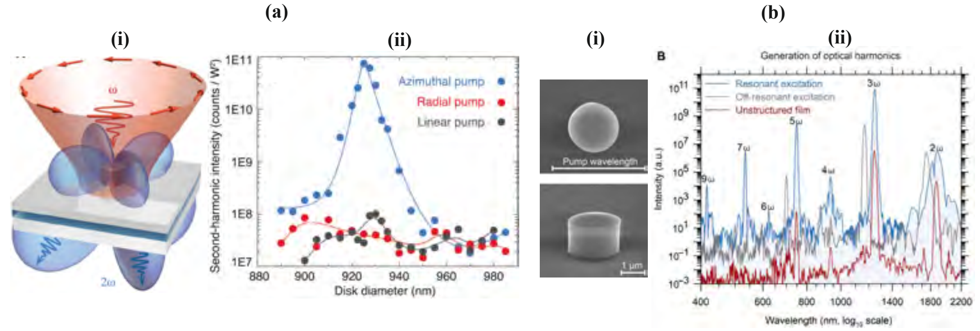

Figure 2.4. Single non-linear disks for high-harmonic generation. (a) AlGaAs nanodisk exhibiting a supercavity mode to boost second harmonic generation (panel (i)). Second harmonic intensity depending on disk diameter for azimuthally-, radially- and linearly-polarized pump (panel (ii)) [66]. (b) SEM images of an AlGaAs nanodisk optimized for 5th and 7th harmonic generation (panel (i)). Non-linear scattering intensity spectra of the nanodisk with resonant and non-resonant excitation and of an AlGaAs unstructured film (panel (ii)) [249].

resonances. It is well known that to achieve sufficiently high second harmonic generation efficiency, one should use a material with large $\chi^{(2)}$ or high-Q resonances. In Ref. [66], the authors propose a nanoantenna made of AlGaAs supporting supercavity modes [69], associated with canceling a low-order multipolar contribution and increasing a high-order contribution by geometrical tuning. This process leads to the amplification of the Q-factor of the mode and occurs due to the interaction between two distinct bare Mie modes. This interaction appears as the spherical shape is transformed into a disk shape. The mechanism behind the formation of the supercavity mode exhibits significant similarities with the mechanisms involved in forming BICs in periodic structures, where it arises from the nullification of the 0th-order Fourier expansion term [129]. Thus, in the literature, supercavity modes are often called quasi-BICs due to incomplete radiation suppression. The authors of Ref. [66] observe a supercavity mode around 1575 nm wavelength with the azimuthal number of 0, varying the aspect ratio of the disk. An azimuthal value of 0 indicates that the excitation of the cavity mode requires the incident beam to have azimuthal polarization. The authors study second harmonic output intensity, both theoretically and experimentally, changing the pump polarization, encompassing not only azimuthal polarization but also radial and linear polarizations, and obtained peak intensity in azimuthally polarized beams as expected (see Figure 2.4(a), panel (ii)). The observed second harmonic generation efficiency of 4.8×10^{-5} W^{-1} at the supercavity mode exhibits an improvement of over two orders of magnitude compared to earlier implementations achieved in solitary nanoresonators [250]. Although metasurfaces and engineered materials based on quantum well heterostructures demonstrate higher non-linear efficiencies, they are constrained by a maximum peak pump power of 100 mW, which these systems can withstand, in contrast to 10 W, reported in the reviewed work [251].

Despite the fact that generation and detection of second and third harmonics in non-linear photonic devices is a standard procedure, observation of higher harmonics in nanostructures remains a challenging task due to the weakness of high harmonic generation growing with the order. Only recently, high harmonic generation in optical gratings and metasurfaces with subwavelength thicknesses has been recorded [254]. The generation of higher harmonics represents a pathway toward creating coherent and compact light sources within the extreme UV spectral range. In Ref. [249], the authors report the detection of up to 7th harmonic employing AlGaAs disk resonators engineered for a supercavity mode. The SEM images of AlGaAs disk resonators enabling 5th and 7th harmonic generation are shown in Figure 2.4(b), panel (i). The theoretical predictions indicate that the enhancement of the high harmonic generation in nanoparticles with supercavity modes is due to direct and cascaded second and third-order non-linear processes. In the direct scenario, high-order non-linear processes are ensured by high-order non-linear susceptibilities $\chi^{(n)}$. In the cascaded scenario, the generation involves several $\chi^{(2)}$ and $\chi^{(3)}$ processes happening subsequently. The authors' theoretical calculations show that odd-order harmonics are favored over even-order harmonics. In order to support that claim, the authors provide measurements of the scattering spectrum of the individual AlGaAs disk (Figure 2.4(b), panel (ii)). Indeed, it reveals that the radiation is dominated by odd harmonics, including 3rd, 5th, and 7th. The non-linear scattering spectra are investigated with respect to the varying excitation wavelength. The high harmonic generation appears to be strongly enhanced when the wavelengths of the laser pump and supercavity mode are aligned. Even under off-resonant excitation, the supercavity mode influences the high harmonic maxima, causing a shift towards the supercavity mode resonance. The observed laser damage threshold is 50 mW.

Dielectric and semiconductor nanostructures supporting spatially extended Mie resonances can be used to enhance non-linear response from 2D materials coupled to them [255, 256]. The investigation of non-linear optical processes in monolayer TMDCs, such as second-harmonic generation, has garnered significant research attention due to their intrinsic non-centrosymmetric nature [257]. Additionally, second-harmonic microscopy has gained recognition as a technique for characterizing crystalline structures [258], detecting defects [259], and quantifying the number of atomic layers [260]. However, the frequency conversion efficiency is restricted by low light propagation length inside atomically thin layers, which poses a significant limitation on their practical applications. Confining the light in monolayer TMDC through metasurface resonances can sufficiently boost the second harmonic generation, opening doors for penetrating the TMDC into non-linear optics [252]. Figure 2.5(a), panel (i), represents a design of a silicon metasurface engineered to boost second harmonic generation efficiency from a WS_2 flake via excitation of a quasi-BIC. A microscopic image of a fabricated metasurface and WS_2 flake is presented in Figure 2.5(a), panel (ii). The magnitude of second harmonic generation from the monolayer of WS_2 on top of the metasurface is demonstrated to be at least 1140 times greater compared to the signal from the same monolayer on an equivalent-thickness silicon film (Fig-

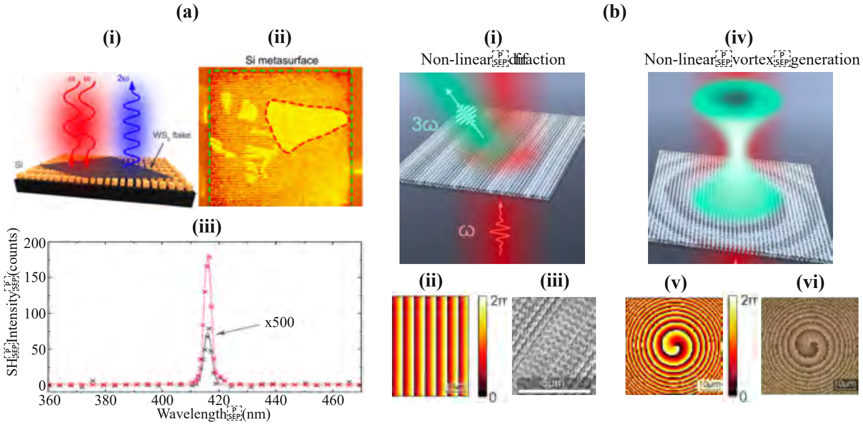

Figure 2.5. Metasurfaces for enhanced non-linear response. (a) Metasurface supporting a quasi-BIC coupled to a monolayer WS_2 (panel (i)). Panel (ii) shows an optical image of the metasurface with WS_2 flake. Panel (iii) presents the second harmonic signal from the WS_2 flake on top of the metasurface (red curve) and silicon film (black curve) [252]. (b) Illustrations of a diffractive metasurface and a metalense, enabling non-linear third harmonic diffraction and vortex beam generation, respectively (panels (i) and (iv)). Phase profile of the diffraction metasurface and the SEM image of the fabricated metasurface (panels (ii) and (v)). Phase profile and optical image of the metalens for focused vortex beam generation (panels (iii) and (vi)) [253].

ure 2.5(a), panel (iii)). This enhancement has been substantially amplified by the presence of the BIC. Importantly, the reported signal enhancement exceeds the one previously obtained in resonant dielectric metasurfaces by more than 15 times. Moreover, the monolayer WS_2 coupled to the metasurface possesses photoluminescence 9 times higher than on top of a silicon slab.

One can control the wavefront of optical signals induced by non-linear effects by engineering the properties of metasurfaces [253]. Non-linear dielectric metasurfaces can be designed to achieve deflection of non-linear beams at a desired angle and generation of non-linear focused vortex beams (see Figure 2.5(b)). The metasurfaces consist of sets of different elliptical nanopillar resonators. Each resonator within these sets comparably contributes to the non-linear conversion efficiency while accumulating a different phase for the third-harmonic signal. This phase covers the entire range from 0 to 2 . The phase accumulation for the third harmonic field within the dielectric metasurface appears in the regime of the Huygens metasurface. Therefore, the meta-atoms should combine magnetic and electric multipolar responses with equal strength, enabling a high forward-to-backward scattering ratio. Importantly, the metasurface should be resonant at fundamental and tripled frequencies to facilitate a strong non-linear signal, which implies high order multipole response at third harmonic frequency. To sustain the high directionality of the field, the response of odd and even multipoles should be perfectly balanced, which is dictated by the generalized Huygens condition. Constructing a 1D superlattice, whose supercell exhibits a smooth phase shift from 0 to 2π along the direction of superlattice periodicity (Figure 2.5(b), panel (ii)), an almost 80% diffraction efficiency can be achieved in the desired diffraction channel. The experimentally measured third harmonic generation efficiency is about $1.4{\times}10^{-4}$ $\mathrm{W}^{-}2$. For the vortex beam generation, the phase profile of the metasurface is designed as shown in Figure 2.5(b), panel (v). Based on such a metalense, the focused vortex beam of the third harmonic is obtained with angular momentum of 1.

2.5 Lasers and nanolasers

As the miniaturization of optical devices from large-scale to nanoscale photonic structures has become a current trend in advanced photonics, new nanoscale coherent emitters called nanolasers have been proposed [261]. In 2003, a pioneer work by David Bergman and Mark Stockman proposed a concept of surface plasmon amplification by stimulated emission of radiation (SPASER) which marked the beginning of the era of spasers and nanolasers [262]. Since then, spasers and nanolasers have obtained various forms and designs [263]. A noble metal nanoparticle covered by active media has been established as the most conventional form of spasers and nanolasers [264]. Further, semiconductor-based nanolasers have appeared as low-threshold and efficient counterparts of metallic ones [265]. Notably, perovskites and quantum dot inclusions have received the greatest recognition due to the high material gain and optical activity provided by these materials [266, 267]. Nanolasers are successfully used for sensing, biological probing, super-resolution imaging techniques and vortex beam generation [30]. Furthermore, the development of nanolasers approaches on-chip integrated optical interconnects and all-optical data processing.

Figure 2.6(a) demonstrates a concept of an optically pumped laser based on collective Mie resonances in linear chains for GaAs nanoparticles cooled down to 77 K [268]. The direct bandgap semiconductor, such as GaAs, simultaneously serves as a high-gain material and high-index medium, useful for Mie resonances. These high-Q resonances manifest in finite chain, originating from slow light effect and Van Hove singularity at the band edge of a guided mode of an infinite chain [271]. Specifically, the mode used for the laser represents an array of alternating coupled electric dipoles, aligned transverse to the axis of the chain. The modes of other nature (magnetic dipole, etc) have demonstrated poorer optical properties, lower Purcell factor and Q-factor. The nanolaser is composed of 100 nanoparticles of cylindrical shape. The number of nanoparticles strongly affects the resulting Q-factor and, consequently, laser threshold. The larger the number of nanoparticles, the lower the threshold of the nanolaser. Moreover, it has been observed that remarkably low laser thresholds (fluence of 5 μ J/cm^2) can be achieved in the chain with critically small gaps between the nanoparticles as shown in Figure 2.6(a), panel (ii). This threshold is more than 10 times smaller than required for nanowire lasers with a footprint over 4 times larger.

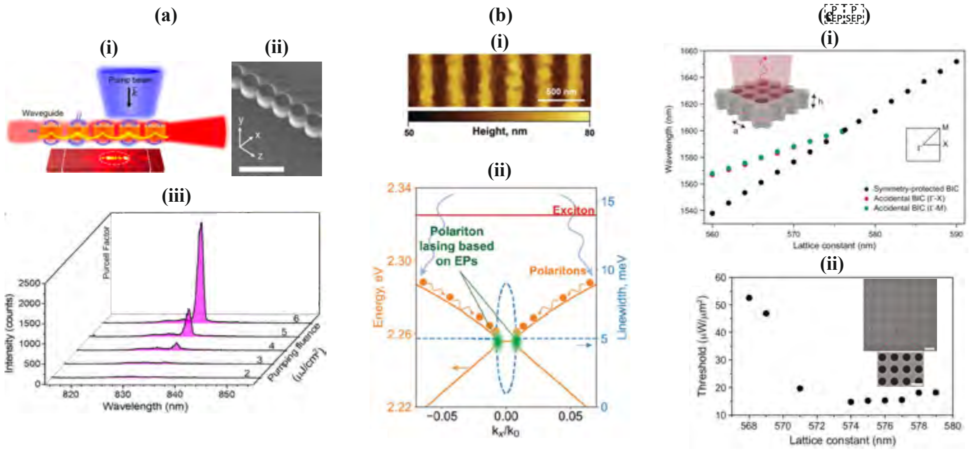

Figure 2.6. Nanolasers based on Mie-resonant photonic structures. (a) Demonstration of lasing from a GaAs chain exploiting van Hove singularity. Panels (i-ii) show a design of the nanolaser and SEM image of the chain. Panel (iii) reveals spectra of emission intensity versus pumping fluence [268]. (b) Energy diagram of a perovskite grating tuned to lasing EP (panel (ii)). Panel (i) shows atomic force microscopy of the perovskite grating [269]. (c) Concept of merging symmetry-protected and accidental BICs and their application to a low-threshold metasurface-based nanolaser. Panel (i) represents eigen wavelengths of accidental and symmetry-protected BICs versus lattice constant of the metasurface. Panel (ii) reveals the dependence of the nanolaser threshold on the lattice constant [270].

The mode of the chain exhibits a clearly defined, in-plane radiation pattern. This feature holds promise for applications in on-chip photonic circuitry, either by coupling to waveguides or using free-space interconnects. Such the chain can be additionally tuned to achieve unidirectionality of light emission via asymmetric femtosecond laser irradiation accompanied by electron-hole plasma excitation. Figure 2.6(a), panel (iii), illustrates intensity spectra of the chain radiation upon increased pumping fluence, indicating narrowing of the emission line typical for transition from superluminescence to lasing regime.

Constructing integrated, energy-efficient lasers with a low threshold poses a significant challenge for nanoscale photonic integrated circuits. One of the approaches for low-threshold or potentially thresholdless lasers relies on Bose-Einstein condensation, when bosons, such as photons and polaritons, are accumulated in a single quantum state [272]. Unlike conventional lasers, the polaritonic lasers based on Bose-Einstein condensation do not require inversion of state population, which makes them extremely attractive from both research and technology prospective [273]. A polaritonic state of matter can be achieved in a strong coupling regime between photons, confined within a cavity mode, and, for instance, excitons that are excited in a semiconductor material [274]. Recently, a new class of perovskite materials, exhibiting strong excitonic response, has penetrated photonics, enabling resonant photonic structures, highly efficient light sources and nanolasers [275]. Despite the limited lifetime of these materials, perovskites maintain to attract attention of the scientific community, promising utilities for photovoltaics and optoelectronics [276]. The outstanding physical properties of perovskites, including their relatively high exciton binding energy, oscillator strength, and strong defect tolerance, empower strong light-matter interactions and non-equilibrium polariton Bose-Einstein condensation even at room temperature [277]. The concept of polaritonic laser composed of a halide perovskite ($MAPbBr_3$) subwavelength grating is presented in Figure 2.6(b) [269]. $MAPbBr_3$ serves as a gain medium, while the grating structure provides high-Q resonances. The grating supports two coupled counterpropagating modes interacting with excitons, producing two exciton polariton sub-branches in the dispersion diagram. Noteworthy, these sub-branches constitute the lower polaritonic branch, and the upper polaritonic branch can be observed at the energies above the exciton transition, yet optical losses significantly quench it. When the pumping fluence reaches sufficiently high value, the system enters the balanced state between sum of loss and gain and interaction energy between photons and excitons. It gives rise to two lasing spots in the reciprocal space, associated with exceptional points. Intriguingly, the balance is achieved below the laser threshold, when the gain does not totally sedate the losses.

Multiple times, it has been demonstrated that high-Q factors of BICs can substantially suppress the threshold of nanolasers [278–281]. The BIC Q-factor in finite periodic structures generally follows N^2 dependence, where N is the number of unit cells in the structure, which originates from k^2 dependence of the Q-factor of a BIC mode in the reciprocal space of infinite periodic structures [270]. However, this behavior can be modified in order to boost the Q-factor of quasi-BICs in Γ-point, employing the concept of merging BICs (see Figure 2.6(c), panel (i)), introduced in Ref. [270]. Changing the structure periodicity, one can approach the parameter sensitive accidental BIC to the symmetry-protected BIC on the dispersion diagram. Once the accidental and symmetry-protected BICs start to merge at the Γ-point, the Q-factor of the infinite structure starts to behave as k^6, which implies higher Q-factor of the fundamental mode of the finite structure. As they finish merging, the behavior turns back to k^2 typical for the BIC in Γ-point. The regime of two merging BICs is called super-BIC and characterized by high-performance optical characteristics, including an ultralow threshold, a single lasing peak, and a high Q-factor. Notably, the threshold of the super-BIC nanolaser is limited by the transparency value of the gain material, as a result of the low radiative loss in the finite photonic structure. Furthermore, the semiconductor active material with high optical gain well-supports the superior optical properties of super-BIC. Compared with other BIC lasers using similar gain materials, the measured threshold values are lower in the super-BIC regime and similar outside the super-BIC regime (Figure 2.6(c), panel (ii)) [281, 282]. Remarkably, the threshold manifests an exceptionally low value, primarily constrained by the transparency level of the gain material. This phenomenon arises due to the low radiative losses of the BIC within the finite photonic structure.

2.6 Summary

To sum up, I have presented the state-of-the-art Mie-tronic devices for advanced wavefront control, high-sensitive sensors, tunable nanophotonics, non-linear optics and nanolasers. Owing to Kerker and Huygens effects, Mie resonances have enabled ultrathin lenses and structural colors. Extremely sharp resonances, produced by BICs in Mie-tronic structures, have established a new generation of optical sensors, particularly refractometers with sensitivity exceeding 600 nm/RIU. Mie-resonant nanostructures have demonstrated high tunability employing phase change, mechanical twists, electro- and thermo-optical effects. Remarkably, semiconductor metasurfaces, supporting BICs, have exhibited outstanding performance for high harmonic generation and non-linear wavefront manipulation, while resonant semiconductor nanoparticles in supercavity regime have shown sufficiently high non-linear signal up to 7th harmonic. Finally, Mie-resonant structures have proved themselves as a promising platform for nanoscale lasers with low thresholds.

Although, Mie-resonant nanodevices offer numerous opportunities for applications in photonics, they still require significant improvements. These structures often possess limited stability, undesirable sensitivity to the surrounding environment and inefficient signal transmission due to dispersion and absorption. Integrating resonant nanodevices into existing photonics technologies can be difficult due to incompatibility of materials and fabrication methods. For instance, the demands of nanoscale structures and precision manufacturing might not align with standard methods for integrated circuits. This misalignment can limit production scalability and creation of reliable devices. To address these challenges, new designs and physical principles of device operation need to be developed.

CHAPTER 3

Virtual excitations: novel electromagnetic phenomena

The class of coherent virtual effects encompasses a variety of optical phenomena that arise within optical systems due to the temporal modulation of incident monochromatic waves by exponentially growing or decaying functions. These phenomena originate from the excitation of optical states within the system, including poles and zeros of the scattering matrix and the intermediate states between them at complex frequencies [81]. While exponentially modulated, the signals can be considered monochromatic with a complex frequency $\omega = \omega' + i\omega''$ [75]. Positive ω'' corresponds to the excitation of states in the upper complex frequency plane, induced by exponentially growing signals, while negative ω'' corresponds to states excited in the lower complex frequency plane due to exponentially decaying signals. Although the approach to describe coherent virtual excitation based on complex frequencies implies unphysical, divergent energy of the system, it still provides valuable insights and predicts the system's response under excitation by time-limited exponential signals with finite energy. The fundamental principle that enables virtual phenomena is the occurrence of losses as an imbalance between the incident and scattered energy [75], even in systems without dissipation, under exponentially growing excitation and the appearance of gain under exponentially decaying excitation [76]. In this chapter, I review the main accomplishments in virtual effects obtained by other researchers. In Section 3.1, I reveal the physical and mathematical background of the coherent virtual absorption (CVA) phenomenon and provide examples illustrating CVA in Fabri-Perot and microring resonators. In Section 3.2, I demonstrate that CVA enables virtual critical coupling, which is far more efficient than standard critical coupling in lossy systems. In Section 3.3, I show that systems of multiple coupled modes under virtual excitation by exponentially decaying signals can exhibit effective gain and PT-symmetry. Finally, I summarize the chapter in Section 3.4.

3.1 Coherent virtual absorption

When radiative and non-radiative losses of a mode of an optical resonator are balanced, the corresponding zero reaches the real frequency axis of the complex frequency plane, which is demonstrated in Figure 1.1. In this case, the system enters the perfect absorption regime, implying that the resonator can fully absorb coherent excitation at the real frequency of the mode. This effect of coherent perfect absorption (CPA) enables the manipulation of light with light via real absorption in the material without the need for optical non-linearities [283]. However, CPA is irrelevant for applications requiring light controlled by light, such as photonic transistors and quantum memories, due to the complete loss of photons carrying information and high thermal heating [284]. On the contrary, CVA allows harvesting light inside the resonator for a potentially long period of time, controlled by incident optical signal, without any unnecessary losses [75, 285, 286].

For consideration of CVA in optical systems, it is convenient to analyze the response of a dielectric slab, a multi-mode cavity coupled to two scattering channels (see Figure 3.1(a)). The optical response of the slab can be found via the Transfer Matrix method (TMM):

$$r = \frac{i(n^2-1)\sin(nkL)}{2n\cos(nkL) - i(n^2-1)\sin(nkL)}, \tag{3.1}$$

$$t = \frac{2n}{2n\cos(nkL) - i(n^2-1)\sin(nkL)}, \tag{3.2}$$

where r and t are reflection and transmission coefficients, n is the refractive index of the slab, L is its thickness. r and t construct 2×2 scattering matrix of the slab, whose eigenvalues $\sigma_{1,2}$ can be obtained as follows:

$$\sigma_{1,2} = t \pm r. \tag{3.3}$$

Complex frequency dependent $\sigma_{1,2}$ contains information about poles and zeros that are attributed to the Fabri-Perot modes of the dielectric slab. As for CPA, zeros of the scattering matrix play a key role in the CVA phenomenon. Figure 3.1(b) shows upper complex frequency half-plane with zeros, corresponding to odd (s_-) and even (s_+) slab modes. Excitation of one of the zeros with an appropriate combination of optical signals at the complex frequency results in complete scattering cancellation and, therefore, full energy storage in the slab. CMT equations for a mode of the slab, excited from two scattering channels, assuming the output signals are totally suppressed, can be derived as follows:

$$\frac{da}{dt} = -i\omega_0 a - \gamma a + \sqrt{\gamma} s_1^+ \pm \sqrt{\gamma} s_2^+, \tag{3.4}$$

$$-s_1^+ + \sqrt{\gamma} a = 0, \tag{3.5}$$

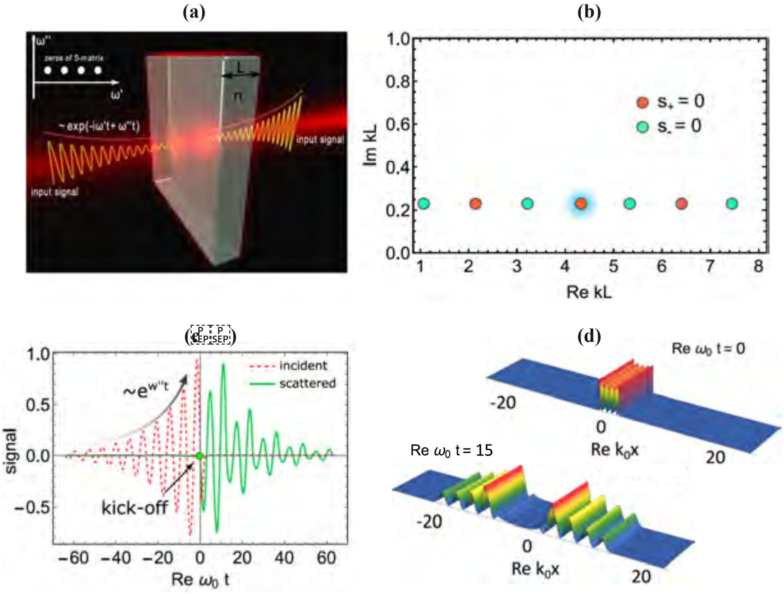

Figure 3.1. The concept of coherent virtual absorption in 1D structures. (a) Schematic view of a dielectric plate, supporting Fabri-Perot resonances, excited at a scattering matrix zero. (b) Complex frequency plane illustrating scattering matrix zeros in the upper plane. ±-sign designates even and odd modes of the plate. (c) Time domain profiles of the incoming and outcoming signals in a coherent virtual absorption scenario. (d) Instantaneous electric field intensity profiles in the dielectric plane at the signal kick-off (top panel) and after some time (bottom panel) [75].

$$-s_2^+ \pm \sqrt{\gamma} a = 0. \tag{3.6}$$

Here, ± sign stands for even/odd Fabri-Perot mode. Solving the system of Equations 3.4- 3.6, one can obtain the form of the input signals, resulting in scattering cancellation:

$$\begin{aligned} s_1^+ &= A e^{-i\omega_0 t + \gamma t}, \\ s_2^+ &= \pm A e^{-i\omega_0 t + \gamma t}, \end{aligned} \tag{3.7}$$

indicating that transmission and reflection of the slab are suppressed when both channels are simultaneously excited by exponentially growing waves at the complex frequency of the slab zero. Moreover, a detailed analysis of Equations 3.4- 3.6 demonstrates that the suppression originates from the destructive interference between input signals and the outgoing field of the Fabri-Perot mode. Figure 3.1(c) presents the time domain dynamics of the incident and scattered fields in the CVA regime. When the slab is excited by an exponentially growing signal with $\omega'' = \gamma$, no scattering response is observed. At the moment of time $\omega_0 t$, the Fabri-Perot mode accumulates all the energy of the incoming radiation within the slab (see Figure 3.1(d), top panel). At $\omega_0 t > 0$, the incident signal is turned off, and the mode emits the accumulated energy into the opened channels as illustrated in field distributions of Figure 3.1(d), bottom panel. The proposed mechanism of CVA can be effectively used to control the energy harvesting and releasing from the cavity along with the transmissivity of one of the incident signals by another.

CVA can be applied to resonant photonic integrated circuits to perfectly pump a microring resonator with subsequent release of the stored energy into a waveguide [286]. Figure 3.2(a) shows a schematic image of a silicon microring coupled to a straight silicon waveguide. Both are embedded into a glass matrix with a significantly lower refractive index. The microring cavity supports two degenerate modes: propagating clockwise and counter-clockwise. Sending a signal to the input port of the waveguide, as shown in Figure 3.2(a), results in the excitation of only the clockwise propagating mode. Its interaction with the counter-clockwise propagating mode is neglected owing to sufficiently small surface roughness, responsible for the reflection between the modes. For such a system, CMT equation can be written as:

$$\frac{da}{dt} = -i\omega_0 a - \gamma_{\mathrm{w}} a + iI\alpha_K |a|^2 a + \sqrt{\gamma_{\mathrm{w}}} s_1, \tag{3.8}$$

$$s_2 = s_1 - \sqrt{2\gamma_{\mathrm{w}}} a, \tag{3.9}$$

$$s_3 = \sqrt{2\gamma_{\mathrm{w}}} a, \tag{3.10}$$

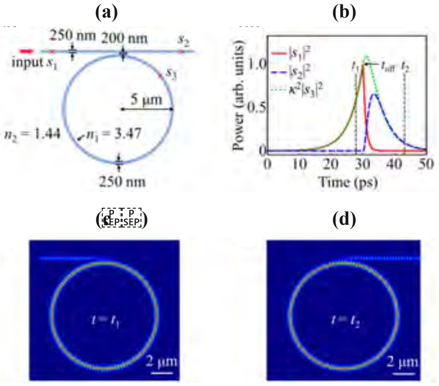

Figure 3.2. Demonstration of coherent perfect absorption phenomena in a microring resonator coupled to a waveguide. (a) Sketch of the microring resonator coupled to the waveguide. (b) Time domain profiles of the input (red solid) and output (blue dashed) signals and mode amplitude (green dotted). (c-d) Instantaneous electric field distributions in the system of the microring resonator and waveguide (c) before and (d) after the kick-off of the incoming signal [286].

where α_K is the effective non-linear Kerr coefficient, given by [248]:

$$\alpha_K = \frac{1}{8} \frac{\int d\mathbf{r}^3 \varepsilon \chi^{(3)} \left(|\mathbf{E} \cdot \mathbf{E}|^2 + |\mathbf{E} \cdot \mathbf{E}^*|^2 \right)}{\left(\int d\mathbf{r}^3 \varepsilon |\mathbf{E}|^2 \right)^2}. \tag{3.11}$$

$\chi^{(3)}$ is the third-order non-linear susceptibility, and I is the variable used to control the intensity of the non-linear effect. In the case of $I = 0$, the system is considered linear, and eventually, CVA can be observed. The temporal dependence of optical power at the input and output ports of the waveguide and the microring are shown in Figure 3.2(b). The input power varies exponentially at the rate $2\gamma_\mathrm{w}$, which corresponds to coherent virtual excitation of the zero of the scattering matrix at $\omega = \omega_0 + i\gamma_\mathrm{w}$. Until the signal is switched off at $t = t_\mathrm{off}$, the microring resonator behaves as a perfect absorber, storing the energy inside the clockwise propagating mode (Figure 3.2(c)). At $t > t_\mathrm{off}$, the signal at the input port diverges from the exponential function dictated by the virtual process, and the microring releases the energy to the output port (Figure 3.2(d)).

Finally, in the case of non-zero Kerr non-linear coefficient ($I = 1$), the system supports CVA up until some instant of time, when the microring mode reaches a critical level of the stored energy, determined by the input intensity and Q-factor of the microring mode. If the intensity is small, which is the case for the early cycles of excitation, or the Q-factor is small, the microring exhibits standard virtual absorption. Otherwise, the resonant frequency of the microring deviates from its linear eigenfrequency due to Kerr non-linearity induced shift, and CVA is broken, resulting in energy release to the output port.

3.2 Virtual critical coupling

The concept of CVA can be used to achieve optimal and reflectionless coupling of incident waves to a cavity, which is well-known as critical coupling [77]. Critical coupling is the regime of the cavity mode when the energy of the incoming signal is entirely transported to the mode, such that no reflected or transmitted fields can be observed [287]. For monochromatic waves, the critical coupling can be obtained by balancing the radiative decay rate γ_w, ensuring interaction between the cavity and the excitation channel, and the intrinsic decay rates γ_i, associated with other channels of loss. Therefore, in a single scattering channel approximation, the critical coupling condition simply requires adding the proper amount of non-radiative losses $\gamma_\mathrm{nr} = \gamma_\mathrm{w}$. Then, the Q-factor of the mode in the critical coupling regime $Q = \omega/2(\gamma_\mathrm{w} + \gamma_\mathrm{i}) = \omega/4\gamma_\mathrm{w}$ is twice reduced compared to the initial one $Q = \omega/2\gamma_\mathrm{w}$, undesirable for the majority of photonic applications, as the maximum absorbed energy is four times less than that observed in the lossless case. It also implies that the excitation efficiency, defined as $\eta = |a(t)|^2 / \int_{-\infty}^{+\infty} |s^+(t)|^2 dt$, is significantly less in the case of loss-induced critical coupling of the cavity and channel in comparison to the lossless and undercoupled case. From this perspective, the monochromatic excitation appears undesirable for both lossless and lossy cavities. Below, it is shown that when monochromatic waves are extended up to complex frequencies, the radiation channel can be critically coupled to the cavity without additional intrinsic losses. The mechanism behind virtual critical coupling is closely related to the CVA phenomenon: the reflected and transmitted signals are canceled out due to destructive interference between the incident field, directly scattered to the channels, and the cavity field, leaking to the channels. For a single port cavity, depicted in Figure 3.3(a), it means destructive interference between out-of-phase oscillating back-scattered fields due to the incident signal and energy already stored in the cavity.

Figure 3.3(b) illustrates a single-mode cavity coupled to multiple scattering channels. In the simplest scenario, one of the scattering channels is used for the excitation, either by real or virtual signals, with a coupling rate γ_w. The other loss channels, contributed by free-space radiative and non-radiative losses of the cavity and leakage to other scattering channels, can be described together by the intrinsic loss rate γ_i. For a single-channel system, one can easily derive the reflection amplitude from CMT depending on real and imaginary parts of the signal frequency:

$$r(\omega', \omega'') = \frac{(\gamma_\mathrm{w} - \gamma_\mathrm{i} - \omega'') - i(\omega' - \omega_0)}{(\gamma_\mathrm{w} + \gamma_\mathrm{i} + \omega'') + i(\omega' - \omega_0)}. \tag{3.12}$$

By definition, the critical coupling of such a single-channel system is achieved at $r(\omega', \omega'') = 0$, satisfied when both real and imaginary parts of the nominator of Equation 3.12 are identical to 0 at $\omega' = \omega$ and $\omega'' = \gamma_\mathrm{w} - \gamma_\mathrm{i}$. For real signals ($\omega'' = 0$), this converges to the standard critical coupling condition $\gamma_\mathrm{i} = \gamma_\mathrm{w}$. The energy stored in the steady state under monochromatic excitation, after all transition processes are over, is given by:

$$|a|^2 = \frac{4Q_\mathrm{w}}{\omega_0} \frac{\gamma_\mathrm{w}^2}{(\gamma_\mathrm{w} + \gamma_\mathrm{i} + \omega'')^2} |s^+|^2, \tag{3.13}$$

where $Q_\mathrm{w} = \omega_0/2\gamma_\mathrm{w}$ is the Q-factor associated with radiation to the excitation channel, s^+ is the amplitude of the incident signal, which, for complex frequency excitation, obeys $e^{i\omega'' t}$. In the case of real frequency signals ($\omega'' = 0$), the energy inside the cavity saturates up to some limit derived as:

$$|a|^2 = \frac{4}{\omega_0} \frac{Q_\mathrm{w}}{(1 + Q_\mathrm{w}/Q_\mathrm{i})^2} |s^+|^2, \tag{3.14}$$

where Q_i is the intrinsic Q-factor. In the cavities without dissipation, Q_i turns to ∞, and the maximum energy at the end of the transient regime converges to $|a|^2 = \frac{4Q_\mathrm{w}}{\omega_0}|s^+|^2$. For the critically coupled cavities at real frequencies, Equation 3.14 changes to $|a|^2 = \frac{Q_\mathrm{w}}{\omega_0}|s^+|^2$, illustrating reduction of the energy in the critically coupled cavity by a factor of 4. In the regime of virtual critical coupling $\omega'' = \gamma_\mathrm{w} - \gamma_\mathrm{i}$, the stored energy exponentially grows in time until the virtual signal is turned off, and the undissipated part of the energy is released.

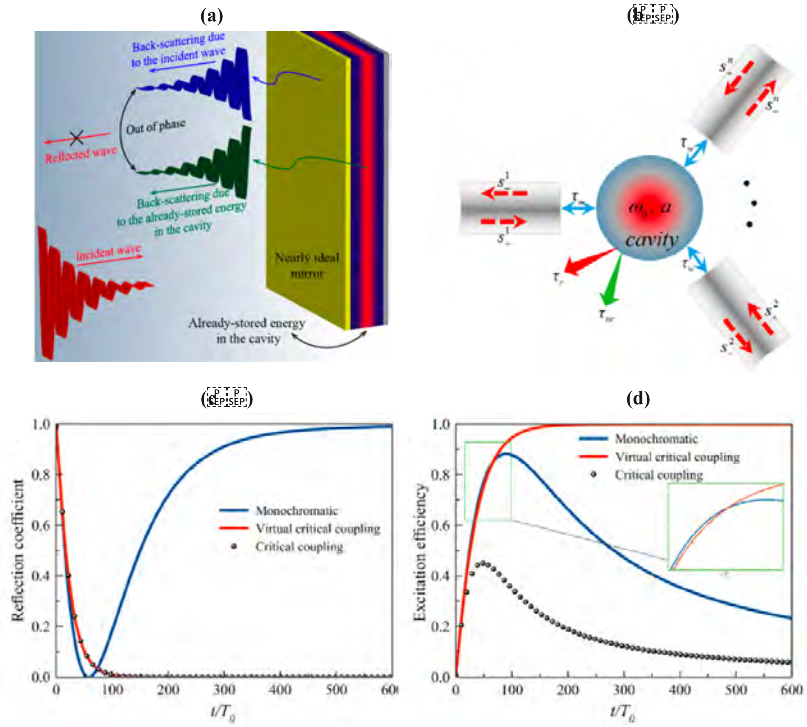

Figure 3.3. Theoretical background of virtual critical coupling. (a) A single mode cavity coupled to n scattering channels. (b) Explanation of virtual critical coupling phenomena as destructive interference between direct and indirect back-scattering. (c) Normalized reflected signal versus time for a lossless system under monochromatic excitation (blue), loss-balanced system in the critical coupling regime (black dots), and lossless system under exponentially growing excitation in the virtual critical coupling regime (red). (d) Excitation efficiency calculated for these three cases [77].

Figures 3.3(c-d) represent the analysis of reflectivity and excitation efficiency of a single mode cavity with $Q_\mathrm{w} = 200$, considered in three different scenarios: lossless cavity, critical coupling, and virtual critical coupling. The amplitude of the input signal is identical to 0 at $t < 0$ and to 1 at $t \geq 0$. When the monochromatic wave pumps the lossless cavity at early excitation cycles, the cavity is undercoupled, and most of the incident energy is reflected back to the pumping channel. However, as the cavity gets slowly pumped, the waves, leaking from the cavity to the channel, become stronger, destructively interfering with the back-reflected waves canceling a part of the reflection. It continues until some moment of time, at which the cavity is critically coupled, although $\gamma_\mathrm{i} = 0$, and the reflectivity becomes 0, indicating a balance between destructively interfering waves. As the energy stored in the cavity grows, the balance is lost, resulting in growing reflectivity upon excitation. Finally, the cavity reaches the maximum stored energy accompanied by total reflection to the scattering channel. Remarkably, the cavity in the monochromatic regime achieves critical coupling faster than in the conventional and virtual critical coupling regimes due to adding to the cavity real or virtual loss. The time instant τ corresponding to the critical coupling regime in the lossless case can be approximated by a simple formula $\tau = \tau_{\mathrm{w}}|r|^2/(2-|r|^2)$, where $\tau_{\mathrm{w}} = 1/\gamma_{\mathrm{w}}$, r is the reflection coefficient of the direct scattering matrix, equal to 1. In the case of critical coupling, both real and complex signals give similar decay of the reflectivity over time. The divergence of the reflectivity from 0 at the beginning of the excitation cycle is owing to the mismatch between the incident signal amplitude and internal mode amplitude, disappearing upon continuous excitation. The results for monochromatic and virtual excitations can be further used to obtain a compound signal based on a real frequency signal at the beginning of the cycle and a complex frequency signal at the end of the cycle, resulting in a faster reflectivity decay at early cycles.

The analysis of the excitation efficiency η of the cavity mode reveals the superiority of the virtual critical coupling approach over the other approaches (see Figure 3.3(d)). For the monochromatic excitation scheme, the efficiency reaches its maximum around $t = 100T_0$ and is generally relatively low, especially in the long-time limit. However, until $t < \tau$, which corresponds to the lossless critical coupling, the efficiency of the monochromatic excitation is slightly higher than the one corresponding to virtual excitation. The excitation efficiency of the lossy cavity in a critical coupling regime demonstrates a 2-fold reduction compared to the lossless cavity because of continuous energy dissipation.

3.3 Virtual gain and parity-time symmetry

When systems are excited by exponentially decaying signals ($\omega'' < 0$), they may exhibit behavior similar to what is typically expected from systems with gain, such as optical amplifiers and lasers [76]. Virtual gain, along with the virtual absorption, can be understood as a mismatch between the incident field intensity in a current moment of time and the scattered field intensity in the current moment of time, originating from the incident field from the previous moment of time with a different amplitude. If the signal grows exponentially, then the incident field at the previous time step is smaller than at the current time step, giving rise to a positive imbalance between excitation and scattering. However, if the signal exponentially decays, its amplitude at the previous time step is larger than at the current time step, producing a negative imbalance and, thus, effective (virtual) gain. Virtual gain opens opportunities for realizing photonic parity-time (PT) symmetric systems in completely passive systems, enabling highly sensitive exceptional points, single-mode and multimode lasers, and anisotropic transmissivity. PT-symmetry is a special type of symmetry that conserves under simultaneous inversion upon space and time. Generally, it implies that the complex refractive index satisfies the condition $n(\mathbf{r}) = n^*(-\mathbf{r})$, which requires

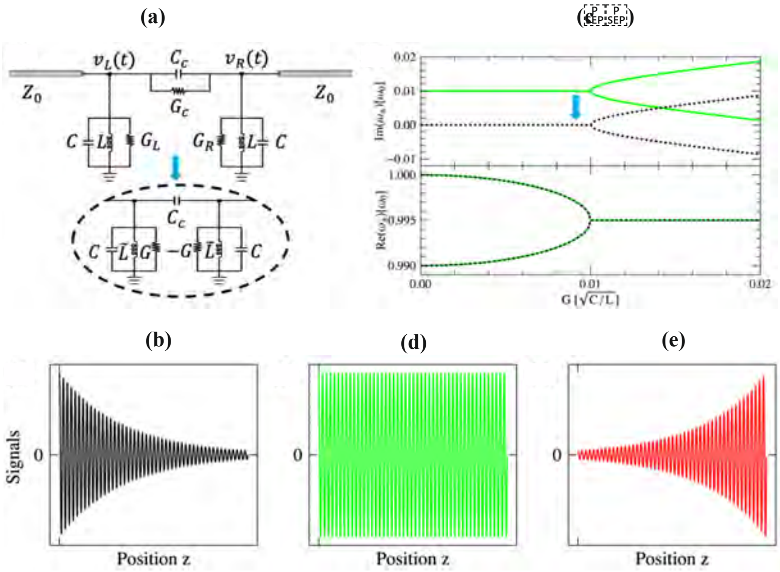

Figure 3.4. (a) Transmission line of a passive PT-symmetrical system. (b) Normalized output signal as a function of spatial coordinate z under monochromatic excitation ($\omega'' = 0$). (c) Imaginary (top) and real (bottom) parts of eigenfrequencies versus the Hermiticity parameter G. The solid green curves correspond to the eigenfrequencies of the passive circuits. The dashed black curves correspond to shifted eigenfrequencies under virtual excitation with $\omega'' = \gamma$. Normalized output signal as a function of z under (b) exponentially decaying excitation at $\omega'' = \gamma$ and (c) exponentially decaying excitation at $\omega'' > \gamma$ [76].

a balanced spatial profile of gain and loss. This requirement applies significant limitations for the practical realization of PT-symmetric systems, especially in optics, as sufficiently stable gain is commonly complicated to achieve. However, it can be overcome in entirely passive systems, implementing lossy systems with coupled modes near exceptional points.

PT-symmetry can be obtained in a strong coupled regime if the interaction constant is larger than the loss/gain rates in a system of interacting resonators with balanced gain and loss. The Hamiltonian of the PT-symmetric system can be written as follows:

$$\hat{H} = \hbar\omega_0 - i(\gamma_{\mathrm{r}} + \gamma_{\mathrm{nr}})gg\omega_0 - i(\gamma_{\mathrm{r}} - \Gamma), \tag{3.15}$$

where $\Gamma = 2\gamma_{\mathrm{r}} + \gamma_{\mathrm{nr}}$ is the gain sufficient to balance all the losses. One can demonstrate that, after applying Hermitian conjugation and multiplying $\hat{H}$ by parity operator $P = 0110$, the Hamiltonian converges to itself, which is the main property of PT-symmetric systems. From Equation 3.16, it follows that the eigenfrequencies of the

PT-symmetric systems obey the relationship:

$$\omega_\pm = \omega_0 \pm \sqrt{g^2 - (\gamma_\mathrm{r} + \gamma_\mathrm{nr})^2} = \omega_0 \pm \sqrt{g^2 - (\gamma_\mathrm{r} - \Gamma)^2}. \tag{3.16}$$

At $g > (\Gamma - \gamma_\mathrm{r})$, it is said that the system is in a PT-symmetry phase with completely real eigenfrequencies, appearing as a two-mode laser with spectrally separated emission lines. Such a spectral separation of lasing frequencies is the direct consequence of strong coupling between the resonators due to the coupling constant exceeding gain/loss. At $g < (\Gamma - \gamma_\mathrm{r})$, the system enters an unstable PT-symmetry broken phase, which results in migration of ω_+ to the realm of light-generating modes in the upper complex frequency plane and migration of ω_- to the domain of leaky modes in the lower complex frequency plane. In the intermediate state ($g = (\Gamma - \gamma_\mathrm{r})$), the system is in the exceptional point, characterized by degenerate eigenfrequencies and eigenmodes.

Virtual PT-symmetry can be exemplified in a transmission line (Figure 3.4(a)) composed of two resonant induction/capacitance circuits, designated as left (L) and right (R), with corresponding conductance G_L and G_R, responsible for the losses. The circuits are coupled through a lossy capacitance C_c with a conductance G_c. This transmission line is equivalent to an optical system of two coupled passive resonators with two external scattering channels. The transmission line is pumped by a voltage signal $v_0(z,t) = V_0 e^{-i\omega t - i\beta z}$, where $\omega = \omega' - i\omega''$ is the complex frequency, and β is the propagation constant. If a monochromatic signal with ω'' is sent through the transmission line, the output signal decays along the line, as presented in Figure 3.4(b), with a rate determined by the conductance of the line, i.e., losses of the circuits. Figure 3.4(c) shows the eigenfrequency spectrum of the transmission line depending on the Hermiticity parameter $G = \pm\left(G_{L/R} - \gamma C + \gamma/\left[L(\omega_0^2 + \gamma^2)\right]\right)$, revealing all three extreme regimes occurring in PT-symmetrical systems. As long as $G < 0.01/\sqrt{C/L}$, the real part of the eigenfrequencies experiences splitting, while the imaginary part remains constant. On the contrary, $G > 0.01/\sqrt{C/L}$ results in the divergent imaginary part and constant real part of the eigenfrequencies. The scattering matrix of this transmission line at a complex frequency can be defined as:

$$\hat{S}(\omega) = -\hat{I} + \frac{i2\hbar\gamma_r}{\hbar\omega - \hat{H}}, \tag{3.17}$$

where γ_r, γ_nr, Γ and γ are related according to relation: $\gamma = \gamma_\mathrm{r} + \gamma_\mathrm{nr} = \Gamma - \gamma_\mathrm{r}$. When excited at the complex frequency $\omega = \omega_0 - i\gamma$, the scattering matrix resembles the properties of an active PT-symmetric system, as the eigenfrequency spectrum undergoes an effective shift towards the real frequency axis. In this case, the output signal does not depend on the z at any time moment (see Figure 3.4(d)), resembling the laser behavior. Further, under excitation with $\omega'' > \gamma$, the amplitude of the signal grows along the propagation direction, imitating amplification (Figure 3.4(e)).

3.4 Summary

In this chapter, I have presented definitions for virtual phenomena, such as coherent virtual absorption (CVA), virtual critical coupling, virtual gain, and PT-symmetry. In Section 3.1, I have demonstrated the analysis of CVA within dielectric structures, specifically focusing on the response of a dielectric slab coupled to scattering channels. The dynamics of the incident and scattered fields in the CVA regime are described, highlighting the complete scattering cancellation and energy storage within the slab without losses. Furthermore, I have reviewed the application of CVA in photonic integrated circuits, particularly for efficient pumping of microring resonators and releasing stored energy into waveguides with considerations for the non-linear Kerr effect on CVA behavior. In Section 3.2, I have shown that the concept of CVA in optical systems can be applied to achieve critical coupling, where incident wave energy fully couples to a cavity mode with no reflected or transmitted fields. Virtual critical coupling, achieved through complex frequency excitation, allows for optimal coupling without additional intrinsic losses, offering higher excitation efficiency than traditional monochromatic and critical coupling approaches at real frequencies. In Section 3.3, I have discussed the concept of virtual gain in passive PT-symmetrical systems when excited by exponentially decaying signals ($\omega'' < 0$). Such signals can lead to behavior resembling systems with actual gain, as observed in optical amplifiers and lasers. Virtual gain arises from the imbalance between incident and scattered field intensities at different time steps, allowing for the realization of PT-symmetrical systems in entirely passive configurations.

Coherent virtual excitation can be extended to a broader range of optical phenomena. In Appendix B I show that virtual gain can be used to obtain optical pulling force from a monochromatic plane wave at a complex frequency. In Appendix F, I reveal that the optical theorem can be revisited at a complex frequency in a completely passive system by demonstrating complete suppression of forward scattering with simultaneous preservation of high backward scattering.

Conclusion

In this thesis, Mie-resonant nanophotonic structures utilizing new optical phenomena, such as virtual excitation and bound states in the continuum, have been investigated. Owing to their strong magnetic response, high Q factors, reconfigurability of optical properties, and ability to manipulate the wavefront, Mie-resonant nanostructures have proven themselves as a sustainable and efficient platform for future nanophotonic devices, encompassing flat optics components, sensors with sensitivity down to single molecule level, and nanoscale light sources. These attributes of the Mie-resonant nanostructures have been exploited in the thesis to obtain unprecedented field enhancement in periodic dielectric gratings and Purcell enhancement in nanoantennas and microdisk resonators. Mie nanoparticles have been suggested for strong optical trapping and tunable nanophotonics. A new class of optical effects occurring under virtual excitation has been explored to achieve pulling optical force in the field of a plane wave and improve back-scattering beyond the bounds of the optical theorem.

Chapter 2 of the thesis has provided a thorough explanation of the theory of light-matter interactions and the theoretical methods applied throughout the study. The general equations of coupled mode theory have been derived and subsequently employed to explain various optical phenomena, including strong and weak coupling regimes in multiple oscillators, the Purcell effect, Fano resonances, and bound states in the continuum. Additionally, the derivation of Mie theory for spherical nanoparticles extended to the complex frequency plane has been presented. The extension of the Mie theory to complex frequencies has enabled a deeper understanding of the nature of Mie resonances, revealing their connection to quasinormal modes of the nanoparticles and predicting the effects that arise under virtual excitations. Furthermore, the fundamentals of optical forces acting on various nanostructures have been introduced to enhance the comprehension of these phenomena.

In Chapter 3, recent advances in Mie-tronics in application to wavefront engineering, sensing, tunable photonics, non-linear optics, and nanolasers have been reviewed. Thanks to the Kerker and Huygens effects appearing upon interference between electric and magnetic Mie resonances, Mie-resonant nanostructures have become a cornerstone in ultra-thin lenses and structural colors. The exceptional sharpness of the resonances, originating from bound states in the continuum, has opened a new era of optical sensors. Notably, refractometers utilizing Mie resonances have achieved remarkable sensitivity, surpassing 600 nm/RIU. Mie-resonant nanostructures have showcased their versatility through the manipulation of their properties by phase change, twistronics, and electro- and thermo-optical effects. Interestingly, semiconductor metasurfaces that support BICs have exhibited exceptional performance in high harmonic generation and non-linear wavefront manipulation. Semiconductor nanoparticles operating in the supercavity regime have demonstrated substantial non-linear signal generation, including up to the 7th harmonic. Mie-resonant structures have emerged as a promising platform for nanoscale lasers with low thresholds.

The definition of virtual phenomena induced by complex frequency excitation has been formulated in Chapter 4. An analysis of virtual absorption within resonant dielectric nanostructures with a specific focus on examining the response of a dielectric slab connected to scattering channels has been provided. The dynamics of both incident and scattered fields in the coherent virtual absorption regime has been elaborated upon, emphasizing the complete cancellation of scattering and energy storage within the slab without incurring losses. Additionally, the practical application of virtual absorption in photonic integrated circuits, particularly for pumping microring resonators, has been examined, and the dramatic impact of the non-linear Kerr effect on virtual absorption efficiency has been discussed. It has demonstrated that the concept of coherent virtual coupling in optical systems can be harnessed to achieve critical coupling, where incident wave energy fully couples to a cavity mode, suppressing reflected or transmitted fields. Virtual critical coupling, achieved through complex frequency excitation, has offered superior excitation efficiency compared to traditional monochromatic and critical coupling approaches at real frequencies. Also, Chapter 4 has introduced the concept of virtual gain appearing under excitations at complex frequencies with negative imaginary parts. The virtual gain has been explained by the disparity in incident and scattered field intensities at different time steps, enabling the realization of PT-symmetrical systems in entirely passive systems.

The Purcell enhancement of excitonic emission from transition metal dichalcogenide microdisk resonators and the Purcell enhancement of Raman signal in plasmonic nanostructures has been investigated. A micro-photoluminescence investigation of the microdisks has revealed emissivity spectra with various enhancement factors depending on the microdisk diameter. It has been shown that the microring with an optimal diameter of 2.2 m provides an enhancement factor of 100 compared to a bare flake. The numerical modeling confirmed by dark-field spectroscopy experiments has revealed that the enhancement is owing to whispery gallery modes localized in the microdisks. On the other hand, silver (plasmonic) dendritic nanostructures have demonstrated the enhancement factor of the field intensity of up to 170, resulting in a giant Raman signal amplification. The study has concerned spatially separated silver dendritic nanostructures synthesized in the pores of the ion-track template SiO_2/Si. The modeling of the electromagnetic wave interaction with the dendrites has indicated numerous “hotspots” occurring in places of intergrowth of the branches of the dendrites - the random distribution of “hotspots” on dendrites results in their broadened scattering spectrum. To sum up, the plasmonic nanostructures have exhibited larger Purcell enhancement than dielectric ones due to extremely small volumes of the plasmonic modes. However, it must be noticed that the electromagnetic contribution to emission amplification coexists with chemical contributions in the case of plasmonic nanostructures, which leads to higher overall signal enhancement.

A design of a tunable phase-change core-shell nanoparticle capable of reversibly switching between nanolaser and cloaking regimes has been proposed. The nanolaser utilizes a semiconductor nanoparticle with gain coated by a film of phase change material. The nanolaser has been theoretically demonstrated to switch between lasing and cloaking regimes at the same operating frequency. The cloaking phase of the nanostructure is linked to the anapole state. The operational characteristics of the nanolaser have been thoroughly studied. The nanolaser has shown thresholdless laser properties, lacking a noticeable kink in the input-light output curve due to the elevated betta and Purcell factors. Furthermore, a reconfigurable metasurface composed of lasing-cloaking metaatoms has been developed with the capability to switch from laser radiation to a non-scattering state reversibly. Additionally, phase-change material-based metasurfaces, recently proposed by Wang et al. and Zhang et al., have been examined in application to electrically tunable nanophotonic devices. Demonstration of electrically tunable phase-change metasurfaces represents an attractive prospect for reconfigurable holograms, diffractive optical elements, adaptive optics, and sensing. Based on GST nanostrips placed on a silver contact layer, Wang et al. have engineered a reflective metasurface that can turn into a perfect absorber with experimentally approved reflectance variation reaching 30%. Zhang et al. have proposed a large-scale metasurface that operates as a deflector in the amorphous phase, diffracting the incident beam into the 1st diffraction order and as a reflector in the crystalline phase. Both metasurfaces have been introduced to work in the reflection mode due to the metallic heater utilized for the phase switch. It limits the application of the proposed metasurfaces in the devices operating in the transmission regime. Another drawback that is suffered by the proposed approaches is the limited lifetime of the phase-change material-based devices. Although phase-change materials can handle millions of switching cycles, Wang et al. and Zhang et al. have reported 100 cycles at maximum, which is insufficient for the real-world applications.

A nanoparticle made of amorphous hydrogenated silicon with engineered bandgap coupled to photochromic spiropyran molecules has been proposed for tunable photonics exhibiting 70% tuning of the scattering peak intensity upon switching the photochromic molecules between transparent spiropyran and colored merocyanine states via optical radiation. Such a pronounced reconfiguration is owing to high-Q magnetic quadrupole states, efficiently excited in the hydrogenated silicon nanoparticles. The bandgap engineering has been used to suppress dissipation losses of silicon in the visible range. The bandgap of amorphous hydrogenated silicon nanoparticles can be tuned by changing the hydrogen concentration. Strong multipole Mie modes with Q-factors exceeding 100 in the visible and NIR regions appearing in such hydrogenated silicon open new opportunities to use nanostructures made of low-loss high-index materials for light manipulation, exploring light–matter interactions and tunable optical devices. Dielectric metasurfaces have been shown to approach the limit of electromagnetic field confinement dictated by plasmonic nanostructures. It has been revealed that the far-field polarization vortex in dielectric metasurfaces corresponding to a parametric off-Γ bound state in the continuum can migrate to the domain of waveguide modes crossing the light line, where it turns into the near-field polarization vortex featured by enhanced near-field localization and, therefore, better mode optical confinement. The improved optical confinement has been achieved through Fourier engineering of the Bloch mode, nullifying the dominant Fourier harmonic amplitude responsible for the near-field. The characteristic scale of the near-field localization for the predicted states has been increased several times compared to the conventional waveguide modes, reaching values up to $\sim \lambda/20$. In perspective, this value can be substantially decreased, beating the confinement in plasmonic structures, by canceling other Fourier harmonic responsible to the next orders of the near-field. However, such smart engineering requires additional degrees of freedom in the design of metasurfaces. It has been verified that this effect is preserved even in the presence of a substrate critical for practical applications. These findings can push the limits of dielectric optical devices requiring large optical mode confinement and efficient overlap of optical mode with thin layers like bio-analytes, 2D materials, and exciton layers. Besides, it has been shown that strong near-field coupling in Mie-resonant dielectric metasurfaces with a complex unit cell can result in an unusual order of magnetic moments resembling antiferromagnetic order in conventional crystals. Two types of resonant dielectric meta-atoms, nanodisks, and nanorings, have been considered, and the overall optical response has been revealed to depend on the mode hybridization and nanoparticle ordering.

Mie-resonant nanoparticles have been studied in application to optical levitodynamics, where they have demonstrated an ability to strongly modify optical potentials and enhance robust levitation over large size ranges. It has been found that the polarizability of silicon nanoparticles determines the optical forces that become tunable from positive to negative, similar to two-level atoms, simply by adjusting the trapping laser frequency with respect to the particle's size. Negative polarizabilities open up possibilities previously unknown to levitodynamics, such as the levitation in intensity minima. Moreover, Mie-resonant nanoparticles have shown 3 times higher mechanical frequencies, almost 2 orders of magnitude larger trap depths, and more than two orders of magnitude larger recoil heating rates compared to standard silica particles, making silicon nanoparticles an attractive alternative for more efficient trapping in optical traps based on counter-propagating beam geometry.

Finally, virtual optical forces and Kerker effects have been observed in Mie-resonant nanoparticles under complex frequency excitation. The common wisdom of the repulsive action of a plane wave on a dielectric slab and Mie nanoparticles has been revised by stepping out to the complex frequency plane and considering its dynamics upon complex excitations. It has been shown that tailoring the time evaluation of the light excitation field allows either enhancement of the repulsive force or achievement of pulling force for a passive resonator of arbitrary shape and composition. These effects have been linked to virtual gain and absorption effects considered in Chapter 4. The pulling optical force has been demonstrated for the Fabry–Perot cavity and a high-refractive-index dielectric nanoparticle. In the case of the Fabry–Perot cavity, the pulling optical force can exist in the complex frequency plane at the complex frequencies between the real frequency axis and quasinormal modes of the cavity. In the case of the Mie-resonant dielectric nanoparticle, the pulling force has been identified in the regions of virtual gain exceeding the scattering at complex frequencies, which appear when the imaginary part of the Mie amplitudes a_l and b_l is negative.

The opportunities that complex frequency excitations open for the scattered wavefront control and Kerker effects have been explored. The possibility to push apart the limitations imposed by optical theorem in passive nanostructures at real frequencies has been discovered at complex frequencies. High refractive index nanoparticles without gain under virtual excitation have manifested scattering signatures that would be impossible under monochromatic excitations, namely, back-scattering enhancement with almost complete cancellation of forward scattering. This unusual scattering regime appears in the zeros of forward scattering efficiency in the lower complex frequency half-plane and does not violate the optical theorem but requires generalization to the complex frequencies. Zero forward scattering has been observed theoretically, and near-zero forward scattering has been obtained numerically. The divergence between numerical and theoretical calculations has been explained by the impossibility of reaching a pure steady state for exponentially decaying signals. Investigation of the scattering regimes in the complex frequency has revealed regions with enhanced transverse Kerker effect, which appears when both forward and backward scattering are suppressed. Excitation of high-index nanoparticles at the complex frequencies of quasinormal modes has revealed significantly enhanced total scattering efficiency interpreted as a virtual lasing regime in a completely passive system.

To conclude, Mie-resonant nanostructures have garnered significant attention over the last decade, resulting in numerous proposals for nanophotonic devices for various applications, including photonic computing, sensing, spectroscopy, imaging, chemical catalysis, and photovoltaics. However, most of these proposals struggle to compete with well-established, mature technologies such as optical fibers in cost, fabrication quality, and efficiency. To make Mie-tronic approaches more practical and competitive, addressing the issue of losses is crucial. The losses can be suppressed by improving the quality of materials and the fabrication processes, and lowering the production costs can be achieved by transitioning to material platforms. Recent investigations push forward silicon nitride and crystalline silicon, as these materials promise negligible extinction and low surface roughness after manufacturing, mitigating overall losses [288,289]. These materials offer advantages such as minimal extinction and low surface roughness after manufacturing, which can help mitigate overall losses. Poor emission properties of these materials can be improved via doping with rare-earth materials, such as erbium and europium ions, which is now an extensively developing research field [290–292]. Doping with rare-earth materials has the potential to enable on-chip optical amplifiers [293], and when individual rare-earth atoms are coupled to photonic nanocavities, they can form the foundation for quantum networks and quantum computing [294].

Investigations of Mie resonances and their mutual interactions in high-index dielectric nanostructures have led to multitudinous discoveries of novel optical phenomena that can potentially improve nanophotonic devices. Bound states in the continuum have been introduced as a platform for the realization of ultra-high Q-factors approaching infinity, which are useful for optical detectors and strong light-matter interactions. Nevertheless, the best Q-factor that has been obtained so far in nanostructures supporting bound states in the continuum barely reaches 5×10^5 [131] which is inferior to the Q-factors of photonic crystal nanocavities [295] and microring resonators [296], well-established decades ago. Moreover, the Q-factor of bound states in the continuum strongly depends on the number of the metasurface unit cells, preventing in-plane miniaturization of these devices. On the other hand, nanobeam cavities require significant extension only in one direction and demonstrate more prominent Q-factors at smaller sizes [297]. Despite the recent demonstrations of Mie-tronic nanostructures supporting supercavity and anapole regimes boosting light-matter interactions, they cannot squeeze light as much as plasmonic nanoparticles. A combination of Mie-resonant photonics with recently developed designs of nanocavities with extreme dielectric confinement [298] can significantly improve Q-factors, electromagnetic mode volumes, and versatility of dielectric nanostructures.

Virtual optical phenomena represent an emerging branch of photonics that holds promise for applications requiring perfect absorption and electromagnetic energy storage. Notably, the concept of coherent virtual absorption has recently been experimentally confirmed in microwave photonics employed for plasma ignition [299], posing a significance of virtual phenomena for industrial applications. Virtual absorption has addressed the persistent issues in plasma ignition, like energy reflections and component damage, by enabling a reflection-free activation of a resonator, thus ensuring the full retention of the incoming energy during the activation process [299]. Furthermore, this innovative approach can be utilized for high-harmonic generation through the nonlinear conversion of the electromagnetic field stored within the cavity during virtual excitation. This technique appears to be a promising means to address the challenge of inefficient nonlinear conversion in nanoscale structures, a critical issue in nanophotonics. However, the experimental realization of this approach at optical frequencies may face obstacles due to the lack of suitably fast optical sources and modulators capable of generating exponentially growing or decaying optical signals.

Appendices

APPENDIX A

Paper 1: Topological enhancement of evanescent field localization in all-dielectric metasurfaces

---

In this manuscript, a new way to improve electromagnetic near-field localization in dielectric metasurfaces based on topological singularities is investigated. The manuscript is published.

The citations in the manuscript refer to reference list included at the end of the manuscript.

Work contributions by the present author: Analytical and numerical calculations, manuscript writing.

Reference information:

S. Lepeshov, M. Yesmantovich, and A. Bogdanov. Topological enhancement of evanescent field localization in all-dielectric metasurfaces. *Optica* 10, 797-800 (2023).

OPTICA

Topological enhancement of evanescent field localization in all-dielectric metasurfaces

SERGEY LEPESHOV,[1,*] MAKSIM YESMANTOVICH,[1] AND ANDREY BOGDANOV[1,2]

[1] *School of Physics and Engineering, ITMO University, Saint Petersburg, Russia*
[2] *Qingdao Innovation and Development Center, Harbin Engineering University, Qingdao, China*
**s.lepeshov@gmail.com*

Received 22 February 2023; revised 3 May 2023; accepted 14 May 2023; published 20 June 2023

Bound states in a continuum in periodic photonic structures can be described as topological defects in the *k*-space. These vortices can migrate within the Brillouin zone when the geometrical parameters of the system vary. In this study, we focus on the migration of the polarization vortex across the light line, from the radiation continuum to the waveguide mode domain. We found that during this transition, the far-field polarization vortex transforms into a near-field vortex. This near-field vortex is characterized by an enhanced localization of the evanescent field due to the vanishing fundamental Fourier harmonic of the Bloch amplitude. This mechanism can be used to improve polaritonic devices and optical sensors based on all-dielectric metasurfaces by increasing the overlap between optical modes and 2D excitons or thin layers of bioanalytes.

https://doi.org/10.1364/OPTICA.488420

All-dielectric nanophotonics has been established as a strong platform for a variety of applications spanning from wavefront control [1,2] and biosensing [3] to nonlinear optics [4] and quantum light sources [5], overshadowing plasmonics in many senses. The supremacy of all-dielectric nanostructures is provided by substantially lower losses in comparison with metals [6]. This allows one to achieve much higher quality factors (Q factors) in the visible and mid-infrared ranges. The radiative losses in dielectric nanostructures can be also substantially suppressed due to the high dielectric contrast, geometry optimization, or destructive interference effects like anapole [7,8] or bound states in the continuum [9,10].

However, despite the advantages of the dielectric nanostructures, they fundamentally provide worse electromagnetic field confinement than plasmonic structures [11]. Indeed, the optical modes of dielectric resonators occupy the whole volume of the resonator and a part of the adjacent space. In turn, metals support surface plasmon resonances that can be localized extremely well. Such a unique ability of plasmonics has been utilized for deep subwavelength waveguides [12], terahertz (THz) photonics [13], optical biosensing [14,15], enhancement of the Purcell effect [16], or even for picoscale light confinement [17]. Thus, the fact that plasmonic structures provide much better confinement than their dielectric counterparts is considered dogma.

In this Letter, we demonstrate that light can be highly localized in dielectric periodic structures by exploiting the vanishing fundamental Fourier harmonic of the Bloch eigenmode [18]. Even in low-contrast dielectrics, spatial localization of the near field can reach values around $(D/2\pi)$ in structures with a subwavelength period $(D \ll \lambda)$. Our approach draws inspiration from bound states in the continuum (BICs), which are non-radiating electromagnetic states with a diverging radiative Q factor [9,10,19]. These BICs can be regarded as topological defects—a polarization vortex capable of migrating in k-space while maintaining structure symmetry [20–22]. Figure 1(a) schematically shows how a parametric off-BIC in a dielectric grating moves along the dispersion curve to the domain of waveguide modes, crossing the light line as the grating height increases, where it turns into a near-field polarization vortex. Moreover, by nullifying the dominant Fourier harmonic of the Bloch mode, we enhance the spatial localization of the mode. Figure 1(b) illustrates the characteristic field localization for a conventional guided mode of the grating (left panel) and the guided mode corresponding to the BIC moved under the light line. Both modes decay exponentially as $e^{-\kappa z}$ but with different characteristic localization scales defined as $h = 1/\kappa$. For the conventional guided mode, the minimal $h \approx \lambda/(2\pi\sqrt{\delta\varepsilon})$, while for the mode with enhanced localization, the minimal $h \approx D/2\pi$. Thus, even in low-contrast dielectrics, the electromagnetic field can be localized at the nanoscale for small periods D.

To gain deeper insight into the mechanism of the enhanced localization and its topological nature, we consider, for instance, a TE-polarized mode of a dielectric grating [see Fig. 1(b)]. The grating consists of infinitely long rectangular bars made of lossless dielectric with permittivity $\varepsilon = 9.86$ that corresponds, for example, to gallium phosphide (GaP) for the wavelength $\lambda = 900$ nm. The period of the grating $D = 270$ nm, the width of the bars $w = 160$ nm, and the height of the structure H varies from 350 to 410 nm. The electric field $\mathbf{E}$ of TE-polarized modes has only y component $E_y(x, y, z)$ that can be expanded into the Fourier series as follows [20]:

$$E_y(x, y, z) = \sum_{n=-\infty}^{\infty} E_y^{(n)} e^{i(k_x+G_n)x} e^{-\kappa_n z} e^{i k_y y}. \tag{1}$$

Here, k_x is the Bloch wavenumber, $G_n = 2\pi n/D$ is the reciprocal lattice vector, $E_y^{(n)}$ is the Fourier amplitude corresponding to the nth Fourier harmonic, and

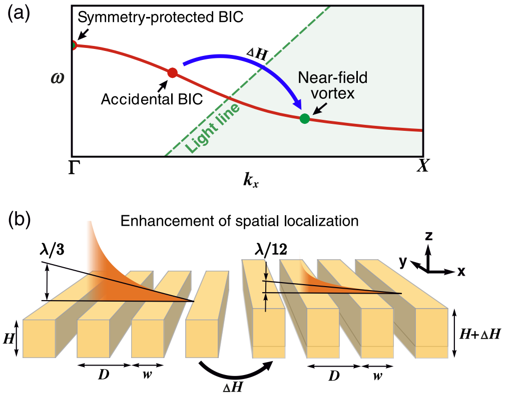

Fig. 1. (a) Dispersion diagram of the BIC mode. The red dots represent the BICs/topological charges of the initial grating. The green dots correspond to the topological charges of the modified grating. (b) Illustration of the concept of the electric field confinement factor boosting in all-dielectric grating by tuning of the grating height.

$$\kappa_n = \sqrt{(k_x + G_n)^2 + k_y^2 - k_0^2}, \qquad (2)$$

where k_0 is the vacuum wavenumber and k_y is the wavevector component along the bars. An integer n encodes the diffraction channels. If κ_n is imaginary, then the nth channel is open (the field propagates along z) and vice versa. For subwavelength structures, there is only one open diffraction channel corresponding to $n = 0$. All other Fourier harmonics contribute to the near field. For the BIC, the complex amplitude of the only open diffraction channel vanishes, i.e., $E_y^{(0)} = 0$, and its spatial localization is defined by the next non-0th Fourier harmonics, namely, by $E_y^{(-1)}$ if $k_x > 0$ or by $E_y^{(+1)}$ if $k_x < 0$. Figure 2(a) shows the dispersion of several TE eigenmodes of the grating with $H = 350$ nm for $k_y = 0$. The dispersion of the eigenmode under consideration is shown with a bold red curve. This mode supports two BICs: (i) symmetry protected at-Γ BIC (point I) and (ii) parametric off-Γ BIC (point II). The BICs are clearly seen in Fig. 2(b) as diverging singularities of the radiative Q factor. The distribution of the electric field of the BICs, leaky mode, and waveguide mode are shown in Fig. 2(c). One can observe that the BICs have much better optical confinement than leaky and waveguide modes. This can be understood from Eq. (1). Indeed, for the symmetry-protected and parametric BICs, the near field behaves as $e^{-\kappa_{(-1)}z}$, while for the leaky and guided modes it behaves as $e^{-\kappa_0 z}$. Besides, the electric field of the mode endures a transformation from an odd (i) to even (iv) configuration [23]. This effect appears due to the Friedrich–Wintgen coupling between the odd and even modes resulting in the formation of the non-radiating BIC and a high-leaky mode [24]. The evolution of the electric field profiles of these modes is shown in the Supplement 1 (Fig. S1).

Figure 3(a) shows the dependence of $|E_y^{(0)}|^2$ calculated in the far-field zone as a function of k_x at the distance of several λ from the grating interface. At the points corresponding to BICs, the 0th Fourier harmonics responsible for the leakage vanishes, i.e., $E_y^{(0)} = 0$. For the leaky modes with a complex k_0, these harmonics contribute to both near and far fields. The overgrowth of $E_y^{(0)}$ for the k_x close to k_0 means that the leaky mode becomes weakly localized in the vicinity of the light line, i.e., $\kappa_0 \to 0$ as $k_x \to k_0$. Figure 3(b) shows the dependence of several Fourier amplitudes $|E_y^{(n)}|^2$ for $n = 0, \pm 1$ calculated at the interface of the grating. At the Γ point, the energy of the mode is equally distributed between the harmonics with $n = \pm 1$ as the BIC is formed by the anti-symmetric combination of two counterpropagating waveguide modes. One can conclude the same for the band-edge state when $k_x = \pm\pi/D$. However, for the BIC, the main part of the energy is stored in the harmonics $n = \pm 1$.

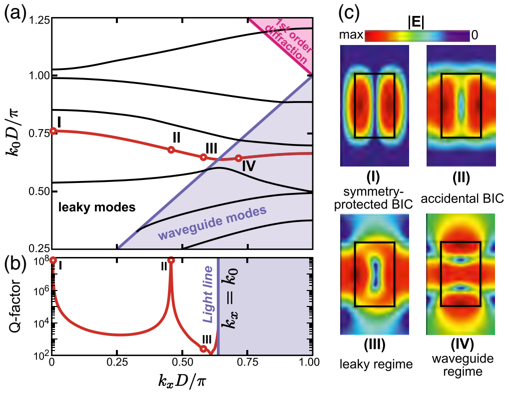

Fig. 2. (a) Band structure of the TE modes of the considered grating in dimensionless units. The red curve denotes the mode with BIC. (b) Dispersion of the Q factor of the BIC mode. Points (I) and (II) are related to symmetry-protected and accidental BIC, respectively, (III) corresponds to the leaky regime, and (IV) to the waveguide regime. (c) Electric field distributions in each of the four regimes of the BIC mode.

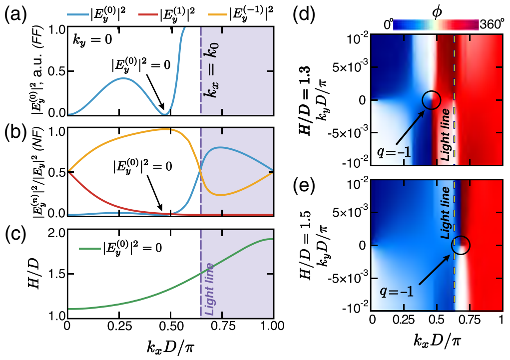

Fig. 3. (a) Dispersion of the 0th Fourier term $|E_y^{(0)}|^2$ in arbitrary units calculated in the far-field zone. (b) Dispersion of the 0th $|E_y^{(0)}|^2$, 1st $|E_y^{(1)}|^2$, and 2nd $|E_y^{(2)}|^2$ Fourier terms calculated in the near-field zone. (c) The aspect ratio of the grating H/D with respect to the location of the zero of $|E_y^{(0)}|^2$ at the dispersion diagram. The violet area denotes the zone below the light line (waveguide regime of the mode). Phase maps of the polarization vector $(E_x^{(0)}, E_y^{(0)})$ calculated in the first Brillouin zone (d) in the case of $|E_y^{(0)}|^2$ zero located in the leaky mode zone $(H/D = 1.3)$ and (e) in the case of $|E_y^{(0)}|^2$ zero located in the waveguide mode zone $(H/D = 1.5)$.

The position of the parametric off-Γ BIC in the k-space is very sensitive to the geometrical parameters of the grating. Figure 3(c) shows the dependence of the Bloch wavenumber k_x for which

$|E_y^{(0)}|^2 = 0$ as a function of the aspect ratio H/D. One can see that for $H/D \approx 1.1$, the parametric BIC becomes close to the symmetry-protected one, forming the merging BIC [25], while for $H/D = 1.5$ and $k_x D/\pi = 0.65$, the BIC crosses the light line turning into a specific waveguide mode, in which the amplitude of the 0th Fourier harmonic is zero. Of course, the BIC cannot be defined under the light line, as all the modes in this domain are non-leaky. On the other hand, BICs is a polarization vortex around the point in the k-space at which the coupling constant (zero-order Fourier amplitude of the Bloch mode) with the radiation continuum vanishes. The *topological charge* q (winding number) can be formally defined the same way in any point of the k-space both under and above the light line as follows [20]:

$$q = \frac{1}{2\pi} \oint_C \mathrm{d}\mathbf{k} \cdot \nabla_{\mathbf{k}} \phi(\mathbf{k}), \quad q \in \mathbb{Z}. \tag{3}$$

Here, $\phi(\boldsymbol{k}) = \arg[E_x^{(0)}(\boldsymbol{k}) + i E_y^{(0)}(\boldsymbol{k})]$, where $\boldsymbol{k} = (k_x, k_y)$, and C is a simple counterclockwise-oriented path enclosing the singular point. Figure 3(d) shows the map of ϕ for the considered band for the grating with aspect ratio $H/D = 1.3$. One can see that the phase incursion around the point corresponding to the BIC is -2π, i.e., the topological charge $q = -1$. The same map but for the case in which the BIC is moved under the light line ($H/D = 1.5$) is plotted in Fig. 3(e). The phase map shows that the topological singularity corresponding to the vanishing 0th Fourier amplitude still exists under the light line and it can be characterized by topological charge defined by Eq. (3). Therefore, the topological singularity in the far-field polarization corresponding to BIC turns into the *near-field polarization vortex* under the light line featured by the enhanced localization of the evanescent field. Conversely, the near-field polarization vortex under the light line can be transformed to a far-field vortex and experimentally resolved by means of leakage radiation microscopy [26,27]. The near-field distribution of the polarization vector in the k-space around the topological singularity is shown in Fig. S2 in the Supplement 1.

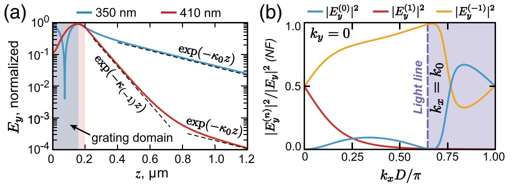

Fig. 4. (a) Normalized z-dependence of E_y calculated at the symmetry plane cross section of the grating for $H = 350$ nm (blue) and $H = 410$ nm (red) in logarithmic scale. The black dashed lines show asymptotes corresponding to $e^{-\kappa_0 z}$ and $e^{-\kappa_{(-1)} z}$ terms. (b) Dispersion of the 0th $|E_y^{(0)}|^2$, 1st $|E_y^{(1)}|^2$, and 2nd $|E_y^{(2)}|^2$ Fourier terms calculated in the near-field zone for $H = 410$ nm.

To demonstrate explicitly the enhancement of near-field localization, we plot the normalized electric field distribution $E_y(z)$ for the same waveguide mode at $k_x D/\pi = 0.67$ in two gratings with $H = 350$ nm (blue curve) and 410 nm (red curve) [Fig. 4(a)]. It can be seen that the field decays as $e^{-\kappa_{(-1)} z}$ for the case of $H = 410$ nm, while it decays $e^{-\kappa_0 z}$ for $H = 350$ nm. The spectra of the Fourier components $E_y^{(n)}$ plotted in Fig. 4(b) for $H = 410$ nm confirm that the enhanced field localization appear due to the vanishing Fourier component $E_y^{(0)}$ at $k_x D/\pi = 0.67$. The dependence of the inverse localization length κ on k_x reveals two local maxima at the Γ point associated with the symmetry-protected BIC and at the topological singularity under the light line (see Fig. S3, Supplement 1). The direct analytical calculation using Eq. (2) gives the characteristic localization length $1/\kappa \approx \lambda/2.8$ for $H = 350$ nm and $1/\kappa \approx \lambda/12$ for $H = 410$ nm, i.e., more than fourfold increase of the localization. One should note that far from the structure, the asymptotics of the electric field for $H = 410$ nm change from $e^{-\kappa_{(-1)} z}$ to $e^{-\kappa_0 z}$, even though the 0th Fourier coefficient should vanish. The discrepancy is explained by the fact that the regime of the enhanced localization as well as the BIC is achieved only in one point of the dispersion curve, and we can only approach this point in the numerical simulations. Therefore, the asymptotics $e^{-\kappa_0 z}$ always appear at large distances from the structure. The proposed mechanism of localization works better in the vicinity of the light line while at the band edge, the 0th and -1st Fourier coefficients are of the same order [see Fig. 3(b)], and therefore no essential improvement of the confinement is observed (Fig. S3, Supplement 1).

Finally, we consider a realistic case when the GaP grating ($n = 3.05$) is on top of a transparent quartz substrate ($n = 1.45$) [28,29]. We consider two gratings with the same period $D = 270$ nm and width of the bars $w = 160$ nm but with different heights of the bars $H = 350$ and 410 nm. The dispersion of the same TE-polarized mode in these gratings is shown in Fig. 5(a). The substrate crucially affects the parametric off-Γ BIC breaking the up-down symmetry. The radiation losses into both substrate and air cannot be eliminated simultaneously due to broken up-down symmetry [30]. However, the complete suppression of the radiation losses in one half-space is possible by the adjustment of geometrical parameters of the structure. It results in the appearance of guided resonances with unidirectional leakage [31].

At $H = 350$ nm, we find the maximum of the radiative Q factor at $k_x \approx 0.47\pi/D$ [blue curve in Fig. 5(b)] between the minima of losses into the substrate and air, which are separated in the k-space (for details, see Supplement 1, Fig. S4). The observed loss minima are the consequence of the divided topological subcharges. For $H = 410$ nm, the minima and associated subcharges move under the light line of air [gray area in Fig. 5(a)]. In this region of the k-space, a genuine off-Γ BIC is possible, as the radiation to air is forbidden due to total internal reflection and therefore only one radiation loss channel is open. Remarkably, the subcharges of the substrate converge into a whole integer charge (Supplement 1, Fig. S4). This occurs even if the grating parameters are not intentionally optimized. The sharp maximum of the Q factor for $H = 410$ nm in Fig. 5(b) corresponds to the genuine off-Γ BIC characterized by the enhanced optical confinement.

In practice, the BIC shown in Fig. 5(b) can be excited from the far field in the finite grating due to the diffraction of the incident light on its edge. The experimental scheme is shown in Fig. 5(b). For the numerical experiment, we consider a finite length GaP grating on SiO_2 substrate consisting of 200 periods. The period, width, and height of the grating are the same as in the infinite case analyzed in Figs. 5(a) and 5(b). The grating is excited by a linearly polarized Gaussian beam with the beam waist $w_0 = 3$ μm [see Fig. 5(c)]. The Gaussian beam falls onto the edge of the grating to ensure the excitation of the modes with large $k_x \sim \pi/D$. The selection of the excited modes by k_x is made by choosing the proper frequency taken from the eigenfrequency dispersion [Fig. 5(a)]. The Gaussian beam is polarized along the y direction (TE polarization). The electric field distributions obtained for $H = 350$ nm

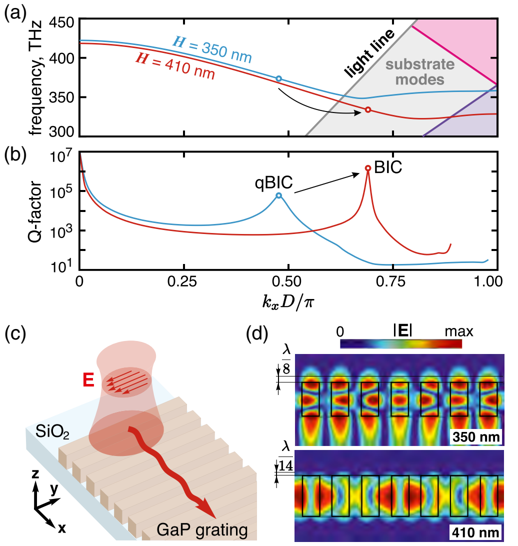

Fig. 5. (a) Frequency and (b) Q factor dispersions of the GaP grating on a quartz substrate calculated for $H = 350$ nm (blue) and $H = 410$ nm (red). Dots on the dispersion diagrams represent quasi-accidental BIC. The black arrow denotes the migration of the accidental quasi-BIC from the leaky mode regime (white zone) to substrate modes (gray zone). (c) Illustration of the concept of Gaussian beam excitation of the waveguide modes in the finite grating. (d) Electric field distribution of the waveguide modes in the finite grating for $H = 350$ nm (top) and $H = 410$ nm (bottom).

and $H = 410$ nm coincide well with the results of the eigenmode calculation for the infinite grating [Fig. 4(b)] and demonstrate the boost of the electric field confinement by tuning the grating height from 350 to 410 nm. The estimated electric field extinction lengths are $\lambda/8$ for 350 nm height and $\lambda/14$ for 410 nm height.

To conclude, we have demonstrated that the far-field polarization vortex in dielectric metasurfaces can be transformed into a near-field polarization vortex with enhanced near-field localization and improved mode optical confinement. This is achieved through Fourier engineering of the Bloch mode, nullifying the dominant Fourier harmonic amplitude responsible for the near field. The scale of near-field localization can be increased by several times compared to conventional waveguide modes, up to a value of $\sim\lambda/10$. In perspective, this value can be substantially decreased approaching confinement in plasmonic structures by using smart optimization of the unit cell [32], machine learning algorithms [33], and Fourier component design of the dielectric permittivity [34].

Acknowledgment. A.B. acknowledges support of the MSHERF (Project 075-15-2021-589).

Disclosures. The authors declare no conflicts of interest.

Data availability. All relevant data are presented in the paper and Supplementary Information. Additional data related to this paper may be requested from the authors.

Supplemental document. See Supplement 1 for supporting content.

REFERENCES AND NOTES

1. S. M. Kamali, E. Arbabi, A. Arbabi, and A. Faraon, Nanophotonics **7**, 1041 (2018).
2. L. Wang, S. Kruk, K. Koshelev, I. Kravchenko, B. Luther-Davies, and Y. Kivshar, Nano Lett. **18**, 3978 (2018).
3. A. Tittl, A. Leitis, M. Liu, F. Yesilkoy, D.-Y. Choi, D. N. Neshev, Y. S. Kivshar, and H. Altug, Science **360**, 1105 (2018).
4. A. Krasnok, M. Tymchenko, and A. Alù, Mater. Today **21**(1), 8 (2018).
5. A. S. Solntsev, G. S. Agarwal, and Y. S. Kivshar, Nat. Photonics **15**, 327 (2021).
6. D. G. Baranov, D. A. Zuev, S. I. Lepeshov, O. V. Kotov, A. E. Krasnok, A. B. Evlyukhin, and B. N. Chichkov, Optica **4**, 814 (2017).
7. A. E. Miroshnichenko, A. B. Evlyukhin, Y. F. Yu, R. M. Bakker, A. Chipouline, A. I. Kuznetsov, B. Luk'yanchuk, B. N. Chichkov, and Y. S. Kivshar, Nat. Commun. **6**, 8069 (2015).
8. Y. Yang and S. I. Bozhevolnyi, Nanotechnology **30**, 204001 (2019).
9. C. W. Hsu, B. Zhen, A. D. Stone, J. D. Joannopoulos, and M. Soljačić, Nat. Rev. Mater. **1**, 16048 (2016).
10. K. Koshelev, A. Bogdanov, and Y. Kivshar, Sci. Bull. **64**(12), 836 (2019).
11. B. Lee, I.-M. Lee, S. Kim, D.-H. Oh, and L. Hesselink, J. Mod. Opt. **57**, 1479 (2010).
12. S. I. Bozhevolnyi, V. S. Volkov, E. Devaux, J.-Y. Laluet, and T. W. Ebbesen, Nature **440**, 508 (2006).
13. A. Ahmadivand, B. Gerislioglu, R. Ahuja, and Y. Kumar Mishra, Mater. Today **32**, 108 (2020).
14. J. R. Mejía-Salazar and O. N. Oliveira, Chem. Rev. **118**, 10617 (2018).
15. J. N. Anker, W. P. Hall, O. Lyandres, N. C. Shah, J. Zhao, and R. P. Van Duyne, in *Nanoscience and Technology* (Co-Published with Macmillan, 2009), pp. 308–319.
16. G. M. Akselrod, C. Argyropoulos, T. B. Hoang, C. Ciracì, C. Fang, J. Huang, D. R. Smith, and M. H. Mikkelsen, Nat. Photonics **8**, 835 (2014).
17. H. Cang, Y. Liu, Y. Wang, X. Yin, and X. Zhang, Nano Lett. **13**, 5949 (2013).
18. Here and throughout the text, localization means optical confinement, i.e., localization along the out-of-plane direction.
19. W. Liu, B. Wang, Y. Zhang, J. Wang, M. Zhao, F. Guan, X. Liu, L. Shi, and J. Zi, Phys. Rev. Lett. **123**, 116104 (2019).
20. B. Zhen, C. W. Hsu, L. Lu, A. D. Stone, and M. Soljačič, Phys. Rev. Lett. **113**, 257401 (2014).
21. E. N. Bulgakov and D. N. Maksimov, Phys. Rev. A **96**, 063833 (2017).
22. P. Hu, J. Wang, Q. Jiang, J. Wang, L. Shi, D. Han, Z.-Q. Zhang, C. T. Chan, and J. Zi, Optica **9**, 1353 (2022).
23. We define parity of the mode with respect to the reflection from the *x*–*z*-symmetry plane of the unit cell.
24. H. Friedrich and D. Wintgen, Phys. Rev. A **32**, 3231 (1985).
25. J. Jin, X. Yin, L. Ni, M. Soljačić, B. Zhen, and C. Peng, Nature **574**, 501 (2019).
26. A. Drezet, A. Hohenau, D. Koller, A. Stepanov, H. Ditlbacher, B. Steinberger, F. R. Aussenegg, A. Leitner, and J. R. Krenn, Mater. Sci. Eng., B **149**, 220 (2008).
27. Y. Zhang, A. Chen, W. Liu, C. W. Hsu, B. Wang, F. Guan, X. Liu, L. Shi, L. Lu, and J. Zi, Phys. Rev. Lett. **120**, 186103 (2018).
28. D. Khmelevskaia, D. Markina, V. Fedorov, G. Ermolaev, A. Arsenin, V. Volkov, A. Goltaev, Y. M. Zadiranov, I. Tzibizov, A. Pushkarev, A. K. Samusev, A. K. Samusev, A. A. Shcherbakov, P. A. Belov, I. S. Mukhin, and S. V. Makarov, Appl. Phys. Lett. **118**, 201101 (2021).
29. G. Ghosh, Opt. Commun. **163**, 95 (1999).
30. C. W. Hsu, B. Zhen, J. Lee, S.-L. Chua, S. G. Johnson, J. D. Joannopoulos, and M. Soljačić, Nature **499**, 188 (2013).
31. X. Yin, J. Jin, M. Soljačić, C. Peng, and B. Zhen, Nature **580**, 467 (2020).
32. K. Y. Lee, S. Yoon, S. H. Song, and J. W. Yoon, Sci. Adv. **8**, eadd8349 (2022).
33. P. R. Wiecha, A. Arbouet, C. Girard, and O. L. Muskens, Photon. Res. **9**, B182 (2021).
34. S.-G. Lee, S.-H. Kim, and C.-S. Kee, Phys. Rev. Lett. **126**, 013601 (2021).

APPENDIX B

Paper 2: Virtual optical pulling force

Pulling optical force induced by plane waves with exponentially decaying temporal profile is theoretically observed. The manuscript is published.

The citations in the manuscript refer to reference list included at the end of the manuscript.

Work contributions by the present author: Analytical and numerical calculations, manuscript writing.

Reference information:

S. Lepeshov and A. Krasnok. Virtual optical pulling force. *Optica* 7, 1024-1030 (2020).

optica

Virtual optical pulling force

Sergey Lepeshov[1] **and Alex Krasnok**[2,*]

[1]ITMO University, St. Petersburg 197101, Russia
[2]Photonics Initiative, Advanced Science Research Center, City University of New York, New York, New York 10031, USA
*Corresponding author: akrasnok@gc.cuny.edu

Received 16 March 2020; revised 15 June 2020; accepted 14 July 2020 (Doc. ID 391569); published 17 August 2020

Progress in light scattering engineering made it feasible to develop optical tweezers allowing capture, hold, and controllable displacement of submicrometer-size particles and biological structures. However, the momentum conservation law imposes a fundamental restriction on the optical pressure to be repulsive in paraxial fields, which severely limits the capabilities of optomechanical control, e.g., preventing attractive force acting on sufficiently subwavelength particles and molecules. Herein, we revisit the issue of optical forces by their analytic continuation to the complex frequency plane and considering their behavior in the transient regime. We show that the exponential excitation at the complex frequency offers an intriguing ability to achieve a pulling force for a passive resonant object of any shape and composition, even in the paraxial approximation. The approach is elucidated on a dielectric Fabry–Perot cavity and a high-refractive-index dielectric nanoparticle, a fruitful platform for intracellular spectroscopy and lab-on-a-chip technologies, where the proposed technique may find unprecedented capabilities.

https://doi.org/10.1364/OPTICA.391569

1. INTRODUCTION

Light scattering is ubiquitous and plays an essential role in the study of nature and conquering light–matter interactions for modern technologies. According to Einstein [1,2], the light quanta (photons) carry the energy $\hbar\omega_0$ and momentum $\hbar\mathbf{k}$, where ω_0 and $|\mathbf{k}| = \omega/c$ are the frequency and wavenumber of a photon, $\hbar$ is the reduced Planck's constant, and c is the speed of light. Hence, every act of light scattering, when a photon changes its direction (or disappears by absorption), is accompanied by a transition of a portion of its momentum to the object. If the object is light enough and the photon momentum flux ($N\hbar\mathbf{k}$, N is the photon density) is large enough, this momentum transition can be detected through a mechanical motion of the object as was done for the first time by Lebedev [3] and Nichols [4]. In the early years, this phenomenon helped to establish the theory of light, but after the work of Arthur Ashkin [5–7], optical forces became a powerful catalyst for modern technologies. Namely, it has been shown that optical scattering allows control of the position of small objects using only electromagnetic forces. In such techniques, the intensity gradient force is applied to trap an object in the lateral plane, whereas the radiation pressure allows control of the object's position along the beam. Today, this laser trapping has become routine for different kinds of optical spectroscopy of single particles and living cells, optical tweezers [8–10], optical binding [11], laser cooling, and lab-on-a-chip technologies, to name just a few [12].

In the paraxial approximation, when the size of the object is small enough, and the beam is unfocused, the intensity gradient over the object size vanishes, and the radiation pressure plays the key role. This case is very important because, for example, for essentially subwave objects (molecules, quantum dots, nanoparticles), it is challenging to achieve strong gradients in freely propagating fields, and the paraxial approximation is inevitable. In this approximation, the momentum conservation law imposes a fundamental restriction on the optical pressure to be repulsive. Indeed, the momentum flux of the scattered light along the wavevector of incident light ($\mathbf{k}_i$) in a passive system is always smaller than the incident momentum flux through the object's surface. In fact, it can be rigorously shown that the optical pulling force is forbidden for a passive object of any shape or composition in a paraxial field [13]. Although different approaches to get around this fundamental restriction have been suggested [14], all of them rely on structuring the incident field [13,15–20], utilizing gain media [21–24], or on modifying the surroundings of the manipulated object [25–28], and hence they require either complex techniques or operate at certain conditions. Note also that negative optical torque is another related area of significant interest today [29,30].

In this work, we revisit the issue of optical forces by stepping out to the complex frequency plane ($\omega = \omega' + i\omega''$) and considering its dynamics upon excitations not amenable to Fourier transformation. We show that tailoring of the time evolution of the light excitation field allows either *enhancement of the repulsive force* or *achievement of pulling force for a passive resonator of arbitrary shape and composition*. This unusual response is caused by the "*virtual absorption*" and "*virtual gain*" effects described in the following. Recently, a similar approach has been suggested to achieve perfect light storage [31], virtual critical coupling [32], virtual parity-time symmetry (PT-symmetry) and associated effects [33], and it has been demonstrated experimentally for acoustic waves [34].

2. CONCEPT

The radiation pressure is obliged to be repulsive in any passive system in the paraxial approximation [13]. For example, consider the case of radiation pressure acting on a dielectric slab [Fig. 1(A)] lit by a monochromatic incident wave with the photon density per unit square and time duration $N_i = c\varepsilon_0 E_0^2/2\hbar\omega$, where E_0^2 is the electric field intensity and ε_0 is the electric constant. This incident light carries the momentum density $N_i\hbar k = N_i\hbar\omega/c$. A part of this momentum gets transmitted through the slab ($TN_i\hbar k$), and another part gets reflected towards the source ($RN_i\hbar k$), with T and R being the transmission and reflection coefficients, respectively. The total pressure on the slab is the vector sum of all these momentum flux densities [35]:

$$F(\omega) = N_i\hbar k[1 + R(\omega) - T(\omega)]. \tag{1}$$

This equation can be rigorously derived from Maxwell's stress tensor approach [35]. For passive media ($R, T \leq 1$), $1 + R > T$, and hence the total pressure is always directed towards beam propagation (positive). Also, for a given reflection, reducing the transmission through dissipation leads to an increase of the pushing force. In the blackbody ($R = 0,\ T = 0$) and perfect reflection ($R = 1,\ T = 0$) cases, this formula gives $F = N_i\hbar k$ and $F = 2N_i\hbar k$, respectively.

We stress that Eq. (1) is a definition of an optical pressure force as a total momentum flow through the surface of a body requires knowledge only T and R. All the processes that take place inside the body are taken into account automatically via transmission and reflection coefficients. This approach is fair not only in the frequency domain but also in the transient regime at any time instant and does not require time averaging. Hence, it can be analytically continued to the complex plane (a special case of a transient regime), which is essential for the following discussion.

Unlike the real frequency axis, where the scattering matrix ($\hat{S}$) of a passive structure and its eigenvalues (λ_i) are bound to $|\lambda_i|^2 \leq 1$ ($|\lambda_i|^2 = 1$ in the Hermitian lossless case), in the complex frequency plane ($\omega = \omega' + i\omega''$), they can take any value between 0 (scattering zero) and ∞ (scattering pole) [36]. Interestingly, knowledge of these poles in the complex plane allows retrieval of all (linear) electromagnetic properties of the structure via the Weierstrass theorem [37]. As a result, the complex continuation of scattering amplitudes (for example, T and R, in the 1D scenario) can also take any value ($|R, T| > 1$). This complex continuation lifts the discussed restriction on optical forces and makes the structure dynamics less trivial, which opens up many opportunities as discussed in what follows.

For example, let us consider this two-port system (Fig. 1) under exponentially growing excitation [$E_i(t) \propto E_0 \exp(\omega'' t)\exp(i\omega' t)$] [Fig. 1(B)]. In this case, as the incoming signal grows in time faster than the decay rate of the cavity, the incoming signal $|E_i|$ and the momentum flux density ($c\varepsilon_0\hbar k|E_i|^2/2\hbar\omega$) can be greater than the corresponding outgoing signal ($|E_t| + |E_r|$) and momentum [$c\varepsilon_0\hbar k(|E_t|^2 + |E_r|^2)/2\hbar\omega$], even in the lossless case. The remaining part of the signal, which is neither reflected nor transmitted, gets stored in the cavity (virtual loss) until the incoming signal keeps the exponential growth. In this case $1 - T(\omega', \omega'') - R(\omega', \omega'') = A > 0$, and the optical pressure can be increased. Here A denotes the stored energy in the object (cavity). Note that this idea of virtual absorption has been suggested in Ref. [31] for perfect energy capture in a resonant cavity for a long time and for release on-demand. This effect turned out to be very promising and found application in many areas [31–33]; it was experimentally realized in Ref. [34] for elastodynamic waves. In the present work, we show that the virtual absorption effect gives a real contribution to the optical radiation pressure and can be utilized for all-optical manipulation.

Further, if the incoming signal exponentially decays faster than the cavity decay rate, the output signal $|E_t| + |E_r|$ [along with the momentum flux density ($c\varepsilon_0\hbar k(|E_t|^2 + |E_r|^2)/2\hbar\omega$)] can be *greater than the input one* [Fig. 1(C)]. In this case, the stored energy becomes effectively "negative," and $1 - T - R = A < 0$, as one would have in a system with a real gain. We refer to this effect as "virtual gain," prove it in the following with analytical and numerical calculations, and demonstrate how it can give rise to negative optical pressure. Note that this complex excitation with negative imaginary frequency has been recently utilized for imaging devices [38] and a virtual PT-symmetry effect [33]. It worth noting that,

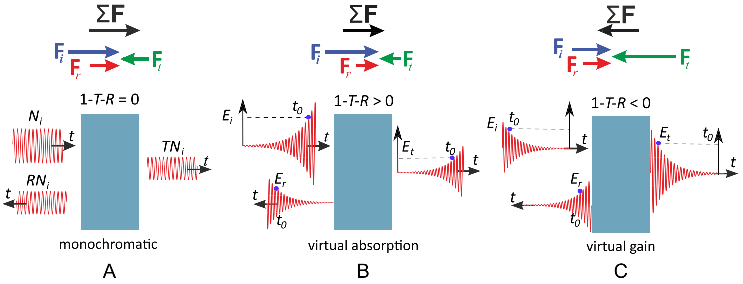

Fig. 1. (A) Schematic of light scattering from a (lossless) dielectric slab. The vector sum of all momenta gives the optical pressure $F = N_i\hbar k(1 + R - T) > 0$. (B) Virtual absorption. As the incoming signal grows in time exponentially faster than the decay rate of the cavity, the incoming signal $|E_i|$ can be greater than outgoing signals $|E_t| + |E_r|$, even in the lossless case. The remaining part of the signal, which is neither reflected nor transmitted, gets stored within the cavity (virtual loss) until the incoming signal keeps the exponential growth. In this case, $1 - T - R > 0$, and the optical pressure can be increased. (C) Virtual gain. As the incoming signal exponentially decays faster than the cavity decay rate, the output signal $|E_t| + |E_r|$ can be greater than the input one, giving rise to the gain behavior. In this case, $1 - T - R < 0$, and the optical pressure can become negative. Top: a sketch of partial forces acting in the system (blue and red arrows) as well as how these forces contribute to the resultant force (green arrow) in each case.

technically, the negative virtual pulling force is equivalent to the appearance of an additional gradient force pointing backward and caused by the exponential decay of the plane wave in time.

3. RESULTS AND DISCUSSION

To elucidate this concept, let us first consider the case of a dielectric slab with dispersionless permittivity $\varepsilon = 40$ (Fig. 2). All results are presented in dimensionless frequencies to make the discussion independent of the frequency range. The actual thickness of the slab in our calculations was 500 nm. The transmission and reflection coefficients in the complex plane [Figs. 2(A) and 2(B)], have nontrivial dependence with poles in the lower half-plane. Such poles are an immutable attribute of any resonant structures and are associated with the modes of the structure [39]. It worth noting that the characteristic decay time of a mode is determined by the position of the corresponding pole, $\tau = 1/\omega''$. The reflection coefficient also possesses zeros, associated with the tunneling effect [$R = 0$, $T = 1$ at the real axis] at the Fabry–Perot resonances.

The results of the calculation of the virtual absorption parameter $A(\omega', \omega'') = 1 - R(\omega', \omega'') - T(\omega', \omega'')$ in the complex frequency plane are presented in Fig. 2(C). This quantity vanishes at the real axis [$A(\omega', 0) = 0$] due to the system hermicity [36]. In the upper (lower) plane, virtual absorption $A(\omega', \omega'')$ is positive (negative) that gives rise to the effective loss (gain) effect. This result is fair as long as the excitation has an exponentially increasing (exponentially decaying) character. Note also that due to the quasi-monochromatic character of the exponential excitation, the calculation results for $A(\omega', \omega'')$, $R(\omega', \omega'')$, and $T(\omega', \omega'')$ are *fair for any time instant*.

The corresponding results of the calculation of the optical pressure are presented in Fig. 2(D). First, we note that in the upper plane [exponentially growing excitation, $E_i(t) \propto E_0 \exp(|\omega''|t)$], as the complex frequency gets increased, the system can come into the zero transmission regime [$T = 0$, Figs. 2(A) and 2(B)]. As a result, the force reaches $F = 2N_i\hbar k$, i.e., the expected value for the perfect reflectors. More remarkably, in the lower plane [exponentially attenuating excitation, $E_i(t) \propto E_0 \exp(-|\omega''|t)$], at a fixed real frequency, the optical pressure experiences the abrupt transition from large positive to large negative values, where the system is expected to experience pulling action from the laser beam [Fig. 2(D)]. This result can be explained as follows. Reflection and transmission coefficients contribute to the resulting radiation force with the opposite sign, and one can expect that their poles compensate each other. However, the presence of reflection zeros near the corresponding poles "deform" the poles. As a result, the optical pressure in the lower complex frequency plane has a nontrivial character with increased and decreased values.

To investigate the effect of complex excitation in the transient regime, we use full-wave FDTD simulations in CST Microwave Studio. To this end, we tailor two incident signals (I, blue curve) corresponding to the Fabry–Perot resonance [$\mathrm{Re}(\omega d/c) = 0.5$] and the middle frequency between two Fabry–Perot resonances [$\mathrm{Re}(\omega d/c) = 0.75$] [Figs. 3(A) and 3(D)]. During the first period (0/ 1.3 ps), the oscillation amplitude of both incident signals is increasing exponentially with $\mathrm{Im}(\omega d/c) = 0.025$, then it reaches monochromatic excitation with the same real frequency (1.3/ 2.5 ps), and then it decays exponentially with $\mathrm{Im}(\omega d/c) = -0.025$. The shape of the chosen excitation signals allows consideration of both exponential growth and exponential decay regimes along with a quite long period of monochromatic excitation for revealing the steady-state regime.

Figures 3(A) and 3(D) show the calculated transmitted (T, yellow curve), and reflected (R, red curve) signals. We note that the reflection and transmission signals at the monochromatic region correspond to the expected values: ($T \sim 1$, $R \sim 0$) for the

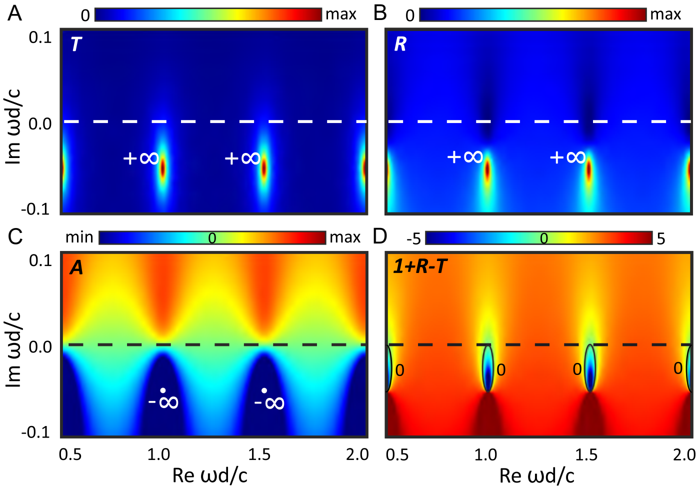

Fig. 2. (A),(B) Transmission and reflection in the complex plane. The dielectric slab is assumed to be lossless, with permittivity $\varepsilon = 40$. (C) Effective absorption in the complex frequency plane calculated as $A(\omega', \omega'') = 1 - R(\omega', \omega'') - T(\omega', \omega'')$. This quantity vanishes at the real axis [$A(\omega', 0) = 0$] due to system losslessness. In the upper (lower) plane, $A(\omega', \omega'')$ is positive (negative) that gives rise to the effective loss (gain) effect. (D) Optical pressure in the complex frequency plane normalized to its value in the perfect absorption case, $F_0 = N_i\hbar k$. As the complex frequency grows in the upper plane, the system can come into the zero transmission regime; as a result, the force reaches $F/F_0 \sim 2$, the value we expect for perfect reflectors. In the lower plane, the difference between the poles of R and T gives the enlarged positive (repulsion) and negative (attraction) force. The black dashed line represents the axis of real frequencies. Black solid curves show contours of zero force.

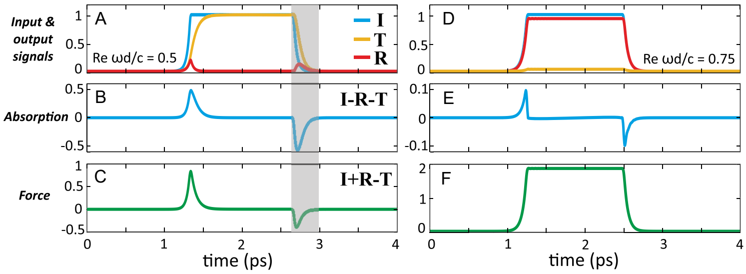

Fig. 3. Transient behavior of incident (I, blue curve), transmitted (T, yellow curve), and reflected (R, red curve) signals obtained in the FDTD simulations and corresponding to (A) the Fabry–Perot resonance [$\mathrm{Re}(\omega d/c) = 0.5$] and (D) the middle between Fabry–Perot resonances [$\mathrm{Re}(\omega d/c) = 0.75$]. During the first time period (0/1.3 ps), the oscillation amplitude of the incident signal is increasing exponentially with $\mathrm{Im}(\omega d/c) = 0.025$, then it reaches monochromatic excitation with the same real frequency (1.3/2.5 ps), and then it decays exponentially with $\mathrm{Im}(\omega d/c) = -0.025$. The reflection and transmission signals at the monochromatic region correspond to the expected values: ($T \sim 1$, $R \sim 0$) for (A) the Fabry–Perot resonance, and in the intermediate case (D) ($T \sim 0$, $R \sim 1$). (B),(E) Transient behavior of the virtual absorption/gain coefficient $A(\omega', \omega'') = 1 - R(\omega', \omega'') - T(\omega', \omega'')$. This value is nonzero only at the exponential pumping and exponential attenuation. (C),(F) Optical radiative force in transient for the chosen excitation. At the Fabry–Perot resonance, the force changes its sign, whereas in the intermediate case, it is always positive, in full agreement with Fig. 2(D). The grey region determines the area of negative force.

Fabry–Perot resonance [Fig. 3(A)], and ($T \sim 0$, $R \sim 1$) in the intermediate case [Fig. 3(D)], which means good incident pulse quality and the absence of energy transfer to other frequencies. The virtual absorption/gain coefficient is nonzero only at the exponential excitation and exponential attenuation periods as expected for the lossless structure [Figs. 3(B) and 3(E)]. The results of the numerical calculation of optical radiative force in the transient regime for the chosen excitation are shown in Figs. 3(C) and 3(F). We see that at the Fabry–Perot resonance, the force changes its sign, whereas in the intermediate case, it always stays positive, in full agreement with analytical results [Fig. 2(D)].

Thus, these results demonstrate the possibility of getting around the restriction caused by the momentum conservation law and achieving negative optical pressure for exponentially decaying signals. We note that the required decay rate depends on the position of the reflection poles and can be made arbitrarily small with an appropriate choice of a mode with a large Q factor. For instance, the recently introduced concept of optical bound states in the continuum (BICs) [40,41] supporting unboundedly large Q factor (the pole is unboundedly close to the real axis) would be a promising platform for negative optical forces in paraxial beams slowly decaying in time.

As another example, important from the application viewpoint, we consider the case of a high-index dielectric nanoparticle. Recently, these particles have attracted a lot of interest from researchers across many interdisciplinary fields, including quantum optics, nonlinear photonics, and biosensing. For biological applications, these subwavelength dielectric particles are demonstrated to be a fruitful platform for *intracellular* spectroscopy and microscopy [42–44]. In our calculations, we have chosen permittivity $\varepsilon = 16$, which corresponds to c-Si in the visible, Ge in near-IR, and SiC in mid-IR [45].

The scattering cross section (Q_{sca}) of the dielectric nanoparticle in the complex frequency plane is presented in Fig. 4(A). As in the previous example, we observe several poles in the lower complex plane that give rise to the corresponding resonances at the real axis [43,46] [Fig. 4(D)]. The fundamental resonance is magnetic dipole (MD), whereas the resonance with the largest Q factor is magnetic quadrupole (MQ). As the frequency grows, the higher-order resonant modes manifest themselves. Here, the anapole state, which corresponds to the $Q_{\mathrm{sca}} \approx 0$ regime (it is not exactly zero because of the MQ mode), is also shown. Recently, the optical radiation force for such a dielectric particle in the monochromatic excitation laser field has been investigated theoretically [47,48] and experimentally [49]. The enhancement of the force around the resonances and its reduction at the zero-backscattering Kerker condition [43] have been reported. While the former is supposed to be used for optical force enhancement, the latter is suggested for stabilization in an optical trap [47]. In Ref. [50] the optical force acting on the Si particles has been utilized for 2D trapping over a substrate and printing onto the substrate by means of radiation pressure. However, the optical pressure in these works is *reported to be always positive for the paraxial optical field* because any act of scattering of the incident photons by the nanoparticle can reduce their forward momentum or, at best, leave it unchanged. In further consideration, we revisit this conclusion and demonstrate how the negative optical radiative force can be achieved in the complex excitation approach.

The radiative optical force in this case of a spherical particle can be calculated analytically by using the method rigorously derived based on the time-averaged Maxwell stress tensor [13,48,51] and found to be consistent with experimental results [49]. According to this method, the time-averaged radiative optical force equals

$$F = \frac{\pi r^2 I}{c}[Q_{\mathrm{ext}} - Q_{\mathrm{sca}}\langle\cos\theta\rangle], \tag{2}$$

$$Q_{\mathrm{sca}}\langle\cos\theta\rangle = \frac{4}{(kR)^2}\sum_l \frac{l(l+2)}{l+1}\mathrm{Re}(a_l a_{l+1}^* + b_l b_{l+1}^*)$$

$$+ \frac{4}{(kR)^2}\sum_l \frac{2l+1}{l(l+1)}\mathrm{Re}\left(a_l b_l^*\right), \tag{3}$$

where Q_{ext} is the extinction cross section ($Q_{\mathrm{ext}} = Q_{\mathrm{abs}} + Q_{\mathrm{sca}}$), Q_{abs} is the absorption cross section, l is the multipole order, R is the particle radius, a_l and b_l are electric and magnetic Mie scattering amplitudes, and $\langle\cos\theta\rangle$ means averaging over all possible angles θ

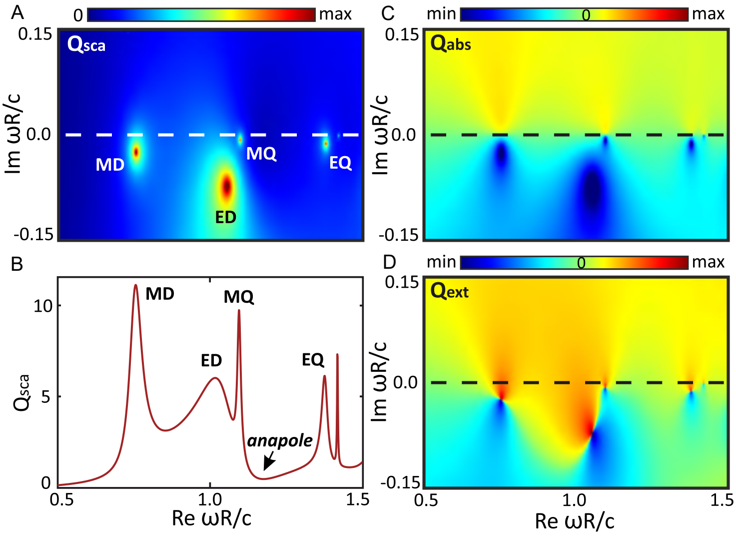

Fig. 4. (A) Scattering cross section (Q_{sca}) of a dielectric particle with permittivity $\varepsilon = 16$ in the complex frequency plane. It demonstrates several poles in the lower complex plane that give rise to the corresponding resonances (B) at the real axis (MD, ED, MQ, and EQ stand for magnetic dipole, electric dipole, magnetic quadrupole, and electric quadrupole modes, respectively). The anapole state corresponds to the $Q_{sca} \approx 0$ regime. (D) Absorption cross section (Q_{abs}) and (D) extinction cross section (Q_{ext}) of the nanoparticle in the complex frequency plane. Despite that the particle is assumed to be lossless $[Q_{abs}(\omega', 0) = 0]$, the results show finite virtual absorption in the upper plane and negative absorption (gain) in the lower plane.

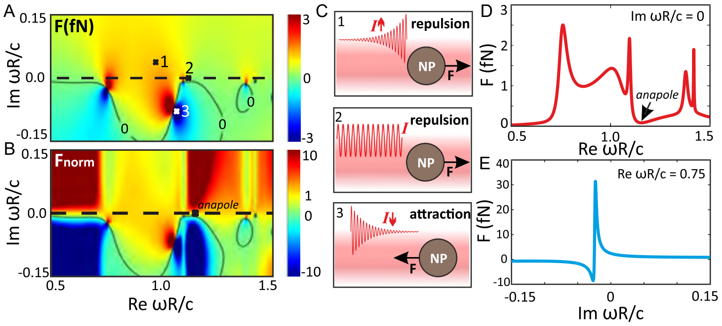

Fig. 5. (A) Optical radiation pressure for the dielectric particle with permittivity $\varepsilon = 16$ in the complex frequency plane. The light intensity is $I = 1\ \mathrm{W/mm^2}$. (B) The same but normalized by its value at the real axis. The black dashed line represents the axis of real frequencies. Black solid curves show contours of zero force. (C) Sketches of the corresponding regimes denoted by crosses in (A). (D) The value of optical radiation pressure at the real frequency axis $[\mathrm{Im}(\omega R/c) = 0]$. (E) Optical radiation pressure as a function of imaginary frequency $\mathrm{Im}(\omega R/c)$ at the fixed real frequency $[\mathrm{Re}(\omega R/c) = 0.75]$, which corresponds to the MD mode.

between the propagation direction and scattering directions [51]. To analytically calculate the values of Q_{ext} and Q_{abs} in the complex plane, we used the exact Mie theory [51]. This approach has also been utilized for the analysis of optical forces in spherical particles of active media and can be generalized to nonparaxial excitation fields [15]. Upon complex excitation, like the Fabry–Perot case above, Q_{abs} exhibits a finite value, even though the particle is lossless $[\mathrm{Im}(\varepsilon) = 0]$ [Fig. 4(C)]. This stems from the virtual absorption and virtual gain effects discussed above. Physically, this virtual loss effect corresponds to the stored energy. In contrast, the virtual gain effect is caused by the amplitude of energy leaking out from the particle exceeding the amplitude of the incoming energy due to its exponential decay. Since the extinction cross section equals the sum of both parts of losses ($Q_{ext} = Q_{abs} + Q_{sca}$), it also demonstrates the alternating behavior in the lower plane [Fig. 4(D)].

The results of the calculation of the optical radiation pressure acting on the dielectric particle with permittivity $\varepsilon = 16$ are presented in Fig. 5(A). Here, by points "1," "2," and "3," we denote the virtual repulsive, repulsive, and virtual pulling regimes, respectively [Fig. 5(C)]. The optical force in the complex frequency plane normalized by its value at the real axis is presented in Fig. 5(D). For comparison, Fig. 5(D) shows the value of optical radiation pressure at the real frequency axis $[\mathrm{Im}(\omega R/c) = 0]$. This result coincides with the reported theoretical works [47] and existing experimental results [49]. Figure 5(E) demonstrates the optical radiation pressure as a function of imaginary frequency $\mathrm{Im}(\omega R/c)$ at the fixed real frequency $[\mathrm{Re}(\omega R/c) = 0.75]$, which corresponds to the MD mode. We observe the characteristic Fano-like transition from enhanced negative to enhanced positive values. Note that the intensity of light in our calculations $I = 1\ \mathrm{W/mm^2}$ coincides with that used in recent experimental works on similar Si nanoparticles [49] in liquids and gives the same absolute value of optical force ($\sim$10 fN).

Lastly, we discuss possible experimental approaches to achieve the reported effects. First, as we mentioned above, the rate of exponential growth or decay required to archive enhanced positive or negative radiation force depends on the position of the poles in the complex plane. These poles may lie close to the real frequency axis in high-Q cavities. An ultimate approach is so-called bound states in the continuum or embedded eigenstates [36,52–54]. In contrast to conventional optical resonances (e.g., plasmonic, Mie, whispering gallery modes), these states are uncoupled from the continuum of radiative modes; hence, in a lossless scenario, their poles lie on the real frequency axis, enabling negative optical pressure for slowly decaying fields. Next, the reported results of this work are rather general and remain fair in the microwave, terahertz (THz), and optics spectral ranges. In microwaves, the generation of such pulses is an established experimental technique. Moreover, since the effect of virtual absorption has been demonstrated experimentally for acoustic waves [34], it raises an intriguing question on the applicability of our findings in acoustics, where unusual acousto-mechanical effects are also of great interest [55]. Finally, it worth mentioning that the total force over the entire *physically real pulse* (i.e., integrable and amenable to Fourier decomposition) is always positive. Nevertheless, exponentially growing/decaying signals can be a good approximation to some regions of realistic pulses. For example, the decaying field of a leaky mode of a microcavity after an abrupt excitation turn-off is well described by an exponentially decaying signal (see Supplement 1, Fig. S3). An object situated in such a field is expected to manifest the negative optical radiative force. We can also suggest several other ways to achieve this effect. One way is to put a particle onto a dielectric substrate, preventing its movement in the forward direction (see Supplement 1, Fig. S3). Another way is to consider a particle that appears in the laser beam in its decaying phase and, therefore, unaware of the pulse back history.

4. CONCLUSIONS

In this work, we have revisited the issue of optical forces by stepping out to the complex frequency plane and considering its dynamics upon complex excitations. We have shown that tailoring of the time evaluation of the light excitation field allows either enhancement of the repulsive force or achievement of pulling force for a passive resonator of arbitrary shape and composition. We have demonstrated how these effects are linked to virtual gain and virtual loss effects. Virtual gain can be achieved when an appropriate transient decay of the excitation signal makes it weaker than the outgoing signal that carries away greater energy and momentum flux density. In turn, the virtual loss effect is achieved when the incoming signal exponentially grows in time. The approach has been demonstrated for the Fabry–Perot cavity and a high-refractive-index dielectric nanoparticle.

Funding. Russian Science Foundation (18-72-10140); Foundation for the Advancement of Theoretical Physics and Mathematics

Acknowledgment. The authors thank Prof. Andrea Alú for fruitful discussions. We acknowledge support from the Russian Science Foundation (Project No. 18-72-10140) and Foundation for the Advancement of Theoretical Physics and Mathematics.

Disclosures. The authors declare no conflicts of interest.

See Supplement 1 for supporting content.

REFERENCES

1. A. Einstein, "Über einen die Erzeugung und Verwandlung des Lichtes betreffenden heuristischen Gesichtspunkt," Ann. Phys. **322**, 132–148 (1905).
2. A. B. Arons and M. B. Peppard, "Einstein's proposal of the photon concept—a translation of the Annalen der Physik paper of 1905," Am. J. Phys. **33**, 367–374 (1965).
3. P. Lebedev, "Untersuchungen über die druckkräfe des lichtes," Ann. Phys. **311**, 433–458 (1901).
4. E. F. Nichols and G. F. Hull, "A preliminary communication on the pressure of heat and light radiation," Phys. Rev. **13**, 307–320 (1901).
5. A. Ashkin, J. M. Dziedzic, J. E. Bjorkholm, and S. Chu, "Observation of a single-beam gradient force optical trap for dielectric particles," Opt. Lett. **11**, 288–290 (1986).
6. A. Ashkin, "Acceleration and trapping of particles by radiation pressure," Phys. Rev. Lett. **24**, 156–159 (1970).
7. A. Ashkin, "History of optical trapping and manipulation of small-neutral particle, atoms, and molecules," IEEE J. Sel. Top. Quantum Electron. **6**, 841–856 (2000).
8. M. L. Juan, M. Righini, and R. Quidant, "Plasmon nano-optical tweezers," Nat. Photonics **5**, 349–356 (2011).
9. M.-C. C. Zhong, X.-B. Bin Wei, J.-H. H. Zhou, Z.-Q. Q. Wang, and Y.-M. M. Li, "Trapping red blood cells in living animals using optical tweezers," Nat. Commun. **4**, 1768 (2013).
10. D. G. Grier, "A revolution in optical manipulation," Nature **424**, 810–816 (2003).
11. K. Dholakia and P. Zemánek, "Colloquium: gripped by light: optical binding," Rev. Mod. Phys. **82**, 1767–1791 (2010).
12. O. M. Maragò, P. H. Jones, P. G. Gucciardi, G. Volpe, and A. C. Ferrari, "Optical trapping and manipulation of nanostructures," Nat. Nanotechnol. **8**, 807–819 (2013).
13. J. Chen, J. Ng, Z. Lin, and C. T. Chan, "Optical pulling force," Nat. Photonics **5**, 531–534 (2011).
14. A. Dogariu, S. Sukhov, and J. Sáenz, "Optically induced 'negative forces'," Nat. Photonics **7**, 24–27 (2013).
15. H. Chen, S. Liu, J. Zi, and Z. Lin, "Fano resonance-induced negative optical scattering force on plasmonic nanoparticles," ACS Nano **9**, 1926–1935 (2015).
16. D. E. Fernandes and M. G. Silveirinha, "Optical tractor beam with chiral light," Phys. Rev. A **91**, 1–6 (2015).
17. S. Sukhov and A. Dogariu, "Negative nonconservative forces: optical 'tractor beams' for arbitrary objects," Phys. Rev. Lett. **107**, 203602 (2011).
18. A. Novitsky, C.-W. Qiu, and H. Wang, "Single gradientless light beam drags particles as tractor beams," Phys. Rev. Lett. **107**, 203601 (2011).
19. O. Brzobohatý, V. Karásek, M. Šiler, L. Chvátal, T. Čižmár, and P. Zemánek, "Experimental demonstration of optical transport, sorting and self-arrangement using a 'tractor beam'," Nat. Photonics **7**, 123–127 (2013).
20. D. Gao, A. Novitsky, T. Zhang, F. C. Cheong, L. Gao, C. T. Lim, B. Luk'yanchuk, and C.-W. Qiu, "Unveiling the correlation between non-diffracting tractor beam and its singularity in Poynting vector," Laser Photon. Rev. **9**, 75–82 (2015).
21. A. Mizrahi and Y. Fainman, "Negative radiation pressure on gain medium structures," Opt. Lett. **35**, 3405–3407 (2010).

22. R. Alaee, J. Christensen, and M. Kadic, “Optical pulling and pushing forces in bilayer PT-symmetric structures,” Phys. Rev. Appl. **9**, 014007 (2018).
23. D. Gao, R. Shi, Y. Huang, and L. Gao, “Fano-enhanced pulling and pushing optical force on active plasmonic nanoparticles,” Phys. Rev. A **96**, 043826 (2017).
24. K. J. Webb and Shivanand, “Negative electromagnetic plane-wave force in gain media,” Phys. Rev. E **84**, 057602 (2011).
25. A. S. Shalin, S. V. Sukhov, A. A. Bogdanov, P. A. Belov, and P. Ginzburg, “Optical pulling forces in hyperbolic metamaterials,” Phys. Rev. A **91**, 063830 (2015).
26. A. Salandrino and D. N. Christodoulides, “Reverse optical forces in negative index dielectric waveguide arrays,” Opt. Lett. **36**, 3103–3105 (2011).
27. M. I. Petrov, S. V. Sukhov, A. A. Bogdanov, A. S. Shalin, and A. Dogariu, “Surface plasmon polariton assisted optical pulling force,” Laser Photon. Rev. **10**, 116–122 (2016).
28. V. Kajorndejnukul, W. Ding, S. Sukhov, C. W. Qiu, and A. Dogariu, “Linear momentum increase and negative optical forces at dielectric interface,” Nat. Photonics **7**, 787–790 (2013).
29. K. Y. Bliokh, A. Y. Bekshaev, and F. Nori, “Extraordinary momentum and spin in evanescent waves,” Nat. Commun. **5**, 3300 (2014).
30. D. Hakobyan and E. Brasselet, “Left-handed optical radiation torque,” Nat. Photonics **8**, 610–614 (2014).
31. D. G. Baranov, A. Krasnok, and A. Alù, “Coherent virtual absorption based on complex zero excitation for ideal light capturing,” Optica **4**, 1457–1461 (2017).
32. Y. Ra’di, A. Krasnok, and A. Alù, “Virtual critical coupling,” ACS Photon. **7**, 1468–1475 (2020).
33. H. Li, A. Mekawy, A. Krasnok, and A. Alù, “Virtual parity-time symmetry,” Phys. Rev. Lett. **124**, 193901 (2020).
34. G. Trainiti, Y. Ra’di, M. Ruzzene, A. Alù, Y. Radi, M. Ruzzene, and A. Alù, “Coherent virtual absorption of elastodynamic waves,” Sci. Adv. **5**, 1–8 (2019).
35. L. Novotny and B. Hecht, *Principles of Nano-Optics*, 2nd ed. (Cambridge University, 2012).
36. A. Krasnok, D. Baranov, H. Li, M.-A. Miri, F. Monticone, and A. Alú, “Anomalies in light scattering,” Adv. Opt. Photon. **11**, 892–951 (2019).
37. A. Krasnok, D. Baranov, H. Li, M.-A. Miri, F. Monticone, and A. Alú, “Anomalies in light scattering,” Adv. Opt. Photon. **11**, 892–951 (2019).
38. A. Archambault, M. Besbes, and J. J. Greffet, “Superlens in the time domain,” Phys. Rev. Lett. **109**, 097405 (2012).
39. V. Grigoriev, A. Tahri, S. Varault, B. Rolly, B. Stout, J. Wenger, and N. Bonod, “Optimization of resonant effects in nanostructures via Weierstrass factorization,” Phys. Rev. A **88**, 011803 (2013).
40. C. W. Hsu, B. Zhen, A. D. Stone, J. D. Joannopoulos, and M. Soljačić, “Bound states in the continuum,” Nat. Rev. Mater. **1**, 16048 (2016).
41. K. Koshelev, G. Favraud, A. Bogdanov, Y. Kivshar, and A. Fratalocchi, “Nonradiating photonics with resonant dielectric nanostructures,” Nanophotonics **8**, 725–745 (2019).
42. A. Krasnok, M. Caldarola, N. Bonod, and A. Alú, “Advanced optical materials spectroscopy and biosensing with optically resonant dielectric nanostructures,” Adv. Opt. Mater. **6**, 1701094 (2018).
43. A. I. Kuznetsov, A. E. Miroshnichenko, M. L. Brongersma, Y. S. Kivshar, B. Luk’yanchuk, and B. Luk’yanchuk, “Optically resonant dielectric nanostructures,” Science **354**, aag2472 (2016).
44. I. Staude and J. Schilling, “Metamaterial-inspired silicon nanophotonics,” Nat. Photonics **11**, 274–284 (2017).
45. D. G. Baranov, D. A. Zuev, S. I. Lepeshov, O. V. Kotov, A. E. Krasnok, A. B. Evlyukhin, and B. N. Chichkov, “All-dielectric nanophotonics: the quest for better materials and fabrication techniques,” Optica **4**, 814–825 (2017).
46. A. E. Krasnok, A. E. Miroshnichenko, P. A. Belov, and Y. S. Kivshar, “All-dielectric optical nanoantennas,” Opt. Express **20**, 20599 (2012).
47. N. O. Länk, P. Johansson, and M. Käll, “Directional scattering and multipolar contributions to optical forces on silicon nanoparticles in focused laser beams,” Opt. Express **26**, 29074 (2018).
48. M. Nieto-Vesperinas, J. J. Sáenz, R. Gómez-Medina, and L. Chantada, “Optical forces on small magnetodielectric particle,” Opt. Express **18**, 11428 (2010).
49. D. A. Shilkin, E. V. Lyubin, M. R. Shcherbakov, M. Lapine, and A. A. Fedyanin, “Directional optical sorting of silicon nanoparticles,” ACS Photon. **4**, 2312–2319 (2017).
50. V. Valuckas, R. Paniagua-Domínguez, A. Maimaiti, P. P. Patra, S. K. Wong, R. Verre, M. Käll, and A. I. Kuznetsov, “Fabrication of monodisperse colloids of resonant spherical silicon nanoparticles: applications in optical trapping and printing,” ACS Photon. **6**, 2141–2148 (2019).
51. C. F. Bohren and D. R. Huffman, *Absorption and Scattering of Light by Small Particles* (Wiley, 1998).
52. C. W. Hsu, B. Zhen, J. Lee, S. L. Chua, S. G. Johnson, J. D. Joannopoulos, and M. Soljačić, “Observation of trapped light within the radiation continuum,” Nature **499**, 188–191 (2013).
53. M. G. Silveirinha, “Trapping light in open plasmonic nanostructures,” Phys. Rev. A **89**, 1–10 (2014).
54. F. Monticone and A. Alù, “Embedded photonic eigenvalues in 3D nanostructures,” Phys. Rev. Lett. **112**, 213903 (2014).
55. I. D. Toftul, K. Y. Bliokh, M. I. Petrov, and F. Nori, “Acoustic radiation force and torque on small particles as measures of the canonical momentum and spin densities,” Phys. Rev. Lett. **123**, 183901 (2019).

APPENDIX C

Paper 3: Tunable phase-change metasurfaces

Here, recent breakthroughs in electrically tunable phase-change metasurfaces are reviewed. The manuscript is published.

The citations in the manuscript refer to reference list included at the end of the manuscript.

Work contributions by the present author: Manuscript writing.

Reference information:

S. Lepeshov and A. Krasnok. Tunable phase-change metasurfaces. *Nature Nanotechnology* 16, 615–616 (2021).

NANOPHOTONICS

Tunable phase-change metasurfaces

The use of phase-change materials makes metasurfaces and nanoantennas electrically tunable and switchable, bringing their functionality to the next level.

Sergey Lepeshov and Alex Krasnok

Compact and ultrathin metasurfaces, that is, two-dimensional arrays of subwavelength nanoantennas whose response depends on the properties of individual meta-atoms and their interactions, have been attracting a great deal of attention as they promise to supplant bulky lenses and mirrors[1,2]. Although metasurfaces have proven to be a versatile platform for passive optics, active tuning of their optical properties is still a challenging task. Phase-change materials (PCMs) open plentiful opportunities for implementing tunable metasurfaces as the reversible transition between amorphous and crystalline phases is accompanied by a considerable change of the refractive index[3]. Until recently, the tunability of PCM-based metasurfaces has been mostly limited to optical writing and thermal annealing. Now, works by Yifei Wang et al.[4] and Yifei Zhang et al.[5] independent of each other overcome these limitations by implementing electrical heating of phase-change materials, fully integrable with the existing optoelectronic circuits.

PCMs, especially chalcogenide alloys such as GeTe, Sb_2S_3 and $Ge_3Sb_2Te_6$ (GST), offer a promising platform for reconfigurable optical functionalities enabled by reliable and repeatable temperature-induced switching of their optical and electrical properties over billions of cycles. The amorphization and crystallization in phase-change metasurfaces have been achieved by ultrafast laser melting or furnace heating[3]. Although the tuning of phase-change materials by electrical heating is already a mature technology in phase-change random access memory (PCRAM), it has not been exploited for tunable metasurfaces.

Wang et al. demonstrate a tunable antenna composed of adjoining silver and GST rectangular nanostrips with 10 μm length (Fig. 1a)[4]. GST is one of the most commonly used PCMs because of its low energy consumption and strong refractive index tunability. The phase switching of the GST antenna is realized by a pulsed current heating the nearby Ag nanostrip. A low but relatively long duration current pulse (10 mA for ~20 μs) causes mild heating of the GST crystal phase below its melting temperature, so that the simultaneous ambient cooling leaves it in the crystal phase. Conversely, a short but high (15 mA) current pulse (15 mA for 500 ns) induces fast heating and melting with subsequent rapid cooling to reset the GST into the amorphous state. The GST–Ag antenna system possesses the localized surface plasmon resonance in the near-infrared range, strongly dependent on the refractive index of the GST. Consequently, the phase switch of GST accompanied by a refractive index change causes a scattering efficiency modulation of ~30%. The authors claim the achievement of various degrees of crystallinity by varying the amplitude and duration of the pulses. Indeed, previous publications on GST nanostructures have also shown intermediate states between the amorphous and crystalline one[6]. This observation opens the ways for multi-level operation and broadens the functionality of PCM-based antennas and metasurfaces. Finally, the authors have engineered a reflective metasurface based on GST nanostrips placed on an Ag contact layer. In this case, the long but weak electrical pulse turns the metasurface into the perfect absorber, while the short but strong one makes the metasurface reflective. The experimentally approved reflectance variation also reaches 30%. All these results bring this work to a qualitatively new level in comparison with previous investigations[7].

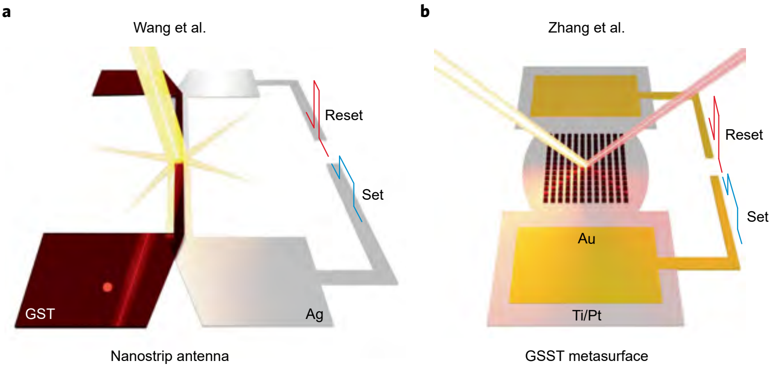

Fig. 1 | Schematic of tunable metastructures. a, Electrically tunable GST–Ag meta-atom, which utilizes localized plasmon resonance to enhance and modulate scattering. **b**, Electrically reconfigurable metasurface capable of switching between reflecting and absorbing regimes. The tunability of both metastructures is achieved by a reversible transition of a PCM from an amorphous to a crystalline state upon mild electrical heating caused by a long weak set pulse and from crystalline to amorphous induced by a short strong reset pulse.

Zhang et al. make one step forward towards the realization of large-scale reconfigurable metasurfaces[5]. Unlike the work of Wang et al. where the metasurface area barely reaches 5 × 5 μm^2, this work achieves 400 × 400 μm^2 area by the optimization of the electrical heater design to improve thermal uniformity and utilization of a fairly novel PCM, $Ge_2Se_2Sb_4Te$ (GSST). Compared to GST, GSST is broadly transparent in the near-infrared region. Besides, while the fast phase transition in GST occurs only in small-volume structures (characteristic size of ~100 nm), GSST allows the engineering of thicker metasurfaces. The proposed metasurface operates in the reflective regime (Fig. 1b). The demonstrated reflectance modulation is also of ~30% and the smooth control of the GSST phase states with different crystallinity is similarly demonstrated by varying the pulse duration and amplitude. More remarkably, the authors suggest a PCM-metasurface with asymmetric meta-atom composed of two disks of different radii. Due to this unit-cell asymmetry, the metasurface serves as an optical beam deflector in the amorphous state and, predominantly, as a reflector in the crystalline state. However, the larger size and beam deflection functionality of the metasurface comes with the price of slower operation (for example, ~500 ms crystallization time in contrast to ~20 μs reported in ref. [4])

Although these works make a breakthrough in the tunable PCM-based metasurfaces, the proposed approaches suffer from several drawbacks. First, the suggested design of the heater forbids operation in the transmission regime, which may be limiting for some applications; the use of transparent electrodes (indium tin oxide or graphene) can potentially solve this problem. Second, since the metasurface heating is sufficient for the phase change, high-power optical radiation itself can cause an undesired transition between the amorphous and crystalline states. Third, the reported modulation amplitude is still too small for real-life applications; employing concepts of machine learning or light scattering engineering should improve this figure of merit[8,9]. Fourth, although PCMs can, in principle, handle millions of crystallization cycles, Wang et al. and Zhang et al. report only 100 and 40 cycles, respectively. Finally, the slow operational speed of these PCM-based metasurfaces is one of the most restricting drawbacks of this technology. Nevertheless, the demonstration of electrically tunable PCM metasurfaces represents an attractive prospect for reconfigurable holograms, diffractive optical elements, adaptive optics and sensing. ❐

Sergey Lepeshov[1]✉ and
Alex Krasnok[2]✉

[1]*Department of Physics and Engineering, ITMO University, St. Petersburg, Russia.*
[2]*Advanced Science Research Center, City University of New York, New York, NY, USA.*
✉*e-mail: s.lepeshov@metalab.ifmo.ru; akrasnok@gc.cuny.edu*

https://doi.org/10.1038/s41565-021-00892-6

References

1. Yu, N. & Capasso, F. *Nat. Mater.* **13**, 139–150 (2014).
2. Glybovski, S. B., Tretyakov, S. A., Belov, P. A., Kivshar, Y. S. & Simovski, C. R. *Phys. Rep.* **634**, 1–72 (2016).
3. Abdollahramezani, S. et al. *Nanophotonics* **9**, 1189–1241 (2020).
4. Wang, Y. et al. *Nat. Nanotechnol.* https://doi.org/10.1038/s41565-021-00882-8 (2021).
5. Zhang, Y. et al. *Nat. Nanotechnol.* https://doi.org/10.1038/s41565-021-00881-9 (2021).
6. Tian, J. et al. *Nat. Commun.* **10**, 396 (2019).
7. Carrillo, S. G.-C., Alexeev, A. M., Au, Y.-Y. & Wright, C. D. *Opt. Express* **26**, 25567 (2018).
8. Koshelev, K., Lepeshov, S., Liu, M., Bogdanov, A. & Kivshar, Y. *Phys. Rev. Lett.* **121**, 193903 (2018).
9. Krasnok, A. et al. *Adv. Opt. Photonics* **11**, 892 (2019).

Competing interests

The authors declare no competing interests.

APPENDIX D

Paper 4: Levitated Optomechanics with Meta-Atoms

This manuscript explores the optical trapping of Mie resonant nanoparticles in a vacuum, and a trapping regime based on intensity minima is identified. The manuscript is published.

The citations in the manuscript refer to reference list included at the end of the manuscript.

Work contributions by the present author: Analytical and numerical calculations, manuscript writing.

Reference information:

S. Lepeshov, N. Meyer, P. Maurer, O. Romero-Isart, and R. Quidant. Levitated Optomechanics with Meta-Atoms. *Physical Review Letters* 130, 233601 (2023).

Levitated Optomechanics with Meta-Atoms

Sergei Lepeshov,[1] Nadine Meyer,[2,3] Patrick Maurer,[4,5] Oriol Romero-Isart,[4,5,*] and Romain Quidant[2,3,†]
[1]*School of Physics and Engineering, ITMO University, Saint Petersburg, Russia*
[2]*Nanophotonic Systems Laboratory, Department of Mechanical and Process Engineering, ETH Zurich, 8092 Zurich, Switzerland*
[3]*Quantum Center, ETH Zurich, 8083 Zurich, Switzerland*
[4]*Institute for Quantum Optics and Quantum Information of the Austrian Academy of Sciences, A-6020 Innsbruck, Austria*
[5]*Institute for Theoretical Physics, University of Innsbruck, A-6020 Innsbruck, Austria*

(Received 30 November 2022; accepted 10 May 2023; published 8 June 2023)

We propose to introduce additional control in levitated optomechanics by trapping a meta-atom, i.e., a subwavelength and high-permittivity dielectric particle supporting Mie resonances. In particular, we theoretically demonstrate that optical levitation and center-of-mass ground-state cooling of silicon nanoparticles in vacuum is not only experimentally feasible but it offers enhanced performance over widely used silica particles in terms of trap frequency, trap depth, and optomechanical coupling rates. Moreover, we show that, by adjusting the detuning of the trapping laser with respect to the particle's resonance, the sign of the polarizability becomes negative, enabling levitation in the minimum of laser intensity, e.g., at the nodes of a standing wave. The latter opens the door to trapping nanoparticles in the optical near-field combining red and blue-detuned frequencies, in analogy to two-level atoms, which is of interest for generating strong coupling to photonic nanostructures and short-distance force sensing.

DOI: 10.1103/PhysRevLett.130.233601

Optical trapping and motional control of polarizable submicron objects in vacuum has become a very active research field [1,2]. Recently, the motion of an optically levitated silica nanoparticle has been cooled to the quantum ground state, either using passive feedback cooling via coherent scattering into a cavity [3–5], or via active feedback cooling [6–8] with shot-noise limited optical detection. In addition, the optical dipole-dipole interaction between two silica nanoparticles trapped in vacuum in two separate optical tweezers has been measured [9], which opens the door to study many-particle physics in vacuum [2,10–16]. Optical trapping and control in vacuum of more complex particles supporting internal resonances has thus far been considered unattainable due to laser absorption, and has been solely studied by using low frequency electric [17–20] or magnetic fields [20–28]. In contrast to optical manipulation, magnetic and electric platforms are less advanced and face additional challenges in terms of motional control in the quantum regime [2].

In this Letter, we analyze the use of Mie resonances supported by silicon nanoparticles [29] for optical levitation in vacuum [30]. We demonstrate that the resonances enable larger trap frequencies and trap depths compared to silica nanoparticles. Remarkably, we also evidence that silicon nanoparticles of few hundred nanometers behave, from the optomechanical standpoint, as a meta-atom whose polarizability changes sign across the resonance. In analogy with two-level atoms, this enables trapping the particle in regions of minimum laser intensity [31–34]. The frequency-dependent sign of the polarizability is foreseen to enable trapping of silicon particles near a surface by using two-color near-field traps [35,36]. The latter is of interest to couple particle's motion to optical microcavities [37] or other integrated photonic systems [38–40]. In the context of optical interaction of many particles, optical resonances pave the way to engineer stronger and more complex types of interactions beyond dipole-dipole interaction. Last but not least, in the context of levitated optomechanics, we theoretically show how to achieve motional ground-state cooling of optically resonant nanoparticles and discuss its distinctive features, including larger cooling rates and even the possibility of entering the strong optomechanical coupling regime in free space [3,41,42].

Let us consider a spherical silicon (Si) particle of radius R, mass m, and homogeneous refractive index $n = n_r + i n_i$, interacting with laser light in ultrahigh vacuum. We consider a standing wave pattern along the z axis that is formed by two x-polarized and counterpropagating focused laser beams of equal wavelength λ, and with a relative phase $\Delta\phi$ [43–46] (Fig. 1). The case $\Delta\phi = 0$ and $\Delta\phi = \pi$ corresponds to the optical configuration with constructive interference and destructive interference at the focal point, respectively. Because of the symmetry of the illumination, the scattering forces experienced by the particle cancel out such that trapping conditions are fully determined by both field intensity gradients and particle polarizability. Unlike subwavelength silica (SiO_2) nanoparticles that behave as nonresonant dipole scatterers, a subwavelength Si nanoparticle supports

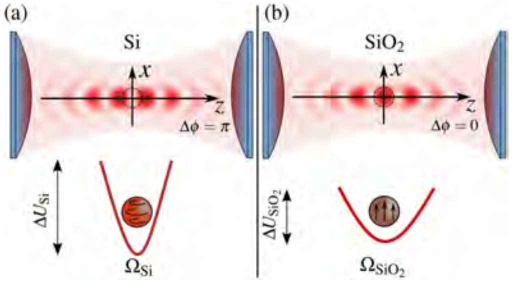

FIG. 1. Illustration of the optical configuration and the corresponding optical potential with trap depth ΔU and trap frequency Ω. In both panels the optical configuration consists of two x-polarized focused laser beams of equal wavelength, counter-propagating along the z axis. The relative phase $\Delta\phi$ specifies the intensity of the standing wave at the focal point. (a) Silicon nanosphere trapped at the intensity minimum ($\Delta\phi = \pi$) (b) Silica nanosphere trapped at the intensity maximum ($\Delta\phi = 0$).

multipolar Mie resonances [29] whose spectral features depend on the real part of the dielectric constant $\epsilon = n^2$ and the ratio R/λ. The enhanced nanoparticle polarizability at a given Mie resonance is expected to substantially increase the total force experienced by the particle, and thereby to increase trap depth and trap frequencies compared to a SiO_2 nanoparticle (Fig. 1). Furthermore, as discussed later, Mie resonances offer an opportunity to control the sign of the force by an appropriate detuning between the Mie resonance and the frequency of the trapping laser, thereby enabling the trapping of particles at a dark spot [Fig. 1(a)].

To test these hypotheses, we use the optical tweezers computational toolbox [47] to calculate the total optical force on a Si nanoparticle with center-of-mass position $\mathbf{r}$ in the standing-wave configuration described above. We set the focal point of the standing wave at $z = 0$ (Fig. 1). Hereafter, we make use of the paraxial approximation such that the optical force acting on a particle placed near the focus has cylindrical symmetry [48]. Hence, the total force is characterized by a force term along the standing-wave axis, denoted by $F_z(\mathbf{r})$, and a force term perpendicular to the optical axis, denoted by $F_\rho(\mathbf{r})$. In Fig. 2(a) we plot $F_z(0,0,z)$ as a function of radius R and axial distance z for $\Delta\phi = \pi$ (dark focal spot) and using the experimental parameters given in Table I. Note that, $F_z(0,0,z)$ changes its sign multiple times both as a function of z due to the standing-wave profile and, remarkably, as a function of radius R as the trapping wavelength swipes across the different Mie resonances. Similar sign flips are observed for the radial force F_ρ as a function of radius R and radial distance x; see Fig. 2(b). For $\Delta\phi = 0$ (bright focal spot) the axial force $F_z(0,0,z)$ displays opposite attractive and repulsive regions while the radial force remains unchanged; see Ref. [49]. Overall three-dimensional trapping can be achieved in the dark, where, in absence of the particle, light destructively interferes. As seen from the map of the optical potential $U(\mathbf{r})$ displayed in Figs. 2(c) and 2(d), the axial trapping position z_0 occurs either at the focal dark point $z_0 = 0$ for radii in the range $R[\text{nm}] \approx (196, 215)$ and in a neighboring bright spot for radii in the range $R[\text{nm}] \approx (216, 284)$ [these radii ranges are highlighted by the black boxes in Figs. 2(a) and 2(b)]. Hereafter, we will exclusively consider optical trapping at the focal point $z_0 = 0$, which requires using either $\Delta\phi = \pi$ (dark trapping) or $\Delta\phi = 0$ (bright trapping) configuration depending on the particle size.

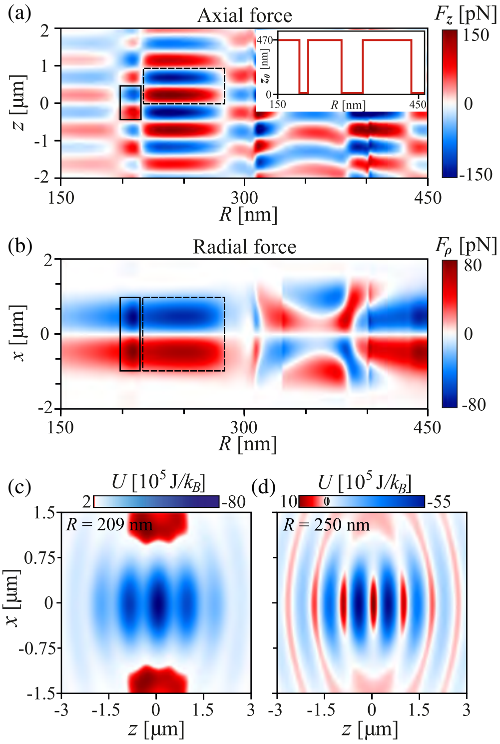

FIG. 2. (a) Axial force $F_z(0,0,z)$ as a function of axial distance z and radius R for $\Delta\phi = \pi$ (dark focal spot). Inset shows the axial trapping position z_0 as a function of radius R. The corresponding ranges $R[\text{nm}] \approx (196, 215)$ and $R[\text{nm}] \approx (216, 284)$ are highlighted by solid and dashed black boxes in (a) and (b). (b) Radial force $F_\rho(x, 0, z_0)$ as a function of the radial distance x, radius R, and z_0 as specified in the inset of (a). (c) Optical potential U for Si nanoparticles with $R = 209$ nm trapped at the dark focal point $z_0 = 0$. (d) Optical potential for Si nanoparticles with $R = 250$ nm trapped at the bright spot $z_0 \neq 0$.

In particle trapping, both the trap depth ΔU and the trap frequencies Ω_z and Ω_ρ are key parameters to quantify the quality of the trap. The trap depth ΔU is defined as the kinetic motional energy required for the particle to escape. The trap frequencies Ω_z and Ω_ρ are defined when the

TABLE I. Table of proposed experimental parameters.

Parameters	Description
$\lambda = 1550$ nm	Laser wavelength
P = 50 mW	Laser power per beam
NA = 0.8	Numerical aperture
$n_{\mathrm{Si}}(\lambda) = 3.48 + \mathrm{i}\,5.3038 \times 10^{-11}$	Refractive index of Si [55]
$n_{\mathrm{SiO_2}}(\lambda) = 1.46 + \mathrm{i}\,5 \times 10^{-9}$	Refractive index of SiO_2 [56]
$\rho_{\mathrm{Si}} = 2330\ \mathrm{kg\,m^{-3}}$	Mass density of Si
$\rho_{\mathrm{SiO_2}} = 2200\ \mathrm{kg\,m^{-3}}$	Mass density of SiO_2

optical potential is expanded around its minimum (in our case, near the focus), namely $U(\mathbf{r}) \approx m\Omega_z^2 z^2/2 + m\Omega_\rho^2 \rho^2/2$. In levitated optomechanics, the mechanical trap frequency along a given axis sets an important timescale for the dynamics. In the quantum regime, the trap frequency is required to be larger than the decoherence rate caused by any noise source other than laser recoil heating. Maximizing trap frequencies is thus desirable for bringing the motion of a particle into the quantum regime. In Fig. 3(a) we plot ΔU and in Fig. 3(b) Ω_z and Ω_ρ as a function of radius R for a particle trapped at $z_0 = 0$ (the upper horizontal axis shows whether the dark $\Delta\phi = \pi$ or bright $\Delta\phi = 0$ configuration is required). For comparison, we also display with the dashed line the case of a SiO_2 nanoparticle for the bright configuration $\Delta\phi = 0$, which is the only possibility to trap a nonresonant dielectric particle. In contrast to what is observed for SiO_2, ΔU and $\Omega_{z,\rho}$ display for Si complex R dependence with regions of both enhancement and diminution. The maximum trap depth is achieved for $R = 209$ nm in the dark trapping and for $R = 250$ nm in the bright trapping (black dotted lines), with trap depths approximately 25 times greater than for SiO_2. Both axial Ω_z and radial Ω_ρ mechanical frequencies also display enhanced values, which can be more than 5 times larger than those of a SiO_2 nanoparticle. Let us remark that the complex features of Figs. 3(a) and 3(b) correlate to the different electric and magnetic modes supported by the particle [57], as we show in [49].

While so far we have focused on conservative dynamics, namely on the optical potential, the interaction of a dielectric particle with laser light also induces dissipative motional dynamics, i.e., laser light recoil heating [58–60]. Recoil heating induces a linear in time increase of center-of-mass energy due to the backaction caused by the scattered light that carries information about the center-of-mass position. The recoil heating rate Γ_μ along the μ axis ($\mu = x,\ y,\ z$) is defined as $\partial_t E_\mu(t) = \Gamma_\mu \hbar \Omega_\mu$, where $E_\mu(t) = \langle p_\mu^2/(2m) + m\Omega_\mu^2 r_\mu^2/2 \rangle$. The expected value represents an ensemble average over trajectories. In the context of quantum ground-state cooling of the center-of-mass motion of a dielectric particle via optical detection, recoil heating is of paramount importance. Figure 3 shows $\Gamma_{x,z}$ for Si (solid) and SiO_2 (dashed) particles as a function of radius R calculated using recent theoretical methods [60]. We observe a complex behavior for Si particles, while SiO_2 shows smooth trends expected for particles in the Rayleigh

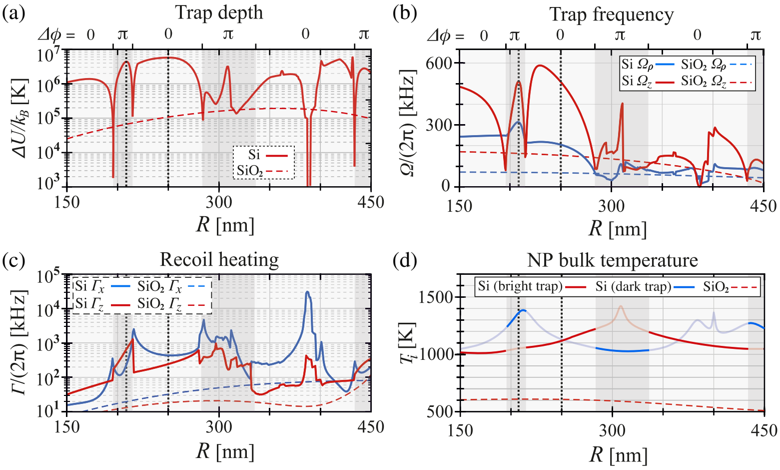

FIG. 3. (a) Trap depth ΔU for $z_0 = 0$ as a function of the radius R for Si (solid) and SiO_2 (dashed). The upper abscissa specifies which relative phase $\Delta\phi$ is used to achieve $z_0 = 0$ for Si. The black dotted lines represent the maximal trap depth at $R \approx 209$ nm (dark), and $R \approx 250$ nm (bright), respectively. (b) Radial trap frequency Ω_ρ (blue) and axial trap frequency Ω_z (red) as a function of the radius R for Si (solid) and SiO_2 (dashed). (c) Recoil heating rate Γ_x along x (blue) and recoil heating rate Γ_z along z (red) as a function of radius R for Si (solid) and SiO_2 (dashed). (d) Internal temperature T_i as a function of radius R for Si in the bright trap (solid red), Si in the dark trap (solid blue), and SiO_2 in the bright trap (red dashed).

regime. In general, $\Gamma_{x,z}$ for Si exceeds SiO_2 for nearly all radii by up to 3 orders of magnitude. This increase is more pronounced for the axial direction. On one hand, higher $\Gamma_{x,z}$ leads to increased decoherence rates at equal power levels. On the other hand, this enhancement implies that more scattered photons carrying information about the particle position are collected, which is advantageous for active feedback cooling, as discussed below. Last but not least, we observe configurations in which $\Gamma_{x,z}$ is comparable or even larger than the trap frequencies, which is a signal of the strong optomechanical coupling regime. The possibility of entering and exploiting the strong optomechanical regime in free space (i.e., without cavities) will be further investigated elsewhere.

Another critical parameter that determines the experimental feasibility of trapping in vacuum is the internal heating of the particle by laser absorption. Thus, it is important to estimate the particle's internal temperature T_i in the different optical trapping configurations under consideration. T_i in high vacuum is estimated by balancing the absorbed laser power and the power emitted by the nanoparticle, which can be calculated using Mie solutions [61–63]; see Ref. [49] for more details. In Fig. 3(d), we show T_i for a Si nanoparticle (solid) in the bright trapping (red) and dark trapping (blue) configuration as a function of radius R for the experimental numbers given in Table I. We observe three local maxima in T_i of the Si nanoparticle that align with excited Mie resonances of a different order; see Ref. [49]. We notice that maximal values of $\Gamma_{x,z}$ coincide with increased T_i. While Si nanoparticles heat up more (around a factor of 2) than SiO_2 nanoparticles (dashed line), the internal temperature is lower than the melting point of bulk Si (≈1700 K).

Let us now show that motional ground state cooling of a Si nanoparticle is experimentally feasible, especially in the dark trapping configuration. Assuming that laser recoil is the dominant source of motional heating, phonon occupation along a given axis, say the optical axis, n_z, is only governed by the detection efficiency η, with $n_z = (\sqrt{1/\eta} - 1)/2 < 1$ [6,7,64]. η is the ratio of detected photons that are scattered from the particle by either increasing or decreasing the center-of-mass kinetic energy along the z axis. Hence, it is key to know the angular dependence of such scattered photons to evaluate the portion of them that can be detected and processed by the experimental configuration. This information is given by the so-called radiation patterns [64], calculated using recent theoretical methods [60]. Figure 4 displays the radiation pattern associated with the motion along the z axis in the $x - z$ plane for a Si nanoparticle in a dark (blue solid) and a SiO_2 nanoparticle in a bright trap (red dashed), and equal radii $R = 209$ nm. It illustrates that, under our conditions, scattered photons feature a very similar angular pattern. The gray shaded area illustrates the collected light fraction governed by the NA. For NA > 0.75, the reached detection efficiencies are equal for both scenarios, and for NA = 0.8 the detection efficiency yields $\eta = 0.41$ for Si and $\eta = 0.42$ for SiO_2. Hence, ground state cooling with $n = 0.28$ is in reach, as already demonstrated for bright traps in [6,7]. Let us emphasize that recoil heating for Si nanoparticles is up to 3 orders of magnitude larger than for SiO_2 implying that ground-state cooling can be achieved either with 3 orders of magnitude faster timescale or with up to 3 orders of magnitude less laser power. In the regimes where the recoil heating rates are comparable or larger than the trapping frequencies, other cooling methods based on the use of light pulses could be employed [65].

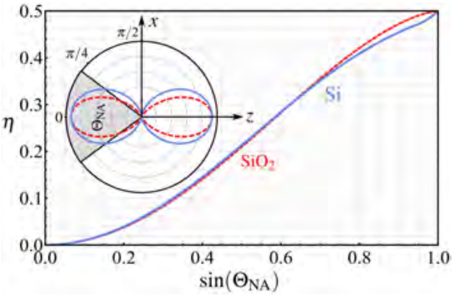

FIG. 4. Detection efficiency η along z as a function of the numerical aperture NA $= \sin \Theta_{NA}$ for Si (solid blue) and SiO_2 (dashed red) at $R = 209$ nm. Inset shows the (normalized) information radiation pattern along z in the x-z plane for both Si (solid blue) and SiO_2 (dashed red).

In summary, we have shown how Mie resonances in silicon nanoparticles introduce an additional degree of control over the dynamics of levitated mechanical oscillators. First, the higher mechanical frequencies, trap depths, and recoil heating rates, as compared to standard silica particles, contribute to increased motional quantum control of nanoparticles. Second, the sign change of the particle's polarizability with the laser frequency enables trapping and center-of-mass ground-state cooling at a laser intensity minimum. We foresee that these unique properties of levitated meta-atoms will open new opportunities in levitodynamics [2], inspired by atom optics. In particular, multiwavelength trapping should enable the accurate control of the distance to an interface [35], critical to the study of surface forces [66], and coupling to photonic structures [67]. Furthermore, parallel trapping of silicon meta-atoms would allow the exploration of interactions beyond the dipole-dipole regime through higher order multipoles, such as electric or magnetic quadrupoles.

We acknowledge valuable discussions with Yuri Kivshar, Ivan Toftul and Massimiliano Rossi. S. L. acknowledges support of Priority 2030 Federal Academic Leadership Program. This research was supported by the European Research Council (ERC) under the grant Agreement No. [951234] (Q-Xtreme ERC-2020-SyG).

[*] Corresponding author.
Oriol.Romero-Isart@uibk.ac.at
[†] Corresponding author.
rquidant@ethz.ch

[1] J. Millen, T. S. Monteiro, R. Pettit, and A. N. Vamivakas, Optomechanics with levitated particles, Rep. Prog. Phys. **83**, 026401 (2020).

[2] C. Gonzalez-Ballestero, M. Aspelmeyer, L. Novotny, R. Quidant, and O. Romero-Isart, Levitodynamics: Levitation and control of microscopic objects in vacuum, Science **374** (2021).

[3] U. Delić, M. Reisenbauer, K. Dare, D. Grass, V. Vuletić, N. Kiesel, and M. Aspelmeyer, Cooling of a levitated nanoparticle to the motional quantum ground state, Science **367**, 892 (2020).

[4] A. Ranfagni, K. Børkje, F. Marino, and F. Marin, Two-dimensional quantum motion of a levitated nanosphere, Phys. Rev. Res. **4**, 033051 (2022).

[5] J. Piotrowski, D. Windey, J. Vijayan, C. Gonzalez-Ballestero, A. de los Ríos Sommer, N. Meyer, R. Quidant, O. Romero-Isart, R. Reimann, and L. Novotny, Simultaneous ground-state cooling of two mechanical modes of a levitated nanoparticle, Nat. Phys. (2023), 10.1038/s41567-023-01956-1.

[6] F. Tebbenjohanns, M. L. Mattana, M. Rossi, M. Frimmer, and L. Novotny, Quantum control of a nanoparticle optically levitated in cryogenic free space, Nature (London) **595**, 378 (2021).

[7] L. Magrini, P. Rosenzweig, C. Bach, A. Deutschmann-Olek, S. G. Hofer, S. Hong, N. Kiesel, A. Kugi, and M. Aspelmeyer, Real-time optimal quantum control of mechanical motion at room temperature, Nature (London) **595**, 373 (2021).

[8] M. Kamba, R. Shimizu, and K. Aikawa, Optical cold damping of neutral nanoparticles near the ground state in an optical lattice, Opt. Express **30**, 26716 (2022).

[9] J. Rieser, M. A. Ciampini, H. Rudolph, N. Kiesel, K. Hornberger, B. A. Stickler, M. Aspelmeyer, and U. Delić, Tunable light-induced dipole-dipole interaction between optically levitated nanoparticles, Science **377**, 987 (2022).

[10] D. R. Burnham and D. McGloin, Holographic optical trapping of aerosol droplets, Opt. Express **14**, 4175 (2006).

[11] K. Dholakia and P. Zemánek, Colloquium: Gripped by light: Optical binding, Rev. Mod. Phys. **82**, 1767 (2010).

[12] W. Lechner, S. J. M. Habraken, N. Kiesel, M. Aspelmeyer, and P. Zoller, Cavity Optomechanics of Levitated Nanodumbbells: Nonequilibrium Phases and Self-Assembly, Phys. Rev. Lett. **110**, 143604 (2013).

[13] S. Liu, Z.-q. Yin, and T. Li, Prethermalization and nonreciprocal phonon transport in a levitated optomechanical array, Adv. Quantum Technol. **3**, 1900099 (2020).

[14] J. Yan, X. Yu, Z. V. Han, T. Li, and J. Zhang, On-demand assembly of optically-levitated nanoparticle arrays in vacuum, arXiv:2207.03641.

[15] P. Verkerk, B. Lounis, C. Salomon, C. Cohen-Tannoudji, J.-Y. Courtois, and G. Grynberg, Dynamics and Spatial Order of Cold Cesium Atoms in a Periodic Optical Potential, Phys. Rev. Lett. **68**, 3861 (1992).

[16] P. S. Jessen, C. Gerz, P. D. Lett, W. D. Phillips, S. L. Rolston, R. J. C. Spreeuw, and C. I. Westbrook, Observation of Quantized Motion of Rb Atoms in an Optical Field, Phys. Rev. Lett. **69**, 49 (1992).

[17] P. Z. G. Fonseca, E. B. Aranas, J. Millen, T. S. Monteiro, and P. F. Barker, Nonlinear Dynamics and Strong Cavity Cooling of Levitated Nanoparticles, Phys. Rev. Lett. **117**, 173602 (2016).

[18] G. P. Conangla, A. W. Schell, R. A. Rica, and R. Quidant, Motion control and optical interrogation of a levitating single nitrogen vacancy in vacuum, Nano Lett. **18**, 3956 (2018).

[19] G. P. Conangla, R. A. Rica, and R. Quidant, Extending vacuum trapping to absorbing objects with hybrid paul-optical traps, Nano Lett. **20**, 6018 (2020).

[20] T. Delord, P. Huillery, L. Nicolas, and G. Hétet, Spin-cooling of the motion of a trapped diamond, Nature (London) **580**, 56 (2020).

[21] T. Wang, S. Lourette, S. R. O'Kelley, M. Kayci, Y. B. Band, D. F. J. Kimball, A. O. Sushkov, and D. Budker, Dynamics of a Ferromagnetic Particle Levitated over a Superconductor, Phys. Rev. Appl. **11**, 044041 (2019).

[22] C. Timberlake, G. Gasbarri, A. Vinante, A. Setter, and H. Ulbricht, Acceleration sensing with magnetically levitated oscillators above a superconductor, Appl. Phys. Lett. **115**, 224101 (2019).

[23] A. Vinante, P. Falferi, G. Gasbarri, A. Setter, C. Timberlake, and H. Ulbricht, Ultralow Mechanical Damping with Meissner-Levitated Ferromagnetic Microparticles, Phys. Rev. Appl. **13**, 064027 (2020).

[24] J. Gieseler, A. Kabcenell, E. Rosenfeld, J. D. Schaefer, A. Safira, M. J. A. Schuetz, C. Gonzalez-Ballestero, C. C. Rusconi, O. Romero-Isart, and M. D. Lukin, Single-Spin Magnetomechanics with Levitated Micromagnets, Phys. Rev. Lett. **124**, 163604 (2020).

[25] C. W. Lewandowski, T. D. Knowles, Z. B. Etienne, and B. D'Urso, High-Sensitivity Accelerometry with a Feedback-Cooled Magnetically Levitated Microsphere, Phys. Rev. Appl. **15**, 014050 (2021).

[26] M. G. Latorre, A. Paradkar, D. Hambraeus, G. Higgins, and W. Wieczorek, A chip-based superconducting magnetic trap for levitating superconducting microparticles, IEEE Trans. Appl. Supercond. **32**, 1 (2022).

[27] M. G. Latorre, G. Higgins, A. Paradkar, T. Bauch, and W. Wieczorek, Superconducting microsphere magnetically levitated in an anharmonic potential, arXiv:2210.13451.

[28] O. Romero-Isart, L. Clemente, C. Navau, A. Sanchez, and J. I. Cirac, Quantum Magnetomechanics with Levitating Superconducting Microspheres, Phys. Rev. Lett. **109**, 147205 (2012).

[29] C. Zhang, Y. Xu, J. Liu, J. Li, J. Xiang, H. Li, J. Li, Q. Dai, S. Lan, and A. E. Miroshnichenko, Lighting up silicon nanoparticles with mie resonances, Nat. Commun. **9**, 2964 (2018).

[30] A. Ashkin and J. M. Dziedzic, Observation of Resonances in the Radiation Pressure on Dielectric Spheres, Phys. Rev. Lett. **38**, 1351 (1977).

[31] R. Grimm, M. Weidemüller, and Y. B. Ovchinnikov, *Optical Dipole Traps for Neutral Atoms*, Advances In Atomic, Molecular, and Optical Physics Vol. 42 (Academic Press, New York, 2000), pp. 95–170, 10.1016/S1049-250X(08)60186-X.

[32] A. Kaplan, N. Friedman, and N. Davidson, Optimized single-beam dark optical trap, J. Opt. Soc. Am. B **19**, 1233 (2002).

[33] A. Jaouadi, N. Gaaloul, B. Viaris de Lesegno, M. Telmini, L. Pruvost, and E. Charron, Bose-Einstein condensation in dark power-law laser traps, Phys. Rev. A **82**, 023613 (2010).

[34] M. L. Juan, G. Molina-Terriza, T. Volz, and O. Romero-Isart, Near-field levitated quantum optomechanics with nanodiamonds, Phys. Rev. A **94**, 023841 (2016).

[35] F. Le Kien, V. I. Balykin, and K. Hakuta, Atom trap and waveguide using a two-color evanescent light field around a subwavelength-diameter optical fiber, Phys. Rev. A **70**, 063403 (2004).

[36] E. Vetsch, D. Reitz, G. Sagué, R. Schmidt, S. T. Dawkins, and A. Rauschenbeutel, Optical Interface Created by Laser-Cooled Atoms Trapped in the Evanescent Field Surrounding an Optical Nanofiber, Phys. Rev. Lett. **104**, 203603 (2010).

[37] K. J. Vahala, Optical microcavities, Nature (London) **424**, 839 (2003).

[38] Y. Akahane, T. Asano, B.-S. Song, and S. Noda, High-q photonic nanocavity in a two-dimensional photonic crystal, Nature (London) **425**, 944 (2003).

[39] P. B. Deotare, M. W. McCutcheon, I. W. Frank, M. Khan, and M. Lončar, High quality factor photonic crystal nanobeam cavities, Appl. Phys. Lett. **94**, 121106 (2009).

[40] L. Magrini, R. A. Norte, R. Riedinger, I. Marinković, D. Grass, U. Delić, S. Gröblacher, S. Hong, and M. Aspelmeyer, Near-field coupling of a levitated nanoparticle to a photonic crystal cavity, Optica **5**, 1597 (2018).

[41] A. Ranfagni, P. Vezio, M. Calamai, A. Chowdhury, F. Marino, and F. Marin, Vectorial polaritons in the quantum motion of a levitated nanosphere, Nat. Phys. **17**, 1120 (2021).

[42] A. de los Ríos Sommer, N. Meyer, and R. Quidant, Strong optomechanical coupling at room temperature by coherent scattering, Nat. Commun. **12**, 276 (2021).

[43] T. Čižmár, V. Garcés-Chávez, K. Dholakia, and P. Zemánek, Optical conveyor belt for delivery of submicron objects, Appl. Phys. Lett. **86**, 174101 (2005).

[44] O. Brzobohatý, V. Karásek, M. Šiler, L. Chvátal, T. Čižmár, and P. Zemánek, Experimental demonstration of optical transport, sorting and self-arrangement using a ‘tractor beam’, Nat. Photonics **7**, 123 (2013).

[45] D. Grass, J. Fesel, S. G. Hofer, N. Kiesel, and M. Aspelmeyer, Optical trapping and control of nanoparticles inside evacuated hollow core photonic crystal fibers, Appl. Phys. Lett. **108**, 221103 (2016).

[46] M. Nikkhou, Y. Hu, J. A. Sabin, and J. Millen, Direct and clean loading of nanoparticles into optical traps at millibar pressures, Photonics **8**, 458 (2021).

[47] T. A. Nieminen, V. L. Loke, A. B. Stilgoe, G. Knöner, A. M. Brańczyk, N. R. Heckenberg, and H. Rubinsztein-Dunlop, Optical tweezers computational toolbox, J. Opt. A **9**, S196 (2007).

[48] L. Novotny and B. Hecht, *Principles of Nano-Optics* (Cambridge University Press, Cambridge, England, 2012).

[49] See Supplemental Material at http://link.aps.org/supplemental/10.1103/PhysRevLett.130.233601, which includes the Refs. [50–54], for more details on the trap characterization, the effective particle polarizability, Mie scattering and absorption cross section and the derivation of the internal temperature of the particle.

[50] J. Chen, J. Ng, Z. Lin, and C. T. Chan, Optical pulling force, Nat. Photonics **5**, 531 (2011).

[51] A. B. Evlyukhin, T. Fischer, C. Reinhardt, and B. N. Chichkov, Optical theorem and multipole scattering of light by arbitrarily shaped nanoparticles, Phys. Rev. B **94**, 205434 (2016).

[52] Ø. Farsund and B. Felderhof, Force, torque, and absorbed energy for a body of arbitrary shape and constitution in an electromagnetic radiation field, Physica A (Amsterdam) **227**, 108 (1996).

[53] C. Schinke, P. Christian Peest, J. Schmidt, R. Brendel, K. Bothe, M. R. Vogt, I. Kröger, S. Winter, A. Schirmacher, S. Lim *et al.*, Uncertainty analysis for the coefficient of band-to-band absorption of crystalline silicon, AIP Adv. **5**, 067168 (2015).

[54] D. Chandler-Horowitz and P. M. Amirtharaj, High-accuracy, midinfrared ($450\ \mathrm{cm}^{-1} \leq \omega \leq 4000\ \mathrm{cm}^{-1}$) refractive index values of silicon, J. Appl. Phys. **97**, 123526 (2005).

[55] J. Degallaix, R. Flaminio, D. Forest, M. Granata, C. Michel, L. Pinard, T. Bertrand, and G. Cagnoli, Bulk optical absorption of high resistivity silicon at 1550 nm, Opt. Lett. **38**, 2047 (2013).

[56] E. D. Palik, *Handbook of Optical Constants of Solids* (Academic Press, New York, 1998), Vol. 3.

[57] Y. Kivshar and A. Miroshnichenko, Meta-optics with mie resonances, Opt. Photonics News **28**, 24 (2017).

[58] V. Jain, J. Gieseler, C. Moritz, C. Dellago, R. Quidant, and L. Novotny, Direct Measurement of Photon Recoil from a Levitated Nanoparticle, Phys. Rev. Lett. **116**, 243601 (2016).

[59] C. Gonzalez-Ballestero, P. Maurer, D. Windey, L. Novotny, R. Reimann, and O. Romero-Isart, Theory for cavity cooling of levitated nanoparticles via coherent scattering: Master equation approach, Phys. Rev. A **100**, 013805 (2019).

[60] P. Maurer, C. Gonzalez-Ballestero, and O. Romero-Isart, Quantum theory of light interaction with a dielectric sphere: Towards 3D ground-state cooling, arXiv:2212.04838.

[61] C. F. Bohren and D. R. Huffman, *Absorption and Scattering of Light by Small Particles* (John Wiley & Sons, New York, 2008).

[62] L. Landström and P. Heszler, Analysis of blackbody-like radiation from laser-heated gas-phase tungsten nanoparticles, J. Phys. Chem. B **108**, 6216 (2004).

[63] J. Bateman, S. Nimmrichter, K. Hornberger, and H. Ulbricht, Near-field interferometry of a free-falling nanoparticle from a point-like source, Nat. Commun. **5**, 1 (2014).

[64] F. Tebbenjohanns, M. Frimmer, and L. Novotny, Optimal position detection of a dipolar scatterer in a focused field, Phys. Rev. A **100**, 043821 (2019).

[65] J. S. Bennett, K. Khosla, L. S. Madsen, M. R. Vanner, H. Rubinsztein-Dunlop, and W. P. Bowen, A quantum optomechanical interface beyond the resolved sideband limit, New J. Phys. **18**, 053030 (2016).

[66] A. A. Geraci, S. B. Papp, and J. Kitching, Short-Range Force Detection Using Optically Cooled Levitated Microspheres, Phys. Rev. Lett. **105**, 101101 (2010).

[67] P. Forn-Díaz, L. Lamata, E. Rico, J. Kono, and E. Solano, Ultrastrong coupling regimes of light-matter interaction, Rev. Mod. Phys. **91**, 025005 (2019).

APPENDIX E

Paper 5: Switchable dual-mode nanolaser: mastering emission and invisibility through phase transition materials

A nanolaser capable of switching between emission and cloaking regimes is suggested and theoretically investigated. The manuscript is published.

The citations in the manuscript refer to reference list included at the end of the manuscript.

Work contributions by the present author: Analytical and numerical calculations, manuscript writing.

Reference information:

S. Lepeshov, A. Vyshnevyy, and A. Krasnok. Switchable dual-mode nanolaser: mastering emission and invisibility through phase transition materials. *Nanophotonics* 12, 3729-3736 (2023).

Research Article

Sergey Lepeshov, Andrey Vyshnevyy and Alex Krasnok*

Switchable dual-mode nanolaser: mastering emission and invisibility through phase transition materials

https://doi.org/10.1515/nanoph-2023-0249
Received April 22, 2023; accepted August 17, 2023;

Abstract: The principle of detailed balance states that objects efficiently emitting radiation at a specific wavelength also efficiently absorb radiation at the same wavelength. This principle presents challenges for the design and performance of photonic devices, including solar cells, nanoantennas, and lasers. A design that successfully integrates the properties of an efficient emitter in one state and invisibility in another state is essential for various applications. In this work, we propose a novel nanolaser design based on a semiconductor nanoparticle with gain enveloped by a phase transition material that enables switching between lasing and cloaking (nonscattering) states at the same operating frequency without modifying the pumping conditions. We thoroughly investigate the operational characteristics of the nanolaser to ensure optimal performance. Our nanolaser design can function with both optical and electric pumping and exhibits the features of a thresholdless laser due to its high beta-factor and strong Purcell enhancement in the tightly confined Mie resonance mode. Additionally, we develop a reconfigurable metasurface comprising lasing-cloaking metaatoms capable of transitioning from lasing to a nonscattering state in a fully reversible manner.

Keywords: nanolaser; invisibility; phase transition materials

1 Introduction

The principle of detailed balance states that efficient light emitters must also strongly interact with light through enhanced absorption and scattering [1–6]. This principle is fundamental for microwave, terahertz (THz), and optical emitters, as it requires equal radiation and reception efficiencies [7–9]. It also leads to Kirchhoff's law, connecting spectral emissivity and absorptivity for systems in thermal equilibrium [10]. This principle enables dual devices, such as receiving-transmitting antennas and radar systems [7], emitting–absorbing nanoantennas [11], and optically pumped laser LEDs [12]. However, these interactions impose fundamental constraints on optical device performance across the spectrum. For example, solar cells with high absorption often face reduced conversion efficiency due to increased thermal radiation, while low-emissivity cells compromise solar energy absorption [13–15]. An ideal solar cell would also be a perfect LED, but the detailed balance prevents this [5]. Overcoming these limitations typically involves nonreciprocal materials based on using strong magnetic field biases, optical nonlinearity, or time-variation methods [2]. Alternatively, distinguishing between light emission and absorption/scattering effects in the frequency or time domain can be employed in a tunable or reconfigurable system.

Modern trends in miniaturization require nanophotonic devices to work in both light-emitting and light-absorbing regimes while becoming invisible to avoid interference with other elements. The shift to nanoscale optical devices has led to the development of nanolasers, a new class of coherent emitters. The concept of surface plasmon amplification by stimulated emission of radiation (SPASER), introduced by David Bergman and Mark Stockman in 2003, marked the beginning of spasers and nanolasers [16]. Numerous designs have since emerged [17], with noble metal nanoparticle-encased active media being particularly promising for optimal overlap between material gain and lasing mode [18–22]. More recently, semiconductor-based nanolasers have become low-threshold, efficient

---

***Corresponding author: Alex Krasnok**, Department of Electrical and Computer Engineering, Florida International University, Miami, FL 33174, USA; and Knight Foundation School of Computing and Information Sciences, Florida International University, Miami, FL 33199, USA, E-mail: akrasnok@fiu.edu. https://orcid.org/0000-0001-7419-781X
Sergey Lepeshov, Department of Electrical and Photonics Engineering, DTU Electro, Technical University of Denmark, DK-2800 Kgs. Lyngby, Denmark, E-mail: serle@dtu.dk. https://orcid.org/0000-0001-5674-1666
Andrey Vyshnevyy, Emerging Technologies Research Center, XPANCEO, Dubai Investment Park 1, Dubai, United Arab Emirates, E-mail: vyshnevyy@xpanceo.com. https://orcid.org/0000-0003-1394-4169

alternatives to plasmonic spasers [23, 24], with perovskites and quantum dot (QD) inclusions attracting attention for their high material gain and optical activity [25–28]. Nanolasers have been successful in applications such as sensing, biological probing, super-resolution imaging, vortex beam generation, on-chip integrated optical interconnects, and all-optical data processing [19].

However, nanolasers show enhanced scattering, especially at the lasing threshold [28], which imposes limitations on their use in optical interconnections and sensing. Differentiating light emission from absorption and scattering phenomena in nanolasers is challenging due to the inability of existing nanolaser designs to shift between various scattering states. They are restricted to transitioning between narrowband laser emissions and broadband resonant or nonresonant scattering by modifying the pump intensity. Recently proposed anapolar lasers have gained attention due to their potential to lower the lasing threshold intensity in configurations that utilize optical pumping [29, 30]. Transitioning this nanolaser to another scattering mode, like one with suppressed scattering from an anapole, necessitates turning off optical pumping, fundamentally altering the system. All this raises the question: *can a nanolaser be cloaked without modifying its pumping conditions?*

In this work, we present a novel method that enables a nanolaser to switch between emission and cloaking (nonscattering) modes at the same operating frequency. Our design features a core–shell nanostructure composed of a semiconductor nanoparticle (NP) enveloped by a phase change material (PCM) [31–33]. The PCM shell enables the refractive index change via the transition between amorphous and crystalline states. This unique nanostructure allows reversible switching between two optical states: coherent light emission [Figure 1(a)] and cloaking [Figure 1(b)]. The cloaking phase is linked to the excitation of an anapole state [34–36]. We investigate the dynamics of the proposed tunable nanolaser in the frequency domain and input-output characteristics in the stationary state. Additionally, by utilizing this single lasing-cloaking metaatom, we develop a reconfigurable metasurface capable of reversibly transitioning from laser radiation to a nonscattering state. We demonstrate that this intelligently designed nanolaser can indeed be cloaked and subsequently restored to the laser state without altering its pumping conditions.

2 Results and discussion

We consider a spherical core–shell nanostructure made of a semiconductor core with material gain and an antimony trisulfide (Sb_2S_3) shell. Sb_2S_3 is a prospective phase-change material with a high dielectric constant, low losses, and strong tunability in the visible range [37, 38]. The permittivity dispersion of Sb_2S_3 (see Supplementary Information) indicates the broadband transparency of this material above the wavelength of 600 nm (frequency below 500 THz) in the amorphous phase.

We assume that the permittivity of the semiconductor core obeys the Drude–Lorentz model [28]:

$$\varepsilon_c(\omega) = \varepsilon_\infty - \frac{f\omega_0^2}{\omega_0^2 - \omega^2 - i\Gamma\omega}, \tag{1}$$

where $\varepsilon_\infty = 13.5$ is the dispersionless part of the permittivity, ω is the angular frequency of light, $\omega_0/2\pi = 474$ THz is the resonant frequency of dipole transitions, $\Gamma = 10^{13}$ s^{-1} is the polarization decay rate, and f is the oscillator strength related to the material gain g and speed of light c as [39] $f = gc\Gamma\sqrt{\varepsilon_\infty}/\omega_0^2$. Chosen parameters are achievable by

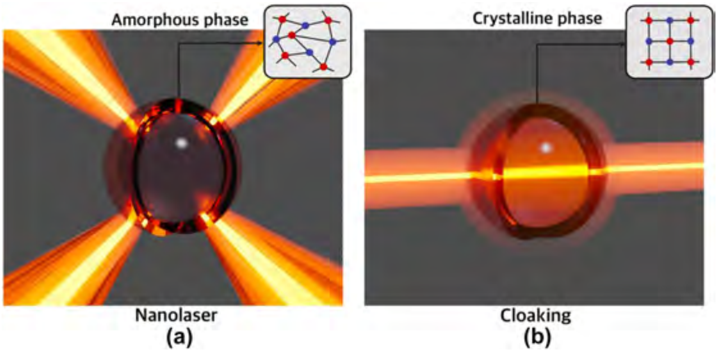

Figure 1: Cloaking a nanolaser. Illustration of the core–shell nanostructure supporting reversible switch between (a) nanolaser regime and (b) cloaking (anapole) regime at the same frequency.

QDs and perovskites at room temperature [28]. The permittivity of 13.5 is typical for high-index semiconductors like GaAs, GaP, InAs, and others. The resonant frequency ω_0 is optimized to achieve maximum spectral overlap with the laser mode.

This model allows us to study the core–shell nanostructure in optically passive ($g \leq 0$) and active ($g > 0$) regimes. To this end, we chose the core radius of $R_c = 109$ nm and the radius of the shell of $R_s = 125$ nm. The optical response of the spherically symmetric core–shell nanostructure can be described by the generalized Mie theory [40]. The scattering cross-section (SCS) spectrum of the nanostructure can be calculated from the Mie multipole expansion [40, 41]:

$$\mathrm{SCS} = \frac{2}{(kR_s)^2}\sum_{l=1}^{\infty}(2l+1)\left(|a_l|^2 + |b_l|^2\right), \tag{2}$$

where l is the multipole order, $k = \omega/c$ is the vacuum wavenumber, a_l and b_l are the frequency-dependent electric and magnetic multipole scattering coefficients.

According to the scattering theory, the optical properties of a system are defined by the eigenmodes of the system, which appear as poles of the scattering matrix coefficients at the corresponding complex eigenfrequencies [42]. Thus, to study the eigenmodes, eigenfrequencies, and their dynamics in the frequency domain, we calculate the SCS of the core–shell nanostructure in the complex frequency plane ($\omega = \omega' + i\omega''$).

The SCS of a passive ($g = 0$) core–shell nanostructure in an amorphous phase depending on the imaginary frequency $\omega''/2\pi$ and wavelength $\lambda = 2\pi c/\omega'$ is shown in Figure 2(a). Due to passivity, the poles associated with the electric and magnetic multipoles of different order are observed in the lower complex frequency plane. The first four modes are magnetic dipole (MD) with an extracted eigenfrequency $\omega_{\mathrm{MD}}/2\pi = 330.6–13.25i$ THz, electric dipole (ED) with $\omega_{\mathrm{ED}}/2\pi = 456–47.75i$ THz, magnetic quadrupole (MQ) with $\omega_{\mathrm{MQ}}/2\pi = 474.0–4.5i$ THz, and electric quadrupole (EQ) with $\omega_{\mathrm{EQ}}/2\pi = 570–13.9i$ THz. The laser threshold can be estimated via the quality factor (Q-factor) of the mode of interest, or in other words, by the amount of gain required to deliver the pole to the real axis [39, 42]. Our calculations reveal that the MQ mode has the highest Q-factor of $Q = 53$ among the first four, making this mode a promising candidate for the nanolaser.

The red marks in Figure 2(a) designate the minima of the SCS located at the real axis ($\omega'' = 0$). In literature, these minima are called non-scattering anapoles responsible for optical invisibility or cloaking [34, 35, 43]. Notably, the electric anapole (EA) is located near the MQ resonance, facilitating the tunability between MQ and EA states. The poles in the complex frequency plane project into resonances at the real axis, Figure 2(b). Also, note that anapole states are not eigenmodes of the system and, as such, they cannot lase, unlike poles [35]. We identify the multipole content of the investigated modes and anapoles of the core–shell in the

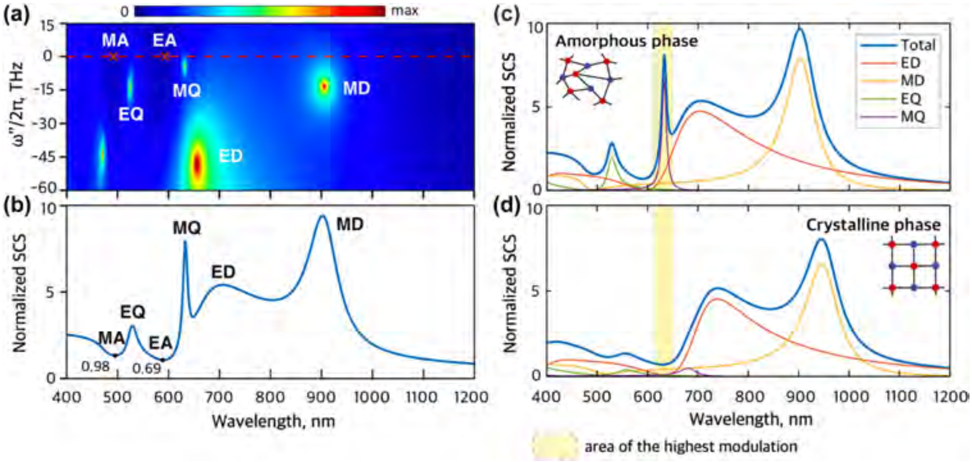

Figure 2: Passive core–shell nanostructure. (a) Normalized scattering cross-section (SCS) of a passive core–shell NP based on Sb_2S_3 shell and semiconductor core depending on wavelength ($\lambda = 2\pi c/\omega'$) and imaginary part of frequency. The bright points (MD, ED, MQ, EQ) on the map represent poles of SCS, i.e., eigenfrequencies of the NP. The red marks (EA, MA) correspond to anapoles of the NP. (b) Normalized SCS at zero imaginary frequency depending on wavelength. (c, d) Multipole decomposition of normalized SCS of the core–shell NP in the amorphous (c) and crystalline (d) phases. The yellow area emphasizes the spectral range of the highest modulation of SCS due to the phase change.

amorphous and crystalline phases by the multipole expansion of the scattering spectra, Figure 2(c and d). The transformation of the Sb_2S_3 shell from amorphous to crystalline state leads to a switch of the scattering response around 633 nm wavelength (yellow area) from MQ resonance to non-scattering EA state.

Next, we study the transition to lasing in the core–shell nanostructure achieved by introducing the material gain ($g > 0$). The nanostructure is designed to maximize the overlap between the lasing MQ mode and material gain. The electric field distribution and the radiation pattern of this mode are shown in the insert of Figure 3(a). After introducing a non-zero value of the material gain, the NP modes start interacting with the material dipole transition, and the initial MQ mode splits into two modes. These modes appear as new distinct poles in the complex frequency plane. Upon increasing the material gain, the poles of the nanostructure shift from their initial positions marked by the green crosses in Figure 3(b). One reaches the real axis when the material gain reaches as high as $g\text{th} = 9.5 \times 10^3$ cm^{-1}, marking the transition to lasing [28, 42]. The transition is accompanied by a sharpening of the SCS at the wavelength of laser radiation, as shown in Figure 3(a). Remarkably, pumping of the gain medium does not significantly change the scattering properties of the nanostructure in the crystalline phase that remains cloaked (Figure 3(c)).

The dynamics of the nanolaser is complicated since the polarization decay rate Γ of the dipole transition in the core is lower than the photonic decay rate of MQ mode $\kappa = 5.65 \times 10^{13}$ s^{-1}. As a result, the dipole moment of the nanolaser gain medium cannot be adiabatically eliminated, which is sometimes referred to as a “superradiant regime” [44, 45]. For simulation of the input–output characteristic, we employ an approach that incorporates collective polarization correlations of emitters in the core into the densities of states and frequency-dependent population functions, thereby obtaining the spontaneous and stimulated emission rates in the convenient form of Fermi’s “golden rule” integrals [46]. Thus, the spontaneous (R_{sp}) and stimulated (R_{stim}) emission rates into the laser mode are evaluated as

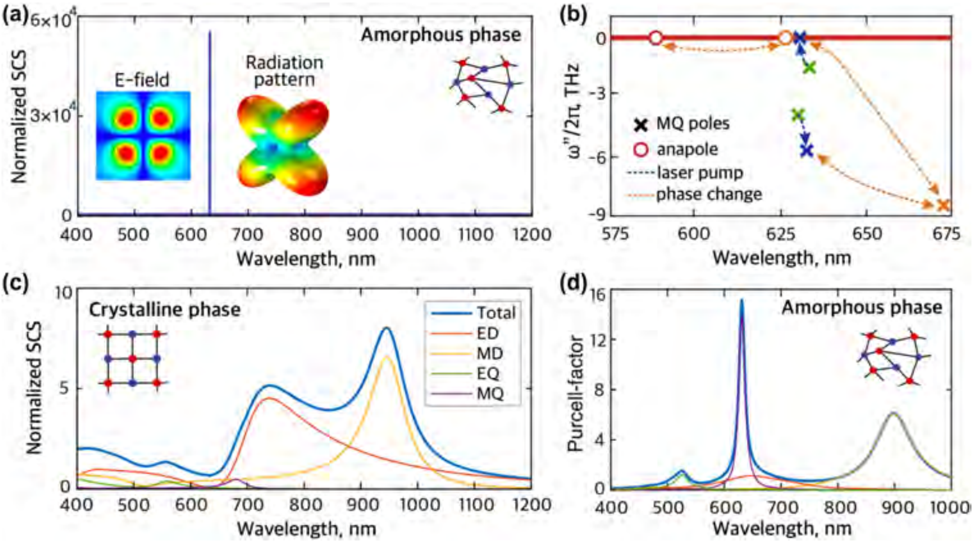

Figure 3: Active core–shell nanostructure. (a) Spectral dependence of normalized SCS of the NP with material gain $g = 9.5 \times 10^3$ cm^{-1} in the amorphous phase of the Sb_2S_3 shell and its multipole decomposition. The ultra-high peak of SCS at 633 nm in the amorphous phase corresponds to the laser regime. Insert shows the electric field profile and radiation pattern of the lasing mode (MQ). (b) Scheme of dynamics of poles and anapole (scattering zero) of the NP upon the laser pump and phase change. Different colors label poles and anapole corresponding to different states. Green corresponds to the system with the core in the amorphous state and ultimately small $g \to 0$. Blue denotes the transition of the NP to the nanolaser (the phase remains amorphous) with $g = 9.5 \times 10^3$ cm^{-1} as the laser pump rises. Orange indicates reversible tuning between amorphous and crystalline phases. (c) Normalized SCS spectrum of the NP with $g = 9.5 \times 10^3$ cm^{-1} in the crystalline phase and its multipole decomposition. The pronounced dip in the crystalline phase is observed around 633 nm. (d) Purcell factor and its partial contributions from different modes of the NP with amorphous shell depending on wavelength.

(see more details on the nanolaser model and coherence in Supplementary Information):

$$R_{\mathrm{sp}} = \frac{1}{4} G\Gamma \frac{n_2(1-n_1)}{n_2-n_1} \frac{\kappa+\Gamma-G/2}{(\omega_0-\omega_{\mathrm{MQ}})^2 + \left(\frac{\kappa+\Gamma-G/2}{2}\right)^2} \tag{3}$$

$$R_{\mathrm{stim}} = \kappa N_p - R_{\mathrm{sp}} \tag{4}$$

where n_2 and n_1 are occupation numbers of the excited and ground states of dipolar transition, $G = \kappa \frac{g}{g_{\mathrm{th}}}\left[1 + 4\left(\frac{\omega_0-\omega_{\mathrm{MQ}}}{\kappa+\Gamma}\right)^2\right]$ and the number of photons in the cavity is:

$$N_{\mathrm{p}} = \frac{\Gamma}{\Gamma+\kappa} \frac{n_2(1-n_1)}{n_2-n_1} \frac{g}{g_{\mathrm{th}}-g} \tag{5}$$

Equations (3)–(5) imply that, in the steady state, the pole cannot cross or even reach the real axis since, as g approaches gth, the number of photons in the cavity grows infinitely. Also, from Eq. (3), it is evident that the beta-factor, i.e., the ratio of spontaneous emission into the laser mode to the total spontaneous emission into all modes, explicitly depends on the material gain, and therefore, it is not a parameter of the nanolaser.

To evaluate spontaneous emission into non-lasing modes, we have numerically determined the spectrum of Purcell enhancement $F(\omega)$ for a monochromatic emitter in the core and performed its multipole decomposition. The result, shown in Figure 3(d), is averaged over dipole orientations and positions within the core [47, 48]. From the Purcell enhancement spectrum, we were able to rigorously compute the beta-factor at transparency ($g = 0$) using: $\beta_0 = \frac{\int_0^\infty F_{\mathrm{MQ}}(\omega)\varepsilon''{}_c(\omega)\mathrm{d}\omega}{\int_0^\infty F(\omega)\varepsilon''{}_c(\omega)\mathrm{d}\omega}$, where $F_{\mathrm{MQ}}(\omega)$ is the contribution of the magnetic quadrupole mode to $F(\omega)$ while $\varepsilon''_c(\omega)$ is the imaginary part of the dielectric function $\varepsilon''_c(\omega)$, given by Eq. (1). After calculations, we obtain $\beta_0 = 0.841$. The emission rate into the nonlasing MD, ED, and EQ modes is: $R^{\mathrm{nl}}_{\mathrm{sp}} = \frac{1-\beta_0}{4\beta_0} G\Gamma \frac{n_2(1-n_1)}{n_2-n_1} \frac{\kappa+\Gamma}{(\omega_0-\omega_{\mathrm{MQ}})^2+(\kappa+\Gamma)^2/4}$. Finally, we include the nonradiative decay of excited emitters with the total rate $R_{\mathrm{nr}} = Nn_2(1-n_1)/\tau_{\mathrm{nr}}$, where $N = 1300$ is the number of emitters and $\tau_{\mathrm{nr}} = 1$ ns is the nonradiative lifetime.

The input-output characteristic of the nanolaser is shown in Figure 4(a). The log–log plot does not exhibit a distinct kink which makes it similar to thresholdless lasers [49, 50]. This can be attributed to the high beta-factor close to 1, and strong Purcell enhancement in the strongly confined Mie resonance mode. The latter makes nonradiative recombination rates relatively small compared to the rates of radiative transitions. In a thresholdless nanolaser, it is impossible to recognize the transition to lasing based only on the input–output curve [51]. To make sure that we work with the correct part of the input–output curve, we have determined the emission linewidth as a function of the absorbed pump power, depicted in Figure 4(b), which clearly shows the onset of coherence at approximately 1 μW of absorbed pump power. On the plateau below 1 μW, the linewidth of about 2 nm is determined by the polarization dephasing rate of the gain medium rather than the lifetime of the cavity photons. Upon increasing the absorbed pump power above 1 μW, the laser linewidth decreases inversely proportional to the output power, which agrees with the Schawlow–Townes law [52] and experimentally observed linewidth dependence in thresholdless nanolasers [49, 50]. As indicated by Figure 4(c), the line narrowing coincides with the onset of stimulated emission in our structure, hence the input–output curve in Figure 4(a) shows the nanolaser operating in the spontaneous emission regime at low powers, the lasing regime dominated by the stimulated emission at high powers and transitional amplified spontaneous emission regime between them. At the same time, linewidth narrowing does not guarantee that the statistics of emitted photons would be Poissonian, as it should be for the coherent state [53]. The number of photons

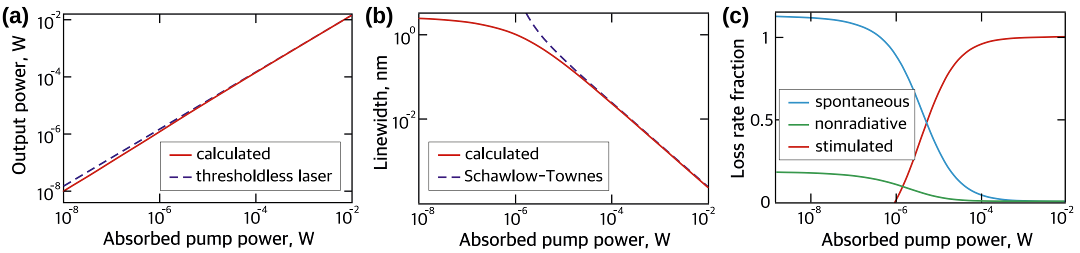

Figure 4: The nanolaser characteristics. (a) Light input–light output curve of the nanolaser. The blue dashed line corresponds to the characteristic of an ideal thresholdless nanolaser (for comparison). (b) Calculated linewidth of the nanolaser as a function of the pump power. (c) Fractions of spontaneous, stimulated emission rates and nonradiative decay in the total pump rate.

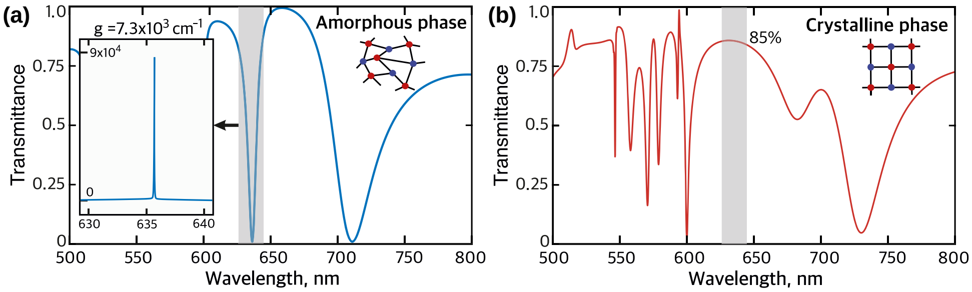

Figure 5: Cloaking a metasurface. (a) Transmittance spectrum of a metasurface composed of a square array of core–shell NPs in amorphous phase without gain. The insert shows the transmittance spectrum in the amorphous phase with gain of 7.3 × 10^3 cm^{-1} in the shaded spectral region. (b) Transmittance spectrum of the metasurface in the crystalline phase with the same gain.

in the cavity [51] is estimated as $N_\text{p} \approx \sqrt{N g_{th}/(dg/dn_2)} \approx 23$, which corresponds to the absorbed pump power of 0.2 mW. However, more accurate calculation (see Supplementary Information) reveals that the laser crosses the coherence threshold at 50 μW, when the mean photon number in the laser mode is 5.7.

Finally, we arrange the core–shell NPs in a square lattice to thoroughly investigate the previously mentioned effects within a more practical metasurface-based transmitter application. The metasurface features a 600 nm period, with NP core and shell radii measuring 109 nm and 125 nm, respectively. We conduct comprehensive numerical analysis of the metasurface's transmittance spectra in both amorphous and crystalline phases, incorporating and excluding gain, using COMSOL Multiphysics (see Figure 5). In the amorphous phase, the passive metasurface transmittance spectrum exhibits a distinct resonance near the magnetic quadrupole (MQ) resonance (Figure 5(a), shaded area). The resonance position is slightly shifted to the longer wavelengths due to interparticle interactions. The Q-factor of the resonance is increased with respect to the single NP MQ resonance, which is explained by the collective coupling of the NPs. This heightened Q-factor facilitates a lower gain lasing threshold.

The insert in Figure 5(a) shows the transmittance spectrum of the amorphous phase metasurface with gain of 7.3 × 10^3 cm^{-1}, around 25 % less than the initial gain of the single NP. The transmittance reveals an ultrasharp peak related to the nanolaser regime when the pole of the metasurface scattering matrix reaches the axis of real frequencies. However, after the phase change from amorphous to crystalline, the peak turns to a broad nonresonant response characterized by approximately 85 % transmittance from 625 nm to 645 nm wavelength, Figure 5(b). This allows us to conclude that the metasurface based on core–shell NPs can be reversibly switched from the emitting nanolaser regime to the transparent cloaking state.

While our study does not specify a particular semiconductor core material for the sake of generalization, the dielectric permittivity we used closely resembles that of indium phosphide (InP), and our design can be readily adapted to other active semiconductor materials, such as III–V semiconductors (GaAs with InGaAs quantum dots) or perovskite materials ($CH_3NH_3PbI_3$, $CsPbX_3$) [28].

3 Conclusions

In this work, we have put forth a nanolaser design that utilizes a semiconductor nanoparticle with gain, coated by a film of phase change material. This design enables the nanolaser to switch between lasing and cloaking modes at the same operating frequency. The cloaking phase of the nanostructure is linked to the anapole state. We have thoroughly examined the operational characteristics of the nanolaser. This nanolaser demonstrates thresholdless laser properties, lacking a noticeable kink in the input-light output curve due to the elevated betta and Purcell factors. Remarkably, the nanolaser functions in the superradiant regime because of the significant cavity losses. In this regime, the macroscopic dipole moment of the gain medium permits the attainment of the threshold at a reduced gain. A unique aspect of this regime is its narrower linewidth, determined by the emitters' dephasing rate rather than the cavity quality factor. Furthermore, we have developed a reconfigurable metasurface composed of lasing-cloaking metaatoms, which can switch from laser radiation to a nonscattering state reversibly. Our findings hold potential for various photonic and nano-optical systems, particularly in situations where the light source needs the ability to transition to a transparent state.

Acknowledgments: Authors thank Dr. Andrea Alu for fruitful discussions. Alex Krasnok thanks the ECE department of Florida International University.

Research funding: Alex Krasnok thanks the ECE department of Florida International University.

Author contribution: All authors have accepted responsibility for the entire content of this manuscript and approved its submission. All the authors discussed the results.

Conflict of interest: Authors state no conflicts of interest.

Informed consent: Informed consent was obtained from all individuals included in this study.

Ethical approval: The conducted research is not related to either human or animal use.

Data availability: The datasets generated and/or analyzed during the current study are available from the corresponding author upon reasonable request.

References

[1] H. A. Lorentz, “The theorem of Poynting concerning the energy in the electromagnetic field and two general propositions concerning the propagation of light,” *Amsterdammer Akad. Wet.*, vol. 4, p. 176, 1896.

[2] S. V. Kutsaev, A. Krasnok, S. N. Romanenko, A. Y. Smirnov, K. Taletski, and V. P. Yakovlev, “Up-and-coming advances in optical and microwave nonreciprocity: from classical to quantum realm,” *Adv. Photonics Res.*, vol. 2, no. 3, p. 2000104, 2021.

[3] C. Caloz, A. Alù, S. Tretyakov, D. Sounas, K. Achouri, and Z.-L. Deck-Léger, “Electromagnetic nonreciprocity,” *Phys. Rev. Appl.*, vol. 10, no. 4, p. 047001, 2018.

[4] V. S. Asadchy, M. S. Mirmoosa, A. Diaz-Rubio, S. Fan, and S. A. Tretyakov, “Tutorial on electromagnetic nonreciprocity and its origins,” *Proc. IEEE*, vol. 108, no. 10, pp. 1684—1727, 2020.

[5] U. Rau, “Reciprocity relation between photovoltaic quantum efficiency and electroluminescent emission of solar cells,” *Phys. Rev. B*, vol. 76, no. 8, p. 085303, 2007.

[6] A. E. Krasnok, A. Maloshtan, D. N. Chigrin, Y. S. Kivshar, and P. A. Belov, “Enhanced emission extraction and selective excitation of NV centers with all-dielectric nanoantennas,” *Laser Photonics Rev.*, vol. 9, no. 4, pp. 385—391, 2015.

[7] C. Balanis, *Antenna Theory*, Hoboken, New Jersey, Wiley, 2005.

[8] D. M. Pozar, *Microwave Engineering*, 4th ed. Hoboken, New Jersey, John Wiley & Sons, Inc., 2011.

[9] L. Novotny and B. Hecht, *Principles of Nano-Optics*, 2nd ed. New York, Cambridge University Press, 2012, p. 9781107005.

[10] D. G. Baranov, Y. Xiao, I. A. Nechepurenko, A. Krasnok, A. Alù, and M. A. Kats, “Nanophotonic engineering of far-field thermal emitters,” *Nat. Mater.*, vol. 18, no. 9, pp. 920—930, 2019.

[11] Z. Zhao, Y. Shi, K. Chen, and S. Fan, “Relation between absorption and emission directivities for dipoles coupled with optical antennas,” *Phys. Rev. A*, vol. 98, no. 1, p. 013845, 2018.

[12] J. Roh, Y. S. Park, J. Lim, and V. I. Klimov, “Optically pumped colloidal-quantum-dot lasing in LED-like devices with an integrated optical cavity,” *Nat. Commun.*, vol. 11, no. 1, p. 271, 2020.

[13] T. Markvart, “Can thermodynamics guide us to make better solar cells?” *IEEE J. Photovolt.*, vol. 9, no. 6, pp. 1614—1624, 2019.

[14] W. Shockley and H. J. Queisser, “Detailed balance limit of efficiency of p-n junction solar cells,” *J. Appl. Phys.*, vol. 32, no. 3, pp. 510—519, 1961.

[15] T. Markvart, “Ideal solar cell efficiencies,” *Nat. Photonics*, vol. 15, no. 3, pp. 163—164, 2021.

[16] D. J. Bergman and M. I. Stockman, “Surface plasmon amplification by stimulated emission of radiation: quantum generation of coherent surface plasmons in nanosystems,” *Phys. Rev. Lett.*, vol. 90, no. 2, p. 027402, 2003.

[17] M. I. Stockman, “The spaser as a nanoscale quantum generator and ultrafast amplifier,” *J. Opt.*, vol. 12, no. 2, p. 024004, 2010.

[18] Y. Liang, C. Li, Y. Huang, and Q. Zhang, “Plasmonic nanolasers in on-chip light sources: prospects and challenges,” *ACS Nano*, vol. 14, no. 11, pp. 14375—14390, 2020.

[19] R.-M. Ma and R. F. Oulton, “Applications of nanolasers,” *Nat. Nanotechnol.*, vol. 14, no. 1, pp. 12—22, 2019.

[20] H. Wu, Y. Gao, P. Xu, et al., “Plasmonic nanolasers: pursuing extreme lasing conditions on nanoscale,” *Adv. Opt. Mater.*, vol. 7, no. 17, p. 1900334, 2019.

[21] S. Gwo and C. Shih, “Semiconductor plasmonic nanolasers: current status and perspectives,” *Rep. Prog. Phys.*, vol. 79, no. 8, p. 086501, 2016.

[22] M. A. Noginov, G. Zhu, A. M. Belgrave, et al., “Demonstration of a spaser-based nanolaser,” *Nature*, vol. 460, no. 7259, pp. 1110—1112, 2009.

[23] T. X. Hoang, S. T. Ha, Z. Pan, et al., “Collective Mie resonances for directional on-chip nanolasers,” *Nano Lett.*, vol. 20, no. 8, pp. 5655—5661, 2020.

[24] C.-Z. Ning, “Semiconductor nanolasers and the size-energy-efficiency challenge: a review,” *Adv. Photonics*, vol. 1, no. 01, p. 1, 2019.

[25] Q. Wei, X. Li, C. Liang, et al., “Recent progress in metal halide perovskite micro- and nanolasers,” *Adv. Opt. Mater.*, vol. 7, no. 17, p. 1900080, 2019.

[26] Z. Liu, J. Yang, J. Du, et al., “Robust subwavelength single-mode perovskite nanocuboid laser,” *ACS Nano*, vol. 12, no. 6, pp. 5923—5931, 2018.

[27] Z. Liu, S. Huang, J. Du, C. Wang, and Y. Leng, “Advances in inorganic and hybrid perovskites for miniaturized lasers,” *Nanophotonics*, vol. 9, no. 8, pp. 2251—2272, 2020.

[28] A. Krasnok and A. Alu, “Active nanophotonics,” *Proc. IEEE*, vol. 108, no. 5, pp. 628—654, 2020.

[29] A. Tripathi, H. R. Kim, P. Tonkaev, et al., “Lasing action from anapole metasurfaces,” *Nano Lett.*, vol. 21, no. 15, pp. 6563—6568, 2021.

[30] J. S. Totero Gongora, A. E. Miroshnichenko, Y. S. Kivshar, and A. Fratalocchi, “Anapole nanolasers for mode-locking and ultrafast pulse generation,” *Nat. Commun.*, vol. 8, no. 1, p. 15535, 2017.

[31] S. Lepeshov and A. Krasnok, “Tunable phase-change metasurfaces,” *Nat. Nanotechnol.*, vol. 16, no. 6, pp. 615—616, 2021.

[32] S. Abdollahramezani, O. Hemmatyar, M. Taghinejad, et al., “Electrically driven reprogrammable phase-change metasurface reaching 80% efficiency,” *Nat. Commun.*, vol. 13, no. 1, p. 1696, 2022.

[33] S. Abdollahramezani, O. Hemmatyar, H. Taghinejad, et al., “Tunable nanophotonics enabled by chalcogenide phase-change materials,” *Nanophotonics*, vol. 9, no. 5, pp. 1189—1241, 2020.

[34] K. V. Baryshnikova, D. A. Smirnova, B. S. Luk'yanchuk, and Y. S. Kivshar, "Optical anapoles: concepts and applications," *Adv. Opt. Mater.*, vol. 7, no. 14, p. 1801350, 2019.

[35] F. Monticone, D. Sounas, A. Krasnok, and A. Alù, "Can a nonradiating mode Be externally excited? Nonscattering states versus embedded eigenstates," *ACS Photonics*, vol. 6, no. 12, pp. 3108–3114, 2019.

[36] S. Lepeshov, A. Krasnok, and A. Alù, "Nonscattering-to-Superscattering switch with phase-change materials," *ACS Photonics*, vol. 6, no. 8, pp. 2126–2132, 2019.

[37] S. K. Chamoli, G. Verma, S. C. Singh, and C. Guo, "Phase change material-based nano-cavity as an efficient optical modulator," *Nanotechnology*, vol. 32, no. 9, p. 095207, 2021.

[38] W. Dong, H. Liu, J. K. Behera, et al., "Wide bandgap phase change material tuned visible photonics," *Adv. Funct. Mater.*, vol. 29, no. 6, p. 1806181, 2019.

[39] A. Y. Song, A. R. K. Kalapala, W. Zhou, and S. Fan, "First-principles simulation of photonic crystal surface-emitting lasers using rigorous coupled wave analysis," *Appl. Phys. Lett.*, vol. 113, no. 4, p. 041106, 2018.

[40] C. F. Bohren and D. R. Huffman, *Absorption and Scattering of Light by Small Particles*, Weinheim, Wiley, 2004.

[41] J. Jackson, *Classical Electrodynamics*, New York, Wiley, 1999.

[42] A. Krasnok, D. Baranov, H. Li, M.-A. Miri, F. Monticone, and A. Alú, "Anomalies in light scattering," *Adv. Opt. Photonics*, vol. 11, no. 4, p. 892, 2019.

[43] A. E. Miroshnichenko, A. B. Evlyukhin, Y. F. Yu, et al., "Nonradiating anapole modes in dielectric nanoparticles," *Nat. Commun.*, vol. 6, no. 1, p. 8069, 2015.

[44] H. A. M. Leymann, A. Foerster, F. Jahnke, J. Wiersig, and C. Gies, "Sub- and superradiance in nanolasers," *Phys. Rev. Appl.*, vol. 4, no. 4, p. 044018, 2015.

[45] F. Jahnke, C. Gies, M. Aßmann, et al., "Giant photon bunching, superradiant pulse emission and excitation trapping in quantum-dot nanolasers," *Nat. Commun.*, vol. 7, no. 1, p. 11540, 2016.

[46] A. A. Vyshnevyy, "Gain-dependent Purcell enhancement, breakdown of Einstein's relations, and superradiance in nanolasers," *Phys. Rev. B*, vol. 105, no. 8, p. 085116, 2022.

[47] H. Chew, "Radiation and lifetimes of atoms inside dielectric particles," *Phys. Rev. A*, vol. 38, no. 7, pp. 3410–3416, 1988.

[48] W. E. Hayenga, H. Garcia-Gracia, H. Hodaei, et al., "Second-order coherence properties of metallic nanolasers," *Optica*, vol. 3, no. 11, p. 1187, 2016.

[49] M. Khajavikhan, A. Simic, M. Katz, et al., "Thresholdless nanoscale coaxial lasers," *Nature*, vol. 482, no. 7384, pp. 204–207, 2012.

[50] I. Prieto, J. M. Llorens, L. E. Muñoz-Camúñez, et al., "Near thresholdless laser operation at room temperature," *Optica*, vol. 2, no. 1, p. 66, 2015.

[51] A. A. Vyshnevyy and D. Y. Fedyanin, "Lasing threshold of thresholdless and non-thresholdless metal-semiconductor nanolasers," *Opt. Express*, vol. 26, no. 25, p. 33473, 2018.

[52] S. J. M. Kuppens, M. P. van Exter, and J. P. Woerdman, "Quantum-limited linewidth of a bad-cavity laser," *Phys. Rev. Lett.*, vol. 72, no. 24, pp. 3815–3818, 1994.

[53] M. O. Scully and M. S. Zubairy, *Quantum Optics*, Cambridge, Cambridge University Press, 1997.

Supplementary Material: This article contains supplementary material (https://doi.org/10.1515/nanoph-2023-0249).

APPENDIX F

Paper 6: Beyond Bounds on Light Scattering with Complex Frequency Excitations

---

The manuscript theoretically proposes an approach to achieve extreme back-scattering, transverse scattering, and lasing in dielectric Mie nanoparticles based on complex frequency excitation. The manuscript is published.

The citations in the manuscript refer to reference list included at the end of the manuscript.

Work contributions by the present author: Numerical calculations.

Reference information:

S. Kim, **S. Lepeshov**, A. Krasnok, and A. Alù. Beyond Bounds on Light Scattering with Complex Frequency Excitations. *Physical Review Letters* 129, 203601 (2022).

Beyond Bounds on Light Scattering with Complex Frequency Excitations

Seunghwi Kim,[1] Sergey Lepeshov,[2] Alex Krasnok,[1,3] and Andrea Alù[1,4,*]
[1] *Photonics Initiative, Advanced Science Research Center, City University of New York, New York, New York 10031, USA*
[2] *DTU Electro, Department of Electrical and Photonics Engineering, Technical University of Denmark,*
Ørsteds Plads 343, Kgs. Lyngby, DK-2800, Denmark
[3] *Department of Electrical and Computer Engineering, Florida International University, Miami, Florida 33174, USA*
[4] *Physics Program, Graduate Center, City University of New York, New York, New York 10016, USA*

(Received 19 February 2022; accepted 30 September 2022; published 8 November 2022)

Light scattering is one of the most established wave phenomena in optics, lying at the heart of light-matter interactions and of crucial importance for nanophotonic applications. Passivity, causality, and energy conservation imply strict bounds on the degree of control over scattering from small particles, with implications on the performance of many optical devices. Here, we demonstrate that these bounds can be surpassed by considering excitations at complex frequencies, yielding extreme scattering responses as tailored nanoparticles reach a quasi-steady-state regime. These mechanisms can be used to engineer light scattering of nanostructures beyond conventional limits for noninvasive sensing, imaging, and nanoscale light manipulation.

DOI: 10.1103/PhysRevLett.129.203601

The study of light scattering by small particles has a long history [1], and it is the basis of a disparate range of phenomena, from the color of the sky to the brightness of stained glasses. Despite its well-established nature, engineering light scattering is not an outdated problem: it remains of paramount interest in photonics [2,3], not only enabling new discoveries [4,5], but also broadening the impact of nanophotonics for various applications, such as optical antennas [6], imaging [7], optical tweezers and trapping [8,9].

Small nanoparticles are typically characterized by a broad donut-shape scattering pattern sustained by their dominant dipolar fields. More exotic scattering features can be achieved in suitably tailored nanoparticle geometries by carefully balancing electric and magnetic dipolar scattering, yielding destructive interference in specific directions that make the scattering more directive. For instance, scattering suppression in either the forward or backward direction can be obtained in nanoparticles satisfying the Kerker conditions [10]. Magnetoelectric, plasmonic [11], and high-index dielectric (DNPs) [12,13] nanoparticles have been shown to support peculiar scattering features, offering opportunities for light manipulation, and establishing the basis for the design of metasurfaces and metamaterials. However, these exotic responses require careful design of the nanoparticle geometries, and they emerge only at specific wavelengths as a function of the available material dispersion. In addition, even when these conditions are met, the scattering from nanoparticles remains limited by causality, passivity, and energy conservation.

Consider, for instance, the problem of realizing a particle with directional backward scattering, i.e., with minimized forward scattering cross section $\sigma_F = (\pi/|k_i|^2)|\sum_{n=1}^{\infty}(2n+1)\times(a_n+b_n)|^2 \simeq 0$, where $k_i = |\mathbf{k}_i|$ is the wave number of the incident wave, n is the multipolar order, and a_n and b_n are electric and magnetic Mie scattering coefficients, corresponding to the amplitude of multipolar scattered waves of order n [2,14]. We assume an $e^{-i\omega t}$ time convention under plane wave excitation $\mathbf{E}_{\rm in} = E_o e^{-i\mathbf{k}_i\cdot\mathbf{z}}\hat{\mathbf{x}}$, where $\hat{\mathbf{x}}$ is a unit vector. According to the optical theorem, the extinction cross section $\sigma_{\rm ext}$ is proportional to the normalized forward scattering amplitude with polarization parallel to the incident wave $\hat{\mathbf{e}}_i \cdot \mathbf{f}(\mathbf{k} = \mathbf{k}_i)$ [2,15]:

$$\sigma_{\rm ext} = \sigma_{\rm abs} + \sigma_{\rm scat} = \frac{4\pi}{k_i}\mathrm{Im}[\hat{\mathbf{e}}_i \cdot \mathbf{f}(\mathbf{k} = \mathbf{k}_i)], \qquad (1)$$

where $\sigma_{\rm abs}$ and $\sigma_{\rm scat}$ are the absorption and scattering cross sections, $\hat{\mathbf{e}}_i$ is the unit polarization vector of the incident wave, and $\mathbf{k}_i$ and $\mathbf{k}$ are the wave vectors of incident and scattered waves, respectively. Equation (1) indicates that $\sigma_{\rm ext}$ must be zero if $\mathbf{f}(\mathbf{k} = \mathbf{k}_i) = 0$, yet in a passive scatterer $\sigma_{\rm abs} \geq 0$, $\sigma_{\rm scat} \geq 0$, hence this condition can be met only if the scattered power is zero at all angles [15–18]. For very small particles, a negligible—yet strictly nonzero—forward scattering can be achieved, with most of the residual scattering distributed at other angles, as in the inset of Fig. 1(a), but a severe trade-off exists between total scattering and residual forward scattering, consistent with Eq. (1) [16]. Passivity fundamentally limits how backward directive a scattering pattern can be.

Active materials can be employed to overcome this limitation, since such particles can support $\sigma_{\rm abs} < 0$, relaxing the constraint on zero forward scattering. Gain provides additional energy, relaxing limitations that stem from power conservation, and offering a broader control

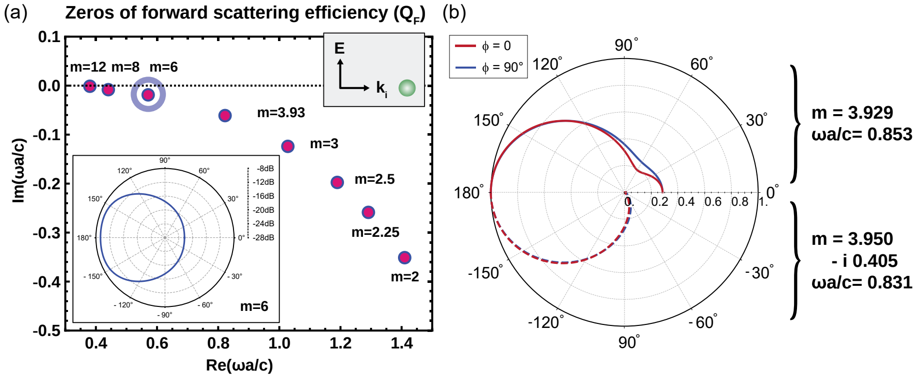

FIG. 1. (a) Evolution of the first zero of the forward scattering efficiency Q_F as we vary the refractive index m of a dielectric sphere. The scattering pattern for $m = 6$ (blue circle) is shown in the inset for excitation at the real part of the complex frequency of the zero. (b) Normalized scattering patterns in the two polarization planes for $m = 3.929$ (solid lines) and $m = 3.950 - i\,0.405$ (dotted lines). Red (blue) lines indicate that the incident waves are parallel (orthogonal) to the scattering plane.

over light scattering. However, it is challenging to embed active media within nanophotonic systems, and typically optical gain comes at the price of stringent bandwidth and stability limitations [19,20]. Moreover, active materials are characterized by unavoidable noise in the form of amplified spontaneous emission or parasitic harmonics in the case of parametric gain [20], which hinder the practical feasibility of active systems for several applications.

The limitations outlined so far implicitly refer to monochromatic excitations. We have recently explored the exotic response of passive nanophotonic systems when excited with signals that oscillate at complex frequencies. Under suitable conditions, we have shown that a tailored resonant linear system excited by a signal oscillating at a complex ω can reach a *quasi-steady-state* response, such that its output after a transient oscillates at the same complex frequency as the input. In this regime, the passivity constraints associated with real frequencies can be overcome, opening new frontiers for light-matter interactions [21]. For instance, based on these principles, we have recently demonstrated a phenomenon analogous to absorption emerging in lossless structures excited at complex frequencies [22,23], with opportunities for efficient energy storage and optical memories [24]. Analogously, coherent excitations at complex frequencies can realize pulling forces, mimicking the emergence of gain [25], which can also be exploited to realize parity-time symmetric phenomena in passive systems [26].

Here, we explore the opportunities that complex frequency excitations open to overcome long-held bounds on scattering. First, we demonstrate that a tailored dielectric sphere can support identically zero forward scattering in its quasi-steady state when excited with a signal oscillating at a suitable complex frequency. Figure 1(a) shows the position of the first zero of the forward scattering efficiency, $Q_F = \sigma_F/\pi a^2$, where a is the sphere radius, evaluated in the complex frequency plane for passive DNPs with different refractive indexes. The zero always lies in the lower complex half-plane, and it can emerge close to the real frequency axis for large refractive indexes. For instance, when $m = 6$ (blue circle in the figure), excitation at the real part of this complex frequency produces the scattering pattern shown in the inset, which is asymmetric with minimized forward scattering and points toward the backward direction. The zero moves farther away from the real axis for lower indexes, implying that a monochromatic excitation at the real part of its frequency generates a larger and larger relative forward scattering.

The forward scattering zeros may be pushed toward the real axis by adding gain to the particle material. The resulting signal amplification corresponds to negative absorption, ensuring that the extinction σ_{ext} can be made identically zero in Eq. (1) even when $\sigma_{\text{scat}} > 0$. In Fig. S3a of Supplemental Material [27], for instance, we show that for the complex refractive index $m = 3.950 - i\,0.405$, the first forward scattering zero lies on the real axis. Figure 1(b) compares the normalized scattering patterns in the two polarization planes at the frequency of this forward zero $\omega_{\text{gain}}a/c = 0.831$ for the active particle (dotted lines), and compares it to the passive scenario $m = 3.929$ [31], evaluated at $\omega_{\text{nogain}}a/c = 0.853$, which corresponds to the real part of the complex frequency zero. We plot half of the angular spectrum for each scenario since the patterns are symmetric, and the red (blue) line indicates the scattered intensity parallel (perpendicular) to the scattering plane. The scattered fields in the forward direction are entirely suppressed in the active particle, while residual fields are still present in the forward scattering for the passive particle.

Interestingly, we can engage the forward scattering zero of a passive particle without relying on material gain, but by exciting it with a signal oscillating at the proper complex

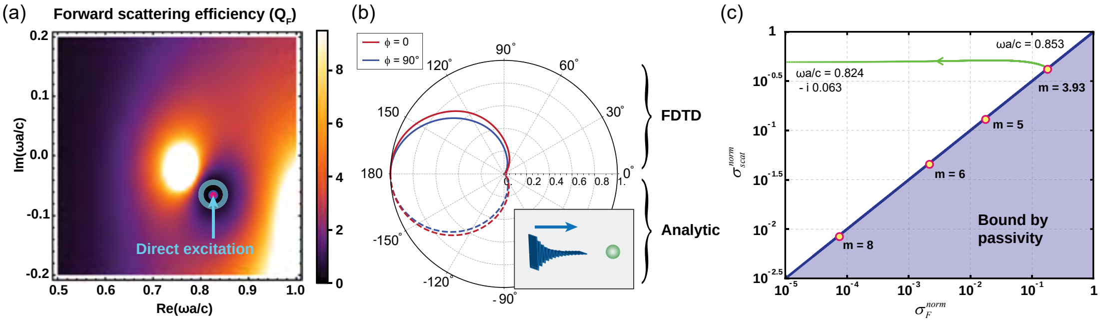

FIG. 2. (a) Density plot of the forward scattering efficiency Q_F in the complex frequency plane. The zero (darkest spot) and pole (brightest spot) are shown in the plot, and the zero is of interest here, marked by the blue circle. (b) Scattering pattern at the complex frequency $\omega a/c = 0.824 - i\,0.063$, demonstrating zero forward scattering in a passive dielectric sphere. The complex excitation impinging on a subwavelength dielectric sphere is schematically illustrated in the inset. These results are retrieved from FDTD simulations (solid lines) and validate our analytical results (dashed lines). (c) The normalized forward and total scattering cross sections are bounded by the thick blue line for any passive DNPs. The cross sections for minimizing forward scattering at $m = 8$, 6, 5 and 3.93 are placed on the bound (the thick blue line). Exciting in the complex frequency plane, as we evolve $\omega a/c = 0.853$ from to $\omega a/c = 0.824 - i\,0.063$, allows us to go beyond the bound (the green line).

frequency. Figure 2(a) shows the forward scattering efficiency in the complex frequency plane for a sphere with refractive index $m = 3.929$. We can observe a forward scattering pole (bright area) and a zero (dark area) in the plotted range of frequencies. We excite the particle with an incident signal with electric field oscillating at a complex frequency $E_i(t) = E_o \exp(-i\mathrm{Re}[\omega]t)\exp(\mathrm{Im}[\omega]t)$, characterized by an exponentially growing or decaying envelope as a function of the sign of $\mathrm{Im}[\omega]$. Here, we excite the sphere with a decaying signal oscillating at $\omega a/c = 0.824 - i\,0.063$, corresponding to the complex frequency of the forward scattering zero marked by the blue circle. Excitations at complex frequencies are unbounded at $\pm\infty$, and hence they are limited to finite temporal intervals. While no one prevents us from analytically continuing the expression of the forward scattering efficiency in the complex frequency plane, as we do in Fig. 2(a), we cannot generally expect that the sphere after a transient reaches a steady-state response oscillating at the same (complex) frequency as the excitation. However, as we show in the following, for excitation of zeros and poles sufficiently close to the real axis, the response of the structure after a short transient can support a quasi-steady-state regime in which the scattered fields oscillate at the same complex frequency. Under this condition, we can find exotic scattering responses as predicted by the singularities in the complex frequency plane.

We performed full-wave time-domain simulations to obtain the temporal evolution of the scattered fields, assuming an excitation at $\omega a/c = 0.824 - i\,0.063$ starting at $t = 0$. After a transient that depends on the way we excited the system for $t < 0$, we observe that the forward scattering converges to zero and the scattering from the particle reaches a quasi-steady-state response (see time evolution in [27]). The normalized scattering pattern in this quasi-steady-state regime retrieved from FDTD simulations (solid line) is compared to the analytically calculated pattern (dashed line) in Fig. 2(b), confirming that the scattering is directed backward, with minimum forward scattering orders of magnitude smaller than the minimum allowed for monochromatic excitations [27]. We stress that this result is achieved with a passive particle, and this exotic response can be explained based on the concept of "virtual gain," enabled when suitably tailored resonances are engaged with exponentially decaying signals oscillating at tailored complex frequencies [25,26]. The sphere scatters in time the energy stored from earlier cycles, for which the input signal was stronger due to its decaying nature. At this complex frequency, the electric and magnetic dipoles reach quasistationary states oscillating out of phase with respect to each other, i.e., $a_1 = -b_1$—a condition that cannot be achieved in a passive scatterer under monochromatic excitation—but which can be obtained here because the dipoles are radiating energy stored at earlier times. In the quasi-steady state, they perfectly cancel each other in the forward direction while interfering constructively in the backward direction.

In order to visualize the phenomenon, we plot the relation between normalized forward scattering cross section $\sigma_F^{\mathrm{norm}} = (\pi\sigma_F/9\lambda_o^2)$ and normalized total scattering cross section $\sigma_{\mathrm{scat}}^{\mathrm{norm}} = (\pi\sigma_{\mathrm{scat}}/3\lambda_o^2)$, where λ_o is the incident wavelength, in Fig. 2(c). The allowed forward scattering cross section in a small particle is bounded by the shaded region in the figure, i.e., it cannot be too small without minimizing the total scattering (see further analysis in [27]). The minimum scattering cross section for different refractive indexes $m = 8$, 6, 5, and 3.93 are located on the curve under harmonic plane wave illumination. Here, we largely surpass this bound using a complex frequency

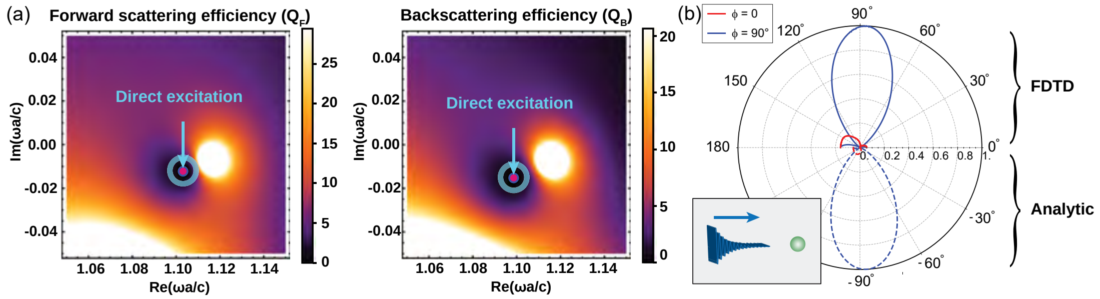

FIG. 3. (a) Density plot of the scattering efficiencies in the forward and backward directions to determine the complex zeros of Q_F and Q_B (marked by the blue circle) in the complex plane. (b) Scattering patterns obtained via FDTD and analytical solutions at the complex frequency ensure zero forward and backward scattering. The simulation and analytical results are in agreement in the quasi-steady state.

excitation: the green line in Fig. 2(c) shows the evolution of the scattering response in this plane as we sweep the frequency from $\omega a/c = 0.853$ (on the right side of the figure) to $\omega a/c = 0.824 - i0.063$ (on the left side of the figure) by linearly interpolating the real and imaginary parts. The green curve representing the evolution of the forward scattering converges to the y axis, enabling a large scattering cross section and zero forward scattering in the quasi-steady state.

Complex frequency excitations can also enable other exotic scattering responses. For instance, by tailoring at the same time dipolar and quadrupolar scattering harmonics in the complex frequency plane, we can induce the cancellation of scattered fields in *both* forward and backward directions, enabling transverse scattering patterns [32,33]. Transverse scattering from DNPs has been explored in [34], but without complete suppression of forward and backward scattering because of the mentioned passivity limitations (see Fig. S7 in Supplemental Material [27]). This response arises because the sphere is near an anapole resonance due to the destructive interference of electric dipole and quadrupole responses. The overall response makes the total scattered power very small [34], consistent with the requirement of minimizing the forward scattering in Eq. (1). Figure 3(a) plots the forward scattering efficiency Q_F in the complex plane around the frequency where transverse scattering happens, i.e., near $\omega a/c = 1.1$ and refractive index $m = 3.929$, indeed finding a forward scattering zero in the lower complex half-plane at $\omega a/c = 1.101 - i0.014$. Because of the close interactions of electric dipole and quadrupole harmonics around this resonance, the backward scattering efficiency $Q_B = \sigma_B/\pi a^2$, where σ_B is the backward scattering cross section, also supports a complex zero at a close location in the complex frequency plane, as shown in Fig. 3(a). By exciting the sphere with $\omega a/c = 1.101 - i0.014$, we indeed obtain the scattering patterns shown in Fig. 3(b), where we compare analytical calculations and FDTD simulations again. The results confirm zero forward and backward scattering and a purely transverse scattering pattern in one plane of polarization.

Another unique scattering constraint that stems from passivity is the maximum scattered power associated with a single scattering harmonic. Consider, for instance, the scattering from a dielectric cylinder under transverse-magnetic (TM) plane wave illumination at frequency ω_{in}. The contribution to the scattering width from the nth multipolar order $(\sigma_{\mathrm{scat}}^{\mathrm{TM}})_n = (2\lambda/\pi)|a_n|^2$, where a_n is the TM Mie scattering coefficient for dielectric cylinders [2]. The maximum contribution to the width for a single harmonic is limited to $2\lambda/\pi$ for passive scatterers in the case of monochromatic excitation since $|a_n| \leq 1$. For complex frequency excitation, however, this bound can be largely surpassed. Specifically, k is complex in the quasi-steady state, so that it can make the Mie coeffcients a_n much larger than unity (see further discussion in [27]). By targeting a pole of the total scattering cross section in the complex frequency plane, it is possible to realize lasinglike behaviors, exciting a *scattering pole*, as the decay rate of the incoming signal, tailored to match the eigenmode resonance of the cylinder, compensates for the radiation loss that bounds the scattering coefficient for monochromatic excitations.

For example, we consider a cylindrical DNP with $m = 3.929$ and evaluate the poles (yellow circles) of $Q_{\mathrm{scat}} = \sum_{n=-\infty}^{\infty} (\sigma_{\mathrm{scat}}^{\mathrm{TM}})_n / 2a$ shown in Fig. 4(a), where a is the radius of the cylindrical particle [27]. The third pole, marked by a hollow blue circle at $\omega a/c = 1.250 - i0.0175$, corresponds to a magnetic quadrupolar mode, whose resonance emerges for monochromatic excitations around the real frequency $\omega a/c = 1.248$. The scattering intensity of the cylindrical DNP $I_{\mathrm{scat}}(r_o, \theta, t)$ at distance r_o reads

$$I_{\mathrm{scat}}(r_o,\theta,t) = I_{\mathrm{in}}(r_o,t)\left|\sum_{n=-\infty}^{\infty}(-i)^n a_n H_n^{(1)}(kr_o)\exp(in\theta)\right|^2. \tag{2}$$

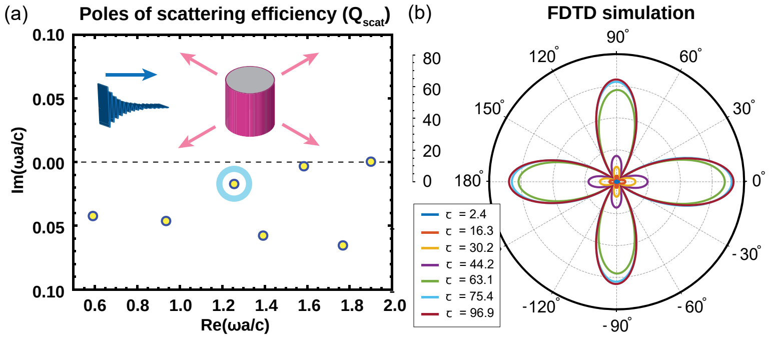

FIG. 4. (a) Poles (yellow circles) of Q_{scat} of each mode are illustrated. The third pole marked by the blue circle is of interest for investigating the scattering pole. (b) Temporal evolution for complex frequency excitations measured at $\tau = t\,\omega/(2\pi) = 2.4$, 16.3, 30.2, 44.2, 63.1, 75.4, and 96.9 from FDTD simulations.

Here, θ is the polar angle, k is the incident wave number, and $H_n^{(1)}(z)$ are the Hankel functions of the first kind. Note that $I_{\text{in}}(r_o, t)$ is the input intensity, including an exponentially decaying contribution. We define the normalized scattering pattern $S_{\text{scat}}(r_o, \theta, t) = I_{\text{scat}}(r_o, \theta, t)/I_{\text{in}}(r_o, t)$ as the ratio of scattering intensity $I_{\text{scat}}(r_o, \theta, t)$ to the input intensity $I_{\text{in}}(t)$ evaluated at the same instant in time. In the quasi-steady state, this function is independent of time, since the scattered fields oscillate at the same complex frequency of the input, thus $S_{\text{scat}}(r_o, \theta) = |\sum_{n=-\infty}^{\infty} (-1)^n a_n H_n^{(1)}(kr_o) \exp(i\,n\theta)|^2$.

We verify with FDTD simulations that we reach a quasi-steady state response exciting at the complex frequency of this scattering pole, as discussed in [27]. Figure 4(b) shows the far-field scattering patterns normalized to the input intensity as time evolves. The scattered intensity decays exponentially in time following the complex frequency excitation, but the ratio $S_{\text{scat}}(r_o, \theta, t)$ increases over time, yielding in the quasi-steady-state values much larger than 1, which is the bound for monochromatic excitations. At this complex frequency, we reach a purely quadrupolar pattern with scattered fields significantly larger than the input fields at the same instant in time, well beyond the passivity bound. The scattering efficiency at $\tau = t\ \text{Re}[\omega]/(2\pi) = 75.4$ is $Q_{\text{scat}} = \sum_{n=-\infty}^{\infty} (\lambda/\pi a)|a_n|^2 = 520.9$, over 2 orders of magnitude larger than its value at the quadrupolar resonance for real frequency excitation, $Q_{\text{scat}} = 3.6$ in Fig. S9a of Supplemental Material [27].

Overall, our results demonstrate that complex frequency excitations can manipulate the scattering of passive resonant objects in exotic ways, going well beyond the limits imposed by passivity. This principle may readily be translated to more complex systems, such as lattices, particle clusters, and metamaterials, and it can be extended to other wave domains, e.g., acoustic systems. Our results demonstrate that in nonmonochromatic settings in which we can tailor the input signal profile in time, the response of a scatterer is not limited by passivity, causality, and energy conservation. These phenomena can be applied to various settings, such as noninvasive sensors, energy-storage, efficient wireless power transfer, directional light source, beam control, high-performance antennas, imaging, and more. Our Letter can also be expanded to be combined with $\mathcal{PT}$ symmetry and exceptional point physics [26], yielding high sensitivity and exotic scattering features.

This work was supported in part by the Simons Foundation and the Air Force Office of Scientific Research.

---

[*] Corresponding author.
aalu@gc.cuny.edu

[1] G. Mie, Beiträge zur Optik trüber Medien, speziell kolloidaler Metallösungen, Ann. Phys. (N.Y.) **330**, 377 (1908).
[2] C. F. Bohren and D. R. Huffman, *Absorption and Scattering of Light by Small Particles* (John Wiley & Sons, New York, 2008).
[3] I. L. Fabelinskii, *Molecular Scattering of Light* (Springer Science & Business Media, New York, 2012).
[4] M. I. Tribelsky and B. S. Luk'yanchuk, Anomalous Light Scattering by Small Particles, Phys. Rev. Lett. **97**, 263902 (2006).
[5] X. Fan, W. Zheng, and D. J. Singh, Light scattering and surface plasmons on small spherical particles, Light **3**, e179 (2014).
[6] P. Mühlschlegel, H.-J. Eisler, O. J. F. Martin, B. Hecht, and D. W. Pohl, Resonant optical antennas, Science **308**, 1607 (2005).
[7] J. Y. Lee *et al.*, Near-field focusing and magnification through self-assembled nanoscale spherical lenses, Nature (London) **460**, 498 (2009).
[8] A. Ashkin, J. M. Dziedzic, J. E. Bjorkholm, and S. Chu, Observation of a single-beam gradient force optical trap for dielectric particles, Opt. Lett. **11**, 288 (1986).
[9] S. Lal, S. E. Clare, and N. J. Halas, Nanoshell-enabled photothermal cancer therapy: Impending clinical impact, Acc. Chem. Res. **41**, 1842 (2008).

[10] M. Kerker, D. S. Wang, and C. L. Giles, Electromagnetic scattering by magnetic spheres, J. Opt. Soc. Am. **73**, 765 (1983).

[11] B. Luk'yanchuk, N. I. Zheludev, S. A. Maier, N. J. Halas, P. Nordlander, H. Giessen, and C. T. Chong, The Fano resonance in plasmonic nanostructures and metamaterials, Nat. Mater. **9**, 707 (2010).

[12] M. Nieto-Vesperinas, R. Gomez-Medina, and J. J. Saenz, Angle-suppressed scattering and optical forces on submicrometer dielectric particles, J. Opt. Soc. Am. A **28**, 54 (2011).

[13] Y. H. Fu, A. I. Kuznetsov, A. E. Miroshnichenko, Y. F. Yu, and B. Luk'yanchuk, Directional visible light scattering by silicon nanoparticles, Nat. Commun. **4**, 1527 (2013).

[14] H. C. van de Hulst, *Light Scattering by Small Particles* (Dover, New York, 1981).

[15] J. D. Jackson *Classical Electrodynamics*, 3rd ed. (John Wiley & Sons, New York, 1999).

[16] A. Alu and N. Engheta, How does zero forward-scattering in magnetodielectric nanoparticles comply with the optical theorem?, J. Nanophoton. **4**, 041590 (2010).

[17] R. Fleury, J. Soric, and A. Alù, Physical bounds on absorption and scattering for cloaked sensors, Phys. Rev. B **89**, 045122 (2014).

[18] R. Fleury, F. Monticone, and A. Alù, Invisibility and Cloaking: Origins, Present, and Future Perspectives, Phys. Rev. Appl. **4**, 037001 (2015).

[19] B. Nistad and J. Skaar, Causality and electromagnetic properties of active media, Phys. Rev. E **78**, 036603 (2008).

[20] A. Krasnok and A. Alù, Active nanophotonics, Proc. IEEE **108**, 628 (2020).

[21] A. Krasnok, D. Baranov, H. Li, M.-A. Miri, F. Monticone, and A. Alú, Anomalies in light scattering, Adv. Opt. Photonics **11**, 892 (2019).

[22] D. G. Baranov, A. Krasnok, and A. Alù, Coherent virtual absorption based on complex zero excitation for ideal light capturing, Optica **4**, 1457 (2017).

[23] G. Trainiti, Y. Ra'di, M. Ruzzene, and A. Alù, Coherent virtual absorption of elastodynamic waves, Sci. Adv. **5**, eaaw3255 (2019).

[24] M. Cotrufo and A. Alù, Excitation of single-photon embedded eigenstates in coupled cavity-atom systems, Optica **6**, 799 (2019).

[25] S. Lepeshov and A. Krasnok, Virtual optical pulling force, Optica **7**, 1024 (2020).

[26] H. Li, A. Mekawy, A. Krasnok, and A. Alù, Virtual Parity-Time Symmetry, Phys. Rev. Lett. **124**, 193901 (2020).

[27] See Supplemental Material at http://link.aps.org/supplemental/10.1103/PhysRevLett.129.203601 for details on the overview of the anti-Kerker effects in active systems, the analysis of the virtual anti-Kerker effects, the virtual generalized Kerker efffects and the scattering pole, and the description of the numerical method. Addditional discussions on the quasi-steady-state responses, the passivity bound, and the introduction to the scattering parameters, which include Refs. [28–30].

[28] A. Ishimaru, *Wave Propagation and Scattering in Random Media* (Academic Press, New York, 1978), Vol. 2.

[29] C. Mätzler, MATLAB functions for Mie scattering, and absorption, version 2 (2002).

[30] M. Kerker, *The scattering of light and other electromagnetic radiation: physical chemistry: A series of monographs* (Academic Press, New York, 2013), Vol. 16.

[31] It is the refractive index of silicon at $\lambda \sim 600$ nm, which is a possible operating wavelength for experimental realization.

[32] Y. X. Ni, L. Gao, A. E. Miroshnichenko, and C. W. Qiu, Controlling light scattering and polarization by spherical particles with radial anisotropy, Opt. Express **21**, 8091 (2013).

[33] J. Y. Lee, A. E. Miroshnichenko, and R.-K. Lee, Simultaneously nearly zero forward and nearly zero backward scattering objects, Opt. Express **26**, 30393 (2018).

[34] H. K. Shamkhi, K. V. Baryshnikova, A. Sayanskiy, P. Kapitanova, P. D. Terekhov, P. Belov, A. Karabchevsky, A. B. Evlyukhin, Y. Kivshar, and A. S. Shalin, Transverse Scattering and Generalized Kerker Effects in All-Dielectric Mie-Resonant Metaoptics, Phys. Rev. Lett. **122**, 193905 (2019).

APPENDIX G

Paper 7: Suppressing material loss in the visible and near-infrared range for functional nanophotonics using bandgap engineering

Here, an approach to mitigate material losses in silicon by hydrogenation is proposed, and high-Q reconfigurable Mie resonances are obtained. The manuscript is published.

The citations in the manuscript refer to reference list included at the end of the manuscript.

Work contributions by the present author: Analytical and numerical calculations, manuscript writing.

Reference information:

M. Wang, A. Krasnok, **S. Lepeshov**, G. Hu, T. Jiang, J. Fang, B. Korgel, A. Alù, and Y. Zheng. Suppressing material loss in the visible and near-infrared range for functional nanophotonics using bandgap engineering. *Nature Communications* 11, 5055 (2020).

nature COMMUNICATIONS

ARTICLE

https://doi.org/10.1038/s41467-020-18793-y OPEN

Suppressing material loss in the visible and near-infrared range for functional nanophotonics using bandgap engineering

Mingsong Wang[1,2], Alex Krasnok[2✉], Sergey Lepeshov[3], Guangwei Hu[2,4], Taizhi Jiang[5], Jie Fang[1], Brian A. Korgel[5], Andrea Alù[2,6✉] & Yuebing Zheng[1✉]

All-dielectric nanostructures have recently opened exciting opportunities for functional nanophotonics, owing to their strong optical resonances along with low material loss in the near-infrared range. Pushing these concepts to the visible range is hindered by their larger absorption coefficient, thus encouraging the search for alternative dielectrics for nanophotonics. Here, we employ bandgap engineering to synthesize hydrogenated amorphous Si nanoparticles (a-Si:H NPs) offering ideal features for functional nanophotonics. We observe significant material loss suppression in a-Si:H NPs in the visible range caused by hydrogenation-induced bandgap renormalization, producing strong higher-order resonant modes in single NPs with *Q* factors up to ~100 in the visible and near-IR range. We also realize highly tunable all-dielectric meta-atoms by coupling a-Si:H NPs to photochromic spiropyran molecules. ~70% reversible all-optical tuning of light scattering at the higher-order resonant mode under a low incident light intensity is demonstrated. Our results promote the development of high-efficiency visible nanophotonic devices.

---

[1] Walker Department of Mechanical Engineering and Texas Materials Institute, The University of Texas at Austin, Austin, TX 78712, USA. [2] Photonics Initiative, Advanced Science Research Center, City University of New York, New York, NY 10031, USA. [3] Department of Physics and Engineering, ITMO University, St. Petersburg 197101, Russia. [4] Department of Electrical and Computer Engineering, National University of Singapore, Singapore 117583, Singapore. [5] McKetta Department of Chemical Engineering, The University of Texas at Austin, Austin, TX 78712, USA. [6] Physics Program, Graduate Center, City University of New York, New York, NY 10016, USA. ✉email: akrasnok@gc.cuny.edu; aalu@gc.cuny.edu; zheng@austin.utexas.edu

Light trapping is crucial in a plethora of photonic applications, including lasers[1], sensing[2], and harmonic generation[3], to name just a few. High-quality resonators facilitate light trapping in the form of localized resonant modes for a time ~$2Q/\omega_0$, where Q is the quality factor of the mode and ω_0 is its eigenfrequency. In practice, the Q factor of a single standing resonance can be defined via its resonance linewidth at half maximum ($\Delta\omega$) as $Q = \omega_0/\Delta\omega$, implying that a higher Q factor possesses narrower resonant lines. Optical resonators supporting high-Q modes include microdisk resonators[4–8], microspheres[9], Bragg reflector microcavities[10], and photonic crystals[11–13], whose high Q factors can go up to $\sim 10^3$–10^6. However, these microscale dielectric resonators are bulky and exhibit modest light–matter interactions when averaged over their large sizes.

Functional nanophotonics requires light localization and hence high Q factors in subwavelength optical resonators. To this end, nanoscale light trapping based on plasmonic resonances of metal nanoparticles[14–21] and on Mie resonances of high-index dielectric nanostructures[2,22] has been explored. However, the Q factor of these nanoresonators is limited by radiative and material losses, and it does not exceed a few tens in the visible range. Although radiative losses can be suppressed with the tailoring of weakly scattering states, such as bound states in the continuum (BIC)[23–26], the material (dissipation) loss requires a fundamentally different approach. High-index dielectric resonant NPs look especially promising due to their lower material loss compared to plasmonic nanoparticles[14–19,27–30], enabling low-loss photonic devices, e.g., nanoantennas, metalenses, and lasers[22,31–37]. Recent studies have also revealed the importance of high-index dielectric nanostructures as versatile platforms for active nanophotonics[38–43]. In contrast to plasmonic structures, where tailoring of the magnetic optical response is a challenging task, the response of high-index dielectric NPs is governed by both magnetic and electric resonances in visible and NIR range[22,44]. Among high-index dielectrics, Si-based NPs have been of particular interest for nanophotonic applications[31], because Si is the choice material for the established semiconductor industry, where fully developed processing and characterization tools can readily be applied to create future CMOS-compatible integrated photonic and electronic systems based on a single-material platform[31,44,45].

Theoretical studies have predicted enhanced Q factors for high-order multipole modes in low-loss high-index dielectric NPs compared with the fundamental dipole mode, because of reduced radiation loss[22,45–47]. However, such modes are fragile and very sensitive to material losses, hence they are hardly observable in practice. For example, crystalline silicon (c-Si) has a broad optical absorption in the wavelength range from 300 to 1150 nm, with an absorption coefficient larger than $1 \times 10^3\,\mathrm{cm}^{-1}$ over the whole visible region[48] that reduces Q factor of the fundamental magnetic dipole (MD)[31] and suppresses all high-order modes. This obstacle has prevented the development of low-loss and compact photonic devices for the visible region, and prompts a further search for alternative materials.

Recent studies have revealed the power of bandgap engineering for tailoring materials with superb optical properties[49]. For example, in ref. [50], it has been reported that increasing the atom spacing may significantly reduce material loss in metal nanoparticles. Another example is the optical properties of phase change materials, in which the amorphous phase exhibits lower material losses[51]. Other studies suggest that the optical losses of materials can be reduced via the formation of a forbidden phonon gap induced by random phononic structures[52]. In this paper, we employ bandgap engineering to tailor hydrogenated amorphous Si nanoparticles (i.e., a-Si:H NPs) and endow them with low dissipation in the visible range. First, we controllably vary the hydrogen concentration and the crystalline structure from crystal to amorphous and demonstrate that, similar to the amorphous phase of phase change materials, a-Si:H NPs exhibit smaller material loss. Next, based on single-nanoparticle spectroscopy of a-Si:H NPs, we report the experimental observation of strong magnetic quadrupole (MQ) and magnetic octupole (MO), with dominant scattering spectral peaks in the visible and NIR regions in subwavelength nanoparticles. In recent years, a-Si:H has been explored as a material platform for nanophotonic structures, including waveguides and nanocavities[37,53–55]. However, these studies mainly focused on the NIR and IR regions. Although a few more recent studies reported a-Si:H nanogratings and nanodisks for visible-wavelength-range applications, reduced loss in a-Si:H has not been fully appreciated and tailored to the visible region, and no higher-order Mie resonances have been explored or observed[56,57].

Here, we show that MO scattering modes have Q factors up to 100 along with prominent peaks in the scattering spectra, which so far have been challenging to realize in experimental nanophotonics. Given the enhanced light–matter interactions, we are able to observe high tunability of the supported resonances by simply adjusting the hydrogen concentration. It should be mentioned that some studies have reported the observation of high-order modes in Si nanostructures in the visible region[44,58]. However, the spectral intensities arising from high-order modes in these studies are weak and their Q factors do not exceed a few tens, owing to aforementioned reasons. Finally, in order to demonstrate the unique opportunities offered by our approach to low-loss functional nanophotonics, we show that the coupling of strong higher-order scattering resonances to a single a-Si:H meta-atom with spiropyran (SP) photochromic molecules results in switchable ~70% tuning of the scattering peak intensity upon changing the state of the photochromic molecules between transparent SP and colored merocyanine (MC) states. This significant all-optical tunability is achieved using a non-laser light source with low incident light intensity.

Results

Bandgap engineering of low-loss hydrogenated a-Si nanoparticles. It is known that the bandgap in Si is induced from short-range ordered structures of neighboring Si atoms, which lead to sp^3-hybridization of s and p valence electrons, forming two bands with decreasing interatomic distance and an indirect bandgap. The bandgap energy of a-Si:H, therefore, depends on the interaction between the sp^3 hybrids of neighboring Si atoms (Fig. 1a), and it is sensitive to the interatomic distance of Si–Si bonds[59,60]. As schematically shown in Fig. 1b, the voids in a-Si:H brought by hydrogen atoms cause a distortion of Si–Si bond, which leads to different bonding angles, smaller Si–Si distances and thus a larger bandgap, compared to c-Si. c-Si has an indirect bandgap (E_g) of 1.16 eV (which corresponds to the wavelength in free space of 1069 nm) and a forbidden direct transition (E_g') of 3.2 eV (wavelength is 387 nm)[48]. As we demonstrate below, by tuning the hydrogen concentration, a-Si:H NPs can obtain the absorption bandgap larger than 1.77 eV (700 nm) via bandgap engineering, and thus sustain a lower loss and strong higher-order scattering modes with high Q factors in the visible range.

The a-Si:H NPs studied here were fabricated by chemical synthesis (detailed information is in “Methods” section)[59,61]. The SEM images of a-Si:H NPs are shown in Supplementary Figs. 1–3. Raman spectroscopy was employed to verify that the distortion of the Si–Si bond, and the amorphous nature of a-Si:H NPs increases with an increase of hydrogen concentration. As shown in Fig. 1c, when the hydrogen concentration is 10 at.%, the Raman peak is at ~495 cm^{-1} and it is relatively narrow (see the green spectrum in Fig. 1c). This peak is brought by the appearance of

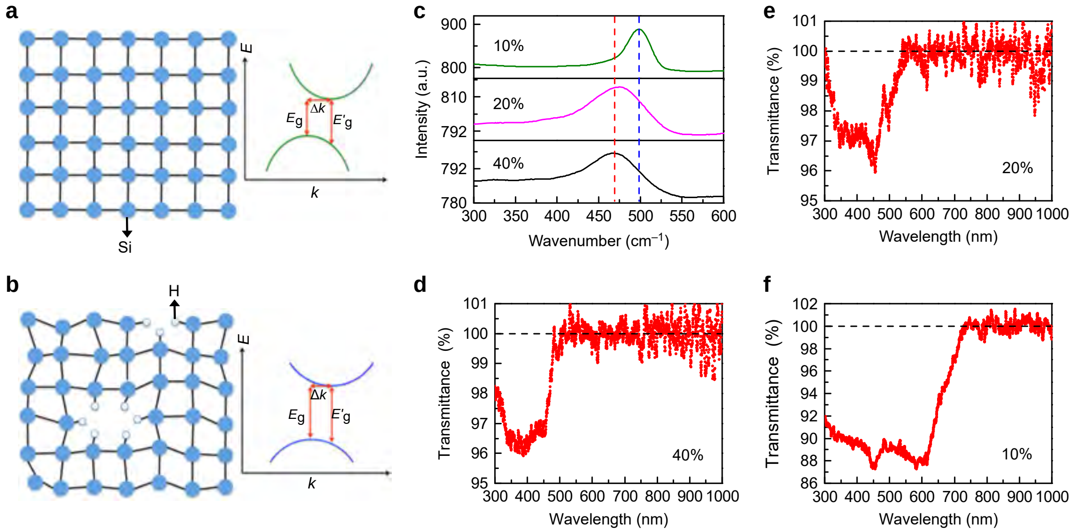

Fig. 1 Bandgap engineering of low-loss hydrogenated a-Si nanoparticles. a, **b** Two-dimensional schematic representations of the atomic arrangement and the bandgap of c-Si (**a**) and a-Si:H (**b**). E is the energy, and k is the wave vector. E_g is the indirect bandgap, E_g' is the direct transition, and Δk is the wave-vector mismatch. **c** Raman spectra of a-Si:H NPs with 40, 20, and 10% of hydrogen. The blue dashed line indicates the peak position of 495 cm^{-1}, and the red dashed line labels the peak position of 470 cm^{-1}. **d**–**f** Transmission spectra of a-Si:H NP(40) (**d**), a-Si:H NP(20) (**e**), and a-Si:H NP(10) (**f**) in ethanol after removing scattering signals.

1–2 nm nanocrystalline Si domains in the amorphous matrix[59]. As the hydrogen concentration increases, the Raman peak becomes broader and shifts to ~470 cm^{-1}, which is associated with a transverse optical phonon mode of a-Si and stretching vibrational modes of Si–Si bonds in a silicon tetrahedron, thus indicating an increase in the disordered nature of a-Si:H NPs[59].

The bandgap of a-Si:H NPs with different hydrogen concentrations is determined from measured transmission spectra of a-Si:H NPs, which are presented in Fig. 1d–f. The optical properties of a-Si:H film can be found in refs. [60,62] for comparison. Scattered signals are subtracted to obtain pure absorption signals (more detailed information is in Supplementary Note 2). Samples with 40 at.%, 20 at.%, and 10 at.% hydrogen (a-Si:H NP(40), a-Si:H NP (20), and a-Si:H NP(10)) have absorption bands starting at ~500, 560, and 710 nm, respectively. This confirms that the absorption bandgap of a-Si:H broadens as the hydrogen concentration decreases, and it can be tuned by varying hydrogen concentration. It should be mentioned that the transmission spectra are obtained through ensemble measurements, so each individual a-Si:H NP may have a slightly different absorption peak than those in Fig. 1d–f.

Dark-field scattering spectra of single NPs were measured (see Supplementary Fig. 6 for the dark-field setup). Figure 2a–c shows the scattering spectra of a single a-Si:H NP(40), a-Si:H NP(20), and a-Si:H NP(10) of diameters 370, 320, and 414 nm, respectively. Three major peaks in each spectrum are observed, which were fitted into three Lorentzian peaks associated, as proven by our theoretical analysis presented below, with MQ resonances at 624 (Fig. 2a), 717 (Fig. 2b) and 961 nm (Fig. 2c), electric dipole (ED) resonances at 694 (Fig. 2a) and 771 nm (Fig. 2b), MD resonances at 849 (Fig. 2a) and 937 nm (Fig. 2b), a MO resonance at 771 nm (Fig. 2c), and an electric quadrupole (EQ) resonance at 807 nm (Fig. 2c), respectively. Remarkably, different from any previously reported SiNPs, MQ, and MO modes in our a-Si:H NPs show a large scattering cross section (SCS; see Fig. 2a–c, blue and dark yellow fitting curves). The strong MQ and MO scattering peaks are repeatable, and consistent with the prediction from Mie scattering theory[47], confirming the low-dissipative nature of a-Si:H NPs in the visible and NIR range. It should be noted that the refractive index of a-Si:H NPs decreases with increased hydrogen concentration, due to the density reduction brought by hydrogenated nanovoids[60]. This causes a-Si:H NPs to have a smaller refractive index than a-SiNPs. The higher hydrogen concentration requires the size of a-Si:H NPs to be larger than the one of SiNPs to keep the Mie resonance peak positions aligned[22]. It is also worth noticing that new studies have been emerging focused on exploring moderate-refractive-index materials ($n > 2$) with low loss in the visible region, such as silicon-rich silicon nitride (SRN), titanium dioxide (TiO_2), and gallium nitride (GaN), as platforms for high-efficient metasurfaces in the visible region[60,62–68]. Several SRN, TiO_2, and GaN nanostructures have been fabricated through top-down approaches, such as SRN nanodisks[63,64], TiO_2 nanofins[65,66], TiO_2 nanoblocks[67,68], and GaN nanopillars[69,70]. Distinct dipole Mie resonances were demonstrated in these nanostructures, but no higher-order modes were observed, possibly because of the limited quality of the nanostructures made via top-down approaches.

In addition, the hydrogen concentration modification here is entirely different from carrier doping, which can also effectively tune the optical response of high-index NPs[71]. Namely, unlike the Drude response of free-carrier doping, hydrogen voids induce a blueshift of the absorption band, which induces a significant decrease of the dissipative loss to shorter wavelengths. However, carrier doping increases the dissipative loss, which has been illustrated by a broadening of the resonance peaks and the formation of a metallic phase[71].

Mie scattering theory is used to confirm the origin of each scattering peak and clarify how the Mie resonance peaks change, as a function of the hydrogen concentration. To model the permittivity of a-Si:H NPs, we use the Maxwell Garnett mixing

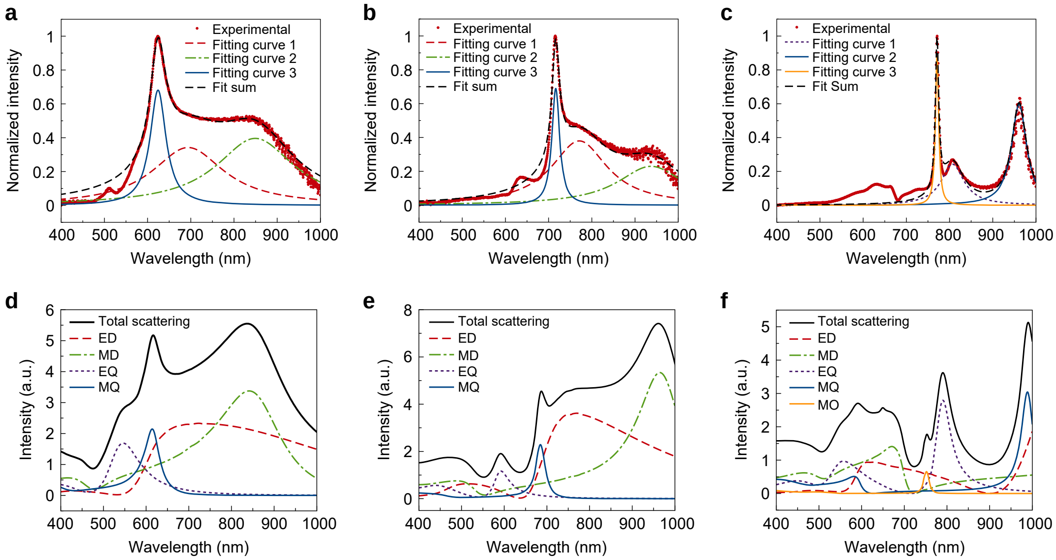

Fig. 2 Single-nanoparticle optical spectroscopy. a–c Scattering spectra of a single a-Si:H NP(40) (radius of ~185 nm) (**a**), a-Si:H NP(20) (radius of ~160 nm) (**b**), and a-Si:H NP(10) (radius of ~207 nm) (**c**). The red dotted curve and black dashed curve are experimental data and fit summary, respectively. The red dashed curve, green doted-dashed curve, and blue curve are fitting curve 1, 2, and 3, respectively (**a**, **b**). Purple doted curve, blue curve, and dark yellow curve are fitting curve 1, 2, and 3, respectively (**c**). **d–f** Scattering spectra along with multipole decomposition calculated with Mie theory. The black curve, red dashed curve, green dashed-dotted curve, purple doted curve, and blue curve represent total, ED, MD, EQ, and MQ scattering, respectively (**d–f**). Dark yellow curve represents MO scattering (**f**).

formula

$$\varepsilon_{\text{a-Si:H}} = \varepsilon_{\text{a-Si}} \frac{(\varepsilon_{\text{voids}} + 2\varepsilon_{\text{a-Si}}) + 2f(\varepsilon_{\text{voids}} - \varepsilon_{\text{a-Si}})}{(\varepsilon_{\text{voids}} + 2\varepsilon_{\text{a-Si}}) - f(\varepsilon_{\text{voids}} - \varepsilon_{\text{a-Si}})}, \qquad (1)$$

where f is the volume fraction of hydrogenated voids and $\varepsilon_{\text{voids}}$ denotes the permittivity of voids, which is assumed to be 1. We also slightly blueshift the permittivity of a-Si (shown in Supplementary Fig. 7) to model the hydrogenation. We have introduced this blueshift to take into account the bandgap renormalization caused by hydrogenation. By using $f = 0.4$ and a blueshift of 140 nm, and $f = 0.65$ and a blueshift of 90 nm, we obtain the best matching of simulated scattering peaks with experimental data of a-Si:H NP(40) (radius of ~185 nm), a-Si:H NP(20) (radius of ~160 nm), and a-Si:H NP(10) (radius of ~207 nm), respectively.

The optical response of fabricated spherical a-Si:H NPs with dielectric permittivity $\varepsilon_{\text{a-Si:H}}$ and radius R are calculated by the Mie light scattering theory[72,73], which gives the following expression for normalized SCS for particles made of a nonmagnetic material:

$$Q_{\text{sct}} = \frac{2}{(kR)^2} \sum_{l=1}^{\infty} (2l+1)\left(|a_l|^2 + |b_l|^2\right), \qquad (2)$$

where l defines the order of resonant mode and k is the wavenumber in the surrounding material. For a single-component particle, the electric (a_l) and magnetic (b_l) scattering amplitudes are given by $a_l = R_l^{(a)} / \left(R_l^{(a)} + iT_l^{(a)}\right)$, $b_l = R_l^{(b)} / \left(R_l^{(b)} + iT_l^{(b)}\right)$, and functions R_l and T_l can be expressed through the Bessel and Neumann functions (see "Methods" for details). The simulated scattering spectra are shown in Fig. 2d–f. The E-field distributions at the scattering peaks at 616 nm in Fig. 2d, 687 nm in Fig. 2e, and 991 nm in Fig. 2f are shown in Supplementary Fig. 8a, b, d, respectively. The E-field distribution profiles reveal the MQ features at these peaks, while the E-field distribution profile at 769 nm shown in Supplementary Fig. 8c displays a MO feature.

We calculated the Q factor of the measured MQ, MO, and MD scattering peaks by the definition[31] $Q = \omega_0/\Delta\omega$, discussed above. The calculated Q factor of MQ modes in Fig. 2a, b are 11 and 30, respectively. These Q factors are several times larger than those of MD modes (5 and 6 for Fig. 2a, b, respectively), suggesting that MQ modes can further boost light–matter interactions because of reduced radiation loss in a-Si:H NPs. The measured MQ scattering peaks are even more pronounced than those in simulations. The reason for the difference resides in the interplay of the resonant overlapping modes, resulting in complicated scattering power patterns. As a result, the amplitudes of the resonances in scattering measurements strongly depend on the experimental setup, whereas we focus on the total SCS in the simulations. Also, this difference between the simulated and measured amplitudes implies that the actual dissipative loss of a-Si:H NPs is smaller than the one obtained by blueshifting the ε dispersion of pure a-Si. Furthermore, in Fig. 2c, we observe the MO resonance with Q factor of ~100, which is ~10–20 times those obtained with plasmonic NPs at lower-order resonances (see Supplementary Note 5 for a detailed discussion).

It is worth noting that we address only material (dissipative) losses in our work. Hence, radiative losses represent the upper limit on the value of Q factor of dielectric nanoparticles. Radiative losses can be further reduced by utilizing, for example, quasi BIC, as recently demonstrated[74]. In order to further increase the Q factor of high-index nanostructures, approaches to suppress both types of losses should be applied simultaneously.

Highly tunable hybrid meta-atom. To demonstrate the superiority of our results for low-loss functional nanophotonics, we show that the coupling of these strong higher-order scattering resonances in a single a-Si:H meta-atom with SP molecules facilitates actively tunable nanostructures possessing low tuning intensities.

In practice, high input powers are needed to achieve strong all-optical tunability in Si due to its weak optical tunability[75,76]. In addition, the interaction length in SiNPs is limited by their nanoscale size. Thus, to achieve sufficient optical tuning of SiNPs, the high incident light intensity is needed. For instance, the intensities used for optically tuning SiNPs via electron–hole plasma excitation and laser reshaping are ~10 GW cm^{-2} and ~21 MW cm^{-2}, respectively[77–79]. High incident light intensities lead to considerable energy consumption, and can cause damage to SiNPs and surrounding materials. Therefore, all-optical tuning techniques relying on low intensities of incident light are desirable.

Here, we demonstrate that coupling higher-order optical resonant modes of a-Si:H NPs with photoswitchable optical resonances of photochromic molecules[19,80,81], such as SP molecules is a promising way to achieve low-intensity all-optical tuning in the visible range. The photochromism of SP is schematically displayed in Supplementary Fig. 11. The absorption spectra of molecules in SP form (blue curve) and MC form (pink curve) states are shown in Fig. 3a. Figure 3b schematically illustrates the investigating structure composed of the tailored a-Si:H NP, supporting strong MQ mode covered by SP molecules. The photoisomerization from SP to MC (from MC to SP) induced by UV (green) light excitation causes strong tuning of the scattering response of the single a-Si:H meta-atom from strong scattering to suppressed scattering, if the resonance of molecules in MC form is aligned with the MQ mode of the NP.

We start with the analytical optimization of geometry to achieve a pronounced effect of scattering tuning. To find the optimal layout, we fix the thickness of the shell (PMMA + SP) to 100 nm, and vary the core radius R from 50 to 200 nm. For analysis, we use the Mie theory for multilayered spheres[82]. The dielectric permittivity of the core is assumed to a-Si:H (40) find above, while the permittivity of PMMA + SP is obtained from experiments on transmission/reflection from the bare PMMA + SP film. The results of analytical calculations of SCS versus R and wavelength in the MC state are summarized in Fig. 3c. We observe a pronounced dip at 580 nm in the scattering spectrum caused by the interaction with the absorption peak of MC molecules. It should be noted that, although a-Si:H NP(10)s have the highest Q factor, their MQ modes exist in the far red side of the visible spectral range and NIR region, and are thus far away from the excitonic resonances of the photochromic molecules. Thus, in our studies we have chosen a-Si:H NP(40)s that can have strong MQ modes ~580 nm and better match with the resonances of the molecules, despite their smaller Q factors. In addition, lower Q factors don't necessarily mean a weaker modulation in our system because a-Si:H NPs with lower Q factors interact with more photochromic molecules in the PMMA + SP film due to the weaker localization of the field.

As the form of the photochromic molecules changes, the scattering spectrum of the meta-atom is drastically transformed. In the fully SP form, the meta-atom possesses scattering peaks at 580 nm, Fig. 3d, caused by different resonant modes of the a-Si:H NP(40) at different radii. The ratio of SCS in both states presented

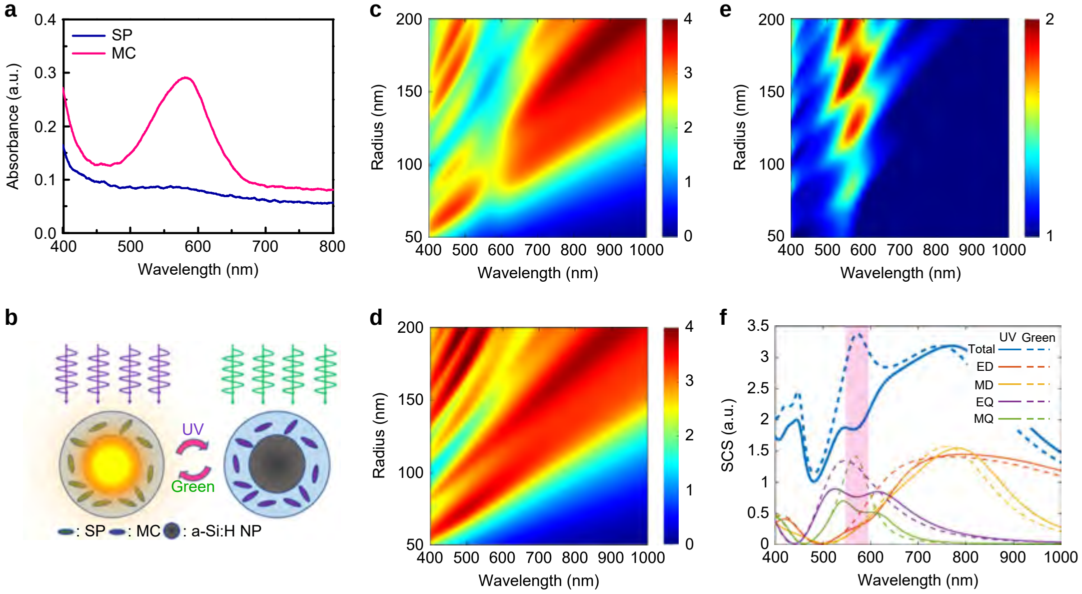

Fig. 3 Designing of the highly tunable photochromic all-dielectric single-particle meta-atom. **a** Absorption spectra of molecules in SP (blue curve) and MC (pink curve) state. **b** Schematic representation of the meta-atom consisting of a-Si:H with 40% of hydrogen core and a shell of SP photochromic molecules. The meta-atom is designed to support a strong higher-order Mie resonance at the absorption resonance of the MC state. The photoisomerization from SP to MC state and from MC to SP state is caused by UV and green light excitation, respectively. **c**, **d** Scattering cross-section (normalized to geometric) map of a core–shell nanostructure (**c**) after UV modification, and (**d**) green light recovery as a function of wavelength and a-Si:H nanoparticle radius. **e** Ratio between scattering cross sections of the core-shell after green light recovery and UV modification. **f** Scattering cross section of the core–shell with the Si core radius of 130 nm and its multipole decomposition. Solid lines correspond to the core-shell after UV modification, dashed lines correspond to the core-shell after green light recovery. The thickness of the PMMA + SP shell is 100 nm.

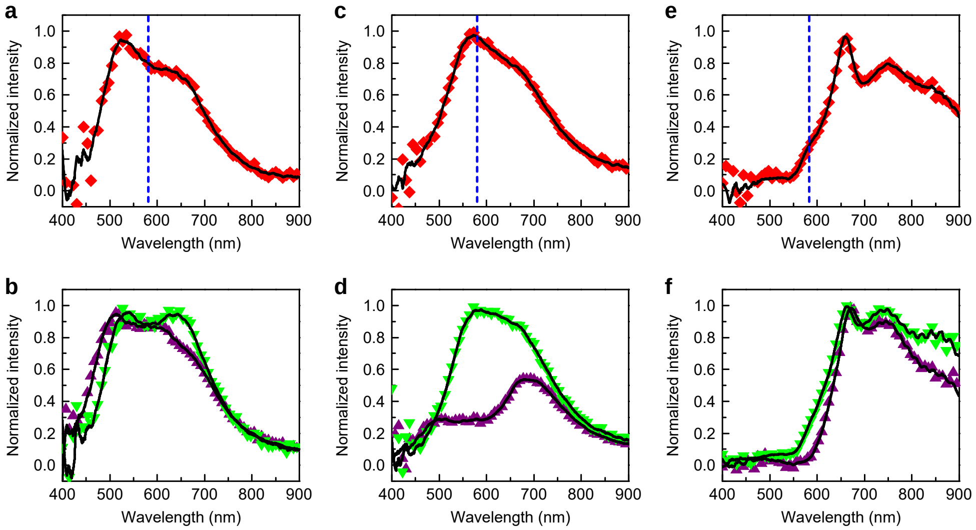

Fig. 4 Tuning of the all-dielectric meta-atom. a–f Scattering spectra of two single a-Si:H NPs(40) (diameter: ~300 and ~325 nm, respectively) (**a**–**d**) and a single a-Si:H NP(20) (diameter: ~280 nm) (**e**, **f**) covered by PMMA + SP layer. **a**, **c**, **e** Right after the sample preparation. **b**, **d**, **f** After the exposure to UV light (purple triangle) and after the exposure to the green light (green triangle). The vertical dashed blue dashed line illustrates the absorption peak of MC molecules. The black curves are smoothed spectral curves.

in Fig. 3e gives the change of SCS. As expected, the coupling between MQ resonance and MC molecules demonstrates a more dramatic change than for the MD resonance. We see that a large tuning effect can be achieved when the MQ resonant mode of a meta-atom with a-Si:H NP(40) core radius of ~130 nm is at 580 nm. This drastic SCS variation is caused by the combination of the strong field enhancement of the MQ mode and the large dipole strength of the photochromic molecules in the SP state. Results of the mode decomposition of the structure in both states are presented in Fig. 3f.

To verify this enhanced tunability, the fabricated a-Si:H NPs have been covered by a spin-coated PMMA + SP film. Figure 4 shows the scattering spectra of two single a-Si:H NP(40)s and one single a-Si:H NP(20) covered by PMMA + SP film. All scattering spectra have been normalized by dividing the transmission spectra of PMMA + SP film without a-Si:H NPs under the same power of dark-field light source to eliminate the contribution of bare molecular absorption. Before light irradiation, these three NPs in PMMA + SP film have MQ peaks centering at 522, 573, and 660 nm, respectively. The MQ peaks of the middle one match with the molecular absorption at 580 nm, while the other two have a large detuning from it. A fluorescence illuminator (mercury lamp) with bandpass filters was used to generate UV and green light, in order to switch the molecules from the SP state to the MC state and vice versa. The estimated maximum light intensities employed in the experiment are 3.8 and 1.1×10^2 W cm^{-2} for UV and green light, respectively (detailed information in "Methods"). These intensities are significantly lower than those used in reported studies of all-optical tuning of SiNPs. For instance, the intensities used for optically tuning SiNPs via electron–hole plasma excitation and laser reshaping are ~10 GW cm^{-2} and ~21 MW cm^{-2}, respectively[77,78].

We observe a remarkable tuning (~70%) of scattered power in the matched scenario near the MQ (Fig. 4c) scattering peak in Fig. 4d. The observed tunability is reversible and is caused by the large field enhancement of the MQ resonant mode. However, when there is a detuning (Fig. 4a, e), negligible scattering change occurs when SP molecules are switched to MC state, i.e., after UV light exposure for ~1.5 min (Fig. 4b, f). This change vanishes when the molecules are switched back to SP form by irradiating the sample with the green light for ~3 min, as shown by Fig. 4b, d, f. This photoswitchable variation confirms that the strong modulation of MQ scattering observed here is derived from the interaction between MQ mode and photochromic molecules. The switching speed of SP molecules in the PMMA film is relatively slow under a low incident light intensity. However, the ultrafast photoswitching of SP molecules has been demonstrated via femtosecond laser, and the entire cycle takes <40 ps (refs. [83,84]). Thus, we think that fast photoswitchable modulation of the optical response of the suggested hybrid meta-atom can be achieved by modifying the environment around SP molecules, and using advanced excitation sources. It is also worth noting that in many vital applications the ultrafast response is not necessarily required, but the strong tunability and reconfigurability are practically needed. The application examples include reconfigurable metasurfaces and metalenses, optical encryption, anti-counterfeiting, smart windows, and biomedical sensing.

Reversible modulation of the scattering intensity was demonstrated in our system, as shown in Supplementary Fig. 12. The result indicates that no sign of photodegradation was observed after five cycles of photoswitching. We should mention that our samples are not optimized for practical applications requiring highly robust performance. Many techniques that strongly improve the robustness of isomerization cycles, such as the covalent attachment of SP molecules to inorganic or macromolecular carriers, have been demonstrated[80]. We believe that more stable hybrid meta-atoms can be realized by applying those techniques.

Discussion

In summary, we have used bandgap engineering to tailor a-Si:H NPs with low dissipation losses in the visible range. As a result, strong higher-order magnetic multipole resonances in the visible and NIR ranges with Q factors up to 100 have been experimentally demonstrated in tailored a-Si:H NPs. The appearance of strong magnetic multipole scattering modes stems from the larger bandgap of a-Si:H NPs compared to pure SiNPs. The bandgap of a-Si:H NPs can be tuned by changing the hydrogen concentration. Strong magnetic multipole scattering modes with narrow linewidths in the visible and NIR regions open new opportunities to use nanostructures made of low-loss high-index materials for light manipulation, exploring light–matter interactions, and tunable optical devices. We show that coupling such strong higher-order scattering resonances in a single a-Si:H meta-atom with photochromic SP molecules results in ~70% tuning of the scattering peak intensity upon switching the photochromic molecules between transparent SP and colored MC states. This photochromatic all-optical tuning of SiNPs requires drastically lower incident light intensity than other reported methods. Our results pave the way to novel devices based on highly tunable all-dielectric single nanostructures with low-intensity requirements.

Methods

Sample preparation. A 10 mL titanium batch reactor (High-Pressure Equipment Company (HiP Co.)) was used for the synthesis. First, 21 µL trisilane (Si_3H_8, 100%, Voltaix) and *n*-hexane (anhydrous, 95%, Sigma-Aldrich) were loaded in the reactor in a nitrogen-filled glove box. The amount of *n*-hexane loaded in the reactor is associated with the reaction pressure inside the reactor during the heating process. In all reactions, the pressure was kept at 34.5 MPa (5000 p.s.i.). The different hydrogen concentration in these a-Si:H NPs is determined by different reaction temperatures[59]. For example, the a-Si:H nanoparticles with a hydrogen concentration of 40% were synthesized at a temperature of 380 °C (ref. [59]). After adding the reagents, the reactor was sealed by using a wrench inside the glove box. Then a vice was used to tightly seal the reactor after removing it from the glove box. The reactor was heated to the target temperature in a heating block for 10 min to allow the complete decomposition of trisilane. After the reaction, an ice bath was used to cool the reactor to room temperature. Colloidal a-Si:H NPs were then extracted from the opened reactor. The nanoparticles were washed by chloroform (99.9%, Sigma-Aldrich) using a centrifuge (at 8000 r.p.m. for 5 min).

There are three main reasons why we didn't study a-Si:H NPs with a hydrogen concentration <10%: (1) a minimum amount of hydrogen is needed to achieve a large enough bandgap change to dramatically reduce the absorption loss of a-Si:H in the visible region; (2) 10% is the smallest hydrogen concentration for the bottom-up approach we employed to fabricate a-Si:H nanospheres; and (3) it is hard to precisely measure the hydrogen concentration of <10% with thermogravimetric analysis.

The SP + PMMA film is prepared by mixing SP (Sigma-Aldrich) molecules with PMMA (Sigma-Aldrich) with a weight ratio of 1:1 in chlorobenzene (2 wt % of SP in chlorobenzene). Then a spin coater (Laurell) is used to coat the mixture on a-Si:H NPs at 2000 r.p.m. for 1 min.

Optical measurements. Before the scattering measurement, a-Si:H NPs were drop coasted on a bare glass substrate. An inverted microscope (Ti-E, Nikon) with a spectrograph (Andor), an EMCCD (Andor) and a halogen white light source (12 V, 100 W) was employed to measure the scattering spectra of single a-Si:H NPs on the bare glass substrate[18,19]. Raman spectra of a-Si:H NPs were measured by the Witec Micro-Raman Spectrometer. A UV-VIS-NIR spectrometer (Ocean Optics) was used to measure the transmission of a-Si:H NPs in ethanol. An epi-fluorescence illuminator (mercury lamp, Nikon) and bandpass filters (central wavelength: 350 nm (UV) and 540 nm (green), bandwidth: 50 nm (UV) or 25 nm (green)) are used to generated UV and green light. The maximum power of UV and green light was measured by a power meter (Thorlabs). Since the mercury lamp is an incoherent light source and the incident light covers the whole rear aperture of the objective, the beam spot diameter used to calculate the incident light intensity is obtained by: $d_{\mathrm{spot}} = d_{\mathrm{aperture}}$/magnification, where d_{aperture} is the diameter of the objective rear aperture and equal to 6.5 mm and magnification is 100 times.

Analytical and numerical simulations. The optical response of a Si nanoparticle with dielectric permittivity $\varepsilon = n^2$ (n is the refractive index of the nanoparticle material) and a radius R located in the free space can be treated via Mie light scattering theory[72,73], which gives the following expression for normalized scattering $[Q_{\mathrm{sct}} = P_{\mathrm{sct}}/(\pi R^2 I)]$ cross section for particles made of a nonmagnetic material:

$$Q_{\mathrm{sct}} = \frac{2}{(kR)^2}\sum_{l=1}^{\infty}(2l+1)\left(|a_l|^2 + |b_l|^2\right), \qquad (3)$$

where l defines the order of partial wave, k is the wavenumber $k = \omega n_{\mathrm{m}}/c$, and $\varepsilon_{\mathrm{m}} = n_{\mathrm{m}}^2$ is the dielectric permittivity of the surrounding medium. The quantity P_{sct} denotes the scattering power, I is the excitation intensity, c is the speed of light, and ε_0 is the dielectric constant.

For a single-component particle, the electric and magnetic scattering amplitudes are given by

$$a_l = \frac{R_l^{(a)}}{R_l^{(a)} + iT_l^{(a)}}, \quad b_l = \frac{R_l^{(b)}}{R_l^{(b)} + iT_l^{(b)}}, \qquad (4)$$

and functions R_l and T_l can be expressed in the following form:

$$R_l^{(a)} = n\psi_l'(kR)\psi_l(nkR) - \psi_l(kR)\psi_l'(nkR), \qquad (5)$$

$$T_l^{(a)} = n\chi_l'(kR)\psi_l(nkR) - \chi_l(kR)\psi_l'(nkR), \qquad (6)$$

$$R_l^{(b)} = n\psi_l'(nkR)\psi_l(kR) - \psi_l(nkR)\psi_l'(kR), \qquad (7)$$

$$T_l^{(b)} = n\chi_l(kR)\psi_l'(nkR) - \chi_l'(kR)\psi_l(nkR). \qquad (8)$$

Here, $\psi_l(x) = \sqrt{\frac{\pi x}{2}}J_{l+1/2}(x)$, $\chi_l(x) = \sqrt{\frac{\pi x}{2}}N_{l+1/2}(x)$, $J_{l+1/2}(x)$, and $N_{l+1/2}(x)$ are the Bessel and Neumann functions, and prime means derivation.

The Mie scattering coefficients can be expressed similarly and can be found in refs. [72,85].

The optical properties of the nanostructures in the optical frequency range have been studied numerically by using CST Microwave Studio. CST Microwave Studio is a full-wave 3D electromagnetic field solver based on a finite-integral time-domain solution technique. A nonuniform mesh was used to improve accuracy in the vicinity of the Si nanoparticles, where the field concentration was significantly large.

Data availability

The data that support the findings of this study are available from the corresponding authors upon reasonable request.

Received: 4 January 2020; Accepted: 7 September 2020;

References

1. Ma, R. M. & Oulton, R. F. Applications of nanolasers. *Nat. Nanotechnol.* **14**, 12–22 (2019).
2. Krasnok, A., Caldarola, M., Bonod, N. & Alú, A. Spectroscopy and biosensing with optically resonant dielectric nanostructures. *Adv. Opt. Mater.* **6**, 1701094 (2018).
3. Krasnok, A., Tymchenko, M. & Alù, A. Nonlinear metasurfaces: a paradigm shift in nonlinear optics. *Mater. Today* **21**, 8–21 (2018).
4. Armani, D. K., Kippenberg, T. J., Spillane, S. M. & Vahala, K. J. Ultra-high-*Q* toroid microcavity on a chip. *Nature* **421**, 925–928 (2003).
5. Zhang, N. et al. High-*Q* and highly reproducible microdisks and microlasers. *Nanoscale* **10**, 2045–2051 (2018).
6. Kryzhanovskaya, N. et al. Enhanced light outcoupling in microdisk lasers via Si spherical nanoantennas. *J. Appl. Phys.* **124**, 163102 (2018).
7. Moiseev, E. I. et al. Light outcoupling from quantum dot-based microdisk laser via plasmonic nanoantenna. *ACS Photonics* **4**, 275–281 (2017).
8. McCall, S. L., Levi, A. F. J., Slusher, R. E., Pearton, S. J. & Logan, R. A. Whispering-gallery mode microdisk lasers. *Appl. Phys. Lett.* **60**, 289–291 (1992).
9. Vassiliev, V. V. et al. Narrow-line-width diode laser with a high-*Q* microsphere resonator. *Opt. Commun.* **158**, 305–312 (1998).
10. Koschorreck, M. et al. Dynamics of a high-*Q* vertical-cavity organic laser. *Appl. Phys. Lett.* **87**, 181108 (2005).
11. Lončar, M., Yoshie, T., Scherer, A., Gogna, P. & Qiu, Y. Low-threshold photonic crystal laser. *Appl. Phys. Lett.* **81**, 2680–2682 (2002).
12. Song, B.-S., Noda, S., Asano, T. & Akahane, Y. Ultra-high-*Q* photonic double-heterostructure nanocavity. *Nat. Mater.* **4**, 207–210 (2005).
13. Painter, O. et al. Two-dimensional photonic band-gap defect mode laser. *Science* **284**, 1819–1821 (1999).
14. Atwater, H. A. & Polman, A. Plasmonics for improved photovoltaic devices. *Nat. Mater.* **9**, 205–213 (2010).
15. Schuller, J. A. et al. Plasmonics for extreme light concentration and manipulation. *Nat. Mater.* **9**, 193–204 (2010).
16. Zia, R., Schuller, J. A., Chandran, A. & Brongersma, M. L. Plasmonics: the next chip-scale technology. *Mater. Today* **9**, 20–27 (2006).
17. Brongersma, M. L., Halas, N. J. & Nordlander, P. Plasmon-induced hot carrier science and technology. *Nat. Nanotechnol.* **10**, 25–34 (2015).
18. Wang, M. et al. Molecular-fluorescence enhancement via blue-shifted plasmon-induced resonance energy transfer. *J. Phys. Chem. C* **120**, 14820–14827 (2016).

19. Wang, M. et al. Controlling plasmon-enhanced fluorescence via intersystem crossing in photoswitchable molecules. *Small* **13**, 1701763 (2017).
20. Wang, M. et al. Plasmon-trion and plasmon-exciton resonance energy transfer from a single plasmonic nanoparticle to monolayer MoS_2. *Nanoscale* **9**, 13947–13955 (2017).
21. Fan, X., Zheng, W. & Singh, D. J. Light scattering and surface plasmons on small spherical particles. *Light Sci. Appl.* **3**, e179–e179 (2014).
22. Kuznetsov, A. I., Miroshnichenko, A. E., Brongersma, M. L., Kivshar, Y. S. & Luk'yanchuk, B. Optically resonant dielectric nanostructures. *Science* **354**, aag2472 (2016).
23. Hsu, C. W., Zhen, B., Stone, A. D., Joannopoulos, J. D. & Soljačić, M. Bound states in the continuum. *Nat. Rev. Mater.* **1**, 16048 (2016).
24. Rybin, M. V. et al. High-*Q* supercavity modes in subwavelength dielectric resonators. *Phys. Rev. Lett.* **119**, 243901 (2017).
25. Krasnok, A. et al. Anomalies in light scattering. *Adv. Opt. Photonics* **11**, 892 (2019).
26. Monticone, F., Sounas, D. L., Krasnok, A. & Alù, A. Can a nonradiating mode be externally excited? Nonscattering states vs. embedded eigenstates. *ACS Photonics* **6**, 3108–3114 (2019).
27. Wang, M. et al. Plasmon–trion and plasmon–exciton resonance energy transfer from a single plasmonic nanoparticle to monolayer MoS_2. *Nanoscale* **9**, 13947–13955 (2017).
28. Maier, S. A. & Atwater, H. A. Plasmonics: Localization and guiding of electromagnetic energy in metal/dielectric structures. *J. Appl. Phys.* **98**, 011101 (2005).
29. Wang, H., Brandl, D. W., Nordlander, P. & Halas, N. J. Plasmonic nanostructures: artificial molecules. *Acc. Chem. Res.* **40**, 53–62 (2007).
30. Halas, N. J., Lal, S., Chang, W. S., Link, S. & Nordlander, P. Plasmons in strongly coupled metallic nanostructures. *Chem. Rev.* **111**, 3913–3961 (2011).
31. Baranov, D. G. et al. All-dielectric nanophotonics: the quest for better materials and fabrication techniques. *Optica* **4**, 814 (2017).
32. Genevet, P., Capasso, F., Aieta, F., Khorasaninejad, M. & Devlin, R. Recent advances in planar optics: from plasmonic to dielectric metasurfaces. *Optica* **4**, 139 (2017).
33. Jahani, S. & Jacob, Z. All-dielectric metamaterials. *Nat. Nanotechnol.* **11**, 23–36 (2016).
34. Krasnok, A. E., Miroshnichenko, A. E., Belov, P. A. & Kivshar, Y. S. All-dielectric optical nanoantennas. *Opt. Express* **20**, 20599 (2012).
35. Krasnok, A. E., Filonov, D. S., Simovski, C. R., Kivshar, Y. S. & Belov, P. A. Experimental demonstration of superdirective dielectric antenna. *Appl. Phys. Lett.* **104**, 133502 (2014).
36. Ha, S. T. et al. Directional lasing in resonant semiconductor nanoantenna arrays. *Nat. Nanotechnol.* **13**, 1042–1047 (2018).
37. Staude, I. & Schilling, J. Metamaterial-inspired silicon nanophotonics. *Nat. Photonics* **11**, 274–284 (2017).
38. Makarov, S. et al. Tuning of magnetic optical response in a dielectric nanoparticle by ultrafast photoexcitation of dense electron-hole plasma. *Nano Lett.* **15**, 6187–6192 (2015).
39. Baranov, D. G., Makarov, S. V., Krasnok, A. E., Belov, P. A. & Alù, A. Tuning of near- and far-field properties of all-dielectric dimer nanoantennas via ultrafast electron-hole plasma photoexcitation. *Laser Photonics Rev.* **10**, 1009–1015 (2016).
40. Bohn, J. et al. Active tuning of spontaneous emission by Mie-resonant dielectric metasurfaces. *Nano Lett.* **18**, 3461–3465 (2018).
41. Shcherbakov, M. R. et al. Ultrafast all-optical switching with magnetic resonances in nonlinear dielectric nanostructures. *Nano Lett.* **15**, 6985–6990 (2015).
42. Rahmani, M. et al. Reversible thermal tuning of all-dielectric metasurfaces. *Adv. Funct. Mater.* **27**, 1–7 (2017).
43. Jang, J. et al. Kerker-conditioned dynamic cryptographic nanoprints. *Adv. Opt. Mater.* **7**, 1801070 (2019).
44. Kuznetsov, A. I., Miroshnichenko, A. E., Fu, Y. H., Zhang, J. & Luk'yanchuk, B. Magnetic light. *Sci. Rep.* **2**, 492 (2012).
45. Fu, Y. H., Kuznetsov, A. I., Miroshnichenko, A. E., Yu, Y. F. & Luk'yanchuk, B. Directional visible light scattering by silicon nanoparticles. *Nat. Commun.* **4**, 1527 (2013).
46. Evlyukhin, A. B. et al. Demonstration of magnetic dipole resonances of dielectric nanospheres in the visible region. *Nano Lett.* **12**, 3749–3755 (2012).
47. Tribelsky, M. I. & Luk'yanchuk, B. S. Anomalous light scattering by small particles. *Phys. Rev. Lett.* **97**, 263902 (2006).
48. Bücher, K., Bruns, J. & Wagemann, H. G. Absorption coefficient of silicon: an assessment of measurements and the simulation of temperature variation. *J. Appl. Phys.* **75**, 1127–1132 (1994).
49. Ning, C.-Z., Dou, L. & Yang, P. Bandgap engineering in semiconductor alloy nanomaterials with widely tunable compositions. *Nat. Rev. Mater.* **2**, 17070 (2017).
50. Khurgin, J. B. & Sun, G. In search of the elusive lossless metal. *Appl. Phys. Lett.* **96**, 181102 (2010).
51. Dong, W. et al. Wide bandgap phase change material tuned visible photonics. *Adv. Funct. Mater.* **29**, 1806181 (2019).
52. Fortmann, C. M. Random phononic structure and indirect optical transitions: an explanationfor the hydrogen dependence of the amorphous silicon band gap? *Phys. Rev. Lett.* **81**, 3683–3686 (1998).
53. Kuyken, B. et al. Nonlinear properties of and nonlinear processing in hydrogenated amorphous silicon waveguides. *Opt. Express* **19**, B146–B153 (2011).
54. Narayanan, K. & Preble, S. F. Optical nonlinearities in hydrogenated-amorphous silicon waveguides. *Opt. Express* **18**, 8998–9005 (2010).
55. Shi, L. et al. Monodisperse silicon nanocavities and photonic crystals with magnetic response in the optical region. *Nat. Commun.* **4**, 1904 (2013).
56. Yue, W. et al. Polarization-encrypted high-resolution full-color images exploiting hydrogenated amorphous silicon nanogratings. *Nanophotonics* **9**, 875–884 (2020).
57. Park, C. S. et al. Structural color filters enabled by a dielectric metasurface incorporating hydrogenated amorphous silicon nanodisks. *Sci. Rep.* **7**, 2556 (2017).
58. Shi, L., Tuzer, T. U., Fenollosa, R. & Meseguer, F. A new dielectric metamaterial building block with a strong magnetic response in the sub-1.5-micrometer region: Silicon colloid nanocavities. *Adv. Mater.* **24**, 5934–5938 (2012).
59. Harris, J. T., Hueso, J. L. & Korgel, B. A. Hydrogenated amorphous silicon (a-Si:H) colloids. *Chem. Mater.* **22**, 6378–6383 (2010).
60. Smets, A. H. M. et al. The relation between the bandgap and the anisotropic nature of hydrogenated amorphous silicon. *IEEE J. Photovolt.* **2**, 94–98 (2012).
61. Pell, L. E., Schricker, A. D., Mikulec, F. V. & Korgel, B. A. Synthesis of amorphous silicon colloids by trisilane thermolysis in high temperature supercritical solvents. *Langmuir* **20**, 6546–6548 (2004).
62. Choi, W. K. Optical properties of hydrogenated amorphous silicon carbide films. *Diffus. Defect Data. Pt A Defect Diffus. Forum* **177**, 29–42 (2000).
63. Park, C.-S. et al. Structural color filters based on an all-dielectric metasurface exploiting silicon-rich silicon nitride nanodisks. *Opt. Express* **27**, 667–679 (2019).
64. Colburn, S. et al. Broadband transparent and CMOS-compatible flat optics with silicon nitride metasurfaces [Invited]. *Opt. Mater. Express* **8**, 2330–2344 (2018).
65. Devlin, R. C., Khorasaninejad, M., Chen, W. T., Oh, J. & Capasso, F. Broadband high-efficiency dielectric metasurfaces for the visible spectrum. *Proc. Natl Acad. Sci. USA* **113**, 10473–10478 (2016).
66. Khorasaninejad, M. et al. Metalenses at visible wavelengths: diffraction-limited focusing and subwavelength resolution imaging. *Science* **352**, 1190–1194 (2016).
67. Wu, Y., Yang, W., Fan, Y., Song, Q. & Xiao, S. TiO_2 metasurfaces: from visible planar photonics to photochemistry. *Sci. Adv.* **5**, eaax0939 (2019).
68. Sun, S. et al. All-dielectric full-color printing with TiO_2 metasurfaces. *ACS Nano* **11**, 4445–4452 (2017).
69. Chen, B. H. et al. GaN metalens for pixel-level full-color routing at visible light. *Nano Lett.* **17**, 6345–6352 (2017).
70. Wang, S. et al. A broadband achromatic metalens in the visible. *Nat. Nanotechnol.* **13**, 227–232 (2018).
71. Lewi, T., Iyer, P. P., Butakov, N. A., Mikhailovsky, A. A. & Schuller, J. A. Widely tunable infrared antennas using free carrier refraction. *Nano Lett.* **15**, 8188–8193 (2015).
72. Savelev, R. S., Sergaeva, O. N., Baranov, D. G., Krasnok, A. E. & Alù, A. Dynamically reconfigurable metal-semiconductor Yagi-Uda nanoantenna. *Phys. Rev. B* **95**, 235409 (2017).
73. Bohren, C. F. & Huffman, D. R. *Absorption and Scattering of Light by Small Particles* (Wiley-VCH Verlag GmbH, 1998).
74. Koshelev, K. et al. Subwavelength dielectric resonators for nonlinear nanophotonics. *Science* **367**, 288–292 (2020).
75. Leuthold, J., Koos, C. & Freude, W. Nonlinear silicon photonics. *Nat. Photonics* **4**, 535–544 (2010).
76. Pala, R. A., Shimizu, K. T., Melosh, N. A. & Brongersma, M. L. A nonvolatile plasmonic switch employing photochromic molecules. *Nano Lett.* **8**, 1506–1510 (2008).
77. Zograf, G. P. et al. Resonant nonplasmonic nanoparticles for efficient temperature-feedback optical heating. *Nano Lett.* **17**, 2945–2952 (2017).
78. Baranov, D. G. et al. Nonlinear transient dynamics of photoexcited resonant silicon nanostructures. *ACS Photonics* **3**, 1546–1551 (2016).
79. Zuev, D. A. et al. Fabrication of hybrid nanostructures via nanoscale laser-induced reshaping for advanced light manipulation. *Adv. Mater.* **28**, 3087–3093 (2016).
80. Klajn, R. Spiropyran-based dynamic materials. *Chem. Soc. Rev.* **43**, 148–184 (2014).

81. Lin, L. et al. Photoswitchable rabi splitting in hybrid plasmon-waveguide modes. *Nano Lett.* **16**, 7655–7663 (2016).
82. Alù, A. & Engheta, N. Polarizabilities and effective parameters for collections of spherical nanoparticles formed by pairs of concentric double-negative, single-negative, and⁄or double-positive metamaterial layers. *J. Appl. Phys.* **97**, 094310 (2005).
83. Buback, J. et al. Ultrafast bidirectional photoswitching of a spiropyran. *J. Am. Chem. Soc.* **132**, 16510–16519 (2010).
84. Kohl-Landgraf, J. et al. Ultrafast dynamics of a spiropyran in water. *J. Am. Chem. Soc.* **134**, 14070–14077 (2012).
85. Aden, A. L. & Kerker, M. Scattering of electromagnetic waves from two concentric spheres. *J. Appl. Phys.* **22**, 1242–1246 (1951).

Acknowledgements

Y.Z., M.S., and J.F. acknowledge the financial support of the National Science Foundation (CBET-1704634), and the National Institute of General Medical Sciences of the National Institutes of Health (DP2GM128446). M.S. acknowledges the financial support of University Graduate Continuing Fellowship of the University of Texas at Austin. A.A., M.S., and A.K. acknowledge the financial support of the Air Force Office of Scientific Research and the National Science Foundation. S.L. acknowledges the financial support by Russian Science Foundation (Project No. 18-72-10140) and Foundation for the Advancement of Theoretical Physics and Mathematics. B.A.K. and T.J. acknowledge the financial support of Robert A. Welch Foundation (grant no. F-1464) and The Center for Dynamics and Control of Materials (CDCM) Materials Research Science and Engineering Center (MRSEC) supported by the NSF (DMR-1720595).

Author contributions

Y.Z, A.A., M.W., and A.K. conceived and coordinated the project. M.W. performed experiments with the assistance of J.F.. A.K., S.L., and G.H. performed the analytical and numerical simulations. T.J. and B.A.K. synthesized the a-Si:H NPs. M.W. and A.K. wrote the manuscript. All authors discussed the results and commented on the manuscript.

Competing interests

The authors declare no competing interests.

Additional information

Supplementary information is available for this paper at https://doi.org/10.1038/s41467-020-18793-y.

Correspondence and requests for materials should be addressed to A.K., A.A. or Y.Z.

Peer review information *Nature Communications* thanks Elizaveta Melik-Gaykazyan and the other, anonymous, reviewers for their contribution to the peer review of this work. Peer reviewer reports are available.

Reprints and permission information is available at http://www.nature.com/reprints

Publisher's note Springer Nature remains neutral with regard to jurisdictional claims in published maps and institutional affiliations.

APPENDIX H

Paper 8: Indirect bandgap $MoSe_2$ resonators for light-emitting nanophotonics

---

Photoluminescence enhancement in bulk $MoSe_2$ microdisk resonators in investigated. The manuscript is published.

The citations in the manuscript refer to reference list included at the end of the manuscript.

Work contributions by the present author: Numerical calculations, manuscript writing.

Reference information:

B. Borodin, F. Benimetskiy, V. Davydov, I. Eliseyev, A. Smirnov, D. Pidgayko, **S. Lepeshov**, A. Bogdanov, and P. Alekseev. Indirect bandgap $MoSe_2$ resonators for light-emitting nanophotonics. *Nanoscale Horizons* 8, 396-403 (2023).

Nanoscale
Horizons

COMMUNICATION

View Article Online
View Journal | View Issue

Cite this: *Nanoscale Horiz.*, 2023, 8, 396

Received 1st October 2022,
Accepted 16th January 2023

DOI: 10.1039/d2nh00465h

rsc.li/nanoscale-horizons

Indirect bandgap $MoSe_2$ resonators for light-emitting nanophotonics†

Bogdan R. Borodin,*[a] Fedor A. Benimetskiy,[b] Valery Yu. Davydov,[a]
Ilya A. Eliseyev,[a] Alexander N. Smirnov,[a] Dmitry A. Pidgayko,[b]
Sergey I. Lepeshov,[b] Andrey A. Bogdanov[b] and Prokhor A. Alekseev[a]

Transition metal dichalcogenides (TMDs) are promising for new generation nanophotonics due to their unique optical properties. However, in contrast to direct bandgap TMD monolayers, bulk samples have an indirect bandgap that restricts their application as light emitters. On the other hand, the high refractive index of these materials allows for effective light trapping and the creation of high-Q resonators. In this work, a method for the nanofabrication of microcavities from indirect TMD multilayer flakes, which makes it possible to achieve pronounced resonant photoluminescence enhancement due to the cavity modes, is proposed. Whispering gallery mode (WGM) resonators are fabricated from bulk indirect $MoSe_2$ using resistless scanning probe lithography. A micro-photoluminescence (μ-PL) investigation revealed the WGM spectra of the resonators with an enhancement factor up to 100. The characteristic features of WGMs are clearly seen from the scattering experiments which are in agreement with the results of numerical simulations. It is shown that the PL spectra in the fabricated microcavities are contributed by two mechanisms demonstrating different temperature dependences. The indirect PL, which is quenched with the temperature decrease, and the direct PL which almost does not depend on the temperature. The results of the work show that the suggested approach has great prospects in nanophotonics.

New concepts

Bulk transition metal dichalcogenides (TMDs) have an extremely high refractive index (∼5) in the visible and IR spectral ranges. It makes them an ideal medium for nanophotonic structures. However, due to an indirect bandgap, the main attention for the application of TMDs in the field of nanophotonics is paid to the creation of dielectric nanophotonic structures for light absorption or low-loss nanophotonics. To date, there are practically no studies devoted to light-emitting TMD nanophotonic structures. Here we introduce a novel type of stand-alone TMD nanocavity as a source of excitonic photoluminescence. Disk whispering-gallery-mode optical nanoresonators were made of bulk indirect bandgap $MoSe_2$. Brand new frictional probe lithography was used to fabricate nanoresonators so as not to disturb the pristine properties of the TMD, which are highly sensitive to any contamination or chemical treatment. The obtained nanoresonators demonstrate strongly enhanced (by two orders of magnitude) photoluminescence in the range of 850 to 1050 nm. Peak positions can be tuned by varying the nanocavity diameter. This work demonstrates a new approach to the fabrication of light-emitting nanophotonic devices from indirect bandgap TMDs and opens up many opportunities for further research.

1 Introduction

Since the discovery of graphene in 2004,[1] layered materials have become one of the most booming topics in many fields, such as materials science,[2] condensed matter physics,[3] optoelectronics,[4] and photonics,[5] *etc.* The most prospective semiconductive materials seem to be transition metal dichalcogenides (TMDCs). This is due to the unique properties of their monolayers such as extraordinary light absorption,[6] large exciton binding energies,[7,8] strong and tailoring photoluminescence,[9–11] the possibility of creating van der Waals heterostructures,[12,13] twisting engineering,[14–16] *etc.* Such an active investigation of TMDC monolayers has revived interest in studying the properties of their bulk samples. These materials in their bulk form were actively studied back in the 1970s.[17–20] However, today, researchers can take a fresh look at their bulk properties using the progress that has been made in understanding physical phenomena and the best modern equipment that allows researchers to look deeper at known properties and to find new ones. Most recent studies have revealed many new outstanding properties of multilayered TMDCs, such as their giant optical anisotropy,[21] polarizing effects,[22] anapole–exciton polaritons,[23] exciton–plasmon–polaritons,[24] exciton–polariton transport,[25] second harmonic generation,[26] *etc.* All the above-mentioned properties make these materials a perfect candidate for a variety of nanophotonic

---

[a] *Ioffe Institute, Saint Petersburg, 194021, Russia. E-mail: brborodin@gmail.com*
[b] *ITMO University, Saint Petersburg, 197101, Russia*

† Electronic supplementary information (ESI) available. See DOI: **https://doi.org/10.1039/d2nh00465h**

applications including lasers,[27,28] waveguides,[25,29,30] high harmonic generation,[30–32] bound states in the continuum,[33,34] *etc.*

However, there is a significant obstacle in the way of the implementation of light-emitting nanophotonic devices. Multilayered TMDCs have an indirect bandgap that results in negligible photoluminescence (PL).[35] To use some of the unique properties of TMDCs, many researchers integrate direct bandgap TMDC monolayers into external photonic circuits/resonators as a source of excitonic photoluminescence.[27,36–38] Because of their thickness, stand-alone monolayers cannot be used to fabricate waveguides or resonators for the visible and near-IR ranges. That requires forming photonic circuits and exciton/PL sources using various technological processes and different materials. All this considerably complicates the on-chip integration of TMDC materials. Another way to solve this problem is to use the Purcell effect to enhance the PL intensity of multilayered TMDCs.[39–41] This approach was successfully used to enhance the light emission of Si in optical cavities.[42–45] Although due to the strong absorption of free charge carriers in Si, the effect was not game-changing.[46–49] Owing to an extremely high refractive index in the visible and near-IR ranges ($n \approx 4$–5),[50,51] high-Q nanocavities with a strong Purcell effect and enhanced emissivity might be made from bulk TMDCs (the principle is illustrated in Fig. 1).[52]

In this work, we create disk whispering-gallery mode (WGM) optical nanoresonators from multilayered $MoSe_2$. Resistless mechanical probe lithography was used to fabricate the nanoresonators so as not to disturb the pristine properties of the TMDCs, which are highly sensitive to any contamination or chemical treatment.[53–55] The obtained nanocavities demonstrate strongly enhanced (by two orders of magnitude) photoluminescence in the range of 850 to 1050 nm. The spectral features correspond to WGM resonances, which were confirmed by numerical simulations and scattering experiments. The results of the work allow the introduction of novel types of standalone TMDC nano- and microcavities as sources of excitonic photoluminescence for on-chip integrated nanophotonic circuits.

2 Experimental

2.1 Sample preparation

Thin-film $MoSe_2$ samples were fabricated by mechanical exfoliation with adhesive tape (blue tape, Nitto) from a commercial bulk crystal (obtained from HQ Graphene, Netherlands) on top of the Au/Si substrate.

2.2 Cavities creation

The cavities were created by resistless frictional mechanical probe lithography. To perform the procedure, we used a Ntegra Aura (NT-MDT) atomic force microscope using DCP (NT-MDT) probes with a curvature radius of 100 nm and a spring constant of 30–85 N m^{-1}. The multi-pass frictional approach was used to prevent defect formation. The force was about 10 μN, and the number of passes amounted to 200 for each resonator. Detailed information on this approach and the cavity creation process is available in our previous work.[56,57]

2.3 Micro-photoluminescence (μ-PL) investigation

The optical properties of the structures were investigated by measuring the PL spectra. For these experiments, a multifunctional optical complex Horiba LabRAM HREvo UV-VIS-NIR-Open equipped with a confocal microscope was used. The spectra were obtained with a spectral resolution of 3 cm^{-1} using a 600 g mm^{-1} grating. We used an Olympus MPLN100× objective lens (NA = 0.9) to obtain information from an area with a diameter of 1 μm. Apart from local measurements, PL mapping with a spatial resolution of 0.5 μm was

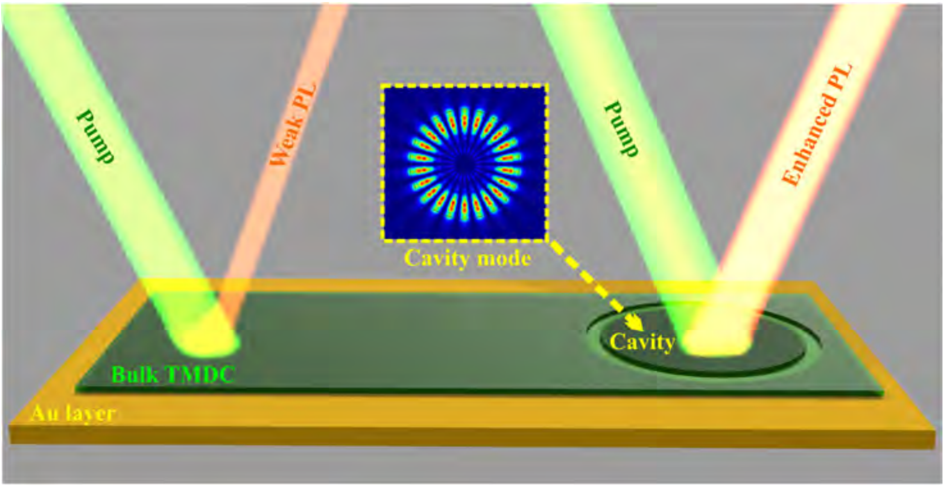

Fig. 1 Principal scheme of PL enhancement in cavities made of indirect bandgap TMDCs. Owing to the indirect bandgap, the PL signal from the bulk flakes is weak. However, it can be enhanced by a cavity.

performed at the same setup using a motorized table. The measurements were performed with continuous-wave (cw) excitation using the 532 nm laser line of a Nd:YAG laser (Laser Quantum Torus). To prevent damage to the structures, the incident laser power was limited to 1 mW.

2.4 Scattering experiments

The microdisks were illuminated with white polarised light (Ocean Optics HL-2000-HP in combination with linear polariser) at an incidence angle of 65 degrees with a low-aperture lens Mitutoyo Plan Apo NIR 10 × 0.26 NA. The radiation scattered by the disks is collected using the Mitutoyo Plan Apo NIR 50 × 0.65 NA which was analysed on a Horiba LabRAM HR 800 UV-VIS-NIR spectrometer. The numerical apertures of the lenses and the angle of incidence are chosen so that the pump does not pass through the collection channel.

3 Results and discussion

3.1 Fabrication of nanocavities

An experimental structure consisting of thin $MoSe_2$ flakes was transferred onto a Si substrate covered with 50 nm of gold. $MoSe_2$ flakes were obtained by micro-mechanical exfoliation and were transferred using a standard approach (*i.e.*, scotch-tape method) without using PDMS to prevent contamination with the polymer.[54] Fig. 2a shows the cross-section of the structure used.

To create a cavity, we firstly found a flake of a thickness of about 70–100 nm that is sufficient to accommodate the WGMs. Then we used frictional scanning probe lithography (f-SPL) to fabricate the cavities.[57] The scheme of the f-SPL is shown in Fig. 2b. f-SPL is a resistless method of lithography based on the mechanical influence of an atomic force microscopy (AFM) probe on the sample surface to remove the material (mechanical-SPL). However, while m-SPL conventionally uses high pressure to deepen the lithographic patterns (“cutting” regime), f-SPL consists of consequent repetitions of the lithographic patterns with a small amount of pressure on the sample. Thus, during f-SPL, the material is gradually rubbed out from the surface. This approach allows the avoidance of cantilever twisting that prevents the formation of artifacts and makes it possible to maintain high resolution even in the case of thick samples. Fig. 2c shows an optical image of the processed flake. It can be seen that two circular cavities are formed from the flake, and the removed material is nearby. Fig. 2d–f demonstrates the AFM images of the cavity creation process. The first is a relatively flat surface of the flake. The second is the surface with a half-thickness trench. The third is the fully separated cavity and the full-thickness trench. The optical properties of such cavities were studied by μ-PL and dark-field spectroscopy.

3.2 Optical properties of nanocavities

As discussed in the introduction, TMDs have many peculiar properties that can appear in the optical response of such structures. However, a combination of photoluminescence and scattering investigations is a reliable method to determine the nature of the observed features. The shape of the spectra and the peak-to-peak distance are strong evidence of resonant phenomena, whether they are WGM or Mie resonances. Thus, the optical properties of the cavities were studied using micro-PL and dark-field spectroscopy. Fig. 3 demonstrates the results of the PL and experimental dark-field (DF) spectroscopy measurements supported by DF numerical calculations. In the μ-PL

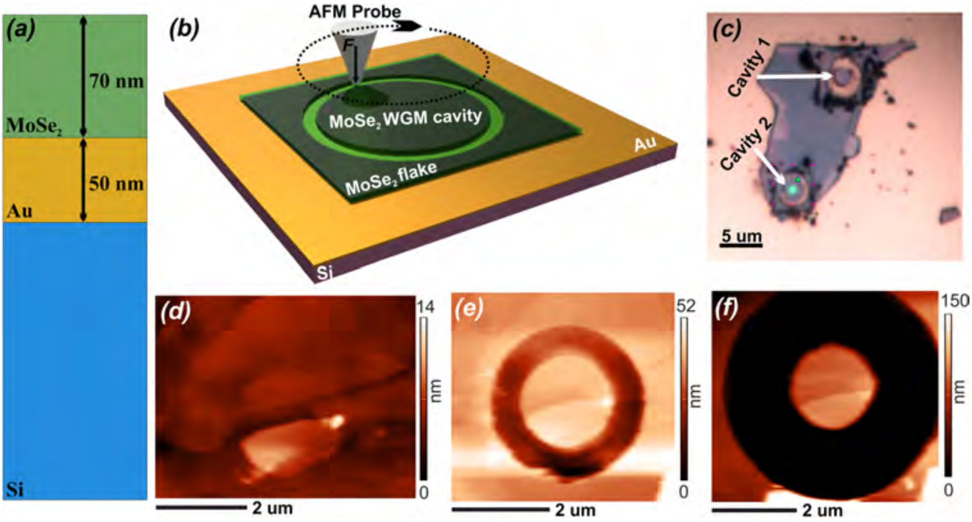

Fig. 2 (a) Cross-section of the sample. (b) Scheme of frictional probe lithography of a cavity. (c) Optical image of the $MoSe_2$ flake with two cavities. (d–f) AFM images of the cavity creation process.

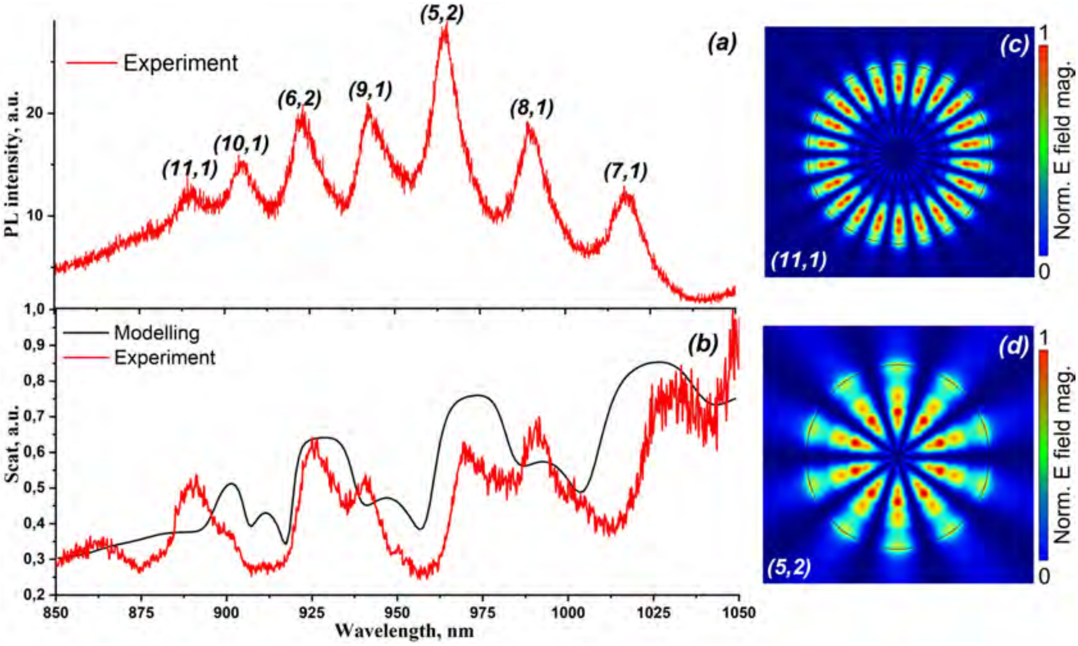

Fig. 3 (a) Photoluminescence and (b) dark-field spectra of the cavity for s-polarised incidence. The red curves correspond to the experimental measurements, the black curve represents the numerical calculations. The numbers in brackets represent the azimuthal and radial numbers (*M*, *n*) for modes corresponding to the associated peaks. (c and d) Electrical field distribution in the cavity for (11, 1) and (5, 2) modes modeled in COMSOL Multiphysics.

spectrum, we observe a series of peaks (see Fig. 3a), which may potentially originate from the whispering gallery mode resonance. Further, we carry out the DF spectroscopy of the cavity previously exposed by the PL measurements. Since the DF spectroscopy deals only with the optical resonances of a cavity, it allows us to unambiguously identify whether the PL peaks have a resonant nature or not. The results are shown in Fig. 3(b, red curve). One can see that we observe the resonant features in the spectral regions similar to those that we get through PL measurements (Fig. 3a).

To prove the optical resonance nature of the PL peaks, we prepare comprehensive numerical simulations of optical scattering in COMSOL Multiphysics. We assume a $MoSe_2$ disk on the top of a Si substrate covered by a layer of Au. The permittivities of $MoSe_2$, Si and Au are taken from ref. 18, 58 and 59. The disk diameter is 2.2 μm, the height is 70 nm, and the thickness of the Au layer is 50 nm. To calculate the scattering spectrum, we illuminate the structure by the s-polarised plane wave with the incident angle of 65° and collect the scattered wave in the numerical aperture of 0.65. The results of the numerical calculation of the DF spectrum are presented in Fig. 3(b, black curve). The experimentally obtained DF spectrum is in a good agreement with the numerical one. Based on the resonant behaviour of the DF spectra and the peak-to-peak comparison, we conclude that the PL peaks have an optical resonance nature. Fig. 3c and d demonstrate the electrical field distribution in the cavity for the (11, 1) and (5, 2) modes modeled in COMSOL Multiphysics.

Conventionally, when TMD monolayers are used as light emitters, the external resonator is tuned to the direct exciton transition[60–62] (*i.e.*, 780 nm/1.57 eV in the $MoSe_2$ case).[9] In our case, we use a bulk TMD layer simultaneously as a resonator and an emitter. Therefore, the absorption of the emitted light is of great importance in our case. Even bulk TMDs have a strong absorbance near the excitonic resonance, while the luminescence is weak.[19,63] Thus, to avoid maximum absorption, we should tune our resonators to the long wavelength tail of the photoluminescence.

Fig. 4 shows the μ-PL data for cavities of various diameters. The spectra consist of a series of peaks that are specific for whispering gallery modes. The size variety of the cavities provides different positions of the maxima and enhancement factors. The 2.2 μm diameter cavity exhibits significantly enhanced PL with an enhancement factor of up to 100. Additionally, one can notice that the PL maxima of the cavities are shifted to the long-wavelength region compared to the PL peak of the flake. Such a red-shift of the PL maxima can be explained by the dominant contribution of the cavity modes to the PL in the long-wavelength region (900–1050 nm) and suppression of the cavity radiation due to the significant $MoSe_2$ material losses in the short-wavelength region (800–900 nm). The PL maximum of the bare $MoSe_2$ appears in the highly absorptive wavelength

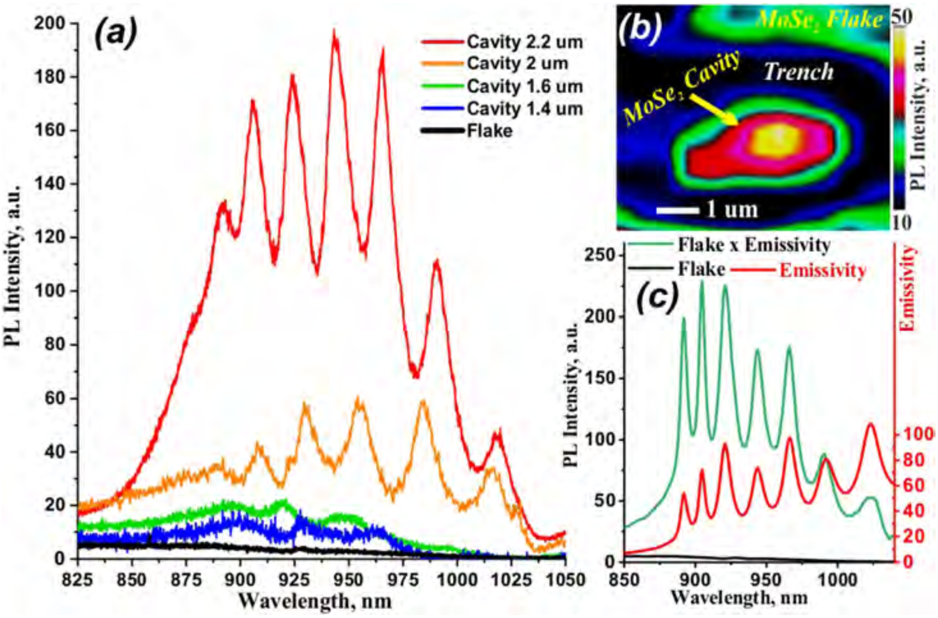

Fig. 4 (a) PL spectra of cavities of various diameters. (b) PL mapping of one of the structures. (c) Calculated emissivity of the 2.2 μm cavity (red curve), the flake spectrum (black curve), and the flake spectrum multiplied by the emissivity (green curve).

range below 900 nm. Therefore, the cavity modes produce a small PL signal in the short-wavelength region where the absorptive losses are simultaneously resonantly enhanced. For this reason, the disks with smaller diameters of 1.4 and 1.6 μm that have a high-Q resonance at the shorter wavelengths did not show such a strong enhancement.[56] Moreover, we created structures of larger diameters (3, 5, and 10 μm). The PL data of these structures are presented in the ESI† in Fig. S1. The 3 μm cavity demonstrates some features related to WGMs.

However, these peaks are significantly weaker than in the 2.2 μm cavity case, and the flake-like PL peak dominates (see Fig. S1, red curve, ESI†). With increasing cavity diameter, all WGM features disappear, and only the unmodified flake photoluminescence remains in the spectra (see Fig. S1, ESI†, purple and blue curves). Such dependence of the PL on the cavity diameter can be explained by competition between the gain and material losses. On one hand, a larger cavity should provide higher enhancement due to the high-quality factor of modes with a higher azimuthal number. On the other hand, a longer light path in larger cavities relates to more intensive absorption by indirect bandgap materials. Consequently, small cavities have low a Q factor but low losses (1.4 and 1.6 μm), large cavities have a high Q factor but high losses (3, 5, and 10 μm), and there is most likely some compromise with satisfying gain and losses (2, and 2.2 μm). Thus, we believe that the 2.2 μm diameter cavity is a compromise between miniature size and enhancement factor (≈100).

The enhanced PL originates from the Purcell effect caused by the whispering gallery modes of the microdisk. The direct evidence of the Purcell effect is the shortening of the lifetime of the excited states. We measured the time-resolved PL for the cavity with the largest enhancement factor (see Fig. 3S in ESI†). Fig. 3S (ESI†) shows the instrument response function (IRF) of the experimental setup and the PL decay curves for the bulk flake and the microcavity with a 2.2 μm diameter, which were measured at 966 nm (see Fig. 4a). The long lifetime part of the IRF curve is associated with the effect of the diffusion tail, which is typical for such types of detectors.[64] The full width at half maximum (FWHM) values for the IRF and PL decay curves were extracted from experimental data and are approximately 80 ps. To analyze the measured spectra more precisely, we approximate them with a two-phase exponential decay function. The time constants for the short lifetime region of the curves are $t_1^{\mathrm{Bulk}} = 37 \pm 2$ ps, $t_1^{\mathrm{Cavity}} = 37 \pm 2$ ps, $t_1^{\mathrm{IRF}} = 36 \pm 2$ ps which are in good agreement with the FWHM values, and the main difference of the measured spectra is observed for the time constants associated with a long lifetime region: $t_2^{\mathrm{Bulk}} = 345 \pm 10$ ps, $t_2^{\mathrm{Cavity}} = 318 \pm 2$ ps, $t_2^{\mathrm{IRF}} = 311 \pm 10$ ps. Such behavior may indicate a decrease of the PL lifetime due to increasing the local density of the optical states for the cavity, but the time resolution limitation and the effect of the diffusion tail make it difficult to interpret the results.

Furthermore, to estimate the impact of the Purcell effect and to validate our experimental results, we perform numerical calculations of the emissivity of the microdisk in COMSOL Multiphysics.[65] In order to calculate the intensity of the emitted field, we utilize the reciprocity theorem. The reciprocity theorem dictates that the electric field intensity emitted by the current distribution is equal to the intensity necessary for excitation of the current distribution. As a consequence, the ability of the cavity to absorb the incident energy matches with its ability to emit. Thus, to estimate the emissivity, it is enough to find the energy absorbed in the microdisk. Fig. 4 (c, red curve) shows the emissivity spectrum of the microdisk with the diameter equal to 2.2 μm. The emissivity is calculated as an integral of the field intensity inside the microdisk. Multiplication of the emissivity and the flake PL spectrum gives the PL of the $MoSe_2$ microdisk. The positions of the peaks obtained in the calculations perfectly match with those that are experimentally measured.

One can notice that conventionally WGM resonators do not emit vertically. However, the presence of defects might serve as a scatterer or antenna, and a finite aperture of the collecting objective provides simultaneous collection in some angle ranges. We can see such defects in our structures (*e.g.*, non-uniform thickness in Fig. 2d). In addition, we have noticed that the PL signals strongly depend on a collection spot. Fig. 4b demonstrates the PL mapping of one of the structures. It can be seen that the PL intensity is not uniformly distributed, and that there are hot spots. So, in our experiments, we chose the spots that demonstrate the maximum PL intensity to record the PL spectra.

3.3 Temperature dependence of photoluminescence

The nature of the PL of such multilayer TMDCs structures is still ambiguous. However, many works point out the optical activity of both direct and indirect transitions in multilayered TMDs.[66–69] The common conclusion is that temperature plays a key role in the activation of an indirect transition. In our case, at room temperature, we have a broad PL spectrum modified by a WGM resonator; therefore, its analysis is nontrivial. For this reason, we investigated the temperature dependence of PL for our structures. The results of the investigation are shown in Fig. 5.

As you can see from Fig. 5a, with the decreasing temperature, the broad spectrum at 300 K (see red line) splits into two components at 175 K (see green line), and finally, at 85 K (see violet line), the long-wavelength peak quenches, and the short-wavelength one becomes dominant in the spectrum. Based on such behavior of the PL, we can assume that the observed PL consists of two near peaks. The direct transition is about 1.4 eV, and the indirect transition is about 1.25 eV. The energy of excitation is much higher than both of these (*i.e.*, excitation is non-resonant). Therefore, at room temperature, most of the excited electrons experience phonon-assisted relaxation to the lowest energy state. There, the electrons commit radiative phonon-assisted recombination that provides the peak at 1.25 eV.

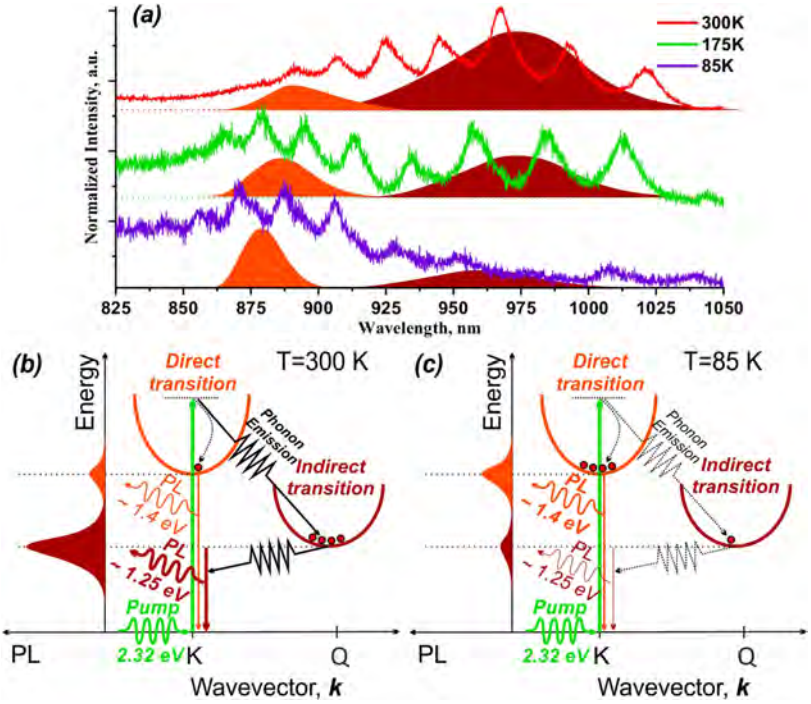

Fig. 5 (a) Temperature dependence of photoluminescence. (b and c) Scheme of optical transitions at 300 K and 85 K, respectively. Orange and red contours are simple guides to the eye for direct and indirect transitions, respectively. Conventional fitting by Gaussian or Lorentzian curves is hampered due to the fact that the PL spectra modified by WGM resonance, and the PL of the thick flake are very weak.

Although, some electrons relax directly to a higher energy state that has a shorter lifetime (*i.e.*, higher oscillator strength) and recombine directly without a phonon that provides the peak at 1.4 eV. This case is illustrated in Fig. 5b that corresponds to the spectrum at 300 K (see Fig. 5a). With decreasing temperature, the PL peaks become narrow, and the phonons start to freeze out which reduces the effectiveness of the phonon-assisted recombination channel. As a consequence, we can see the separation of direct and indirect peaks and the formation of a ''trough'' at 930 nm between them (see Fig. 5a, 175 K). At 85 K, the phonons are almost frozen out, and the phonon-assisted channel is ineffective. Therefore, the indirect peak can barely be seen, and the direct channel becomes dominant. This case is illustrated in Fig. 5c that corresponds to the spectrum at 85 K (see Fig. 5a). Although, as discussed earlier, the cavities mainly enhance the tails of the PL peaks. So, the actual energies of transitions are probably slightly higher than those we observe here.

4 Conclusions

To conclude, we investigated the optical properties of nanophotonic WGM disk resonators. The resonators were fabricated from bulk indirect bandgap $MoSe_2$ *via* resistless mechanical scanning probe lithography. The diameter of the cavities varied from 1.4 to 10 μm, and the thickness was 70 nm. A micro-photoluminescence investigation revealed WGM-like PL spectra with various enhancement factors depending on the cavity diameter. It was shown that the optimal cavity diameter is 2.2 μm, which provides an enhancement factor of $\approx$100 compared to the pristine flake. Scattering experiments and modeling also revealed WGM spectra and confirmed the data obtained by micro-PL. Moreover, we investigated the temperature dependence of a cavity PL. The results showed that the PL has two components – short-wavelength ($\approx$885 nm) and long-wavelength ($\approx$990 nm) components. With decreasing temperature, the long-wavelength component quenches, while the short-wavelength one becomes dominant. Based on these results, we assume that two transitions are simultaneously active in the PL of our structures – direct ($\approx$1.4 eV) and indirect ($\approx$1.25 eV).

Thus, in this work, we demonstrated a novel approach to the fabrication of light-emitting nanophotonic devices based on bulk indirect bandgap TMDs and investigated the optical properties of several of them. We believe that this approach might be promising to create other light-emitting nanophotonic devices from bulk TMDs and reveal their fascinating properties.

Author contributions

B. R. B. performed the probe lithography, analyzed the data obtained, and prepared the initial manuscript. F. A. B. fabricated the samples. V. Yu. D., I. A. E., and A. N. S. carried out the micro-photoluminescence investigations. D. A. P. performed a scattering study. S. I. L. and A. A. B. provided theoretical support and calculations. P. A. A. and A. A. B. supervised the research and provided essential contributions to interpreting the results. All coauthors assisted in writing the manuscript.

Conflicts of interest

There are no conflicts to declare.

Acknowledgements

There is no funding to report. We thank Mikhail M. Glazov and Ivan V. Iorsh for fruitful discussions.

References

1 K. S. Novoselov, A. K. Geim, S. V. Morozov, D.-e Jiang, Y. Zhang, S. V. Dubonos, I. V. Grigorieva and A. A. Firsov, *Science*, 2004, **306**, 666–669.
2 S. Manzeli, D. Ovchinnikov, D. Pasquier, O. V. Yazyev and A. Kis, *Nat. Rev. Mater.*, 2017, **2**, 1–15.
3 D. M. Kennes, M. Claassen, L. Xian, A. Georges, A. J. Millis, J. Hone, C. R. Dean, D. Basov, A. N. Pasupathy and A. Rubio, *Nat. Phys.*, 2021, **17**, 155–163.
4 Y. Jing, B. Liu, X. Zhu, F. Ouyang, J. Sun and Y. Zhou, *Nanophotonics*, 2020, **9**, 1675–1694.
5 K. F. Mak and J. Shan, *Nat. Photonics*, 2016, **10**, 216–226.
6 M. Bernardi, M. Palummo and J. C. Grossman, *Nano Lett.*, 2013, **13**, 3664–3670.
7 M. M. Ugeda, A. J. Bradley, S.-F. Shi, H. Felipe, Y. Zhang, D. Y. Qiu, W. Ruan, S.-K. Mo, Z. Hussain and Z.-X. Shen, *et al.*, *Nat. Mater.*, 2014, **13**, 1091–1095.
8 A. Hanbicki, M. Currie, G. Kioseoglou, A. Friedman and B. Jonker, *Solid State Commun.*, 2015, **203**, 16–20.
9 P. Tonndorf, R. Schmidt, P. Böttger, X. Zhang, J. Börner, A. Liebig, M. Albrecht, C. Kloc, O. Gordan and D. R. Zahn, *et al.*, *Opt. Express*, 2013, **21**, 4908–4916.
10 S. Tongay, J. Zhou, C. Ataca, J. Liu, J. S. Kang, T. S. Matthews, L. You, J. Li, J. C. Grossman and J. Wu, *Nano Lett.*, 2013, **13**, 2831–2836.
11 F. Benimetskiy, V. Sharov, P. Alekseev, V. Kravtsov, K. Agapev, I. Sinev, I. Mukhin, A. Catanzaro, R. Polozkov and E. Alexeev, *et al.*, *APL Mater.*, 2019, **7**, 101126.
12 A. K. Geim and I. V. Grigorieva, *Nature*, 2013, **499**, 419–425.
13 S. Fan, Q. A. Vu, M. D. Tran, S. Adhikari and Y. H. Lee, *2D Mater.*, 2020, **7**, 022005.
14 J. Michl, S. Tarasenko, F. Lohof, G. Gies, M. von Helversen, R. Sailus, S. Tongay, T. Taniguchi, K. Watanabe and T. Heindel, *et al.*, *Phys. Rev. B*, 2022, **105**, L241406.
15 K. Tran, J. Choi and A. Singh, *2D Mater.*, 2020, **8**, 022002.
16 S. Shabani, D. Halbertal, W. Wu, M. Chen, S. Liu, J. Hone, W. Yao, D. N. Basov, X. Zhu and A. N. Pasupathy, *Nat. Phys.*, 2021, **17**, 720–725.
17 A. Goldberg, A. Beal, F. Levy and E. Davis, *Philos. Mag.*, 1975, **32**, 367–378.
18 A. Beal and H. Hughes, *J. Phys. C-Solid State Phys.*, 1979, **12**, 881.
19 J. A. Wilson and A. Yoffe, *Adv. Phys.*, 1969, **18**, 193–335.
20 A. Anedda and E. Fortin, *J. Phys. Chem. Solids*, 1980, **41**, 865–869.

21 G. Ermolaev, D. Grudinin, Y. Stebunov, K. V. Voronin, V. Kravets, J. Duan, A. Mazitov, G. Tselikov, A. Bylinkin and D. Yakubovsky, *et al.*, *Nat. Commun.*, 2021, **12**, 1–8.

22 N. Berahim, I. S. Amiri, T. Anwar, S. R. Azzuhri, M. M. Nasir, R. Zakaria, W. Y. Chong, C. K. Lai, S. H. Lee and H. Ahmad, *et al.*, *Results Phys.*, 2019, **12**, 7–11.

23 R. Verre, D. G. Baranov, B. Munkhbat, J. Cuadra, M. Käll and T. Shegai, *Nat. Nanotechnol.*, 2019, **14**, 679–683.

24 H. Zhang, B. Abhiraman, Q. Zhang, J. Miao, K. Jo, S. Roccasecca, M. W. Knight, A. R. Davoyan and D. Jariwala, *Nat. Commun.*, 2020, **11**, 1–9.

25 F. Hu, Y. Luan, M. Scott, J. Yan, D. Mandrus, X. Xu and Z. Fei, *Nat. Photonics*, 2017, **11**, 356–360.

26 S. Busschaert, R. Reimann, M. Cavigelli, R. Khelifa, A. Jain and L. Novotny, *ACS Photonics*, 2020, **7**, 2482–2488.

27 Y. Ye, Z. J. Wong, X. Lu, X. Ni, H. Zhu, X. Chen, Y. Wang and X. Zhang, *Nat. Photonics*, 2015, **9**, 733–737.

28 Y. Li, J. Zhang, D. Huang, H. Sun, F. Fan, J. Feng, Z. Wang and C.-Z. Ning, *Nat. Nanotechnol.*, 2017, **12**, 987–992.

29 Z. Fei, M. Scott, D. Gosztola, J. Foley IV, J. Yan, D. Mandrus, H. Wen, P. Zhou, D. Zhang and Y. Sun, *et al.*, *Phys. Rev. B*, 2016, **94**, 081402.

30 B. Munkhbat, B. Küçüköz, D. G. Baranov, T. J. Antosiewicz and T. O. Shegai, *Laser Photonics Rev.*, 2022, **17**, 2200057.

31 A. R. Khan, L. Zhang, K. Ishfaq, A. Ikram, T. Yildrim, B. Liu, S. Rahman and Y. Lu, *Adv. Funct. Mater.*, 2022, **32**, 2105259.

32 A. Autere, H. Jussila, Y. Dai, Y. Wang, H. Lipsanen and Z. Sun, *Adv. Mater.*, 2018, **30**, 1705963.

33 N. Muhammad, Y. Chen, C.-W. Qiu and G. P. Wang, *Nano Lett.*, 2021, **21**, 967–972.

34 N. Bernhardt, K. Koshelev, S. J. White, K. W. C. Meng, J. E. Froch, S. Kim, T. T. Tran, D.-Y. Choi, Y. Kivshar and A. S. Solntsev, *Nano Lett.*, 2020, **20**, 5309–5314.

35 S. Tongay, J. Zhou, C. Ataca, K. Lo, T. S. Matthews, J. Li, J. C. Grossman and J. Wu, *Nano Lett.*, 2012, **12**, 5576–5580.

36 L. Wang, X. Zhou, S. Yang, G. Huang and Y. Mei, *Photon. Res.*, 2019, **7**, 905–916.

37 A. Krasnok, S. Lepeshov and A. Alú, *Opt. Express*, 2018, **26**, 15972–15994.

38 T. Ren, P. Song, J. Chen and K. P. Loh, *ACS Photonics*, 2018, **5**, 353–358.

39 E. M. Purcell, *Confined Electrons and Photons*, Springer, 1995, pp. 839–839.

40 L. Eswaramoorthy, S. Mokkapati and A. Kumar, *J. Phys. D: Appl. Phys.*, 2022, **55**, 225103.

41 H. Ling, R. Li and A. R. Davoyan, *ACS Photonics*, 2021, **8**, 721–730.

42 C.-H. Cho, C. O. Aspetti, J. Park and R. Agarwal, *Nat. Photonics*, 2013, **7**, 285–289.

43 M. Fujita, *Nat. Photonics*, 2013, **7**, 264–265.

44 J. Valenta, M. Greben, S. Dyakov, N. Gippius, D. Hiller, S. Gutsch and M. Zacharias, *Sci. Rep.*, 2019, **9**, 1–9.

45 Y. Gong, S. Ishikawa, S.-L. Cheng, M. Gunji, Y. Nishi and J. Vŭković, *Phys. Rev. B: Condens. Matter Mater. Phys.*, 2010, **81**, 235317.

46 R. D. Kekatpure and M. L. Brongersma, *Nano Lett.*, 2008, **8**, 3787–3793.

47 P. M. Fauchet, *J. Lumin.*, 1998, **80**, 53–64.

48 R. Elliman, M. Forcales, A. Wilkinson and N. Smith, *Nucl. Instrum. Methods Phys. Res., Sect. B*, 2007, **257**, 11–14.

49 B. K. Ridley, *Quantum processes in semiconductors*, Oxford university press, 2013.

50 C. Hsu, R. Frisenda, R. Schmidt, A. Arora, S. M. de Vasconcellos, R. Bratschitsch, H. S. van der Zant and A. Castellanos-Gomez, *Adv. Opt. Mater.*, 2019, **7**, 1900239.

51 G.-H. Jung, S. Yoo and Q.-H. Park, *Nanophotonics*, 2019, **8**, 263–270.

52 J. Sung, D. Shin, H. Cho, S. W. Lee, S. Park, Y. D. Kim, J. S. Moon, J.-H. Kim and S.-H. Gong, *Nat. Photonics*, 2022, **16**, 792–797.

53 X. Du, I. Skachko, A. Barker and E. Y. Andrei, *Nat. Nanotechnol.*, 2008, **3**, 491–495.

54 J. J. Schwartz, H.-J. Chuang, M. R. Rosenberger, S. V. Sivaram, K. M. McCreary, B. T. Jonker and A. Centrone, *ACS Appl. Mater. Interfaces*, 2019, **11**, 25578–25585.

55 R. Garcia, A. W. Knoll and E. Riedo, *Nat. Nanotechnol.*, 2014, **9**, 577–587.

56 B. Borodin, F. Benimetskiy, V. Y. Davydov, I. Eliseyev, S. Lepeshov, A. Bogdanov and P. Alekseev, *J. Phys.: Conf. Ser.*, 2021, 012020.

57 B. Borodin, F. Benimetskiy and P. Alekseev, *J. Phys.: Conf. Ser.*, 2021, 012090.

58 C. Schinke, P. Christian Peest, J. Schmidt, R. Brendel, K. Bothe, M. R. Vogt, I. Kröger, S. Winter, A. Schirmacher and S. Lim, *et al.*, *AIP Adv.*, 2015, **5**, 067168.

59 P. B. Johnson and R.-W. Christy, *Phys. Rev. B: Solid State*, 1972, **6**, 4370.

60 V. Ardizzone, L. De Marco, M. De Giorgi, L. Dominici, D. Ballarini and D. Sanvitto, *Nanophotonics*, 2019, **8**, 1547–1558.

61 M. Li, I. Sinev, F. Benimetskiy, T. Ivanova, E. Khestanova, S. Kiriushechkina, A. Vakulenko, S. Guddala, M. Skolnick and V. M. Menon, *et al.*, *Nat. Commun.*, 2021, **12**, 1–10.

62 I. Sinev, M. Li, F. Benimetskiy, T. Ivanova, S. Kiriushechkina, A. Vakulenko, S. Guddala, D. Krizhanovskii, A. Samusev and A. Khanikaev, *J. Phys.: Conf. Ser.*, 2021, 012142.

63 N. Dong, Y. Li, Y. Feng, S. Zhang, X. Zhang, C. Chang, J. Fan, L. Zhang and J. Wang, *Sci. Rep.*, 2015, **5**, 1–10.

64 F. Ceccarelli, G. Acconcia, A. Gulinatti, M. Ghioni, I. Rech and R. Osellame, *Adv. Quantum Technol.*, 2021, **4**, 2000102.

65 S. A. Dyakov, M. V. Stepikhova, A. A. Bogdanov, A. V. Novikov, D. V. Yurasov, M. V. Shaleev, Z. F. Krasilnik, S. G. Tikhodeev and N. A. Gippius, *Laser Photonics Rev.*, 2021, **15**, 2000242.

66 T. V. Shubina, M. Remškar, V. Y. Davydov, K. G. Belyaev, A. A. Toropov and B. Gil, *Ann. Phys.*, 2019, **531**, 1800415.

67 E. Malic, M. Selig, M. Feierabend, S. Brem, D. Christiansen, F. Wendler, A. Knorr and G. Berghäuser, *Phys. Rev. Mater.*, 2018, **2**, 014002.

68 O. Smirnova, I. Eliseyev, A. Rodina and T. Shubina, *J. Phys.: Conf. Ser.*, 2020, 012038.

69 S. Brem, A. Ekman, D. Christiansen, F. Katsch, M. Selig, C. Robert, X. Marie, B. Urbaszek, A. Knorr and E. Malic, *Nano Lett.*, 2020, **20**, 2849–2856.

APPENDIX

Paper 9: Optically induced antiferromagnetic order in dielectric metasurfaces with complex supercells

---

Optical resonances in lattices of alternating out-of-phase oscillating magnetic dipoles in dielectric nanostructures are investigated theoretically and experimantally. The manuscript is published.

The citations in the manuscript refer to reference list included at the end of the manuscript.

Work contributions by the present author: Numerical calculations, manuscript writing.

Reference information:

A. Rahimzadegan, **S. Lepeshov**, W. Zhou, D.-Y. Choi, J. Sautter, D. Arslan, C. Zou, S. Fasold, C. Rockstuhl, T. Pertsch, Y. Kivshar, and I. Staude. Optically induced antiferromagnetic order in dielectric metasurfaces with complex supercells. *Journal of the Optical Society of America B* 40, 994-998 (2023).

Journal of the Optical Society of America B
OPTICAL PHYSICS

Optically induced antiferromagnetic order in dielectric metasurfaces with complex supercells

Aso Rahimzadegan,[1,*] Sergey Lepeshov,[2] Wenjia Zhou,[3,4] Duk-Yong Choi,[5] Jürgen Sautter,[3] Dennis Arslan,[3,4] Chengjun Zou,[3,4] Stefan Fasold,[3] Carsten Rockstuhl,[1,6] Thomas Pertsch,[1,7] Yuri Kivshar,[5] and Isabelle Staude[3,4]

[1] *Institute of Theoretical Solid State Physics, Karlsruhe Institute of Technology, 76131 Karlsruhe, Germany*
[2] *ITMO University, St. Petersburg, Russia*
[3] *Institute of Applied Physics, Abbe Center of Photonics, Friedrich Schiller University Jena, 07745 Jena, Germany*
[4] *Institute of Solid State Physics, Friedrich Schiller University Jena, 07743 Jena, Germany*
[5] *Nonlinear Physics Center, Research School of Physics, Australian National University, Canberra, ACT 2601, Australia*
[6] *Institute of Nanotechnology, Karlsruhe Institute of Technology, 76021 Karlsruhe, Germany*
[7] *Fraunhofer Institute for Applied Optics and Precision Engineering, 07745 Jena, Germany*
**aso.rahimzadegan@kit.edu*

Received 17 October 2022; revised 28 February 2023; accepted 1 March 2023; posted 1 March 2023; published 6 April 2023

Metasurfaces are 2D planar lattices of nanoparticles that allow the manipulation of incident light properties. Because of that attribute, metasurfaces are promising candidates to replace bulky optical components. Traditionally, metasurfaces are made from a periodic arrangement of identical unit cells. However, more degrees of freedom are accessible if an increasing number of structured unit cells are combined. The present study explores a type of dielectric metasurface with complex supercells composed of Mie-resonant dielectric nanocylinders and nanoscale rings. We numerically and experimentally demonstrate the signature of an optical response that relies on the structures sustaining staggered optically induced magnetic dipole moments. The optical response is associated with an optical antiferromagnetism. The optical antiferromagnetism exploits the presence of pronounced coupling between dissimilar Mie-resonant dielectric nanoparticles. The coupling is manipulated by engineering the geometry and distance between the nanoparticles, which ultimately enhances their effective magnetic response. Our results suggest possible applications in resonant nanophotonics by broadening the modulation capabilities of metasurfaces.

https://doi.org/10.1364/JOSAB.478307

1. INTRODUCTION

Metasurfaces have attracted a lot of attention in photonics in recent years [1–11]. Current trends call for creating highly transparent, functional, and active metasurfaces with high-index dielectric nanoparticles [12–14]. Dielectric nanoparticles with a high refractive index can be excited to sustain electric and magnetic Mie resonances at optical frequencies. The negligible absorption and strong scattering of dielectric resonant nanoparticles bring about a pronounced coupling of these components in a metasurface. As a result, the emergent electromagnetic response of a metasurface is vastly different from the response of the isolated nanoparticle [15,16]. The coupling effects in periodic metasurfaces with identical nanoparticles have been extensively studied [9,10,16–19]. However, coupling in periodic metasurfaces with dissimilar nanoparticles is less explored [15]. Note that coupling here refers to the renormalization of the optical response of the nanoparticles (for example, the resonance frequencies), when they interact with each other, as compared to their isolated optical responses.

Some years ago, it was predicted theoretically that a hybrid dimer structure composed of metal split-ring resonators and silicon nanospheres could exhibit a novel type of optically induced magnetic order termed as optical antiferromagnetic (**AFM**) order [20]. In the optical antiferromagnetic order, the induced magnetic dipole moments of the dissimilar nanoparticles are antiparallel. This is in contrast to the conventional parallel magnetic dipole (i.e., the optical ferromagnetic (**FM**) order), in which the induced dipole moments are equal and collinear. These effects have not been observed in optics. Still, theory predicted that a similar AFM order could be expected in anisotropic lattices composed of dielectric nanocylinders and nanotubes [21].

In this work, based on the theoretical work in [21], we have fabricated and analyzed all-dielectric periodic metasurfaces with complex supercells that, in contrast to unit cells containing only a single nanoparticle, give rise to what we believe, to the best of our knowledge, are novel scattering states, as shown in Fig. 1. The supercells of these metasurfaces are composed of

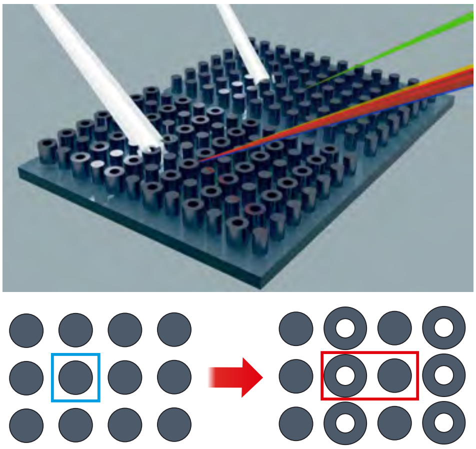

Fig. 1. A complex lattice unit cell: The transition from a single particle cell to a dimer cell gives rise to new scattering states.

two nanoparticles: a nanocylinder and a nanotube. These two dissimilar nanoparticles, in a complex supercell, have shown AFM order [21]. Here, we studied the optical response of metasurfaces with isotropic and anisotropic arrangements of these two components, as shown in Fig. 2 for a range of incidence angles, including normal incidence. The parameters are designed for the near-IR region. We experimentally demonstrated the signature of staggered magnetic dipole momenta in the transmittance spectra of the metasurfaces. We observed that AFM states can give rise to very high-quality resonances that extend over a wide range of incidence angles. The sharp resonance, like the Fano resonance or the bound state in the continuum, can be linked to the interference of the radiation from the antiparallel induced magnetic moments of dissimilar nanoparticles. By introducing dissimilar nanoparticles in the metasurface structure, new scattering states arise that provide more degrees of freedom to modulate the impinging light.

2. RESULTS AND DISCUSSION

A. Metasurface Structure

We designed and fabricated two types of all-dielectric metasurfaces with complex unit cells composed of dissimilar nanoparticles of Mie-resonant nanocylinders and nanotubes. We should note that using two nanocylinders with different sizes can also lead to AFM states. However, the nanotube can provide a broader magnetic resonance, which facilitates the design process. In the design process, we have looked for setups with pronounced antiparallel magnetic moments. Figure 2(a) shows the structure and scanning electron micrograph of an anisotropic metasurface composed of periodic rows of nanocylinders and nanotubes termed an "anisotropic metasurface." Figure 2(b) shows the "isotropic metasurface" composed of a checkerboard lattice of nanotubes and nanocylinders. The size parameters are mentioned in the figure caption. The design follows our theoretical study in [21].

The materials used for the nanoparticles and the substrate are silicon and silica glass, respectively. For wavelengths between 950 and 1600 nm, the two materials have a small dispersion. Furthermore, the absorption losses are negligible. In this wavelength range, the refractive index of silicon and silica is about 3.5 and 1.5, respectively. The silicon nanoparticles, nanocylinders, and nanotubes are fabricated on a thick glass substrate with the surrounding material being air.

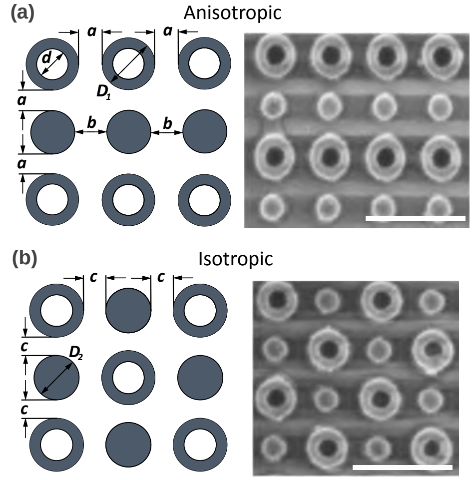

Fig. 2. Two types of silicon metasurfaces with a complex unit cell composed of dissimilar periodic lattices of resonant nanocylinders and nanotubes: (a) Structure and scanning electron micrograph of a metasurface composed of periodic rows of nanocylinders and nanotubes, termed an anisotropic metasurface. Here, $a = 150$ nm and $b = 300$ nm. The periodicity of the supercell is 930 nm and 550 nm. (b) The isotropic metasurface is composed of a checkerboard lattice of nanoparticles. Here, $c = 185$ nm. For both arrangements, the nanotube outer diameter is $D_1 = 400$ nm, the nanotube inner diameter is $d = 200$ nm, and the nanocylinder diameter is $D_2 = 230$ nm. The periodicity of the supercell is $500\sqrt{2} \approx 707$ nm. Each nanoparticle has a height of 300 nm. The scale bars are 1 µm.

B. Methods

To fabricate the metasurface, we coated a 300 nm thick hydrogenated amorphous silicon (a-Si:H) film onto glass (SCHOTT-N-BK7, Schott AG) via plasma-enhanced chemical vapor deposition (PECVD). First, a positive electron beam resist (ZEP520A, Zeon Corp.) was spin-coated on the film. In the next step, the nanoparticle patterns were formed using e-beam lithography and the subsequent development in ZED-N50 (Zeon). Next, a 50 nm thick aluminum layer was evaporated onto the sample. Then, the resist was removed using ZDMAC (Zeon). The silicon film was etched in CHF$_3$ plasma with a small addition of SF$_6$, which led to a highly anisotropic etching profile. Finally, the residual aluminum etch mask was removed using a wet etching solution.

To measure the metasurface transmittance spectra, we used an automated custom-built incoherent white light spectroscopy setup with complete control over the incidence angle and polarization. The sample was mounted on an automated step motor to not only move the sample, but also to rotate it along a single axis for the angular measurements. The setup had an

NA of 0.044, which corresponds to a half-angle of 2.5°. The divergence angle (half-angle) of the incident beam equaled 0.8°. The spectrometer used a scanning slit that corresponds to a 2 nm bandwidth, but the scanning was done in 0.8 nm steps. Moreover, the angular spectrum was sampled in steps of 2°.

We used a finite element method (using CST Studio Suite) to simulate the transmittance of the metasurfaces and the induced magnetic field distribution of the nanoparticles inside the lattice.

C. Transmittance for Normal Incidence

In this subsection, we focus on the anisotropic metasurface under normal incidence illumination. Figures 3(a) and 3(b) show the simulated transmittance spectra calculated under normal incidence for the all-dielectric metasurface with an anisotropic arrangement of nanocylinders and nanotubes, as shown in Fig. 2(a). The insets show the magnetic field distribution in designated resonance frequencies. The transmittance spectra are very different for the two polarizations of the external field, and they reflect different types of resonances supported by the metasurfaces.

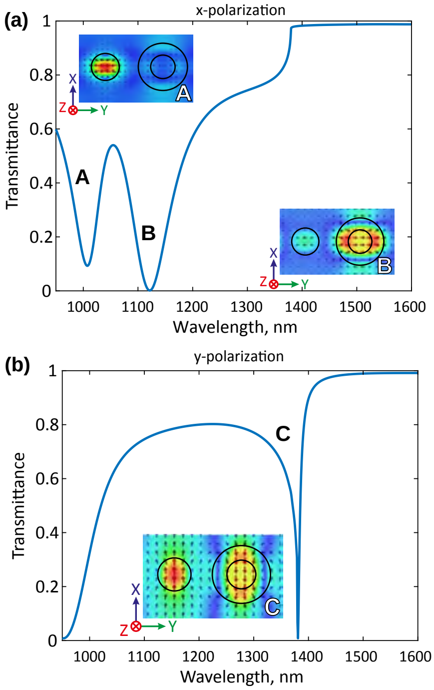

Fig. 3. Transmittance spectra of all-dielectric metasurfaces with anisotropic arrangements of nanocylinders and nanotubes as shown in Fig. 2(a), for two different polarizations of the external field: (a) x-polarization, and (b) y-polarization. For x-polarization, two distinct magnetic dipole resonances are observed at 1010 nm and 1124 nm (mode A and mode B), as shown in the insets of (a). For y-polarization, a hybrid response with the AFM order is observed at 1397 nm (mode C), as confirmed by the magnetic field distribution shown in the inset. The onset of the first diffraction order is at $930\ \text{nm} \times 1.5 = 1395\ \text{nm}$.

For x polarization [Fig. 3(a)] (i.e., a magnetic field along the y axis), two distinct magnetic dipole resonances are observed at wavelengths of 1010 nm and 1124 nm (mode A and mode B), as shown in the insets of Fig. 3(a). For mode A, the magnetic dipole moment of the nanocylinder is dominant with an out-of-phase resonance; for mode B, the magnetic dipole of the nanotube is dominant with an in-phase resonance. The sudden transition at 1400 nm is due to the onset of the first diffraction order.

For y polarization, as shown in Fig. 3(b), at the resonance mode C, a hybrid resonance with an AFM order is observed at 1397 nm. The magnetic field distribution, shown in the inset, displays an antiparallel orientation of the induced magnetic dipole moments of the nanotube and the nanocylinder. It is observed that the induced magnetic dipole moment of the nanotube is in-phase with the external magnetic field, while the induced dipole moment of the nanocylinder is out-of-phase. The pronounced coupling of the two nanoparticles led to the emergence of a what we believe is a novel antiparallel mode. A strong magnetic interaction near the onset of diffraction has also been observed in the literature [22]. We noticed that such an antiparallel mode cannot exist for periodic arrangements with unit cells composed of single nanoparticles.

As explained in [21], AFM and FM states can be tuned by changing the distances of nanotubes and nanocylinders. With an increasing distance, the coupling of the nanocylinders and nanotubes decays rapidly and the AFM modes cannot be excited. At a closer distance, the AFM-like response can be excited with an induced magnetic moment and opposite phase among dissimilar nanoparticles. The distance-dependent magnetic response is a unique feature of a complex supercell structure. The sensitivity of the AFM mode to slight variations manifests in the observed high-quality resonance. Due to this sensitivity, however, the mode is prone to fabrication defects, which makes experimental observations challenging.

D. Metasurface Characterization

This subsection shows the experimental characterization of the fabricated metasurfaces for an extended illumination angle of up to 30°, and the results are compared to the simulation data.

Figure 4 shows the simulated and experimental data for the transmittance of the anisotropic and isotropic metasurfaces under oblique TE- and TM-polarized light illuminated in the XZ or YZ plane. The axes are shown in the inset. The simulation and experimental measurements show good agreement, especially for pronounced resonances.

The complex structure of the supercell leads to the splitting of the fundamental magnetic dipole mode of a single nanoparticle into various modes with different polarization and order of the dipoles. The transmittance dips observed in the experimental measurement is the evident fingerprints of the AFM/FM ordering predicted by the simulations. From the calculation of the magnetic field distributions of the modes at the resonances obtained using CST, we derived two types of modes: AFM magnetic modes with x, y, and z orientation of the moments and FM magnetic modes directed along the y axis. We have marked these modes in Fig. 4 with black dashed lines. Remarkably, the FM order occurs only along the y axis [Figs. 4(b) and 4(e)] when the magnetic field vector is parallel to the dimer axis.

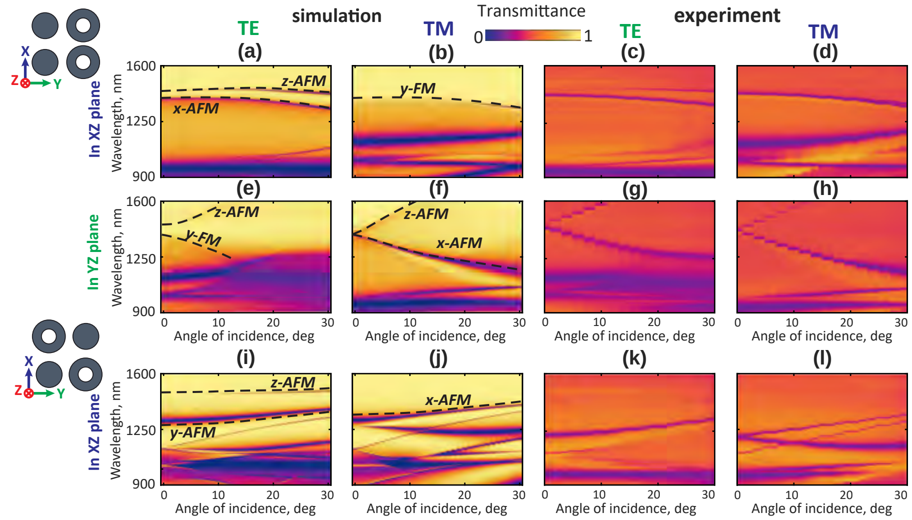

Fig. 4. (a)–(d) Experimental and simulated spectral and angular dependence of transmittance of anisotropic metasurface for TE- and TM-polarized light incident in the YZ plane. (e)–(h) Same dependence of transmittance for light incident in the XZ plane. (i)–(l) Experimental and simulated spectral and angular dependence of transmittance of isotropic metasurface for TE- and TM-polarized light incident in the XZ plane. The black dashed lines highlight the FM and AFM modes of the proposed metasurfaces.

Note that Figs. 4(b) and 4(e) are equivalent for normal incidence. Their transmittance spectrum is plotted in Fig. 3(a) (titled as the x polarization). Moreover, Figs. 4(a) and 4(f) are also equivalent for normal incidence angles. Their transmittance spectrum is plotted in Fig. 3(b) (title as the y polarization). The C mode in Fig. 3(b) is an x-AFM mode, as the antiparallel dipole moments are in the x axis.

A deviation from the normal incidence opens the scattering channel for modes with a z axis oriented AFM state [cf. Figs. 4(a), 4(e), 4(f), and 4(i)]. At normal incidence, the magnetic field vector is directed along the x or y axis. Therefore, it prevents the coupling of the incident wave to the vertically polarized magnetic AFM mode. However, an external magnetic field along the z axis enables an antiparallel magnetic dipole moment excitation along the z axis. Interestingly, this mode can already appear for a very slight deviation from normal incidence.

Compared to the simulated data note that the experimental measurements for the transmittance were substantially lower, and the dips were substantially less pronounced. These discrepancies are due to fabrication imperfections. As evident from the SEM images of Fig. 2, the surfaces were not as smooth as assumed in the simulations. This roughness caused the light to scatter into a nonspecular, diffusive direction that is not collected by the spectrometer. Moreover, contamination of the sample would have a similar effect. In addition, the size of the nanoparticles was not as homogeneously distributed as designed; this undesired disorder can lead to the broadening and dampening of resonances. Finally, the actual material from which the resonators were made could also suffer from a higher density of surface states. These, indeed, could lead to an additional absorption that affects the background transmission over an extended spectral region.

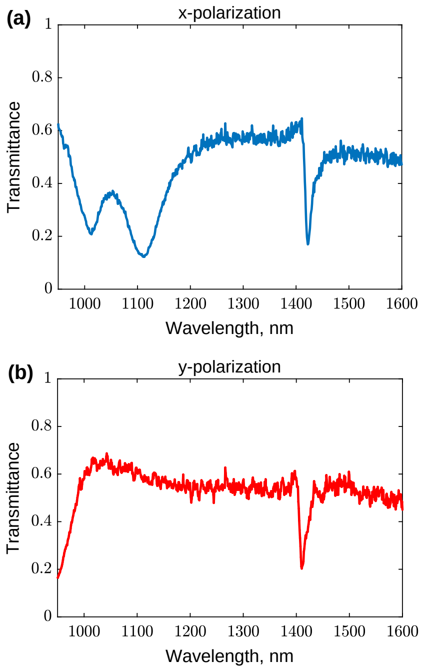

Fig. 5. Experimental transmittance spectra of the anisotropic metasurface measured for (a) x-polarized and (b) y-polarized plane waves.

Figure 5 shows the measured spectra for the anisotropic metasurface under normal incidence. The results can be compared to the simulated data in Fig. 2. Moreover, the data shall be interpreted with a look at the experimental angular data of Fig. 4.

For x polarization [Fig. 5(a)], as predicted in the simulation results [Fig. 3(a)], two distinct magnetic dipole resonances were observed at wavelengths near 1000 and 1100 nm. Furthermore, we also observed a resonance at around 1400 nm. This resonance was not predicted in the simulation results. However, comparing the experimental and simulation results in Figs. 4(b) and 4(d) for tilted angles, we observed a resonance (y-FM) that has been broadened in the experimental results. Therefore, we ascribed this dip to a slight angular misalignment in the measurement setup and also broadening of resonances due to imperfections that have resulted in the resonance around 1400 nm.

For a y polarization incidence [Fig. 5(b)], a resonance was observed near 1400 nm. As predicted by the simulations, this resonance could be linked to the y-AFM mode. However, the resonance was not as sharp as in the simulations. Fabrication imperfections can explain the broadening and reduction in sharpness. Lattice constants can be quite precise during fabrication, while nanoparticle sizes can be prone to imperfections in the fabrication.

3. CONCLUSION

We studied Mie-resonant dielectric metasurfaces with a complex supercell created by two types of resonant dielectric nanoparticles (namely, nanocylinders and nanotubes) arranged in square/rectangular lattices. We demonstrated, for the first time to the best of our knowledge, the effects of pronounced near-field coupling of meta-atoms in such dielectric metasurfaces that can be observed in the optically induced staggered magnetic dipole moments. We revealed that the overall optical response of the metasurfaces depends on the mode hybridization and nanoparticle ordering. In particular, we observed an optically induced response corresponding to a staggered structure of optically induced magnetic dipole moments that can be associated with the physics of the so-called artificial optical antiferromagnetism. We believe our results may suggest novel applications in resonant nanophotonics by broadening the modulation capabilities of metasurfaces with complex unit cells.

Funding. Alexander von Humboldt-Stiftung; Australian Research Council (DP210101292); Deutsche Forschungsgemeinschaft (RO 3640/7-2, 1524/10-2, STA 1426/1-2 (278747906), STA 1426/2-1, the Excellence Cluster 3D Matter Made to Order (EXC 2082/1 (390761711)), CRC 1375 (398816777)); Army Research Office (FA520921P0034).

Acknowledgment. Author Yuri Kivshar acknowledges Boris Lukyanchuk for encouraging discussions of the problem at the initial stage of this project. Kivshar acknowledges financial support from the Australian Research Council, International Technology Center Indo-Pacific (ITC IPAC) via the Army Research Office, and the Alexander von Humboldt Foundation. Credits: Author Aso Rahimzadegan did the writing, editing, experimental measurement, and setup. Author Sergey Lepeshov did the simulations and plotted the figures. Author Wenjia Zhou contributed to the writing, simulations, and measurements. Author Duk-Yong Choi fabricated the samples. Author Dennis Arslan built the experimental measurement setup and contributed to the writing. Author Chengjun Zou contributed to the analysis of the modes. Author Stefan Fasold measured the SEM images. Author Jürgen Sautter supervised the project. Finally, authors Kivshar, Carsten Rockstuhl, Isabelle Staude, and Thomas Pertsch reviewed and edited the paper and supervised the project.

Disclosures. The authors declare no conflicts of interest.

Data availability. Data underlying the results presented in this paper are not publicly available at this time, but may be obtained from the authors upon reasonable request.

REFERENCES

1. N. Yu and F. Capasso, “Flat optics with designer metasurfaces,” Nat. Mater. **13**, 139–150 (2014).
2. S. Chen, W. Liu, Z. Li, H. Cheng, and J. Tian, “Metasurface-empowered optical multiplexing and multifunction,” Adv. Mater. **32**, 1805912 (2019).
3. O. Quevedo-Teruel, H. Chen, A. Díaz-Rubio, *et al.*, “Roadmap on metasurfaces,” J. Opt. **21**, 073002 (2019).
4. H.-T. Chen, A. J. Taylor, and N. Yu, “A review of metasurfaces: physics and applications,” Rep. Prog. Phys. **79**, 076401 (2016).
5. Y. Bao, J. Ni, and C.-W. Qiu, “A minimalist single-layer metasurface for arbitrary and full control of vector vortex beams,” Adv. Mater. **32**, 1905659 (2019).
6. A. Rahimzadegan, D. Arslan, D. Dams, A. Groner, X. Garcia-Santiago, R. Alaee, I. Fernandez-Corbaton, T. Pertsch, I. Staude, and C. Rockstuhl, “Beyond dipolar Huygens’ metasurfaces for full-phase coverage and unity transmittance,” Nanophotonics **9**, 75–82 (2019).
7. X. Ni, A. V. Kildishev, and V. M. Shalaev, “Metasurface holograms for visible light,” Nat. Commun. **4**, 2807 (2013).
8. L. Huang, S. Zhang, and T. Zentgraf, “Metasurface holography: from fundamentals to applications,” Nanophotonics **7**, 1169–1190 (2018).
9. V. E. Babicheva and A. B. Evlyukhin, “Metasurfaces with electric quadrupole and magnetic dipole resonant coupling,” ACS Photon. **5**, 2022–2033 (2018).
10. A. Rahimzadegan, T. D. Karamanos, R. Alaee, A. G. Lamprianidis, D. Beutel, R. W. Boyd, and C. Rockstuhl, “A comprehensive multipolar theory for periodic metasurfaces,” Adv. Opt. Mater. **10**, 2102059 (2022).
11. C.-W. Qiu, T. Zhang, G. Hu, and Y. Kivshar, “Quo vadis, metasurfaces?” Nano Lett. **21**, 5461–5474 (2021).
12. S. Kruk and Y. Kivshar, “Functional meta-optics and nanophotonics governed by Mie resonances,” ACS Photon. **4**, 2638–2649 (2017).
13. I. Staude, T. Pertsch, and Y. S. Kivshar, “All-dielectric resonant meta-optics lightens up,” ACS Photon. **6**, 802–814 (2019).
14. J. Hu, A. I. Kuznetsov, V. J. Sorger, and I. Staude, “Tunable nanophotonics,” Nanophotonics **11**, 3741–3743 (2022).
15. N. Liu and H. Giessen, “Coupling effects in optical metamaterials,” Angew. Chem. – Int. Ed. **49**, 9838–9852 (2010).
16. S. Tretyakov, *Analytical Modeling in Applied Electromagnetics* (Artech House, 2003).
17. A. Epstein and G. V. Eleftheriades, “Huygens’ metasurfaces via the equivalence principle: design and applications,” J. Opt. Soc. Am. B **33**, A31–A50 (2016).
18. A. B. Evlyukhin, V. R. Tuz, V. S. Volkov, and B. N. Chichkov, “Bianisotropy for light trapping in all-dielectric metasurfaces,” Phys. Rev. B **101**, 205415 (2020).
19. M. B. Ross, C. A. Mirkin, and G. C. Schatz, “Optical properties of one-, two-, and three-dimensional arrays of plasmonic nanostructures,” J. Phys. Chem. C **120**, 816–830 (2016).
20. A. E. Miroshnichenko, B. Luk’yanchuk, S. A. Maier, and Y. S. Kivshar, “Optically induced interaction of magnetic moments in hybrid metamaterials,” ACS Nano **6**, 837–842 (2012).
21. S. Lepeshov and Y. Kivshar, “Near-field coupling effects in Mie-resonant photonic structures and all-dielectric metasurfaces,” ACS Photon. **5**, 2888–2894 (2018).
22. A. Rahimzadegan, R. Alaee, T. D. Karamanos, R. W. Boyd, and C. Rockstuhl, “Colossal enhancement of the magnetic dipole moment by exploiting lattice coupling in metasurfaces,” J. Opt. Soc. Am. B **38**, C217–C224 (2021).

APPENDIX J

Paper 10: Self-organized spatially separated silver 3D dendrites as efficient plasmonic nanostructures for surface-enhanced Raman spectroscopy applications

---

In this manuscript, Raman spectroscopy enhanced by localized surface plasmon resonances in silver dendrite nanostructures is investigated. The manuscript is published.

The citations in the manuscript refer to reference list included at the end of the manuscript.

Work contributions by the present author: Numerical calculations.

Reference information:

D. Yakimchuk, E. Kaniukov, **S. Lepeshov**,V. Bundyukova, S. Demyanov, G. Arzumanyanm, N. Doroshkevich, K. Mamatkulov, A. Bochmann, M. Presselt, O. Stranik, S. Khubezhov, A. Krasnok, A. Alù, and V. Sivakov. Self-organized spatially separated silver 3D dendrites as efficient plasmonic nanostructures for surface-enhanced Raman spectroscopy applications. *Journal of Applied Physics* 126, 233105 (2019).

Journal of
Applied Physics

ARTICLE

scitation.org/journal/jap

Self-organized spatially separated silver 3D dendrites as efficient plasmonic nanostructures for surface-enhanced Raman spectroscopy applications

Cite as: J. Appl. Phys. **126**, 233105 (2019); doi: 10.1063/1.5129207
Submitted: 30 September 2019 · Accepted: 21 November 2019 ·
Published Online: 19 December 2019

View Online Export Citation CrossMark

Dzmitry V. Yakimchuk,[1,a)] Egor Yu Kaniukov,[2,3] Sergey Lepeshov,[4] Victoria D. Bundyukova,[1]
Sergey E. Demyanov,[1] Grigory M. Arzumanyanm,[5,6] Nelya V. Doroshkevich,[6] Kahramon Z. Mamatkulov,[6]
Arne Bochmann,[7] Martin Presselt,[8] Ondrej Stranik,[8] Soslan A. Khubezhov,[9] Aleksander E. Krasnok,[4,10]
Andrea Alù,[10,11,12] and Vladimir A. Sivakov[8]

AFFILIATIONS

[1] Cryogenic Research Division, Scientific-Practical Materials Research Centre, NAS of Belarus, Minsk 220072, Belarus
[2] Institute of Chemistry of New Materials of National Academy of Sciences of Belarus, 36 St. Francyska Skaryny, 220141 Minsk, Belarus
[3] Department of Electronics Materials Technology, National University of Science and Technology MISiS, 4 Leninskiy Prospekt, 119049 Moscow, Russian Federation
[4] Department of Physics, ITMO University, 49 Avenue Kronverksky, 197101 St. Petersburg, Russian Federation
[5] Joint Institute for Nuclear Research, 6 St. Joliot-Curie, 141980 Dubna, Russian Federation
[6] Department of Nanotechnology and New Materials, Dubna State University, 19 St. Universitetskaya, 141982 Dubna, Russian Federation
[7] Ernst-Abbe-Hochschule Jena, 2 St. Carl-Zeiß-Promenade, 07745 Jena, Germany
[8] Leibniz Institute of Photonic Technology, 9 St. Albert-Einstein-Straße, 07745 Jena, Germany
[9] Department of Physics, North-Ossetian State University, 46 St. Vatutina, 362025 Vladikavkaz, Russian Federation
[10] Photonics Initiative, Advanced Science Research Center, 85 St. Nicholas Terrace, New York, New York 10031, USA
[11] Physics Program, Graduate Center City University of New York, 85 St. Nicholas Terrace, New York, New York 10031, USA
[12] Department of Electrical Engineering, City College of New York, 85 St. Nicholas Terrace, New York, New York 10031, USA

[a)] **Author to whom correspondence should be addressed:** dim2yakim@gmail.com

ABSTRACT

Surface-enhanced Raman spectroscopy (SERS) is a promising optical method for analyzing molecular samples of various nature. Most SERS studies are of an applied nature, indicating a serious potential for their application in analytical practice. Dendritelike nanostructures have great potential for SERS, but the lack of a method for their predictable production significantly limits their implementation. In this paper, a method for controllably obtaining spatially separated, self-organized, and highly-branched silver dendrites via template synthesis in pores of SiO_2/Si is proposed. The dendritic branches have nanoscale roughness, creating many plasmon-active "hotspots" required for SERS. The first held 3D modeling of the external electromagnetic wave interaction with such a dendrite, as well as experimental data, confirms this theory. Using the example of a reference biological analyte, which is usually used as a label for other biological molecules, the dendrites' SERS-sensitivity up to 10^{-15}M was demonstrated with an enhancement factor of 10^8. The comparison of simulation results with SERS experiments allows distinguishing the presence of electromagnetic and chemical contributions, which have a different effect at various analyte concentrations.

I. INTRODUCTION

Raman spectroscopy—a measurement of the inelastic light scattering from a molecule with quantized vibrational signature—is a highly innovative technique of modern biomedical analysis and clinical and biological studies.[1] These areas have been experiencing a fast development, which has lasted for more than 40 years after the discovery that inherently weak Raman signals can be significantly enhanced for molecules adsorbed onto a rough metal surface. This effect, which can be attributed mainly to the strong electric field enhancement around subwavelength metal roughness, is called Surface-Enhanced Raman Scattering (SERS)[2–5] and has been demonstrated for various plasmonic structures, including plasmonic nanoantennas,[6] dimers with sub-10-nm gaps,[7] disordered nanoparticle clusters, metamaterials, and metasurfaces.[8]

Electromagnetic mechanisms usually provide the primary role in SERS amplification. Excitation of surface plasmons, i.e., coherent oscillations of free electrons at the metal-dielectric boundaries, causes regions of a strong electric field (hotspots) arising near metal nanostructures and at the junctions between them.[9–11] The SERS enhancement factor caused by this electric field localization is roughly proportional to the fourth power of the electric field amplitude. The subsequent analysis has shown that SERS is inherent not only to metals, such as copper (Cu),[12] silver (Ag),[13] and gold (Au),[14] but also to resonant all-dielectric nanostructures,[15] demonstrating the universal nature of this effect, associated with the local electric field enhancement. However, in some cases, the chemical contribution is a factor responsible for the sharp growth of the Raman scattering cross section due to the interaction of the analyte molecule with the metallic surface.[16–19]

Tremendous progress in the area of Raman-based sensors led to the creation of the surfaces allowing Raman signal detection from a few or even single molecules.[20] The SERS enhancement factor (*EF*), which is usually defined as

$$EF = \frac{I_{SERS}}{C_{SERS}}\frac{C_R}{I_R}, \tag{1}$$

has been demonstrated to be as large as 10^5–10^{11} (cf. Ref. 21). Here, I_{SERS} stands for the Raman intensity obtained for the SERS substrate under a certain analyte concentration C_{SERS}, and I_{R} corresponds to the Raman intensity obtained under non-SERS conditions at analyte concentration C_{R}.

However, the adoption of SERS remains limited, to a great extent, due to the fabrication difficulties of effective and affordable nanostructured plasmonic SERS surfaces. So far, SERS substrate fabrication techniques include lithography,[7] laser ablation,[22] templated electrodeposition,[23] wet chemistry,[24,25] and self-assembly.[8,26] The self-assembly technique is often considered the most promising because of its simplicity and cost- and time-effectiveness. For example, based on this approach, highly-branched dendritic nanostructures with sub-10-nm gaps between neighboring branches can be fabricated.[27–29] However, self-assembly techniques lack control over resulting structures. Thus, despite relatively satisfactory results,[30] regularly reproducible detection of ultrasmall concentrations of the analyte (in particular, single molecules) using dendrites was not demonstrated. The main problem is related to the formation of bulk agglomerates,[27,31–33] which limit stable detection at ultralow concentrations of molecules due to the analyte penetration into the interior of such structures. As a result, the excitation laser does not access the analyte localization region and, consequently, the signal from the analyte is poorly recorded.

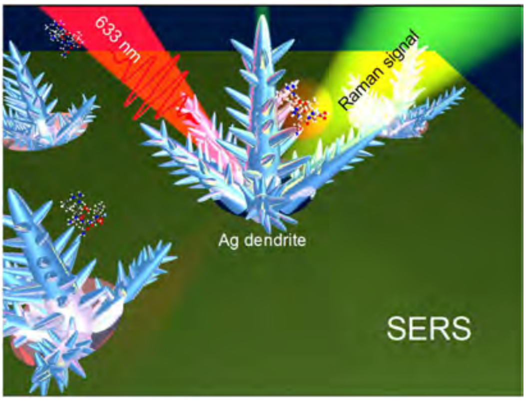

FIG. 1. Schematic representation of enhanced Raman scattering from a molecule nearby a silver dendrite.

For that reason, such a problem can be solved by the spatial separation of nanostructures using porous templates: polymer track membranes, anodized aluminum oxide, porous silicon, etc.[34–37] The formation of metallic nanostructures in the pores matrix is usually carried out using two methods: electrochemical deposition and electroless galvanic displacement. The first method is used to produce nanostructures filling the pore volume (for example, in the formation of nanorods)[38] and the second, when it is required, to realize individual nanoparticles or thin metallic layers on the pores' surface.[39]

In this paper, we develop and demonstrate a novel technique for the fabrication of spatially separate silver dendrites, presented schematically in Fig. 1, via self-organization of Ag nanostructures in pores of SiO_2/Si templates. We investigate the microstructure, morphology, optical features, and SERS properties of fabricated nanostructures. Also, we show that observed templates allow us to achieve a SERS enhancement factor of $\sim 10^8$ with a single molecule detection possibility ($\sim 10^{-15}$ M) of Ellman's reagent, which is usually used as a label for other biological molecules.

II. MATERIALS AND METHODS

As templates for the synthesis of silver dendrites, a swift heavy ion-track porous SiO_2 matrix on the *p*-type silicon substrate (12 Ohm·cm with orientation ⟨100⟩) was used with a 170 nm thick silicon oxide layer and pore sizes of 800 nm. The procedure of obtaining porous SiO_2/Si templates is described in our previous paper.[36] The parameters of the porous template were determined using ellipsometry.[40,41] The SiO_2/Si pore density over the surface was found to be 10^7 cm^{-2} according to SEM studies determined by ImageJ.[42]

The formation of Ag nanostructures in the pores of the SiO_2 template on the Si substrate was carried out by the electroless galvanic displacement method using an aqueous solution of Ag nitrate ($AgNO_3$) and hydrofluoric acid (HF), which dissociates in water into individual cations and anions (Ag^+, NO_3^-, H^+, and F^-) as was published in our previous publication.[43] The resulted ions participate in three parallel processes:[44,45] the electrochemical reduction of $[Ag]^+$ ions to a metallic silver state on Si or metal [Eq. (2)] with simultaneous anodic and cathodic oxidation of Si [Eq. (3)], and also SiO_2 dissolution in hydrofluoric acid [Eq. (4)]. Schematically, the processes taking place in the pore of the SiO_2/Si template are shown in Fig. 2,

$$4Ag^+ + Si + 6F^- \rightarrow 4Ag + SiF_6^{2-}, \quad Si + 6HF \rightarrow H_2SiF_6 + 4H^+ + 4e^-, \\ Ag^+ + e^- \rightarrow Ag, \quad H_2 \rightarrow 2H^+ + 2e^-. \tag{2}$$

$$Si + 2H_2O \rightarrow SiO_2 + 4H^+ + 4e^-. \tag{3}$$

$$SiO_2 + 6HF \rightarrow H_2SiF_6 + 2H_2O. \tag{4}$$

Scanning electron microscopy (SEM, Carl Zeiss ULTRA 55, FE-SEM) was chosen to characterize the surface morphology of the obtained samples.

The EBSD (electron backscattered diffraction) analysis of the samples was performed using a scanning electron microscope equipped with a Schottky emitter (Zeiss Ultra 55) and a high-resolution EBSD camera (Bruker e-Flash^{HR}) using an acceleration voltage of 20 kV at a nominal sample current of 1.5 nA, a sample tilt of 60° with respect to the primary electron beam, and a scanning step width of 12 nm. The resolution of the Kikuchi patterns was 160×120 pixels applying a 10×10 binning and using integration times of 40 ms. There were no problems with charging issues. The data were evaluated using a commercial software package (Bruker Quantax; Esprit 2.1) as well as the MATLAB toolbox MTEX.[46]

To clarify the crystal structure of silver dendrites, the X-ray diffraction (XRD) patterns were measured using an X'Pert Pro X-ray diffractometer from PANalytical B.V. in the Bragg-Brentano arrangement.

The chemical state of the formed nanostructures was determined by X-ray photoelectron spectroscopy (XPS) in ultrahigh-vacuum (10^{-9} mbar) by the K-Alpha ThermoScientific system with a monochromatic X-ray source Al-K-alpha 1.486 keV. To neutralize the surface charge, a compensation gun was used. The density of data collection of high-resolution spectra was 0.1 eV.

The scattering properties (LSPR—Localized Surface Plasmon Resonance) of the metal nanostructures were recorded with a dark-field microspectroscopy similarly as in Ref. 47. Briefly, the microspectroscopy system consisting of an upright microscope (AxioImager Z1m, Carl Zeiss) was combined with a fiber-coupled spectrometer (Spectra Pro 2300i, Princeton Instruments) and was used in the dark-field top illumination settings. The microscope was equipped with a color camera (AxioCam Mrc5, Carl Zeiss) to record the overview images of the samples. The scattering signal was recorded from a circular area with a diameter of 15 μm (10× objective; NA = 0.2, 150 μm diameter aperture in front of the collecting fiber) from the middle of the overview image. The scattering signals were corrected with respect to the background and lamp spectrum.

The SERS measurements were performed using the commercially available confocal microspectrometer "Confotec CARS" (SOL Instruments Ltd., Belarus) setup equipped with several laser systems including a 633 nm laser.[48] During measurements, a 600 lines per millimeter grating was used with a spectral resolution of ~2 cm^{-1}, and the same objective (Leica 100×, 0.9 NA) was employed for focusing the laser beam on the sample and for collecting the backscattered light. The laser power of 50 μW within an exposure time of 1 s was exploited. For the SERS studies, Ellman's reagent $C_{14}H_8N_2O_8S_2$ [5,50-dithiobis-(2-nitrobenzoic acid)] or DTNB was used as a model analyte in different concentrations: 10^{-4}M, 10^{-7}M, 10^{-10}M, 10^{-13}M, and 10^{-15}M. DTNB is a popular marker for various biological molecules. For the registration of ultralow concentrations (10^{-13}M and

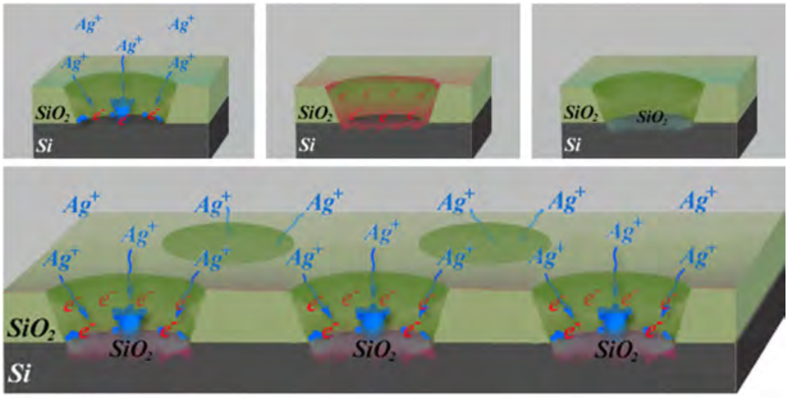

FIG. 2. Schematic representation of the processes involved in the reduction of $[Ag]^+$ ions occurring in pores of a template SiO_2 on Si: (a) Ag reduction; (b) SiO_2 etching; (c) Si oxidization; (d) all processes simultaneously.

10^{-15}M) of the analyte, $10 \times 10\,\mu m^2$ mapping was used. For comparing with SERS spectra, the Raman spectrum was measured from 10^{-2} M of DTNB on the SiO_2/Si template without silver.

CST Microwave Studio is a full-wave 3D electromagnetic field solver based on the finite-integral time-domain (FITD) solution technique. A nonuniform mesh was used to improve accuracy near the Ag nanorods where the field concentration was significantly large.[49] The SiO_2 substrate thickness was taken to be 170 nm. The lengths of big and small dendritics were ~1130 nm and 170 nm, respectively. The thicknesses of the big and small dendrites were 180 nm and 70 nm, respectively. The radius of the rounded outgrowths was 53 nm.

III. RESULTS AND DISCUSSION

All the pores of the ion-track SiO_2/p-Si template are filled with dendritic silver nanostructures, as shown in Fig. 3(a). The SEM image of a single pore filled with silver nanostructures is presented in Fig. 3(b). The image reveals that the nanostructures have the form of dendrites containing the main trunk, lateral branches, and many rounded outgrowths on them. Due to the presence of nanoscale inhomogeneities between dendrites' branches, the formation of "hotspots" can be expected with the enhanced electric field, which can be used for boosting the SERS effect.

The detailed structure of dendrites local features was evaluated by electron backscattered diffraction (EBSD). Figures 3(d) and 3(e) show the EBSD orientation maps with an inverse pole figure related color coding with regard to the sample surface normal direction z (IPFZ). For cubic systems, red color means that ⟨100⟩ crystal directions are parallel to the normal direction of the sample; green or blue colors are for ⟨110⟩ or ⟨111⟩ directions aligned to the normal direction, respectively. Our results suggest the presence of many blue spots around the main trunk, which corresponds to the ⟨111⟩ crystal growth direction. Further investigations of grain boundary relations inside the nanostructure reveal that most of the grain boundaries are coincidence site lattice (CSL[50]) grain boundaries Σ3 (twin grain boundary) and few Σ9 (for more details see Methods).

The crystallinity of silver dendrites in the pores of the SiO_2/p-Si template was determined using the X-ray diffraction method. Figure 3(f) shows the XRD pattern of the produced structure. Unlike the typical diffraction patterns of silver dendrites,[30,51] we observe a

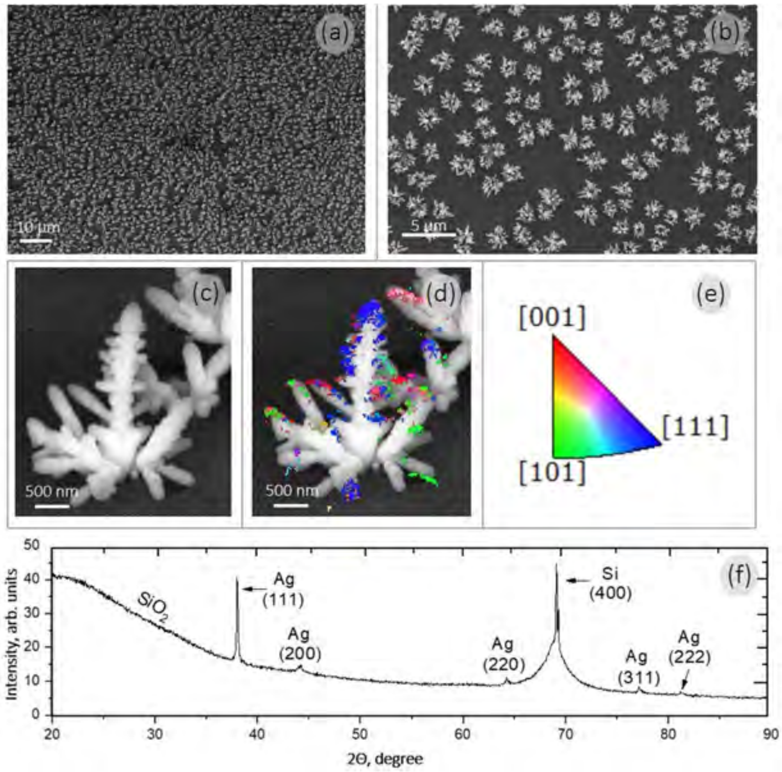

FIG. 3. Morphology and microstructure of observed SiO_2(Ag)/Si structures: (a), (b), and (c) overview and single feature SEM micrographs; (d) and (e) EBSD analysis of silver dendrite; (f) X-ray diffraction pattern; lattice parameter (a) of Ag dendrites is 4.0816 Å.

broad background signal coming from the amorphous SiO_2 layer. The peak at 2θ about 69° corresponds to the signal from monocrystalline Si with a highly broadened value due to the high defectiveness of the near-surface layers, which is the consequence of a template creating via ion-track technology on the irradiation stage with swift heavy ions. Ag dendrites have a cubic crystalline structure and are characterized by a set of reflexes from planes (111), (200), (220), (311), and (222). The broadened peak of the (200) reflex, also, points to the polycrystalline nature of the observed Ag precipitate. The high intensity of the (111) reflex indicates the priority direction of crystallite growth along this direction that correlates with EBSD observations in Figs. 3(d) and 3(e).

The result of XPS is presented in Fig. 4. The asymmetric spectra for the Ag 3d line and the presence of low-intensity plasmon loss peaks confirm the metallic nature of the dendrites being formed.[52]

To investigate the optical properties of the fabricated dendritic Ag nanostructures numerically, we perform the full-wave simulations using the commercial software CST Microwave Studio [Figs. 5(a) and 5(b)]. The simulation results indicate that the most intense "hotspots" are located between the neighboring dendrite branches, where the electric field enhancement reaches 12 as shown in Fig. 5(b). It is known that the SERS enhancement factor caused by electric field localization is roughly proportional to the fourth power of the electric field amplitude ($\sim E^4$). This gives us an estimation for the enhancement factor of $\sim 10^4$.

The typical scattering spectrum (for more details, see Methods) of the dendritic nanostructures is shown in Fig. 5(c). The complexness of the structure gives rise to the spectral broadening of the measured scattering spectra.[43] Moreover, the scattered light-collecting area has a radius of 15 μm, and hence each spectrum is averaged over ~50 nanostructures, which causes its additional broadening. As a result, the scattering spectrum in Fig. 5(c) does not exhibit sharp peaks in the range of 500–750 nm with a broadband resonant behavior nearby excitation wavelength (633 nm).

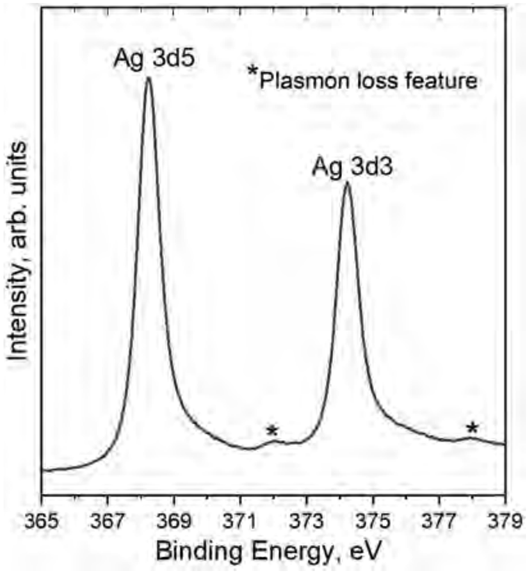

FIG. 4. XPS of spatially separated silver dendrites.

Next, in order to demonstrate the performance of the resulting structures as a sensor, the SERS measurements using DTNB as a model analyte were performed (for details, see Methods). Figure 6 summarizes the obtained results. We attributed the observed most intense bands at 1062, 1150, 1331, and 1555 cm^{-1} to the DTNB[53] analyte. The evolution of SERS spectra shows the possibility of the detection of ultralow concentrations of the model DTNB analyte by applying localized silver dendrite nanostructures, which correspond to *EF* at least 10^8.

According to modern concepts of Raman signal amplification mechanisms by plasmonic nanostructures, the highest amplification of the Raman signal occurs in "hotspots" due to the increased electromagnetic field strength in these places [Fig. 5(a)]. The closer the molecule under study to the "hotspots" is, the more intense the signal is recorded. However, given the fact that each dendrite has a large number of "hotspots," signal amplification by means of an electromagnetic mechanism is determined by all such places simultaneously. Even taking into account this fact, the obtained result of the amplification of the Raman signal is orders of magnitude higher than the numerical calculation. The *EF* value of 10^8 exceeds by several orders of magnitude the results of numerical simulations. We believe that this indicates the existence of a strong chemical contribution to the SERS enhancement. This contribution can be caused by the following mechanisms: a change in the polarization of the molecule[16,17] (static charge transfer, causing an amplification of up to 10 times) and the transition of a charge from a molecule to a metal (or vice versa) with the formation of a new metal-molecule bond, the analyte creates new allowed energy levels.[17,19,54] The energy difference of these levels coincides or lies near the energy of the exciting wave, which leads to resonant Raman scattering. It is known that such a mechanism can provide the amplification of $\sim 10^2$–10^3 [55] and even more.[56] Thus, the cumulative gain factor of 10^8 is determined by the electromagnetic ($EF_{\text{e.m.}}$) and chemical (EF_{chem}) contributions,[57,58]

$$EF = EF_{\text{e.m.}} \times EF_{\text{chem}}. \tag{5}$$

The appearance of new allowed levels in the energy spectrum of the molecule can lead to differences in comparison with the Raman spectrum of a bare analyte. Indeed, our results show [Fig. 6(a)] that the main lines are shifted to the blue side, and with a decrease in the analyte concentration, this effect gets enhanced. This behavior of the SERS spectra can be explained in the following way. With a sufficient amount of analyte molecules, both amplification mechanisms are involved: electromagnetic, which does not affect the spectrum change, and chemical, which causes the shift of the combination bands and is noticeably weaker than the electromagnetic one. With a decrease in the analyte concentration, the role of the electromagnetic mechanism is weakened, because fewer

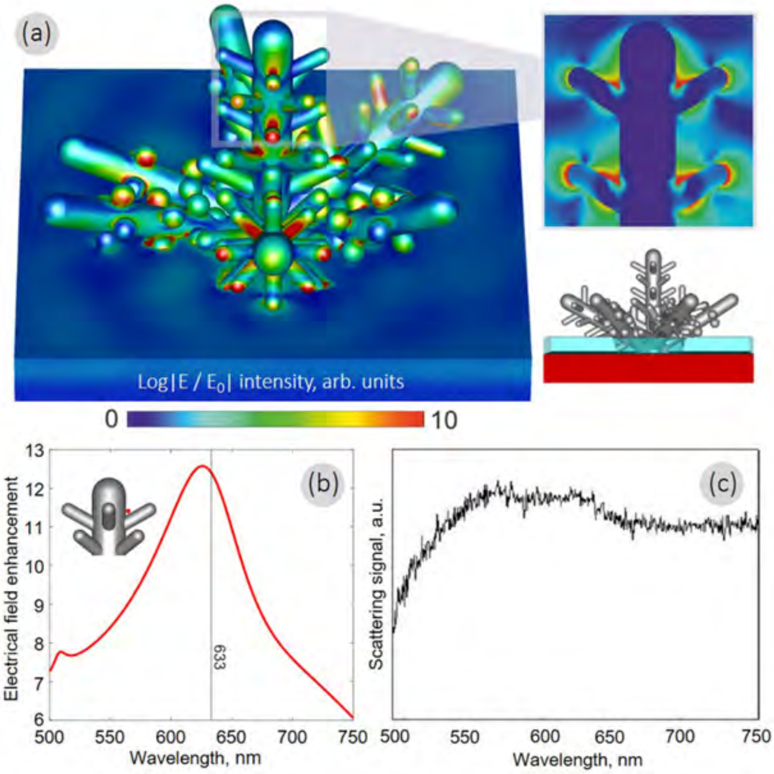

FIG. 5. (a) Distribution of the electric field over the surface of silver dendrite located in the pore of the SiO_2/Si template (E—local field, E_0—incident field). (b) Electrical field enhancement spectrum in the point indicated by the inset. (c) Scattering spectrum of the dendritic nanostructures in the pores of the SiO_2/Si template.

molecules get into "hotspots." Molecules, which still fall into these regions, fit closely to the metal and, at several angstroms distances, create a molecular-metal complex with silver. Thus, the molecule gets additional allowed energy levels. For that reason, the resonant transitions between these levels can also be enhanced by the electromagnetic mechanism. A decrease in concentration leads to the fact that molecules that fall into "hotspots" at distances of several tens of nanometers from metal do not form a bond with the silver surface. This is a consequence of the dominant effect of the chemical contribution to the SERS spectrum and a more noticeable shift in the combination lines. Note that the formation of new molecule-metal complexes can occur not only in "hotspots" but also in other regions of the metal, which also affects the characteristic shape of the SERS spectrum with a decrease of the electromagnetic mechanism role.

There are various ways to create SERS substrates with plasmon-active metal inclusions in modern literature. For example, a highly sensitive SERS substrate was also demonstrated by Kumar *et al.*[59] and Sharma *et al.*[60] They have enough sensitivities for detecting ultralow concentrations of target molecules, and they also have a number of limitations associated with the complexity of manufacturing such substrates. The ion-track technology used in this work to create the SERS substrates is well suited for research purposes because it allows controlling template pore diameter in a very simple way. The pore diameter is very important for obtaining spatially separated silver dendrites because this parameter influences the diffusion-limitation processes in the pores on the silver structures growing stage that is necessary for the growth of dendrites. We will discuss this in more details in a future work where we will consider silver morphology dependence on the template pore diameter. In this work, the presented results made it possible to determine that it is necessary to use templates with pore diameters of 800 nm for the growth of spatially separated silver dendrites. To obtain such pore diameters, classical lithography is also well suited. Therefore, in the future, this technique can be used to obtain ordered arrays of silver dendrites. Obtaining ordered silver nanostructures will not influence *EF* because "hotspots" are arranged randomly on the dendrites. However, ordered structures are still relevant[61] because they will increase the analytical usefulness of SERS active substrates.

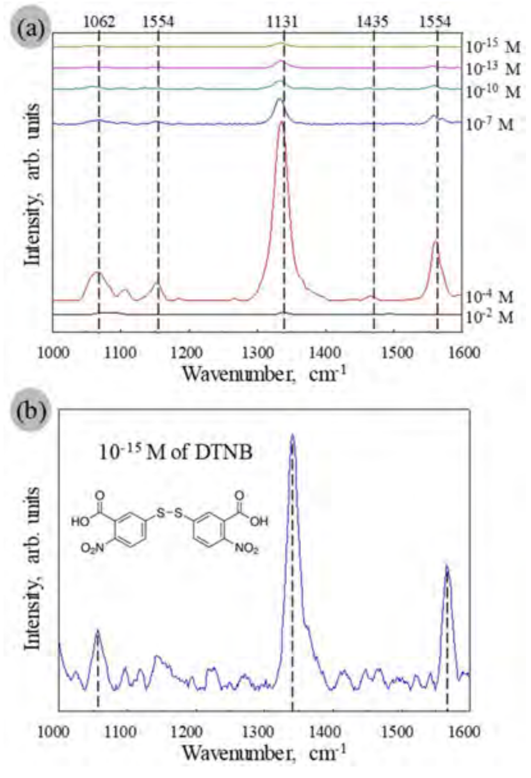

FIG. 6. (a) Raman spectrum for a dried alcohol solution of DTNB with a concentration of 10^{-2} M (black curve), as well as SERS spectra obtained at $\lambda = 633$ nm excitation from spatially separated Ag dendrites for analyte concentrations of 10^{-4}M, 10^{-7}M, 10^{-10}M, 10^{-13}M, and 10^{-15}M. (b) Zoomed SERS spectrum of DNTB with the concentration of 10^{-15}M.

IV. CONCLUSIONS

Spatially separated Ag dendritic nanostructures in the pores of the ion-track template SiO_2/Si were synthesized using directed self-organization of Ag in a limited volume. Microstructure and optical features of SiO_2(Ag)/Si nanostructures have been studied numerically and experimentally. It has been shown that the Ag nanostructures have the form of dendrites. The SERS measurement results indicate the possibility of ultralow analyte concentration detection, comparable to the concentrations of single molecules. The high sensitivity of the fabricated structures is justified by the coexistence of electromagnetic and chemical contributions to the Raman signal amplification. The modeling of the electromagnetic wave interaction with dendrites indicates that the appearance of "hotspots" occurs in places of twinning (intergrowth of the branches of the dendrite). The fabricated dendrites have a large number of "hotspots" with an electric field enhancement factor of 12. The random distribution of "hotspots" on a dendrite leads to its broadened scattering spectrum. We strongly believe that the simplicity, reproducibility, and scalability of the presented method for the formation of spatially separated dendrites make it promising for various vital applications in photonics, chemistry, and biology.

ACKNOWLEDGMENTS

The authors acknowledge the support of the work in frames of the H2020-MSCA-RISE2017-778308-SPINMULTIFILM Project, Russian Foundation for Basic Research (Project No. 19-32-50058), Ministry of Education and Science of the Russian Federation in the framework of Increase Competitiveness Program of NUST "MISiS" (No. K4-2018-036), implemented by a governmental decree dated 16 March 2013, N 211, Ministry of Education and Science of Russian Federation (Project No. 2.2267.2017/4.6), and the Scientific-technical program "Technology-SG" (Project No. 3.1.5.1).

REFERENCES

[1] C. Krafft, I. W. Schie, T. Meyer, M. Schmitt, and J. Popp, Chem. Soc. Rev. **45**, 1819 (2016).
[2] M. Moskovits, J. Raman Spectrosc. **36**, 485 (2005).
[3] K. Kneipp, H. Kneipp, I. Itzkan, R. R. Dasari, and M. S. Feld, J. Phys.: Condens. Matter **14**, R597 (2002).
[4] C. Höppener and L. Novotny, Q. Rev. Biophys. **45**, 209 (2012).
[5] D. Yakimchuk, E. Kaniukov, V. Bundyukova, S. Demyanov, and V. Sivakov, "Self-organization of plasmonic nanostructures in pores of silica template for SERS," in *Fundamental and Applied Nano-Electromagnetics II* (Springer, Dordrecht, 2019), Chap. 5, pp. 75–90.
[6] E. Ringe, B. Sharma, A.-I. Henry, L. D. Marks, and R. P. Van Duyne, Phys. Chem. Chem. Phys. **15**, 4110 (2013).
[7] A. Gopalakrishnan, M. Chirumamilla, F. De Angelis, A. Toma, R. P. Zaccaria, and R. Krahne, ACS Nano **8**, 7986 (2014).
[8] S. Gwo, C. Y. Wang, H. Y. Chen, M. H. Lin, L. Sun, X. Li, W. L. Chen, Y. M. Chang, and H. Ahn, ACS Photonics **3**, 1371 (2016).
[9] G. Santoro, S. Yu, M. Schwartzkopf, P. Zhang, S. Koyiloth Vayalil, J. F. H. Risch, M. A. Rübhausen, M. Hernández, C. Domingo, and S. V. Roth, Appl. Phys. Lett. **104**, 243107 (2014).
[10] K. Kneipp, Phys. Today **60**, 40 (2007).
[11] Y. Xia and D. J. Campbell, J. Chem. Educ. **84**, 91 (2007).
[12] E. Kaniukov, D. Yakimchuk, G. Arzumanyan, H. Terryn, K. Baert, A. Kozlovskiy, M. Zdorovets, E. Belonogov, and S. Demyanov, Philos. Mag. **97**, 2268 (2017).
[13] T. V. Shahbazyan and M. I. Stockman, *Plasmonics: Theory and Applications* (Springer Netherlands, Dordrecht, 2013).
[14] B. Sharma, R. R. Frontiera, A.-I. Henry, E. Ringe, and R. P. Van Duyne, Mater. Today **15**, 16 (2012).
[15] A. Krasnok, M. Caldarola, N. Bonod, and A. Alú, Adv. Opt. Mater. **6**, 1701094 (2018).
[16] K. Kneipp, J. Phys. Chem. C **120**, 21076 (2016).
[17] L. J. Zhao, L. Jensen, and G. C. Schatz, J. Am. Chem. Soc. **128**, 2911 (2006).
[18] J. F. Arenas, M. S. Woolley, I. L. Tocón, J. C. Otero, and J. I. Marcos, J. Chem. Phys. **112**, 7669 (2000).
[19] L. Xia, M. Chen, X. Zhao, Z. Zhang, J. Xia, H. Xu, and M. Sun, J. Raman Spectrosc. **45**, 533 (2014).
[20] S. Nie, Science **275**, 1102 (1997).
[21] A. Balčytis, Y. Nishijima, S. Krishnamoorthy, A. Kuchmizhak, P. R. Stoddart, R. Petruškevičius, and S. Juodkazis, Adv. Opt. Mater. **6**, 1800292 (2018).

[22] S. V. Makarov, V. A. Milichko, I. S. Mukhin, I. I. Shishkin, D. A. Zuev, A. M. Mozharov, A. E. Krasnok, and P. A. Belov, Laser Photonics Rev. **10**, 91 (2016).

[23] M. E. Abdelsalam, S. Mahajan, P. N. Bartlett, J. J. Baumberg, and A. E. Rusell, J. Am. Chem. Soc. **129**, 7399 (2007).

[24] A. Y. Panarin, S. N. Terekhov, K. I. Kholostov, and V. P. Bondarenko, Appl. Surf. Sci. **256**, 6969 (2010).

[25] H. Bandarenka, K. Artsemyeva, S. Redko, A. Panarin, S. Terekhov, and V. Bondarenko, Phys. Status Solidi C **10**, 624 (2013).

[26] D. Dong, L. W. Yap, D. M. Smilgies, K. J. Si, Q. Shi, and W. Cheng, Nanoscale **10**, 5065 (2018).

[27] P. R. Brejna and P. R. Griffiths, Appl. Spectrosc. **64**, 493 (2010).

[28] T. Qiu, X. L. Wu, Y. F. Mei, P. K. Chu, and G. G. Siu, Appl. Phys. A: Mater. Sci. Process. **81**, 669 (2005).

[29] T. Qiu, X. L. Wu, J. C. Shen, Y. Xia, P. N. Shen, and P. K. Chu, Appl. Surf. Sci. **254**, 5399 (2008).

[30] M. M. Alam, W. Ji, H. N. Luitel, Y. Ozaki, T. Watari, and K. Nakashima, RSC Adv. **4**, 52686 (2014).

[31] W. Ye, C. Shen, J. Tian, C. Wang, C. Hui, and H. Gao, Solid State Sci. **11**, 1088 (2009).

[32] X. Sun, L. Lin, Z. Li, Z. Zhang, and J. Feng, Mater. Lett. **63**, 2306 (2009).

[33] C. K. Senthil Kumaran, S. Agilan, D. Velauthapillai, N. Muthukumarasamy, M. Thambidurai, A. Ranjitha, R. Balasundaraprabhu, and T. S. Senthil, Adv. Mater. Res. **678**, 27 (2013).

[34] S. J. Hurst, E. K. Payne, L. Qin, and C. A. Mirkin, Angew. Chem. Int. Ed. **45**, 2672 (2006).

[35] H. Masuda and K. Fukuda, Science **268**, 1466 (1995).

[36] E. Y. Kaniukov, J. Ustarroz, D. V. Yakimchuk, M. Petrova, H. Terryn, V. Sivakov, and A. V. Petrov, Nanotechnology **27**, 115305 (2016).

[37] H. Bandarenka, K. Girel, S. Zavatski, A. Panarin, and S. Terekhov, Materials **11**, 852 (2018).

[38] Y. Cao and T. E. Mallouk, Chem. Mater. **20**, 5260 (2008).

[39] M. Wirtz and C. R. Martin, Adv. Mater. **15**, 455 (2003).

[40] V. Bundyukova, E. Kaniukov, A. Shumskaya, A. Smirnov, M. Kravchenko, and D. Yakimchuk, EPJ Web Conf. **201**, 01001 (2019).

[41] D. Yakimchuk, V. Bundyukova, A. Smirnov, and E. Kaniukov, Phys. Status Solidi B **256**, 1800316 (2019).

[42] V. Bundyukova, D. Yakimchuk, E. Shumskaya, A. Smirnov, M. Yarmolich, and E. Kaniukov, Mater. Today: Proc. **7**, 828 (2019).

[43] D. Yakimchuk, E. Kaniukov, V. Bundyukova, L. Osminkina, S. Teichert, S. Demyanov, and V. Sivakov, MRS Commun. **8**, 95 (2018).

[44] M. Abouda-Lachiheb, N. Nafie, and M. Bouaicha, Nanoscale Res. Lett. **7**, 455 (2012).

[45] W. Ye, Y. Chang, C. Ma, B. Jia, G. Cao, and C. Wang, Appl. Surf. Sci. **253**, 3419 (2007).

[46] R. Krakow, R. J. Bennett, D. N. Johnstone, Z. Vukmanovic, W. Solano-Alvarez, S. J. Lainé, J. F. Einsle, P. A. Midgley, C. M. F. Rae, and R. Hielscher, Proc. R. Soc. A **473**, 20170274 (2017).

[47] N. Jahr, M. Anwar, O. Stranik, N. Hädrich, N. Vogler, A. Csaki, J. Popp, and W. Fritzsche, J. Phys. Chem. C **117**, 7751 (2013).

[48] V. I. Fabelinsky, D. N. Kozlov, S. N. Orlov, Y. N. Polivanov, I. A. Shcherbakov, V. V. Smirnov, K. A. Vereschagin, G. M. Arzumanyan, K. Z. Mamatkulov, K. N. Afanasiev, A. N. Lagarkov, I. A. Ryzhikov, A. K. Sarychev, I. A. Budashov, N. L. Nechaeva, and I. N. Kurochkin, J. Raman Spectrosc. **49**, 1145 (2018).

[49] P. B. Johnson and R. W. Christy, Phys. Rev. B **6**, 4370 (1972).

[50] A. P. Sutton and R. W. Balluffi, *Interfaces in Crystalline Materials* (Oxford Clarendon Press, New York, 1995).

[51] R. He, X. Qian, Y. Jie, and Z. Zhu, Chem. Phys. Lett. **369**, 454 (2003).

[52] G. B. Hoflund, Z. F. Hazos, and G. N. Salaita, Phys. Rev. B **62**, 11126 (2000).

[53] C. C. Lin and C. W. Chang, Biosens. Bioelectron. **51**, 297 (2014).

[54] J. F. Arenas, M. S. Woolley, I. L. Tocon, J. C. Otero, and J. I. Marcos, J. Chem. Phys. **112**, 7669 (2000).

[55] S. K. Saikin, R. Olivares-Amaya, D. Rappoport, M. Stopa, and A. Aspuru-Guzik, Phys. Chem. Chem. Phys. **11**, 9401 (2009).

[56] D. P. Fromm, A. Sundaramurthy, A. Kinkhabwala, P. J. Schuck, G. S. Kino, and W. E. Moerner, J. Chem. Phys. **124**, 061101 (2006).

[57] S. K. Saikin, Y. Chu, D. Rappoport, K. B. Crozier, and A. Aspuru-Guzik, J. Phys. Chem. Lett. **1**, 2740 (2010).

[58] A. Otto, J. Raman Spectrosc. **36**, 497 (2005).

[59] P. Kumar, R. Khosla, M. Soni, D. Deva, and S. K. Sharma, Sens. Actuators B **246**, 477 (2017).

[60] S. Sharma, V. Prakash, and S. K. Mehta, Trends Anal. Chem. **86**, 155 (2017).

[61] X. Zhang, Q. Zhou, J. Ni, Z. Li, and Z. Zhang, Physica E **44**, 460 (2011).

Bibliography

[1] A. Yariv, "Optical electronics in modern communications," *(No Title)*, 1997.

[2] C. Xiang, S. M. Bowers, A. Bjorlin, R. Blum, and J. E. Bowers, "Perspective on the future of silicon photonics and electronics," *Applied Physics Letters*, vol. 118, no. 22, 2021.

[3] D. Thomson, A. Zilkie, J. E. Bowers, T. Komljenovic, G. T. Reed, L. Vivien, D. Marris-Morini, E. Cassan, L. Virot, J.-M. Fédéli, *et al.*, "Roadmap on silicon photonics," *Journal of Optics*, vol. 18, no. 7, p. 073003, 2016.

[4] M. Girtan, "Is photonics the new electronics?," *Materials Today*, vol. 17, no. 3, pp. 100–101, 2014.

[5] E. Ozbay, "Plasmonics: merging photonics and electronics at nanoscale dimensions," *science*, vol. 311, no. 5758, pp. 189–193, 2006.

[6] R. A. Minasian, "Photonic signal processing of microwave signals," *IEEE Transactions on Microwave Theory and Techniques*, vol. 54, no. 2, pp. 832–846, 2006.

[7] V. J. Urick, D. C. Mikeska, and M. E. Godinez, "Photonics for electronic inteference suppression," in *2017 IEEE Avionics and Vehicle Fiber-Optics and Photonics Conference (AVFOP)*, pp. 1–2, IEEE, 2017.

[8] B. E. Saleh and M. C. Teich, *Fundamentals of photonics.* john Wiley & sons, 2019.

[9] S. Yin, P. B. Ruffin, and T. Francis, *Fiber optic sensors.* CRC press, 2017.

[10] A. E. Siegman, *Lasers.* University science books, 1986.

[11] P. N. Prasad, *Nanophotonics.* John Wiley & Sons, 2004.

[12] M. O. Scully and M. S. Zubairy, "Quantum optics," 1999.

[13] N. Gisin, G. Ribordy, W. Tittel, and H. Zbinden, "Quantum cryptography," *Reviews of modern physics*, vol. 74, no. 1, p. 145, 2002.

[14] R. Horodecki, P. Horodecki, M. Horodecki, and K. Horodecki, "Quantum entanglement," *Reviews of modern physics*, vol. 81, no. 2, p. 865, 2009.

[15] A. Kavokin and G. Malpuech, *Cavity polaritons.* Elsevier, 2003.

[16] A. Krasnok, S. Lepeshov, and A. Alú, “Nanophotonics with 2d transition metal dichalcogenides,” *Optics express*, vol. 26, no. 12, pp. 15972–15994, 2018.

[17] F. Bonaccorso, Z. Sun, T. Hasan, and A. Ferrari, “Graphene photonics and optoelectronics,” *Nature photonics*, vol. 4, no. 9, pp. 611–622, 2010.

[18] F. J. García de Abajo, “Graphene nanophotonics,” *Science*, vol. 339, no. 6122, pp. 917–918, 2013.

[19] S. A. Maier *et al.*, *Plasmonics: fundamentals and applications*, vol. 1. Springer, 2007.

[20] J. D. Joannopoulos, P. R. Villeneuve, and S. Fan, “Photonic crystals,” *Solid State Communications*, vol. 102, no. 2-3, pp. 165–173, 1997.

[21] T. J. Cui, D. R. Smith, and R. Liu, *Metamaterials.* Springer, 2010.

[22] H.-T. Chen, A. J. Taylor, and N. Yu, “A review of metasurfaces: physics and applications,” *Reports on progress in physics*, vol. 79, no. 7, p. 076401, 2016.

[23] A. Kinkhabwala, Z. Yu, S. Fan, Y. Avlasevich, K. Müllen, and W. Moerner, “Large single-molecule fluorescence enhancements produced by a bowtie nanoantenna,” *Nature photonics*, vol. 3, no. 11, pp. 654–657, 2009.

[24] J. Mejía-Salazar and O. N. Oliveira Jr, “Plasmonic biosensing: Focus review,” *Chemical reviews*, vol. 118, no. 20, pp. 10617–10625, 2018.

[25] J.-F. Li, C.-Y. Li, and R. F. Aroca, “Plasmon-enhanced fluorescence spectroscopy,” *Chemical Society Reviews*, vol. 46, no. 13, pp. 3962–3979, 2017.

[26] A. H. Fikouras, M. Schubert, M. Karl, J. D. Kumar, S. J. Powis, A. Di Falco, and M. C. Gather, “Non-obstructive intracellular nanolasers,” *Nature Communications*, vol. 9, no. 1, p. 4817, 2018.

[27] P. Nativo, I. A. Prior, and M. Brust, “Uptake and intracellular fate of surface-modified gold nanoparticles,” *ACS nano*, vol. 2, no. 8, pp. 1639–1644, 2008.

[28] Y. H. Bae and K. Park, “Targeted drug delivery to tumors: myths, reality and possibility,” 2011.

[29] G. B. Braun, T. Friman, H.-B. Pang, A. Pallaoro, T. H. De Mendoza, A.-M. A. Willmore, V. R. Kotamraju, A. P. Mann, Z.-G. She, K. N. Sugahara, *et al.*, “Etchable plasmonic nanoparticle probes to image and quantify cellular internalization,” *Nature materials*, vol. 13, no. 9, pp. 904–911, 2014.

[30] R.-M. Ma and R. F. Oulton, “Applications of nanolasers,” *Nature nanotechnology*, vol. 14, no. 1, pp. 12–22, 2019.

[31] J. K. Jaiswal, E. R. Goldman, H. Mattoussi, and S. M. Simon, "Use of quantum dots for live cell imaging," *Nature methods*, vol. 1, no. 1, pp. 73–78, 2004.

[32] P. Kumari, B. Ghosh, and S. Biswas, "Nanocarriers for cancer-targeted drug delivery," *Journal of drug targeting*, vol. 24, no. 3, pp. 179–191, 2016.

[33] L. Han, Q. Cai, D. Tian, D. K. Kong, X. Gou, Z. Chen, S. M. Strittmatter, Z. Wang, K. N. Sheth, and J. Zhou, "Targeted drug delivery to ischemic stroke via chlorotoxin-anchored, lexiscan-loaded nanoparticles," *Nanomedicine: Nanotechnology, Biology and Medicine*, vol. 12, no. 7, pp. 1833–1842, 2016.

[34] L. R. Hirsch, R. J. Stafford, J. Bankson, S. R. Sershen, B. Rivera, R. Price, J. D. Hazle, N. J. Halas, and J. L. West, "Nanoshell-mediated near-infrared thermal therapy of tumors under magnetic resonance guidance," *Proceedings of the National Academy of Sciences*, vol. 100, no. 23, pp. 13549–13554, 2003.

[35] W. Bogaerts and L. Chrostowski, "Silicon photonics circuit design: methods, tools and challenges," *Laser & Photonics Reviews*, vol. 12, no. 4, p. 1700237, 2018.

[36] R. Kirchain and L. Kimerling, "A roadmap for nanophotonics," *Nature Photonics*, vol. 1, no. 6, pp. 303–305, 2007.

[37] D. Pile, "Nanophotonics is big," *Nature Photonics*, vol. 8, no. 12, pp. 878–879, 2014.

[38] D. G. Baranov, D. A. Zuev, S. I. Lepeshov, O. V. Kotov, A. E. Krasnok, A. B. Evlyukhin, and B. N. Chichkov, "All-dielectric nanophotonics: the quest for better materials and fabrication techniques," *Optica*, vol. 4, no. 7, pp. 814–825, 2017.

[39] J. M. Arrazola, V. Bergholm, K. Brádler, T. R. Bromley, M. J. Collins, I. Dhand, A. Fumagalli, T. Gerrits, A. Goussev, L. G. Helt, *et al.*, "Quantum circuits with many photons on a programmable nanophotonic chip," *Nature*, vol. 591, no. 7848, pp. 54–60, 2021.

[40] W. Bogaerts, R. Baets, P. Dumon, V. Wiaux, S. Beckx, D. Taillaert, B. Luyssaert, J. Van Campenhout, P. Bienstman, and D. Van Thourhout, "Nanophotonic waveguides in silicon-on-insulator fabricated with cmos technology," *Journal of Lightwave Technology*, vol. 23, no. 1, p. 401, 2005.

[41] L. A. Coldren, S. W. Corzine, and M. L. Mashanovitch, *Diode lasers and photonic integrated circuits*. John Wiley & Sons, 2012.

[42] B. Jalali and S. Fathpour, "Silicon photonics," *Journal of lightwave technology*, vol. 24, no. 12, pp. 4600–4615, 2006.

[43] Z. Huang, J. E. Carey, M. Liu, X. Guo, E. Mazur, and J. C. Campbell, “Microstructured silicon photodetector,” *Applied Physics Letters*, vol. 89, no. 3, 2006.

[44] D. Auston, P. Lavallard, N. Sol, and D. Kaplan, “An amorphous silicon photodetector for picosecond pulses,” *Applied Physics Letters*, vol. 36, no. 1, pp. 66–68, 1980.

[45] D. Liang and J. E. Bowers, “Recent progress in lasers on silicon,” *Nature photonics*, vol. 4, no. 8, pp. 511–517, 2010.

[46] A. N. Z. Rashed, A. E.-N. A. Mohammed, W. F. Zaky, I. Amiri, and P. Yupapin, “The switching of optoelectronics to full optical computing operations based on nonlinear metamaterials,” *Results in Physics*, vol. 13, p. 102152, 2019.

[47] J. Leuthold, C. Koos, and W. Freude, “Nonlinear silicon photonics,” *Nature photonics*, vol. 4, no. 8, pp. 535–544, 2010.

[48] A. Krasnok, M. Tymchenko, and A. Alù, “Nonlinear metasurfaces: a paradigm shift in nonlinear optics,” *Materials Today*, vol. 21, no. 1, pp. 8–21, 2018.

[49] D. G. Baranov, M. Wersall, J. Cuadra, T. J. Antosiewicz, and T. Shegai, “Novel nanostructures and materials for strong light–matter interactions,” *Acs Photonics*, vol. 5, no. 1, pp. 24–42, 2018.

[50] X. Lu, A. McClung, and K. Srinivasan, “High-q slow light and its localization in a photonic crystal microring,” *Nature Photonics*, vol. 16, no. 1, pp. 66–71, 2022.

[51] T. Ling, S.-L. Chen, and L. J. Guo, “Fabrication and characterization of high q polymer micro-ring resonator and its application as a sensitive ultrasonic detector,” *Optics express*, vol. 19, no. 2, pp. 861–869, 2011.

[52] T. Baba, “Slow light in photonic crystals,” *Nature photonics*, vol. 2, no. 8, pp. 465–473, 2008.

[53] J. G. Pedersen, S. Xiao, and N. A. Mortensen, “Limits of slow light in photonic crystals,” *Physical Review B*, vol. 78, no. 15, p. 153101, 2008.

[54] P. R. West, S. Ishii, G. V. Naik, N. K. Emani, V. M. Shalaev, and A. Boltasseva, “Searching for better plasmonic materials,” *Laser & photonics reviews*, vol. 4, no. 6, pp. 795–808, 2010.

[55] F. Wang, R. E. Christiansen, Y. Yu, J. Mørk, and O. Sigmund, “Maximizing the quality factor to mode volume ratio for ultra-small photonic crystal cavities,” *Applied Physics Letters*, vol. 113, no. 24, 2018.

[56] R. Paniagua-Dominguez, S. T. Ha, and A. I. Kuznetsov, “Active and tunable nanophotonics with dielectric nanoantennas,” *Proceedings of the IEEE*, vol. 108, no. 5, pp. 749–771, 2019.

[57] S. V. Makarov, A. S. Zalogina, M. Tajik, D. A. Zuev, M. V. Rybin, A. A. Kuchmizhak, S. Juodkazis, and Y. Kivshar, “Light-induced tuning and reconfiguration of nanophotonic structures,” *Laser & Photonics Reviews*, vol. 11, no. 5, p. 1700108, 2017.

[58] S. Abdollahramezani, O. Hemmatyar, H. Taghinejad, A. Krasnok, Y. Kiarashinejad, M. Zandehshahvar, A. Alù, and A. Adibi, “Tunable nanophotonics enabled by chalcogenide phase-change materials,” *Nanophotonics*, vol. 9, no. 5, pp. 1189–1241, 2020.

[59] J. Hu, A. I. Kuznetsov, V. J. Sorger, and I. Staude, “Tunable nanophotonics,” 2022.

[60] Y. Kivshar, “All-dielectric meta-optics and non-linear nanophotonics,” *National Science Review*, vol. 5, no. 2, pp. 144–158, 2018.

[61] A. I. Kuznetsov, A. E. Miroshnichenko, M. L. Brongersma, Y. S. Kivshar, and B. Luk’yanchuk, “Optically resonant dielectric nanostructures,” *Science*, vol. 354, no. 6314, p. aag2472, 2016.

[62] G. Mie, “Zur kinetischen theorie der einatomigen körper,” *Annalen der Physik*, vol. 316, no. 8, pp. 657–697, 1903.

[63] W. Liu and Y. S. Kivshar, “Generalized kerker effects in nanophotonics and meta-optics,” *Optics express*, vol. 26, no. 10, pp. 13085–13105, 2018.

[64] P. Woźniak, P. Banzer, and G. Leuchs, “Selective switching of individual multipole resonances in single dielectric nanoparticles,” *Laser & Photonics Reviews*, vol. 9, no. 2, pp. 231–240, 2015.

[65] G. P. Zograf, M. I. Petrov, D. A. Zuev, P. A. Dmitriev, V. A. Milichko, S. V. Makarov, and P. A. Belov, “Resonant nonplasmonic nanoparticles for efficient temperature-feedback optical heating,” *Nano letters*, vol. 17, no. 5, pp. 2945–2952, 2017.

[66] K. Koshelev, S. Kruk, E. Melik-Gaykazyan, J.-H. Choi, A. Bogdanov, H.-G. Park, and Y. Kivshar, “Subwavelength dielectric resonators for nonlinear nanophotonics,” *Science*, vol. 367, no. 6475, pp. 288–292, 2020.

[67] Y. Kivshar, “The rise of mie-tronics,” *Nano Letters*, vol. 22, no. 9, pp. 3513–3515, 2022.

[68] R. Won, “Into the ‘mie-tronic’era,” *Nature Photonics*, vol. 13, no. 9, pp. 585–587, 2019.

[69] M. V. Rybin, K. L. Koshelev, Z. F. Sadrieva, K. B. Samusev, A. A. Bogdanov, M. F. Limonov, and Y. S. Kivshar, “High-q supercavity modes in subwavelength dielectric resonators,” *Physical review letters*, vol. 119, no. 24, p. 243901, 2017.

[70] P. M. Piechulla, E. Slivina, D. Bätzner, I. Fernandez-Corbaton, P. Dhawan, R. B. Wehrspohn, A. N. Sprafke, and C. Rockstuhl, “Antireflective huygens’ metasurface with correlated disorder made from high-index disks implemented into silicon heterojunction solar cells,” *Acs Photonics*, vol. 8, no. 12, pp. 3476–3485, 2021.

[71] A. E. Krasnok, I. S. Maksymov, A. I. Denisyuk, P. A. Belov, A. E. Miroshnichenko, C. R. Simovski, and Y. S. Kivshar, “Optical nanoantennas,” *Physics-Uspekhi*, vol. 56, no. 6, p. 539, 2013.

[72] A. H. Dorrah and F. Capasso, “Tunable structured light with flat optics,” *Science*, vol. 376, no. 6591, p. eabi6860, 2022.

[73] X. Wang, Z. Nie, Y. Liang, J. Wang, T. Li, and B. Jia, “Recent advances on optical vortex generation,” *Nanophotonics*, vol. 7, no. 9, pp. 1533–1556, 2018.

[74] A. Tittl, A. Leitis, M. Liu, F. Yesilkoy, D.-Y. Choi, D. N. Neshev, Y. S. Kivshar, and H. Altug, “Imaging-based molecular barcoding with pixelated dielectric metasurfaces,” *Science*, vol. 360, no. 6393, pp. 1105–1109, 2018.

[75] D. G. Baranov, A. Krasnok, and A. Alu, “Coherent virtual absorption based on complex zero excitation for ideal light capturing,” *Optica*, vol. 4, no. 12, pp. 1457–1461, 2017.

[76] H. Li, A. Mekawy, A. Krasnok, and A. Alù, “Virtual parity-time symmetry,” *Physical Review Letters*, vol. 124, no. 19, p. 193901, 2020.

[77] Y. Ra’di, A. Krasnok, and A. Alú, “Virtual critical coupling,” *ACS Photonics*, vol. 7, no. 6, pp. 1468–1475, 2020.

[78] J. D. Jackson, “Classical electrodynamics,” 1999.

[79] C. F. Bohren and D. R. Huffman, *Absorption and scattering of light by small particles.* John Wiley & Sons, 2008.

[80] L. Novotny and B. Hecht, *Principles of nano-optics.* Cambridge university press, 2012.

[81] A. Krasnok, D. Baranov, H. Li, M.-A. Miri, F. Monticone, and A. Alú, “Anomalies in light scattering,” *Advances in Optics and Photonics*, vol. 11, no. 4, pp. 892–951, 2019.

[82] H. A. Haus and W. Huang, “Coupled-mode theory,” *Proceedings of the IEEE*, vol. 79, no. 10, pp. 1505–1518, 1991.

[83] A. Yariv, "Coupled-mode theory for guided-wave optics," *IEEE Journal of Quantum Electronics*, vol. 9, no. 9, pp. 919–933, 1973.

[84] S. E. Miller, "Coupled wave theory and waveguide applications," *Bell System Technical Journal*, vol. 33, no. 3, pp. 661–719, 1954.

[85] A. Yariv, Y. Xu, R. K. Lee, and A. Scherer, "Coupled-resonator optical waveguide:? a proposal and analysis," *Optics letters*, vol. 24, no. 11, pp. 711–713, 1999.

[86] F. Alpeggiani, N. Parappurath, E. Verhagen, and L. Kuipers, "Quasinormal-mode expansion of the scattering matrix," *Physical Review X*, vol. 7, no. 2, p. 021035, 2017.

[87] S. Franke, J. Ren, S. Hughes, and M. Richter, "Fluctuation-dissipation theorem and fundamental photon commutation relations in lossy nanostructures using quasinormal modes," *Physical Review Research*, vol. 2, no. 3, p. 033332, 2020.

[88] V. M. Rao and S. Hughes, "Single quantum-dot purcell factor and β factor in a photonic crystal waveguide," *Physical Review B*, vol. 75, no. 20, p. 205437, 2007.

[89] S. Fan, W. Suh, and J. D. Joannopoulos, "Temporal coupled-mode theory for the fano resonance in optical resonators," *JOSA A*, vol. 20, no. 3, pp. 569–572, 2003.

[90] B. Nistad and J. Skaar, "Causality and electromagnetic properties of active media," *Physical Review E*, vol. 78, no. 3, p. 036603, 2008.

[91] H. J. Weber and G. B. Arfken, *Essential mathematical methods for physicists, ISE*. Elsevier, 2003.

[92] A. Yariv, "Critical coupling and its control in optical waveguide-ring resonator systems," *IEEE Photonics Technology Letters*, vol. 14, no. 4, pp. 483–485, 2002.

[93] C. E. Rüter, K. G. Makris, R. El-Ganainy, D. N. Christodoulides, M. Segev, and D. Kip, "Observation of parity–time symmetry in optics," *Nature physics*, vol. 6, no. 3, pp. 192–195, 2010.

[94] A. E. Krasnok, A. P. Slobozhanyuk, C. R. Simovski, S. A. Tretyakov, A. N. Poddubny, A. E. Miroshnichenko, Y. S. Kivshar, and P. A. Belov, "An antenna model for the purcell effect," *Scientific reports*, vol. 5, no. 1, p. 12956, 2015.

[95] R. C. Hilborn, "Einstein coefficients, cross sections, f values, dipole moments, and all that," *American Journal of Physics*, vol. 50, no. 11, pp. 982–986, 1982.

[96] U. Hohenester and U. Hohenester, "Photonic local density of states," *Nano and Quantum Optics: An Introduction to Basic Principles and Theory*, pp. 259–295, 2020.

[97] E. M. Purcell, “Spontaneous emission probabilities at radio frequencies,” in *Confined Electrons and Photons: New Physics and Applications*, pp. 839–839, Springer, 1995.

[98] J. I. Cirac, “Interaction of a two-level atom with a cavity mode in the bad-cavity limit,” *Physical Review A*, vol. 46, no. 7, p. 4354, 1992.

[99] J. P. Marangos, “Electromagnetically induced transparency,” *Journal of modern optics*, vol. 45, no. 3, pp. 471–503, 1998.

[100] W. Heiss, “The physics of exceptional points,” *Journal of Physics A: Mathematical and Theoretical*, vol. 45, no. 44, p. 444016, 2012.

[101] H. Hodaei, A. U. Hassan, S. Wittek, H. Garcia-Gracia, R. El-Ganainy, D. N. Christodoulides, and M. Khajavikhan, “Enhanced sensitivity at higher-order exceptional points,” *Nature*, vol. 548, no. 7666, pp. 187–191, 2017.

[102] W. Chen, Ş. Kaya Özdemir, G. Zhao, J. Wiersig, and L. Yang, “Exceptional points enhance sensing in an optical microcavity,” *Nature*, vol. 548, no. 7666, pp. 192–196, 2017.

[103] G. M. Akselrod, C. Argyropoulos, T. B. Hoang, C. Ciracì, C. Fang, J. Huang, D. R. Smith, and M. H. Mikkelsen, “Probing the mechanisms of large purcell enhancement in plasmonic nanoantennas,” *Nature Photonics*, vol. 8, no. 11, pp. 835–840, 2014.

[104] A. L. Crook, C. P. Anderson, K. C. Miao, A. Bourassa, H. Lee, S. L. Bayliss, D. O. Bracher, X. Zhang, H. Abe, T. Ohshima, *et al.*, “Purcell enhancement of a single silicon carbide color center with coherent spin control,” *Nano letters*, vol. 20, no. 5, pp. 3427–3434, 2020.

[105] P. T. Kristensen, C. Van Vlack, and S. Hughes, “Generalized effective mode volume for leaky optical cavities,” *Optics letters*, vol. 37, no. 10, pp. 1649–1651, 2012.

[106] D. Englund, D. Fattal, E. Waks, G. Solomon, B. Zhang, T. Nakaoka, Y. Arakawa, Y. Yamamoto, and J. Vučković, “Controlling the spontaneous emission rate of single quantum dots in a two-dimensional photonic crystal,” *Physical review letters*, vol. 95, no. 1, p. 013904, 2005.

[107] A. E. Krasnok, A. Maloshtan, D. N. Chigrin, Y. S. Kivshar, and P. A. Belov, “Enhanced emission extraction and selective excitation of nv centers with all–dielectric nanoantennas,” *Laser & Photonics Reviews*, vol. 9, no. 4, pp. 385–391, 2015.

[108] A. G. Curto, G. Volpe, T. H. Taminiau, M. P. Kreuzer, R. Quidant, and N. F. Van Hulst, “Unidirectional emission of a quantum dot coupled to a nanoantenna,” *Science*, vol. 329, no. 5994, pp. 930–933, 2010.

[109] M. P. Busson, B. Rolly, B. Stout, N. Bonod, and S. Bidault, “Accelerated single photon emission from dye molecule-driven nanoantennas assembled on dna,” *Nature communications*, vol. 3, no. 1, p. 962, 2012.

[110] H. Beutler, “Über absorptionsserien von argon, krypton und xenon zu termen zwischen den beiden ionisierungsgrenzen 2 p 3 2/0 und 2 p 1 2/0,” *Zeitschrift für Physik*, vol. 93, pp. 177–196, 1935.

[111] U. Fano, “Sullo spettro di assorbimento dei gas nobili presso il limite dello spettro d’arco,” *Il Nuovo Cimento (1924-1942)*, vol. 12, no. 3, pp. 154–161, 1935.

[112] A. E. Miroshnichenko, S. Flach, and Y. S. Kivshar, “Fano resonances in nanoscale structures,” *Reviews of Modern Physics*, vol. 82, no. 3, p. 2257, 2010.

[113] M. F. Limonov, M. V. Rybin, A. N. Poddubny, and Y. S. Kivshar, “Fano resonances in photonics,” *Nature Photonics*, vol. 11, no. 9, pp. 543–554, 2017.

[114] M. Sarrazin, J.-P. Vigneron, and J.-M. Vigoureux, “Role of wood anomalies in optical properties of thin metallic films with a bidimensional array of subwavelength holes,” *Physical Review B*, vol. 67, no. 8, p. 085415, 2003.

[115] M. F. Limonov, “Fano resonance for applications,” *Advances in Optics and Photonics*, vol. 13, no. 3, pp. 703–771, 2021.

[116] S. Han, L. Cong, F. Gao, R. Singh, and H. Yang, “Observation of fano resonance and classical analog of electromagnetically induced transparency in toroidal metamaterials,” *Annalen der Physik*, vol. 528, no. 5, pp. 352–357, 2016.

[117] M. V. Rybin, D. S. Filonov, P. A. Belov, Y. S. Kivshar, and M. F. Limonov, “Switching from visibility to invisibility via fano resonances: theory and experiment,” *Scientific reports*, vol. 5, no. 1, p. 8774, 2015.

[118] A. B. Khanikaev, C. Wu, and G. Shvets, “Fano-resonant metamaterials and their applications,” *Nanophotonics*, vol. 2, no. 4, pp. 247–264, 2013.

[119] S. Soria, S. Berneschi, M. Brenci, F. Cosi, G. N. Conti, S. Pelli, and G. C. Righini, “Optical microspherical resonators for biomedical sensing,” *Sensors*, vol. 11, no. 1, pp. 785–805, 2011.

[120] V. S. Ilchenko, A. A. Savchenkov, A. B. Matsko, and L. Maleki, “Nonlinear optics and crystalline whispering gallery mode cavities,” *Physical review letters*, vol. 92, no. 4, p. 043903, 2004.

[121] C. W. Hsu, B. Zhen, A. D. Stone, J. D. Joannopoulos, and M. Soljačić, “Bound states in the continuum,” *Nature Reviews Materials*, vol. 1, no. 9, pp. 1–13, 2016.

[122] Y. Liang, K. Koshelev, F. Zhang, H. Lin, S. Lin, J. Wu, B. Jia, and Y. Kivshar, "Bound states in the continuum in anisotropic plasmonic metasurfaces," *Nano Letters*, vol. 20, no. 9, pp. 6351–6356, 2020.

[123] F. Monticone, D. Sounas, A. Krasnok, and A. Alù, "Can a nonradiating mode be externally excited? nonscattering states versus embedded eigenstates," *ACS Photonics*, vol. 6, no. 12, pp. 3108–3114, 2019.

[124] S. Lannebère and M. G. Silveirinha, "Optical meta-atom for localization of light with quantized energy," *Nature communications*, vol. 6, no. 1, p. 8766, 2015.

[125] F. Monticone and A. Alu, "Embedded photonic eigenvalues in 3d nanostructures," *Physical Review Letters*, vol. 112, no. 21, p. 213903, 2014.

[126] W. Suh, Z. Wang, and S. Fan, "Temporal coupled-mode theory and the presence of non-orthogonal modes in lossless multimode cavities," *IEEE Journal of Quantum Electronics*, vol. 40, no. 10, pp. 1511–1518, 2004.

[127] W. Suh, M. Yanik, O. Solgaard, and S. Fan, "Displacement-sensitive photonic crystal structures based on guided resonance in photonic crystal slabs," *Applied physics letters*, vol. 82, no. 13, pp. 1999–2001, 2003.

[128] E. Melik-Gaykazyan, K. Koshelev, J.-H. Choi, S. S. Kruk, A. Bogdanov, H.-G. Park, and Y. Kivshar, "From fano to quasi-bic resonances in individual dielectric nanoantennas," *Nano Letters*, vol. 21, no. 4, pp. 1765–1771, 2021.

[129] A. A. Bogdanov, K. L. Koshelev, P. V. Kapitanova, M. V. Rybin, S. A. Gladyshev, Z. F. Sadrieva, K. B. Samusev, Y. S. Kivshar, and M. F. Limonov, "Bound states in the continuum and fano resonances in the strong mode coupling regime," *Advanced Photonics*, vol. 1, no. 1, pp. 016001–016001, 2019.

[130] K. Koshelev, S. Lepeshov, M. Liu, A. Bogdanov, and Y. Kivshar, "Asymmetric metasurfaces with high-q resonances governed by bound states in the continuum," *Physical review letters*, vol. 121, no. 19, p. 193903, 2018.

[131] J. Jin, X. Yin, L. Ni, M. Soljačić, B. Zhen, and C. Peng, "Topologically enabled ultrahigh-q guided resonances robust to out-of-plane scattering," *Nature*, vol. 574, no. 7779, pp. 501–504, 2019.

[132] B. Zhen, C. W. Hsu, L. Lu, A. D. Stone, and M. Soljačić, "Topological nature of optical bound states in the continuum," *Physical review letters*, vol. 113, no. 25, p. 257401, 2014.

[133] T. Yoda and M. Notomi, "Generation and annihilation of topologically protected bound states in the continuum and circularly polarized states by symmetry breaking," *Physical Review Letters*, vol. 125, no. 5, p. 053902, 2020.

[134] M. Sidorenko, O. Sergaeva, Z. Sadrieva, C. Roques-Carmes, P. Muraev, D. Maksimov, and A. Bogdanov, “Observation of an accidental bound state in the continuum in a chain of dielectric disks,” *Physical Review Applied*, vol. 15, no. 3, p. 034041, 2021.

[135] M. G. Silveirinha, “Trapping light in open plasmonic nanostructures,” *Physical review A*, vol. 89, no. 2, p. 023813, 2014.

[136] S. Lepeshov, M. Wang, A. Krasnok, O. Kotov, T. Zhang, H. Liu, T. Jiang, B. Korgel, M. Terrones, Y. Zheng, *et al.*, “Tunable resonance coupling in single si nanoparticle–monolayer ws2 structures,” *ACS applied materials & interfaces*, vol. 10, no. 19, pp. 16690–16697, 2018.

[137] E. Bulgakov, K. Pichugin, and A. Sadreev, “Exceptional points in a dielectric spheroid,” *Physical Review A*, vol. 104, no. 5, p. 053507, 2021.

[138] Y. Yang, I. I. Kravchenko, D. P. Briggs, and J. Valentine, “All-dielectric metasurface analogue of electromagnetically induced transparency,” *Nature communications*, vol. 5, no. 1, p. 5753, 2014.

[139] M. V. Rybin, K. B. Samusev, I. S. Sinev, G. Semouchkin, E. Semouchkina, Y. S. Kivshar, and M. F. Limonov, “Mie scattering as a cascade of fano resonances,” *Optics express*, vol. 21, no. 24, pp. 30107–30113, 2013.

[140] X. Zambrana-Puyalto and N. Bonod, “Purcell factor of spherical mie resonators,” *Physical Review B*, vol. 91, no. 19, p. 195422, 2015.

[141] B. Carrascal, G. Estevez, P. Lee, and V. Lorenzo, “Vector spherical harmonics and their application to classical electrodynamics,” *European Journal of Physics*, vol. 12, no. 4, p. 184, 1991.

[142] A. E. Krasnok, C. R. Simovski, P. A. Belov, and Y. S. Kivshar, “Superdirective dielectric nanoantennas,” *Nanoscale*, vol. 6, no. 13, pp. 7354–7361, 2014.

[143] K. V. Baryshnikova, D. A. Smirnova, B. S. Luk’yanchuk, and Y. S. Kivshar, “Optical anapoles: concepts and applications,” *Advanced Optical Materials*, vol. 7, no. 14, p. 1801350, 2019.

[144] R. Wang and L. Dal Negro, “Engineering non-radiative anapole modes for broadband absorption enhancement of light,” *Optics Express*, vol. 24, no. 17, pp. 19048–19062, 2016.

[145] B. Luk’yanchuk, R. Paniagua-Domínguez, A. I. Kuznetsov, A. E. Miroshnichenko, and Y. S. Kivshar, “Suppression of scattering for small dielectric particles: anapole mode and invisibility,” *Philosophical Transactions of the Royal Society A: Mathematical, Physical and Engineering Sciences*, vol. 375, no. 2090, p. 20160069, 2017.

[146] E. A. Gurvitz, K. S. Ladutenko, P. A. Dergachev, A. B. Evlyukhin, A. E. Miroshnichenko, and A. S. Shalin, “The high-order toroidal moments and anapole states in all-dielectric photonics,” *Laser & Photonics Reviews*, vol. 13, no. 5, p. 1800266, 2019.

[147] M. Aspelmeyer, T. J. Kippenberg, and F. Marquardt, “Cavity optomechanics,” *Reviews of Modern Physics*, vol. 86, no. 4, p. 1391, 2014.

[148] A. Ivinskaya, N. Kostina, A. Proskurin, M. I. Petrov, A. A. Bogdanov, S. Sukhov, A. V. Krasavin, A. Karabchevsky, A. S. Shalin, and P. Ginzburg, “Optomechanical manipulation with hyperbolic metasurfaces,” *ACS Photonics*, vol. 5, no. 11, pp. 4371–4377, 2018.

[149] D. L. Andrews, *Structured light and its applications: An introduction to phase-structured beams and nanoscale optical forces.* Academic press, 2011.

[150] D. B. Ruffner and D. G. Grier, “Optical forces and torques in nonuniform beams of light,” *Physical review letters*, vol. 108, no. 17, p. 173602, 2012.

[151] A. H. Yang, S. D. Moore, B. S. Schmidt, M. Klug, M. Lipson, and D. Erickson, “Optical manipulation of nanoparticles and biomolecules in sub-wavelength slot waveguides,” *Nature*, vol. 457, no. 7225, pp. 71–75, 2009.

[152] A. Ashkin, J. M. Dziedzic, J. E. Bjorkholm, and S. Chu, “Observation of a single-beam gradient force optical trap for dielectric particles,” *Optics letters*, vol. 11, no. 5, pp. 288–290, 1986.

[153] M. Capitanio and F. S. Pavone, “Interrogating biology with force: single molecule high-resolution measurements with optical tweezers,” *Biophysical journal*, vol. 105, no. 6, pp. 1293–1303, 2013.

[154] I. Heller, T. P. Hoekstra, G. A. King, E. J. Peterman, and G. J. Wuite, “Optical tweezers analysis of dna–protein complexes,” *Chemical reviews*, vol. 114, no. 6, pp. 3087–3119, 2014.

[155] C. Gonzalez-Ballestero, M. Aspelmeyer, L. Novotny, R. Quidant, and O. Romero-Isart, “Levitodynamics: Levitation and control of microscopic objects in vacuum,” *Science*, vol. 374, no. 6564, p. eabg3027, 2021.

[156] M. Brown, S. Muleady, W. Dworschack, R. Lewis-Swan, A. Rey, O. Romero-Isart, and C. Regal, “Time-of-flight quantum tomography of an atom in an optical tweezer,” *Nature Physics*, vol. 19, no. 4, pp. 569–573, 2023.

[157] M. Dienerowitz, M. Mazilu, and K. Dholakia, “Optical manipulation of nanoparticles: a review,” *Journal of nanophotonics*, vol. 2, no. 1, p. 021875, 2008.

[158] G. Rui, X. Wang, and Y. Cui, “Manipulation of metallic nanoparticle with evanescent vortex bessel beam,” *Optics express*, vol. 23, no. 20, pp. 25707–25716, 2015.

[159] A. Mizrahi and Y. Fainman, “Negative radiation pressure on gain medium structures,” *Optics letters*, vol. 35, no. 20, pp. 3405–3407, 2010.

[160] K. C. Neuman and S. M. Block, “Optical trapping,” *Review of scientific instruments*, vol. 75, no. 9, pp. 2787–2809, 2004.

[161] A. Rohrbach, “Stiffness of optical traps: quantitative agreement between experiment and electromagnetic theory,” *Physical review letters*, vol. 95, no. 16, p. 168102, 2005.

[162] J. Piotrowski, D. Windey, J. Vijayan, C. Gonzalez-Ballestero, A. de los Ríos Sommer, N. Meyer, R. Quidant, O. Romero-Isart, R. Reimann, and L. Novotny, “Simultaneous ground-state cooling of two mechanical modes of a levitated nanoparticle,” *Nature Physics*, pp. 1–5, 2023.

[163] V. J. Sorger, R. F. Oulton, R.-M. Ma, and X. Zhang, “Toward integrated plasmonic circuits,” *MRS bulletin*, vol. 37, no. 8, pp. 728–738, 2012.

[164] S. V. Boriskina, T. A. Cooper, L. Zeng, G. Ni, J. K. Tong, Y. Tsurimaki, Y. Huang, L. Meroueh, G. Mahan, and G. Chen, “Losses in plasmonics: from mitigating energy dissipation to embracing loss-enabled functionalities,” *Advances in Optics and Photonics*, vol. 9, no. 4, pp. 775–827, 2017.

[165] G. Baffou and R. Quidant, “Thermo-plasmonics: using metallic nanostructures as nano-sources of heat,” *Laser & Photonics Reviews*, vol. 7, no. 2, pp. 171–187, 2013.

[166] N. Liu, M. Mesch, T. Weiss, M. Hentschel, and H. Giessen, “Infrared perfect absorber and its application as plasmonic sensor,” *Nano letters*, vol. 10, no. 7, pp. 2342–2348, 2010.

[167] M. J. Heck, J. F. Bauters, M. L. Davenport, D. T. Spencer, and J. E. Bowers, “Ultra-low loss waveguide platform and its integration with silicon photonics,” *Laser & Photonics Reviews*, vol. 8, no. 5, pp. 667–686, 2014.

[168] Y. Akahane, T. Asano, B.-S. Song, and S. Noda, “Fine-tuned high-q photonic-crystal nanocavity,” *Optics express*, vol. 13, no. 4, pp. 1202–1214, 2005.

[169] L. Shi, T. U. Tuzer, R. Fenollosa, and F. Meseguer, “A new dielectric metamaterial building block with a strong magnetic response in the sub-1.5-micrometer region: silicon colloid nanocavities,” *Advanced materials*, vol. 24, no. 44, pp. 5934–5938, 2012.

[170] A. V. Kildishev, A. Boltasseva, and V. M. Shalaev, “Planar photonics with metasurfaces,” *Science*, vol. 339, no. 6125, p. 1232009, 2013.

[171] A. Krasnok, S. Glybovski, M. Petrov, S. Makarov, R. Savelev, P. Belov, C. Simovski, and Y. Kivshar, “Demonstration of the enhanced purcell factor in all-dielectric structures,” *Applied Physics Letters*, vol. 108, no. 21, 2016.

[172] J. Yan, Z. Zheng, Z. Lou, J. Li, B. Mao, and B. Li, “Enhancement of exciton emission in ws 2 based on the kerker effect from the mode engineering of individual si nanostripes,” *Nanoscale Horizons*, vol. 5, no. 10, pp. 1368–1377, 2020.

[173] T. Ryu, M. Kim, Y. Hwang, M.-K. Kim, and J.-K. Yang, “High-efficiency soi-based metalenses at telecommunication wavelengths,” *Nanophotonics*, vol. 11, no. 21, pp. 4697–4704, 2022.

[174] M. Kerker, D.-S. Wang, and C. Giles, “Electromagnetic scattering by magnetic spheres,” *JOSA*, vol. 73, no. 6, pp. 765–767, 1983.

[175] R. Alaee, R. Filter, D. Lehr, F. Lederer, and C. Rockstuhl, “A generalized kerker condition for highly directive nanoantennas,” *Optics letters*, vol. 40, no. 11, pp. 2645–2648, 2015.

[176] H. K. Shamkhi, K. V. Baryshnikova, A. Sayanskiy, P. Kapitanova, P. D. Terekhov, P. Belov, A. Karabchevsky, A. B. Evlyukhin, Y. Kivshar, and A. S. Shalin, “Transverse scattering and generalized kerker effects in all-dielectric mie-resonant metaoptics,” *Physical review letters*, vol. 122, no. 19, p. 193905, 2019.

[177] M. Liu and D.-Y. Choi, “Extreme huygens’ metasurfaces based on quasi-bound states in the continuum,” *Nano letters*, vol. 18, no. 12, pp. 8062–8069, 2018.

[178] M. Hentschel, K. Koshelev, F. Sterl, S. Both, J. Karst, L. Shamsafar, T. Weiss, Y. Kivshar, and H. Giessen, “Dielectric mie voids: confining light in air,” *Light: Science & Applications*, vol. 12, no. 1, p. 3, 2023.

[179] A. Epstein and G. V. Eleftheriades, “Huygens’ metasurfaces via the equivalence principle: design and applications,” *JOSA B*, vol. 33, no. 2, pp. A31–A50, 2016.

[180] M. Khoury, H. Quard, T. Herzig, J. Meijer, S. Pezzagna, S. Cueff, M. Abbarchi, H. S. Nguyen, N. Chauvin, and T. Wood, “Light emitting si-based mie resonators: Toward a huygens source of quantum emitters,” *Advanced Optical Materials*, vol. 10, no. 21, p. 2201295, 2022.

[181] Y. Wu, Y. Chen, Q. Song, and S. Xiao, “Dynamic structural colors based on all-dielectric mie resonators,” *Advanced Optical Materials*, vol. 9, no. 11, p. 2002126, 2021.

[182] K. Kumar, H. Duan, R. S. Hegde, S. C. Koh, J. N. Wei, and J. K. Yang, “Printing colour at the optical diffraction limit,” *Nature nanotechnology*, vol. 7, no. 9, pp. 557–561, 2012.

[183] Z. Xuan, J. Li, Q. Liu, F. Yi, S. Wang, and W. Lu, “Artificial structural colors and applications,” *The Innovation*, vol. 2, no. 1, 2021.

[184] M. Khorasaninejad and F. Capasso, “Metalenses: Versatile multifunctional photonic components,” *Science*, vol. 358, no. 6367, p. eaam8100, 2017.

[185] W. T. Chen, A. Y. Zhu, V. Sanjeev, M. Khorasaninejad, Z. Shi, E. Lee, and F. Capasso, “A broadband achromatic metalens for focusing and imaging in the visible,” *Nature nanotechnology*, vol. 13, no. 3, pp. 220–226, 2018.

[186] E. Arbabi, A. Arbabi, S. M. Kamali, Y. Horie, and A. Faraon, “High efficiency double-wavelength dielectric metasurface lenses with dichroic birefringent meta-atoms,” *Optics Express*, vol. 24, no. 16, pp. 18468–18477, 2016.

[187] S. Colburn, A. Zhan, and A. Majumdar, “Varifocal zoom imaging with large area focal length adjustable metalenses,” *Optica*, vol. 5, no. 7, pp. 825–831, 2018.

[188] N. Yu, P. Genevet, M. A. Kats, F. Aieta, J.-P. Tetienne, F. Capasso, and Z. Gaburro, “Light propagation with phase discontinuities: generalized laws of reflection and refraction,” *science*, vol. 334, no. 6054, pp. 333–337, 2011.

[189] M. Decker, I. Staude, M. Falkner, J. Dominguez, D. N. Neshev, I. Brener, T. Pertsch, and Y. S. Kivshar, “High-efficiency dielectric huygens’ surfaces,” *Advanced Optical Materials*, vol. 3, no. 6, pp. 813–820, 2015.

[190] J. L. Santos and F. Farahi, *Handbook of optical sensors*. Crc Press, 2014.

[191] B. H. Lee, Y. H. Kim, K. S. Park, J. B. Eom, M. J. Kim, B. S. Rho, and H. Y. Choi, “Interferometric fiber optic sensors,” *sensors*, vol. 12, no. 3, pp. 2467–2486, 2012.

[192] Y.-J. Rao, “In-fibre bragg grating sensors,” *Measurement science and technology*, vol. 8, no. 4, p. 355, 1997.

[193] Y. Guo, J. Zhu, L. Xiong, and J. Guan, “Finger motion detection based on optical fiber bragg grating with polyimide substrate,” *Sensors and Actuators A: Physical*, vol. 338, p. 113482, 2022.

[194] C. E. Campanella, A. Cuccovillo, C. Campanella, A. Yurt, and V. M. Passaro, “Fibre bragg grating based strain sensors: Review of technology and applications,” *Sensors*, vol. 18, no. 9, p. 3115, 2018.

[195] G. Yan, A. P. Zhang, G. Ma, B. Wang, B. Kim, J. Im, S. He, and Y. Chung, “Fiber-optic acetylene gas sensor based on microstructured optical fiber bragg gratings,” *IEEE Photonics Technology Letters*, vol. 23, no. 21, pp. 1588–1590, 2011.

[196] A. P. Zhang, G. Yan, S. Gao, S. He, B. Kim, J. Im, and Y. Chung, “Microfluidic refractive-index sensors based on small-hole microstructured optical fiber bragg gratings,” *Applied Physics Letters*, vol. 98, no. 22, 2011.

[197] S. Gupta, T. Mizunami, T. Yamao, and T. Shimomura, “Fiber bragg grating cryogenic temperature sensors,” *Applied optics*, vol. 35, no. 25, pp. 5202–5205, 1996.

[198] C. García-Meca, S. Lechago, A. Brimont, A. Griol, S. Mas, L. Sánchez, L. Bellieres, N. S. Losilla, and J. Martí, “On-chip wireless silicon photonics: from reconfigurable interconnects to lab-on-chip devices,” *Light: Science & Applications*, vol. 6, no. 9, pp. e17053–e17053, 2017.

[199] H.-H. Hsiao, Y.-C. Hsu, A.-Y. Liu, J.-C. Hsieh, and Y.-H. Lin, “Ultrasensitive refractive index sensing based on the quasi-bound states in the continuum of all-dielectric metasurfaces,” *Advanced Optical Materials*, vol. 10, no. 19, p. 2200812, 2022.

[200] Y. Chen, C. Zhao, Y. Zhang, and C.-w. Qiu, “Integrated molar chiral sensing based on high-q metasurface,” *Nano Letters*, vol. 20, no. 12, pp. 8696–8703, 2020.

[201] S. Romano, M. Mangini, E. Penzo, S. Cabrini, A. C. De Luca, I. Rendina, V. Mocella, and G. Zito, “Ultrasensitive surface refractive index imaging based on quasi-bound states in the continuum,” *ACS nano*, vol. 14, no. 11, pp. 15417–15427, 2020.

[202] Y. Liu, W. Zhou, and Y. Sun, “Optical refractive index sensing based on high-q bound states in the continuum in free-space coupled photonic crystal slabs,” *Sensors*, vol. 17, no. 8, p. 1861, 2017.

[203] S. Romano, G. Zito, S. Torino, G. Calafiore, E. Penzo, G. Coppola, S. Cabrini, I. Rendina, and V. Mocella, “Label-free sensing of ultralow-weight molecules with all-dielectric metasurfaces supporting bound states in the continuum,” *Photonics Research*, vol. 6, no. 7, pp. 726–733, 2018.

[204] F. Yesilkoy, E. R. Arvelo, Y. Jahani, M. Liu, A. Tittl, V. Cevher, Y. Kivshar, and H. Altug, “Ultrasensitive hyperspectral imaging and biodetection enabled by dielectric metasurfaces,” *Nature Photonics*, vol. 13, no. 6, pp. 390–396, 2019.

[205] Y. Zhang, Z. Liang, D. Meng, Z. Qin, Y. Fan, X. Shi, D. R. Smith, and E. Hou, “All-dielectric refractive index sensor based on fano resonance with high sensitivity in the mid-infrared region,” *Results in Physics*, vol. 24, p. 104129, 2021.

[206] M. M. Miller and A. A. Lazarides, “Sensitivity of metal nanoparticle surface plasmon resonance to the dielectric environment,” *The Journal of Physical Chemistry B*, vol. 109, no. 46, pp. 21556–21565, 2005.

[207] Y. Zhao, A. N. Askarpour, L. Sun, J. Shi, X. Li, and A. Alù, “Chirality detection of enantiomers using twisted optical metamaterials,” *Nature communications*, vol. 8, no. 1, p. 14180, 2017.

[208] Y. Tang and A. E. Cohen, "Optical chirality and its interaction with matter," *Physical review letters*, vol. 104, no. 16, p. 163901, 2010.

[209] M. Decker and I. Staude, "Resonant dielectric nanostructures: a low-loss platform for functional nanophotonics," *Journal of Optics*, vol. 18, no. 10, p. 103001, 2016.

[210] L. Kang, R. P. Jenkins, and D. H. Werner, "Recent progress in active optical metasurfaces," *Advanced Optical Materials*, vol. 7, no. 14, p. 1801813, 2019.

[211] D. Van Thourhout and J. Roels, "Optomechanical device actuation through the optical gradient force," *Nature Photonics*, vol. 4, no. 4, pp. 211–217, 2010.

[212] W. Tang, W. Lyu, J. Lu, F. Liu, J. Wang, W. Yan, and M. Qiu, "Micro-scale opto-thermo-mechanical actuation in the dry adhesive regime," *Light: Science & Applications*, vol. 10, no. 1, p. 193, 2021.

[213] J.-Y. Ou, E. Plum, J. Zhang, and N. I. Zheludev, "An electromechanically reconfigurable plasmonic metamaterial operating in the near-infrared," *Nature nanotechnology*, vol. 8, no. 4, pp. 252–255, 2013.

[214] H. Du, F. S. Chau, and G. Zhou, "Mechanically-tunable photonic devices with on-chip integrated mems/nems actuators," *Micromachines*, vol. 7, no. 4, p. 69, 2016.

[215] B. V. Lahijani, M. Albrechtsen, R. Christiansen, C. Rosiek, K. Tsoukalas, M. Sutherland, and S. Stobbe, "Electronic-photonic circuit crossings," *arXiv preprint arXiv:2204.14257*, 2022.

[216] L. Yin and G. P. Agrawal, "Impact of two-photon absorption on self-phase modulation in silicon waveguides," *Optics letters*, vol. 32, no. 14, pp. 2031–2033, 2007.

[217] Z. Shan, X. Hu, X. Wang, Q. Tan, X. Yang, Y. Li, H. Liu, X. Wang, W. Huang, X. Zhu, *et al.*, "Phonon-assisted electro-optical switches and logic gates based on semiconductor nanostructures," *Advanced Materials*, vol. 31, no. 33, p. 1901263, 2019.

[218] M. Rahmani, L. Xu, A. E. Miroshnichenko, A. Komar, R. Camacho-Morales, H. Chen, Y. Zárate, S. Kruk, G. Zhang, D. N. Neshev, *et al.*, "Reversible thermal tuning of all-dielectric metasurfaces," *Advanced Functional Materials*, vol. 27, no. 31, p. 1700580, 2017.

[219] J.-Y. Ou, E. Plum, J. Zhang, and N. I. Zheludev, "Giant nonlinearity of an optically reconfigurable plasmonic metamaterial," *Advanced Materials*, vol. 28, no. 4, pp. 729–733, 2016.

[220] D. Floess, M. Hentschel, T. Weiss, H.-U. Habermeier, J. Jiao, S. G. Tikhodeev, and H. Giessen, “Plasmonic analog of electromagnetically induced absorption leads to giant thin film faraday rotation of 14°,” *Physical Review X*, vol. 7, no. 2, p. 021048, 2017.

[221] S. Lepeshov, A. Krasnok, and A. Alú, “Nonscattering-to-superscattering switch with phase-change materials,” *ACS Photonics*, vol. 6, no. 8, pp. 2126–2132, 2019.

[222] M. Wuttig, H. Bhaskaran, and T. Taubner, “Phase-change materials for non-volatile photonic applications,” *Nature photonics*, vol. 11, no. 8, pp. 465–476, 2017.

[223] W. Zhang, R. Mazzarello, and E. Ma, “Phase-change materials in electronics and photonics,” *MRS Bulletin*, vol. 44, no. 9, pp. 686–690, 2019.

[224] L. Lu, Z. Dong, F. Tijiptoharsono, R. J. H. Ng, H. Wang, S. D. Rezaei, Y. Wang, H. S. Leong, P. C. Lim, J. K. Yang, *et al.*, “Reversible tuning of mie resonances in the visible spectrum,” *ACS nano*, vol. 15, no. 12, pp. 19722–19732, 2021.

[225] T. Chu, H. Yamada, S. Ishida, and Y. Arakawa, “Compact 1× n thermo-optic switches based on silicon photonic wire waveguides,” *Optics Express*, vol. 13, no. 25, pp. 10109–10114, 2005.

[226] P. P. Iyer, R. A. DeCrescent, T. Lewi, N. Antonellis, and J. A. Schuller, “Uniform thermo-optic tunability of dielectric metalenses,” *Physical Review Applied*, vol. 10, no. 4, p. 044029, 2018.

[227] T. Badloe, J. Kim, I. Kim, W.-S. Kim, W. S. Kim, Y.-K. Kim, and J. Rho, “Liquid crystal-powered mie resonators for electrically tunable photorealistic color gradients and dark blacks,” *Light: Science & Applications*, vol. 11, no. 1, p. 118, 2022.

[228] N. S. Salakhova, I. M. Fradkin, S. A. Dyakov, and N. A. Gippius, “Twist-tunable moiré optical resonances,” *Physical Review B*, vol. 107, no. 15, p. 155402, 2023.

[229] J. Beeckman, K. Neyts, and P. J. Vanbrabant, “Liquid-crystal photonic applications,” *Optical Engineering*, vol. 50, no. 8, pp. 081202–081202, 2011.

[230] M. J. Stephen and J. P. Straley, “Physics of liquid crystals,” *Reviews of Modern Physics*, vol. 46, no. 4, p. 617, 1974.

[231] J. F. Algorri, V. Urruchi, N. Bennis, and J. M. Sánchez-Pena, “A novel high-sensitivity, low-power, liquid crystal temperature sensor,” *Sensors*, vol. 14, no. 4, pp. 6571–6583, 2014.

[232] Y. Ni, C. Chen, S. Wen, X. Xue, L. Sun, and Y. Yang, “Computational spectropolarimetry with a tunable liquid crystal metasurface,” *eLight*, vol. 2, no. 1, p. 23, 2022.

[233] A. Komar, Z. Fang, J. Bohn, J. Sautter, M. Decker, A. Miroshnichenko, T. Pertsch, I. Brener, Y. S. Kivshar, I. Staude, *et al.*, “Electrically tunable all-dielectric optical metasurfaces based on liquid crystals,” *Applied Physics Letters*, vol. 110, no. 7, 2017.

[234] D. Franklin, R. Frank, S.-T. Wu, and D. Chanda, “Actively addressed single pixel full-colour plasmonic display,” *Nature communications*, vol. 8, no. 1, p. 15209, 2017.

[235] S. Carr, D. Massatt, S. Fang, P. Cazeaux, M. Luskin, and E. Kaxiras, “Twistronics: Manipulating the electronic properties of two-dimensional layered structures through their twist angle,” *Physical Review B*, vol. 95, no. 7, p. 075420, 2017.

[236] A. Ciarrocchi, F. Tagarelli, A. Avsar, and A. Kis, “Excitonic devices with van der waals heterostructures: valleytronics meets twistronics,” *Nature Reviews Materials*, vol. 7, no. 6, pp. 449–464, 2022.

[237] F. He, Y. Zhou, Z. Ye, S.-H. Cho, J. Jeong, X. Meng, and Y. Wang, “Moiré patterns in 2d materials: A review,” *ACS nano*, vol. 15, no. 4, pp. 5944–5958, 2021.

[238] F. Wu, T. Lovorn, and A. H. MacDonald, “Topological exciton bands in moiré heterojunctions,” *Physical review letters*, vol. 118, no. 14, p. 147401, 2017.

[239] H. Yu, G.-B. Liu, J. Tang, X. Xu, and W. Yao, “Moiré excitons: From programmable quantum emitter arrays to spin-orbit–coupled artificial lattices,” *Science advances*, vol. 3, no. 11, p. e1701696, 2017.

[240] W. Chen, Z. Sun, Z. Wang, L. Gu, X. Xu, S. Wu, and C. Gao, “Direct observation of van der waals stacking–dependent interlayer magnetism,” *Science*, vol. 366, no. 6468, pp. 983–987, 2019.

[241] L. Balents, C. R. Dean, D. K. Efetov, and A. F. Young, “Superconductivity and strong correlations in moiré flat bands,” *Nature Physics*, vol. 16, no. 7, pp. 725–733, 2020.

[242] M. Förg, A. S. Baimuratov, S. Y. Kruchinin, I. A. Vovk, J. Scherzer, J. Förste, V. Funk, K. Watanabe, T. Taniguchi, and A. Högele, “Moiré excitons in mose2-wse2 heterobilayers and heterotrilayers,” *Nature communications*, vol. 12, no. 1, p. 1656, 2021.

[243] B. Huang, M. A. McGuire, A. F. May, D. Xiao, P. Jarillo-Herrero, and X. Xu, “Emergent phenomena and proximity effects in two-dimensional magnets and heterostructures,” *Nature Materials*, vol. 19, no. 12, pp. 1276–1289, 2020.

[244] A. Brenier, D. Jaque, and A. Majchrowski, “Bi-functional laser and non-linear optical crystals,” *Optical Materials*, vol. 28, no. 4, pp. 310–323, 2006.

[245] J. Lin, “Non-linear crystals for tunable coherent sources,” *Optical and quantum electronics*, vol. 22, pp. S283–S313, 1990.

[246] R. W. Boyd, A. L. Gaeta, and E. Giese, “Nonlinear optics,” in *Springer Handbook of Atomic, Molecular, and Optical Physics*, pp. 1097–1110, Springer, 2008.

[247] V. Venkataraman, K. Saha, and A. L. Gaeta, “Phase modulation at the few-photon level for weak-nonlinearity-based quantum computing,” *Nature Photonics*, vol. 7, no. 2, pp. 138–141, 2013.

[248] A. Rodriguez, M. Soljačić, J. D. Joannopoulos, and S. G. Johnson, “χ (2) and χ (3) harmonic generation at a critical power in inhomogeneous doubly resonant cavities,” *Optics express*, vol. 15, no. 12, pp. 7303–7318, 2007.

[249] A. Zalogina, L. Carletti, A. Rudenko, J. V. Moloney, A. Tripathi, H.-C. Lee, I. Shadrivov, H.-G. Park, Y. Kivshar, and S. S. Kruk, “High-harmonic generation from a subwavelength dielectric resonator,” *Science Advances*, vol. 9, no. 17, p. eadg2655, 2023.

[250] M. Celebrano, X. Wu, M. Baselli, S. Großmann, P. Biagioni, A. Locatelli, C. De Angelis, G. Cerullo, R. Osellame, B. Hecht, *et al.*, “Mode matching in multiresonant plasmonic nanoantennas for enhanced second harmonic generation,” *Nature nanotechnology*, vol. 10, no. 5, pp. 412–417, 2015.

[251] J. Lee, N. Nookala, J. S. Gomez-Diaz, M. Tymchenko, F. Demmerle, G. Boehm, M.-C. Amann, A. Alu, and M. A. Belkin, “Ultrathin second-harmonic metasurfaces with record-high nonlinear optical response,” *Advanced Optical Materials*, vol. 4, no. 5, pp. 664–670, 2016.

[252] N. Bernhardt, K. Koshelev, S. J. White, K. W. C. Meng, J. E. Froch, S. Kim, T. T. Tran, D.-Y. Choi, Y. Kivshar, and A. S. Solntsev, “Quasi-bic resonant enhancement of second-harmonic generation in ws2 monolayers,” *Nano Letters*, vol. 20, no. 7, pp. 5309–5314, 2020.

[253] L. Wang, S. Kruk, K. Koshelev, I. Kravchenko, B. Luther-Davies, and Y. Kivshar, “Nonlinear wavefront control with all-dielectric metasurfaces,” *Nano letters*, vol. 18, no. 6, pp. 3978–3984, 2018.

[254] S. Ghimire, A. D. DiChiara, E. Sistrunk, P. Agostini, L. F. DiMauro, and D. A. Reis, “Observation of high-order harmonic generation in a bulk crystal,” *Nature physics*, vol. 7, no. 2, pp. 138–141, 2011.

[255] Q. Yuan, L. Fang, H. Fang, J. Li, T. Wang, W. Jie, J. Zhao, and X. Gan, “Second harmonic and sum-frequency generations from a silicon metasurface integrated with a two-dimensional material,” *ACS Photonics*, vol. 6, no. 9, pp. 2252–2259, 2019.

[256] F. J. Löchner, A. George, K. Koshelev, T. Bucher, E. Najafidehaghani, A. Fedotova, D.-Y. Choi, T. Pertsch, I. Staude, Y. Kivshar, *et al.*, "Hybrid dielectric metasurfaces for enhancing second-harmonic generation in chemical vapor deposition grown mos2 monolayers," *Acs Photonics*, vol. 8, no. 1, pp. 218–227, 2020.

[257] C. Janisch, Y. Wang, D. Ma, N. Mehta, A. L. Elías, N. Perea-López, M. Terrones, V. Crespi, and Z. Liu, "Extraordinary second harmonic generation in tungsten disulfide monolayers," *Scientific reports*, vol. 4, no. 1, p. 5530, 2014.

[258] H. Ma, J. Liang, H. Hong, K. Liu, D. Zou, M. Wu, and K. Liu, "Rich information on 2d materials revealed by optical second harmonic generation," *Nanoscale*, vol. 12, no. 45, pp. 22891–22903, 2020.

[259] H. G. Rosa, L. Junpeng, L. C. Gomes, M. J. Rodrigues, S. C. Haur, and J. C. Gomes, "Second-harmonic spectroscopy for defects engineering monitoring in transition metal dichalcogenides," *Advanced Optical Materials*, vol. 6, no. 5, p. 1701327, 2018.

[260] X.-L. Li, W.-P. Han, J.-B. Wu, X.-F. Qiao, J. Zhang, and P.-H. Tan, "Layer-number dependent optical properties of 2d materials and their application for thickness determination," *Advanced Functional Materials*, vol. 27, no. 19, p. 1604468, 2017.

[261] R. Chen, T.-T. D. Tran, K. W. Ng, W. S. Ko, L. C. Chuang, F. G. Sedgwick, and C. Chang-Hasnain, "Nanolasers grown on silicon," *Nature Photonics*, vol. 5, no. 3, pp. 170–175, 2011.

[262] D. J. Bergman and M. I. Stockman, "Surface plasmon amplification by stimulated emission of radiation: quantum generation of coherent surface plasmons in nanosystems," *Physical review letters*, vol. 90, no. 2, p. 027402, 2003.

[263] S. I. Azzam, A. V. Kildishev, R.-M. Ma, C.-Z. Ning, R. Oulton, V. M. Shalaev, M. I. Stockman, J.-L. Xu, and X. Zhang, "Ten years of spasers and plasmonic nanolasers," *Light: Science & Applications*, vol. 9, no. 1, p. 90, 2020.

[264] S. H. Pan, Q. Gu, A. El Amili, F. Vallini, and Y. Fainman, "Dynamic hysteresis in a coherent high-β nanolaser," *Optica*, vol. 3, no. 11, pp. 1260–1265, 2016.

[265] C.-Z. Ning, "Semiconductor nanolasers," *physica status solidi (b)*, vol. 247, no. 4, pp. 774–788, 2010.

[266] J. Xing, X. F. Liu, Q. Zhang, S. T. Ha, Y. W. Yuan, C. Shen, T. C. Sum, and Q. Xiong, "Vapor phase synthesis of organometal halide perovskite nanowires for tunable room-temperature nanolasers," *Nano letters*, vol. 15, no. 7, pp. 4571–4577, 2015.

[267] S. Strauf and F. Jahnke, “Single quantum dot nanolaser,” *Laser & Photonics Reviews*, vol. 5, no. 5, pp. 607–633, 2011.

[268] T. X. Hoang, S. T. Ha, Z. Pan, W. K. Phua, R. Paniagua-Domínguez, C. E. Png, H.-S. Chu, and A. I. Kuznetsov, “Collective mie resonances for directional on-chip nanolasers,” *Nano Letters*, vol. 20, no. 8, pp. 5655–5661, 2020.

[269] M. Masharin, A. Samusev, A. Bogdanov, I. Iorsh, H. Demir, and S. Makarov, “Room-temperature exceptional-point-driven polariton lasing from perovskite metasurface,” *Advanced Functional Materials*, p. 2215007, 2023.

[270] M.-S. Hwang, H.-C. Lee, K.-H. Kim, K.-Y. Jeong, S.-H. Kwon, K. Koshelev, Y. Kivshar, and H.-G. Park, “Ultralow-threshold laser using super-bound states in the continuum,” *Nature Communications*, vol. 12, no. 1, p. 4135, 2021.

[271] C. L. Cortes and Z. Jacob, “Photonic analog of a van hove singularity in metamaterials,” *Physical Review B*, vol. 88, no. 4, p. 045407, 2013.

[272] J. Kasprzak, M. Richard, S. Kundermann, A. Baas, P. Jeambrun, J. M. J. Keeling, F. Marchetti, M. Szymańska, R. André, J. Staehli, *et al.*, “Bose–einstein condensation of exciton polaritons,” *Nature*, vol. 443, no. 7110, pp. 409–414, 2006.

[273] H. Deng, G. Weihs, D. Snoke, J. Bloch, and Y. Yamamoto, “Polariton lasing vs. photon lasing in a semiconductor microcavity,” *Proceedings of the National Academy of Sciences*, vol. 100, no. 26, pp. 15318–15323, 2003.

[274] C. Weisbuch, M. Nishioka, A. Ishikawa, and Y. Arakawa, “Observation of the coupled exciton-photon mode splitting in a semiconductor quantum microcavity,” *Physical review letters*, vol. 69, no. 23, p. 3314, 1992.

[275] A. K. Jena, A. Kulkarni, and T. Miyasaka, “Halide perovskite photovoltaics: background, status, and future prospects,” *Chemical reviews*, vol. 119, no. 5, pp. 3036–3103, 2019.

[276] Y. Zhang, C.-K. Lim, Z. Dai, G. Yu, J. W. Haus, H. Zhang, and P. N. Prasad, “Photonics and optoelectronics using nano-structured hybrid perovskite media and their optical cavities,” *Physics Reports*, vol. 795, pp. 1–51, 2019.

[277] R. Su, A. Fieramosca, Q. Zhang, H. S. Nguyen, E. Deleporte, Z. Chen, D. Sanvitto, T. C. Liew, and Q. Xiong, “Perovskite semiconductors for room-temperature exciton-polaritonics,” *Nature Materials*, vol. 20, no. 10, pp. 1315–1324, 2021.

[278] Y. Ren, P. Li, Z. Liu, Z. Chen, Y.-L. Chen, C. Peng, and J. Liu, “Low-threshold nanolasers based on miniaturized bound states in the continuum,” *Science Advances*, vol. 8, no. 51, p. eade8817, 2022.

[279] J.-H. Yang, Z.-T. Huang, D. N. Maksimov, P. S. Pankin, I. V. Timofeev, K.-B. Hong, H. Li, J.-W. Chen, C.-Y. Hsu, Y.-Y. Liu, *et al.*, "Low-threshold bound state in the continuum lasers in hybrid lattice resonance metasurfaces," *Laser & Photonics Reviews*, vol. 15, no. 10, p. 2100118, 2021.

[280] W. Bi, X. Zhang, M. Yan, L. Zhao, T. Ning, and Y. Huo, "Low-threshold and controllable nanolaser based on quasi-bic supported by an all-dielectric eccentric nanoring structure," *Optics Express*, vol. 29, no. 8, pp. 12634–12643, 2021.

[281] A. Kodigala, T. Lepetit, Q. Gu, B. Bahari, Y. Fainman, and B. Kanté, "Lasing action from photonic bound states in continuum," *Nature*, vol. 541, no. 7636, pp. 196–199, 2017.

[282] C. Huang, C. Zhang, S. Xiao, Y. Wang, Y. Fan, Y. Liu, N. Zhang, G. Qu, H. Ji, J. Han, *et al.*, "Ultrafast control of vortex microlasers," *Science*, vol. 367, no. 6481, pp. 1018–1021, 2020.

[283] Y. Chong, L. Ge, H. Cao, and A. D. Stone, "Coherent perfect absorbers: time-reversed lasers," *Physical review letters*, vol. 105, no. 5, p. 053901, 2010.

[284] J. Zhang, K. F. MacDonald, and N. I. Zheludev, "Controlling light-with-light without nonlinearity," *Light: Science & Applications*, vol. 1, no. 7, pp. e18–e18, 2012.

[285] G. Trainiti, Y. Ra'di, M. Ruzzene, and A. Alù, "Coherent virtual absorption of elastodynamic waves," *Science advances*, vol. 5, no. 8, p. eaaw3255, 2019.

[286] Q. Zhong, L. Simonson, T. Kottos, and R. El-Ganainy, "Coherent virtual absorption of light in microring resonators," *Physical Review Research*, vol. 2, no. 1, p. 013362, 2020.

[287] A. V. Kavokin, J. J. Baumberg, G. Malpuech, and F. P. Laussy, *Microcavities*, vol. 21. Oxford university press, 2017.

[288] C. A. Rosiek, G. Arregui, A. Vladimirova, M. Albrechtsen, B. Vosoughi Lahijani, R. E. Christiansen, and S. Stobbe, "Observation of strong backscattering in valley-hall photonic topological interface modes," *Nature Photonics*, pp. 1–7, 2023.

[289] J. Liu, G. Huang, R. N. Wang, J. He, A. S. Raja, T. Liu, N. J. Engelsen, and T. J. Kippenberg, "High-yield, wafer-scale fabrication of ultralow-loss, dispersion-engineered silicon nitride photonic circuits," *Nature communications*, vol. 12, no. 1, p. 2236, 2021.

[290] B. Casabone, C. Deshmukh, S. Liu, D. Serrano, A. Ferrier, T. Hümmer, P. Goldner, D. Hunger, and H. de Riedmatten, "Dynamic control of purcell enhanced emission of erbium ions in nanoparticles," *Nature communications*, vol. 12, no. 1, p. 3570, 2021.

[291] A. M. Dibos, M. T. Solomon, S. E. Sullivan, M. K. Singh, K. E. Sautter, C. P. Horn, G. D. Grant, Y. Lin, J. Wen, F. J. Heremans, *et al.*, "Purcell enhancement of erbium ions in tio2 on silicon nanocavities," *Nano Letters*, vol. 22, no. 16, pp. 6530–6536, 2022.

[292] A. Gritsch, L. Weiss, J. Früh, S. Rinner, and A. Reiserer, "Narrow optical transitions in erbium-implanted silicon waveguides," *Physical Review X*, vol. 12, no. 4, p. 041009, 2022.

[293] Y. Liu, Z. Qiu, X. Ji, A. Lukashchuk, J. He, J. Riemensberger, M. Hafermann, R. N. Wang, J. Liu, C. Ronning, *et al.*, "A photonic integrated circuit–based erbium-doped amplifier," *Science*, vol. 376, no. 6599, pp. 1309–1313, 2022.

[294] M. Raha, S. Chen, C. M. Phenicie, S. Ourari, A. M. Dibos, and J. D. Thompson, "Optical quantum nondemolition measurement of a single rare earth ion qubit," *Nature communications*, vol. 11, no. 1, p. 1605, 2020.

[295] T. Asano, B.-S. Song, and S. Noda, "Analysis of the experimental q factors (~ 1 million) of photonic crystal nanocavities," *Optics express*, vol. 14, no. 5, pp. 1996–2002, 2006.

[296] Y.-X. Yin, X.-P. Zhang, X.-J. Yin, Y. Li, X.-R. Xu, J.-M. An, Y.-D. Wu, X.-P. Liu, and D.-M. Zhang, "High-q-factor tunable silica-based microring resonators," in *Photonics*, vol. 8, p. 256, MDPI, 2021.

[297] P. B. Deotare, M. W. McCutcheon, I. W. Frank, M. Khan, and M. Lončar, "High quality factor photonic crystal nanobeam cavities," *Applied Physics Letters*, vol. 94, no. 12, 2009.

[298] M. Albrechtsen, B. Vosoughi Lahijani, R. E. Christiansen, V. T. H. Nguyen, L. N. Casses, S. E. Hansen, N. Stenger, O. Sigmund, H. Jansen, J. Mørk, *et al.*, "Nanometer-scale photon confinement in topology-optimized dielectric cavities," *Nature Communications*, vol. 13, no. 1, p. 6281, 2022.

[299] T. Delage, J. Sokoloff, O. Pascal, V. Mazières, A. Krasnok, and T. Callegari, "Plasma ignition via high-power virtual perfect absorption," *ACS Photonics*, 2023.